LBL-13937

Lawrence Berkeley Laboratory
UNIVERSITY OF CALIFORNIA

EARTH SCIENCES DIVISION

MATHEMATICAL MODELING OF THE BEHAVIOR OF GEOTHERMAL SYSTEMS UNDER EXPLOITATION

Gudmundur Svavar Bodvarsson
(Ph.D. thesis)

MASTER

January 1982

NOTICE

PORTIONS OF THIS REPORT ARE ILLEGIBLE. It has been reproduced from the best available copy to permit the broadest possible availability.

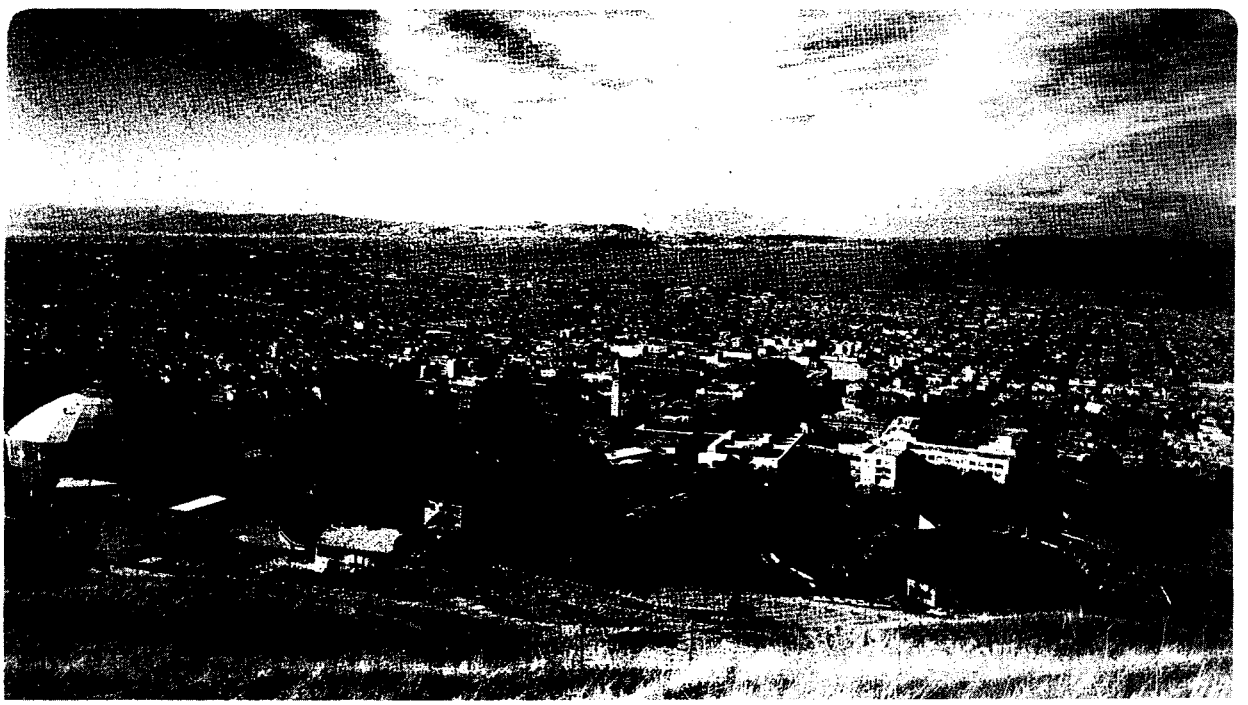

Prepared for the U.S. Department of Energy under Contract W-7405-ENG-48

DISTRIBUTION OF THIS DOCUMENT IS UNLIMITED

DISCLAIMER

This report was prepared as an account of work sponsored by an agency of the United States Government. Neither the United States Government nor any agency Thereof, nor any of their employees, makes any warranty, express or implied, or assumes any legal liability or responsibility for the accuracy, completeness, or usefulness of any information, apparatus, product, or process disclosed, or represents that its use would not infringe privately owned rights. Reference herein to any specific commercial product, process, or service by trade name, trademark, manufacturer, or otherwise does not necessarily constitute or imply its endorsement, recommendation, or favoring by the United States Government or any agency thereof. The views and opinions of authors expressed herein do not necessarily state or reflect those of the United States Government or any agency thereof.

DISCLAIMER

Portions of this document may be illegible in electronic image products. Images are produced from the best available original document.

LBL--13937

DE82 010925

LBL-13937

DISCLAIMER

This book was prepared as an account of work sponsored by an agency of the United States Government. Neither the United States Government nor any agency thereof, nor any of their employees, makes any warranty, express or implied, or assumes any legal liability or responsibility for the accuracy, completeness, or usefulness of any information, apparatus, product, or process disclosed, or represents that its use would not infringe privately owned rights. Reference herein to any specific commercial product, process, or service by trade name, trademark, manufacturer, or otherwise, does not necessarily constitute or imply its endorsement, recommendation, or favoring by the United States Government or any agency thereof. The views and opinions of authors expressed herein do not necessarily state or reflect those of the United States Government or any agency thereof.

MATHEMATICAL MODELING OF THE BEHAVIOR OF GEOTHERMAL SYSTEMS UNDER EXPLOITATION

Gudmundur Svavar Bodvarsson

Earth Sciences Division
Lawrence Berkeley Laboratory
University of California
Berkeley, California 94720

Ph.D. Thesis

January 1982

This work was supported by the Assistant Secretary for Conservation and Renewable Energy, Office of Renewable Technology, Division of Geothermal and Hydropower Technologies of the U. S. Department of Energy under Contract No. W-7405-ENG-48.

DISTRIBUTION OF THIS DOCUMENT IS UNLIMITED

MGW

MATHEMATICAL MODELING OF THE BEHAVIOR OF GEOTHERMAL SYSTEMS UNDER EXPLOITATION

Gudmundur Svavar Bodvarsson

Degree: Doctor of Philosophy, Major Subject: Engineering

Signature: P. A. Witherspoon
P. A. Witherspoon, Thesis Committee Chairman

ABSTRACT

Analytical and numerical methods have been used in this investigation to model the behavior of geothermal systems under exploitation. The work is divided into three parts: (1) development of a numerical code, (2) theoretical studies of geothermal systems, and (3) field applications.

A new single-phase three-dimensional simulator, capable of solving heat and mass flow problems in a saturated, heterogeneous porous or fractured medium has been developed. The simulator uses the integrated finite difference method for formulating the governing equations and an efficient sparse solver for the solution of the linearized equations.

In the theoretical studies, various reservoir engineering problems have been examined. These include (a) well-test analysis, (b) exploitation strategies, (c) injection into fractured rocks, and (d) fault-charged geothermal reservoirs.

(a) The interpretation of results from two-phase well tests are complicated by the lack of relative permeability data. It was found that the most important data are the saturation values for the immobile liquid cutoff. Analysis of well tests can yield the relative permeability parameters in terms of the flowing enthalpy, but not the in-situ saturations.

(b) Numerical simulation studies of a two-phase reservoir with a shallow steam zone show that it is more beneficial in the long run to produce from the lower-enthalpy liquid zone rather than from the shallower steam zone.

(c) An integrated analytical/numerical approach has been used to study injection into fractured geothermal reservoirs. The results show that if the injection wells are properly sited, premature breakthrough of the cold water at the production wells through fractures will not occur.

(d) A semi-analytical model has been developed for fault-charged reservoirs. Using temperature profiles from wells, the model was applied to the hydrothermal system at Susanville, California, and the recharge rate from an inferred fault was estimated.

Finally, numerical simulators were used to analyze injection test data from Krafla, Iceland, and to model the Baca field in New Mexico. Analysis of these tests yields values for transmissivity and storativity of the Krafla reservoir. The Baca simulations show that due to the low transmissivity it is questionable whether the reservoir can supply steam for the proposed 50 MW_e power plant for 30 years.

This work is dedicated to my parents.

TABLE OF CONTENTS

LIST OF FIGURES ix

LIST OF TABLES xvii

NOMENCLATURE xviii

ACKNOWLEDGEMENTS xxiv

INTRODUCTION 1
- Objective and Organization of Present Work 2
- Basic Characteristics of Geothermal Systems 4
- Classification of Geothermal Fields. 7
- Methods of Analyzing Geothermal Systems 8
- The Use of Distributed-Parameter Models 11

CODE DEVELOPMENT 14
- Background. 14
- Numerical Code 18
  - Governing Equations 18
  - Deformation 20
  - Assumptions 22
  - Numerical Formulation 23
  - Program Structure 28
  - Validation 33
- Summary of Code Development 48

THEORETICAL STUDIES 49
- Analysis of Well Tests in Geothermal Reservoirs 50
  - Injection Testing of Hot-water Reservoirs 51
  - Effects of Relative Permeability Parameters in Two-Phase Reservoirs 66
- Reservoir Exploration Strategies 92
  - Reservoir with a steam cap 93
  - Single-phase liquid-dominated reservoir 119
  - Vapor-dominated reservoirs 121
  - Conclusions 123
- Injection into Fractured Geothermal Reservoirs 125
  - Basic Model 128
  - Analytical Approach 128
    - Mathematical model 128
    - Results of the analytical study 134

Numerical Studies 154
Comparison of analytical and numerical results . 160
Importance of assumptions employed in analytical approach 160
Importance of permeability in rock matrix . . 167
Application to Field Examples 184
Conclusions 188
Fault-charged Geothermal Reservoirs. 191
Mathematical Model 194
Evolution of Fault-Charged Hydrothermal Systems . . 199
Early-time behavior 201
Intermediate-time behavior 203
Late-time behavior 203
Evolution of the Thermal Field in the Aquifer. . . 205
Heat losses from the aquifer 210
Heat losses at the surface 217
Steady-state conditions 217
Applications to the Susanville Hydrothermal System. . 220
Conclusions 230
Summary of Theoretical Studies. 231

FIELD APPLICATIONS 233
Modeling of Well Tests at Krafla, Iceland 234
Reservoir Model. 237
Well Testing at Krafla 240
Field-Wide Modeling of the Baca Field, New Mexico . . . 257
Geology 259
Reservoir Capacity 261
Volumetric estimation 261
Sensitivity of results 266
Reservoir Longevity 267
Numerical approach 267
Comparison between lumped- and distributed-parameter models 284
Conclusions 290
Summary of Field Application Studies 293

CONCLUSIONS 295

REFERENCES 302

APPENDICES 324
Appendix A: Input Guide for Program PT 324
Appendix B: Equation of State for Liquid Water . . 340
Appendix C: Simultaneous Solution of Thermal Equations for Fracture and Rock . . . 344
Appendix D: Solution of Equations for Fault-Charged Reservoirs 347

LIST OF FIGURES

Figure 1. Schematic diagram of topics studied 3

Figure 2. Conceptual reservoir model (after White, 1973) . . 5

Figure 3. Typical consolidation curve 21

Figure 4. Typical node-connection network and nomenclature. . 24

Figure 5. Comparison between analytical and numerical solution for the Theis problem 34

Figure 6. Comparison between analytical and numerical solution for the constant-pressure problem . . . 36

Figure 7. Comparison between analytical and numerical solution in the fluid duct 40

Figure 8. Type curves for horizontal fracture problem (after Gringarten, 1971) 42

Figure 9. Mesh used for horizontal fracture problem . . . 43

Figure 10. Comparison between analytical and numerical solution for $h_D = 1$ 44

Figure 11. Mesh used for the vertical fracture problem (after Palen, 1980) 46

Figure 12. Comparison between numerical values obtained and values given by Cinco-Ley (1977) 47

Figure 13. Model used in the study of injection into a porous media geothermal reservoir. 54

Figure 14. Pressure behavior at an observation well (r = 2.5 m) during cold water (100°C) injection into a 300°C geothermal reservoir. . . 56

Figure 15. Transient injection pressure behavior, when 100°C water is injected into a 300°C reservoir, for different values of transmissivity and storativity of the reservoir. 58

Figure 16. Injection pressure behavior, when 100°C water is injected into a well located in a cold-spot (lower temperature region) 59

Figure 17. Schematic diagram showing reservoir conditions immediately after injection 61

Figure 18. Pressure fall-off after 1.2 days of injection . . 62

Figure 19. Pressure transient behavior during a production test, immediately following 1.2 days of injection 63

Figure 20. The Corey and the "X" relative permeability curves 71

Figure 21. The relationship between flowing enthalpy and liquid saturation for linear relative permeability curves 72

Figure 22. The relationship between kinematic viscosity and liquid saturation for linear relative permeability curves 74

Figure 23. Pressure transient behavior during a well test in a two-phase reservoir 75

Figure 24. Flowing enthalpy during a well test in a two-phase reservoir 76

Figure 25. The relationship between flowing enthalpy and liquid relative permeability curves 78

Figure 26. The relationship between flowing enthalpy and vapor relative permeability for Corey and "X" relative permeability curves. 79

Figure 27. The relationship between the rise in flowing enthalpy and the initial flowing enthalpy for a porosity of $\phi = .05$ 83

Figure 28. The relationship between flowing enthalpy and liquid saturation for the Corey relative permeability curves 85

Figure 29. The relationship between the rise in flowing enthalpy and the initial flowing enthalpy for a porosity of $\phi = .25$ 86

Figure 30. The relationship between porosity and the rise in flowing enthalpy 87

Figure 31. The relationship between flow rate and the rise in flowing enthalpy 89

Figure 32. A schematic reservoir model of the Olkaria geothermal field 96

Figure 33. Initial reservoir conditions. 98

Figure 34. Pressure transients for Case 1 101

Figure 35. Changes in vapor saturation due to production from vapor zone 103

Figure 36. Changes in mass flow rate during production from vapor zone (Case 1) 104

Figure 37. Temperature changes due to production from vapor zone (Case 1) 106

Figure 38. Pressure changes due to production from liquid zone (Case 2). 108

Figure 39. Pressure changes with time in three different parts of the reservoir (Case 2) 110

Figure 40. Vapor saturation changes due to production from liquid zone (Case 2) 111

Figure 41. Flow rate changes due to production from liquid zone (Case 2) 113

Figure 42. Flow rate changes during production from both vapor and liquid zones (Case 3) 115

Figure 43. Pressure changes during simulation of Case 4 . . 117

Figure 44. Vapor saturation changes during simulation of Case 4 118

Figure 45. Flow rate changes during simulation of Case 4 . . 120

Figure 46. Basic model of an injection well penetrating a reservoir with equally spaced horizontal fractures 129

Figure 47. Schematic of analytical model 130

Figure 48. Plots of thermal fronts at various dimensionless times τ for $\theta < 0.01$; η is dimensionless vertical distance and ξ is dimensionless advancement along the fracture 136

Figure 49. Plots of thermal fronts at various dimensionless times τ for $\theta < 100$ 137

Figure 50. Type curves for the movement of the thermal front in the fracture for various values of θ . . 139

Figure 51. Advancement of the thermal front in the rock matrix for small values of θ. 145

Figure 52. Advancement of the thermal front in the rock matrix for large values of θ. 146

Figure 53. Temperature distribution in the fracture and rock matrix at various dimensionless times . . . 147

Figure 54. Diffuseness of the thermal front at intermediate times 149

Figure 55. Diffuseness of the thermal front at late times . . 150

Figure 56. The heat transfer mechanism in the system at late times for the reverse case - hot-water injection into a colder reservoir. 151

Figure 57. Heat flux density along the fracture at late times. The parameter Q_d represents dimensionless energy loss from fracture to rock. . . . 153

Figure 58. Schematic of the mesh used in the numerical calculations 155

Figure 59. Comparison of the analytical and numerical results for $\theta = 0.01$ 157

Figure 60. The effects of numerical dispersion on the thermal front at various times 158

Figure 61. Graphical integration showing an intermediate-time thermal front isotherm as $T_D = 0.44$ . . . 159

Figure 62. Comparison of analytical and numerical results (with relaxed assumptions) for advancement of the thermal front along the fracture 161

Figure 63. Temperature distribution in the rock matrix at various times; no horizontal conduction . . . 162

Figure 64. Thermal diffusion into the rock matrix at various times; horizontal conduction 163

Figure 65. The late-time heat transfer mechanism for the rock-fracture system when horizontal conduction is considered. 165

Figure 66. Effect of permeable rock matrix on the advancement of the thermal front along the fracture . . 169

Figure 67. Schematic model of convection-dominated rock/fracture system 172

Figure 68. Mesh used in the study of convection-dominated systems 175

Figure 69. Pressure distribution along the dimensionless radial coordinate r_D for $\omega < 0.01$ 177

Figure 70. Pressure distribution along the dimensionless coordinate r_D for $\omega = 1$ 178

Figure 71. Pressure distribution along the dimensionless radial coordinate r_D for $\omega > 100$ 179

Figure 72. Dimensionless fluid flow along the fracture q_{HD} . 180

Figure 73. Cumulative flow from fracture to rock matrix . . 182

Figure 74. Location of the thermal front in the fractures versus time for different fracture spacing . . . 185

Figure 75. Geological model of the Cerro Prieto geothermal field (after Tsang et al., 1979) 187

Figure 76. Temperature profile from a well at Klamath Falls, Oregon (after O'Brien et al., 1981) 193

Figure 77. The mathematical model considered for fault problem 195

Figure 78. Evolution of a fault-charged hydrothermal system for $\xi_1 = 1.0$ 200

Figure 79. Evolution of a fault-charged hydrothermal system for $\xi_1 = 1.0$ 202

Figure 80. Comparison between the present solution and the Lauwerier solution 204

Figure 81. Evolution of the thermal field in the aquifer . . 206

Figure 82. θ_1-dependence of the temperature profile along the aquifer for $\tau_1 = .01$ 207

Figure 83. θ_1-dependence of the temperature profile along the aquifer for $\tau_1 = .10$ 208

Figure 84. θ_1-dependence of the temperature profile along the aquifer for $\tau_1 = 1.0$ 209

Figure 85. Dimensionless heat loss (Q_D) from the aquifer to the caprock and bedrock 211

Figure 86. Total dimensionless heat losses (Q_{D_t}) from the aquifer for $\theta_1 = .0001$ 213

Figure 87. Total dimensionless heat losses (Q_{D_t}) from the aquifer for $\theta_1 = .01$ 214

Figure 88. Total dimensionless heat losses (Q_{D_t}) from the aquifer for $\theta_1 = 1.0$ 215

Figure 89. Total dimensionless heat losses (Q_{D_t}) from the aquifer for $\theta_1 = 100$ 216

Figure 90. Heat losses at the ground surface. 218

Figure 91. Steady-state temperature distribution in the aquifer for various values of κ/σ. 219

Figure 92. Steady-state heat losses from the aquifer for various values of σ 221

Figure 93. Temperature contours at 1150 m elevation at Susanville (after Benson et al., 1981). . . . 223

Figure 94. Comparison between observed and calculated temperature contour data 225

Figure 95. Comparison between calculated and observed temperature profiles in wells 226

Figure 96. Calculated heat flows at Susanville 229

Figure 97. The spreading zone in North Iceland. Mapped by Kristjan Saemundsson (after Bjornsson et al., 1979) 235

Figure 98. Outline geological map of the Krafla Caldera and associated fissure swarm. Mapped by Kristjan Saemundsson (after Bjornsson et al., 1979) 236

Figure 99. Wells drilled to date at Krafla geothermal field (after Stefansson, 1981) 238

Figure 100. Sectional geological drawing of the Krafla geothermal field (after Stefansson, 1981) . . . 239

Figure 101. Simplified casing diagram for Krafla well K3-13. . 242

Figure 102. Injection-test data for well KJ-13 244

Figure 103. Comparison between observed and calculated water-level data for well KJ-13 246

Figure 104. Advancement of the cold water front along the fracture 249

Figure 105. Fluid compressibility versus vapor saturation for a temperature of 300°C and the Corey relative permeability curves 252

Figure 106. Injection-test data for well KG-12 254

Figure 107. Comparison between calculated and observed water-level data for well KG-12 255

Figure 108. Base map of the Valles Caldera showing shallow temperature gradients (°F/100 ft), geophysical survey lines (e.g., A-A'), specific faults, and the estimated hot water reservoir boundary . . 258

Figure 109. Geologic cross sections of the Valles Caldera region (after Bailey and Smith, 1978). . . . 260

Figure 110. Deep reservoir temperature contour (3000 ft ASL) in °F (after Union, 1978) 263

Figure 111. Shallow temperature gradients and telluric profiles along survey line B-B' 264

Figure 112. The mesh used in the longevity study for "closed reservoir" cases 268

Figure 113. The temperature, pressure, and saturation behavior in the production node for three of the constant flow rate cases 271

Figure 114. Variation with time of boiling rates and vapor saturation for the constant production, closed-boundary case 272

Figure 115. Production rate versus time for the closed-boundary case 276

Figure 116. Mesh-dependence: pressure behavior in the production node 278

Figure 117. Relative permeability curves used in the study . . 281

Figure 118. Effects of relative permeability curves . . . 282

Figure 119. Comparison between lumped- and distributed-parameter models 288

LIST OF TABLES

Table 1. Input blocks for program PT. 29

Table 2. Validation problem #3: Comparison between analytical and numerical solutions for the conduction problem 37

Table 3. Validation problem #4: Comparison between analytical and numerical solutions for the convection problem 39

Table 4. Parameters used in the study of injection testing of porous media reservoirs 56

Table 5. Reservoir parameters used in the Olkaria study. . . 97

Table 6. Parameters used in the study of the effects of horizontal conduction. 164

Table 7. Parameters and grid spacing used in the nonisothermal permeable rock study 170

Table 8. Parameters used in multifractured reservoir . . . 186

Table 9. Parameters used for the Susanville model 224

Table 10. Parameters used in simulation of Baca field . . . 269

Table 11. Summary of cases and primary results. 274

Table 12. Relative permeability equations. 280

Table 13. Major subroutines and their functions 324

NOMENCLATURE

a	geothermal gradient (°C)
a_p	implicit factor for pressure
a_T	implicit factor for temperature
a_v	coefficient of compressibility (pa^{-1})
A	surface area (m^2)
A_e	energy accumulation term
A_m	mass accumulation term
b	fracture aperture (m)
B	bedrock thickness (m), also boiling rate (kg/s)
c	heat capacity (J/kg°C)
C_c	compression index (pa^{-1})
C_k	slope of e-log k curve (m^{-2})
C_r	dimensionless parameter for vertical fractures
C_s	swelling index (pa^{-1})
d	upstream weighting factor
D	thickness of rock matrix (bedrock)(m)
$D_{m,n}$	distance from nodal point of node m to the interface (m)
$D_{n,m}$	distance from nodal point of node n to the interface (m)
e	void ratio
e_f	internal energy of fluid (J/kg)
e_o	reference void ratio
g	acceleration due to gravity (m/s^2)
G_f	mass source/sink (kg/m^3s)
G_H	heat source/sink (J/m^3s)

h	in-place enthalpy (J/kg)
h_f	flowing enthalpy (J/kg)
H	aquifer thickness (m)
H_w	wellhead enthalpy (J/kg)
H_{sl}	saturated liquid enthalpy (J/kg)
H_{sv}	saturated vapor enthalpy (J/kg)
J_o	Bessel function of the first kind, zero order
J_1	Bessel function of the first kind, first order
k	absolute permeability (m^2)
k_o	reference permeability (m^2)
k_r	permeability in radial direction (m^2)
k_{rl}	relative permeability of the liquid phase
k_{rv}	relative permeability of the vapor phase
k_z	permeability in vertical direction (m^2)
m	slope of pressure-log time plot (pa/s)
n	number of fractures
$\vec{n}$	unit vector normal to the interface
p	Laplace parameter
P	pressure
P_D	dimensionless pressure
q	flow rate (m^3/s)
q_{FH}	volumetric flow along fracture (m^3/s)
q_{HD}	dimensionless flow along fracture
q_s	theoretical steam requirement (kg/s)
q_t	total flow rate (m^3/s)

q_{SF}	sandface flow rate (kg/s)
q_{WH}	wellhead flow rate (kg/s)
Q	heat flux (J/s)
Q_D	dimensionless energy losses
Q_{D_s}	dimensionless energy losses at the ground surface
Q_{D_t}	total dimensionless energy losses
Q_e	dimensionless energy flux
Q_H	energy losses from rock matrix to fracture (J/s)
Q_m	dimensionless mass flux
r	radial coordinate (m)
r_c	radial distance from injection well to the location of uniform energy sweep (m)
r_D	dimensionless radial distance
r_f	fracture radius (m)
r_w	well radius (m)
R	radial distance from injection well to the location of the thermal front (m)
R_D	dimensionless distance to constant pressure boundary
R_o	radial distance from injection well to the constant pressure boundary (m)
s	water level (m)
S	saturation
S_q	steam quality
S_{rl}	residual liquid saturation
S_{rv}	residual vapor saturation

t	time (sec)
t_c	time of uniform energy sweep (sec)
t_D	dimensionless time
T	temperature (°C)
T_{b1}	temperature at ground surface (°C)
T_{b2}	temperature of the lower boundary below bedrock (°C)
T_D	dimensionless temperature
T_g	dimensionless geothermal gradient, $T_g = aD/(T_f - T_{b1})$
T_i	injection temperature (°C)
T_m	hydraulic mobility
T_o	initial temperature (°C)
T_{TF}	the isotherm defined as the thermal front, generally $T_{TF} = 1/2(T_i + T_o)$ (°C)
u	temperature in the fracture/aquifer in the Laplace domain
v	temperature in the rock matrix (caprock) in the Laplace domain
v_d	Darcy velocity (m/s)
v_H	velocity of the hydrodynamic front (m/s)
v_T	velocity of the thermal front (m/s)
V	volume (m^3)
w	temperature in the bedrock in Laplace domain
Y_0	Bessel function of the second kind, zero order
Y_1	Bessel function of the second kind, first order
x	distance from the fault (m)
x_f	linear extent of vertical fracture (m)
z	vertical coordinate (m)

α_r	rock expansivity ($°C^{-1}$)
α_t	total expansivity ($°C^{-1}$)
α_w	fluid expansivity ($°C^{-1}$)
β_r	rock compressibility (pa^{-1})
β_t	total compressibility (pa^{-1})
β_w	fluid compressibility (pa^{-1})
γ	dimensionless heat capacity, $\gamma = \rho_2 c_2/\rho_1 c_1$
η	similarity parameter, $\eta = r/\sqrt{t}$ or
	dimensionless vertical coordinate, $\eta = z/D$
η_g	directional cosine for the gravity term
θ	dimensionless energy potential, $\theta = \rho_f c_f b/\rho_r c_r D$
θ_1	dimensionless heat capacity, $\theta_1 = (B/D)(\rho_a c_a/\rho_1 c_1)$
κ	dimensionless thermal conductivity, $\kappa = \lambda_2/\lambda_1$
λ	thermal conductivity (J/m-s-°C)
μ	dynamic viscosity (kg/m-s)
ν	kinematic viscosity (m^2/s)
ν_l	kinematic viscosity of the liquid phase (m^2/s)
ν_t	total kinematic viscosity, $1/\nu_t = (k_{rl}/\nu_l) + (k_{rv}/\nu_v)$
ν_v	kinematic viscosity of the vapor phase (m^2/s)
ξ	dimensionless distance from injection well, $\xi = \lambda\pi r^2(2 + \theta)/\rho_w c_w qD$
ξ_1	dimensionless distance from fault, $\xi_1 = \lambda_1 x/p_w c_w qD$
ρ	density (kg/m^3)
ρ_g	fluid density at the interface (for gravity calculations, kg/m^3)
	$\rho_g = 1/2(\rho_n + \rho_m)$

$(\rho c)_M$	integrated heat capacity for node m, $(\rho c)_M = \phi\rho_w c_w + (1 - \phi)\rho_r c_r$ (J/m^3-°C)
σ	dimensionless geometrical parameter $\sigma = B/D$
σ'	effective stress (kg/m-s^2)
σ_N	normal stress (kg/m-s^2)
τ	dimensionless time (injection problem) $\tau = \lambda t/\rho_r c_r D^2$
τ_1	dimensionless time (fault problem), $\tau_1 = \lambda_1 t/\rho_1 c_1 D^2$
ϕ	porosity
ω	dimensionless transmissivity, $\omega = (D/b)(k_r/k_f)$

subscripts

a	aquifer
f	fracture/fault
ℓ	liquid water
m	node m
n	node n
r	rock matrix
v	vapor
w	fluid
1	caprock
2	bedrock

ACKNOWLEDGMENTS

I would first like to express my gratitude to Prof. P. A. Witherspoon for accepting me in a doctoral program at Berkeley, where I was able to participate in his excellent research environment. His encouragement and critical review of this work is most appreciated. To my thesis advisor, Dr. Chin Fu Tsang, I convey my gratitude for his invaluable guidance and insight. I sincerely thank Prof. W. H. Somerton for his critical review of this work.

Many friends and colleagues at Lawrence Berkeley Laboratory have been an inspiration to me. I extend my gratitude to Dr. Marcelo Lippmann for his friendship and critical review of this work. I thank Dr. T. N. (Nari) Narasimhan for sharing his expertise in mass transport in porous media and Dr. Karsten Pruess for educating me in the physics of two-phase flow. The moral support given to me by my friend Mike Wilt is gratefully appreciated. Also my thanks are due to Sally Benson, Einar T. Eliasson, Walter Palen, Michael O'Sullivan, Ron Schroeder, Valgardur Stefansson, and others for their help and stimulating discussions. It is with gratitude that I acknowledge the expert typing of Lois Armetta and careful drawing of the figures by Marilee Bailey.

Finally, if not for the help and encouragement of my wife Maria, this work would not have been completed. She and my son Daniel were a constant source of inspiration to me during this period.

Financial support given to me by the Icelandic Student Loan Association and by the Assistant Secretary for Conservation and Renewable Energy, Office of Renewable Technology, Division of Geothermal and Hydropower Technologies of the U. S. Department of Energy, Contract No. W-7405-ENG-48, is gratefully acknowledged.

INTRODUCTION

In recent years considerable research has been devoted to the study of geothermal systems in the United States. This increased interest in geothermal energy is primarily due to the diminishing availability of fossil fuels, and the subsequent need to develop alternate energy resources. The ultimate goal of research into nuclear, solar, and geothermal energy resources is to develop methodology economically feasible for the generation of electicity from these alternate energy resources in order to complement and gradually decrease the need for fossil fuels. However, recent changes in the administration in Washington have resulted in a change in the direction of energy-related research. As this is written all indications are that federal funds for geothermal research will be severely decreased in the next few years, drastically curtailing the potential contribution of geothermal energy to power needs in the United States.

The development of most geothermal fields in the United States for electrical power production, space heating, or other applications is in the beginning stages. Although over 900 MW are presently produced at The Geysers, California, representing the largest power production from any single geothermal field in the world, the exploitation of most other high-temperature geothermal systems is only in the exploration stage if existant at all. Exploitation of low-temperature geothermal resources in the United States has hardly begun, as only a small fraction of the potential low-temperature areas in the U.S. have undergone deep exploratory drilling.

By comparison, electrical power has been produced from geothermal fields in such countries as Italy and New Zealand for many decades. Furthermore, use of geothermal energy for space heating is widely employed by many countries, especially in Europe. In Iceland approximately 75 percent of the homes are heated by geothermal energy, and there are plans to increase that number to over 85 percent within the next five years. These examples illustrate that the enormous potential of geothermal energy. The reduction of federal funds for geothermal research in the United States may drastically decrease the near-future impact of geothermal energy on the overall energy picture in the United States.

OBJECTIVE AND ORGANIZATION OF PRESENT WORK

The objective of the present work is to study the physical behavior of geothermal systems in order to obtain a better understanding of their response to exploitation. These studies may be subdivided into three parts as shown in Figure 1:

(1) development of a numerical code for simulation studies of geothermal systems;

(2) theoretical studies of geothermal systems under exploitation;

(3) application of the numerical code and the results of theoretical studies to actual field conditions.

In the first part, a new numerical simulator, capable of solving one- two- or three-dimensional mass and heat transport problems in heterogeneous porous and/or fractured rocks, is described. The simulator

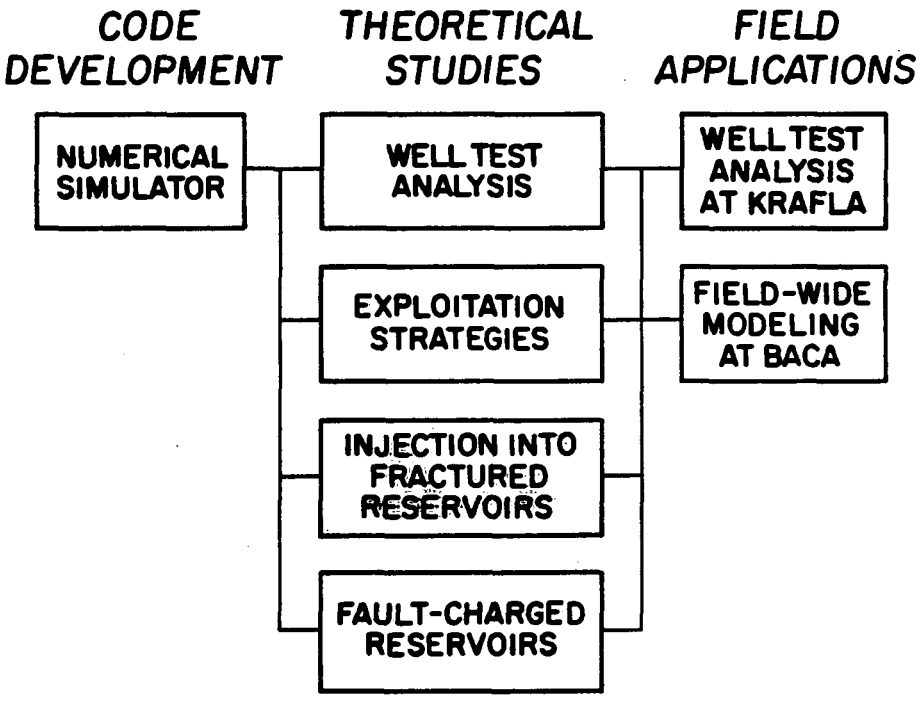

Figure 1. Schematic diagram of topics studied. [XBL 8111-4851]

is very general as it allows for temperature and/or pressure-dependent rock and fluid properties. It has the option of solving the mass and energy equations separately or a complete, simultaneous solution of both can be chosen using an efficient sparse solver. The development of this new simulator was necessary so that complex problems such as injection into fractured reservoirs could be solved efficiently.

In the second part of this dissertation, the simulator as well as analytical methods are employed for theoretical studies of geothermal systems. Four fundamental problems of current interest to the geothermal community are addressed: well test analysis of single- and two-phase wells, reservoir exploitation strategies, injection into fractured reservoirs, and recharge into fault-charged reservoirs. The analysis of these problems gives valuable insights into the basic physics governing mass and heat flow in geothermal systems.

In the final part, the basic background obtained in the theoretical studies is applied to field data. Well test data from the Krafla geothermal field in Iceland are analyzed using the new simulator and important reservoir parameters are determined. Field-wide simulation studies of the Baca field, New Mexico, are carried out in an effort to estimate the potential of the reservoir for electrical power production.

BASIC CHARACTERISTICS OF GEOTHERMAL SYSTEMS

The basic characteristics of geothermal systems are shown in Figure 2. The basic features include a heat source, a permeable aquifer, relatively

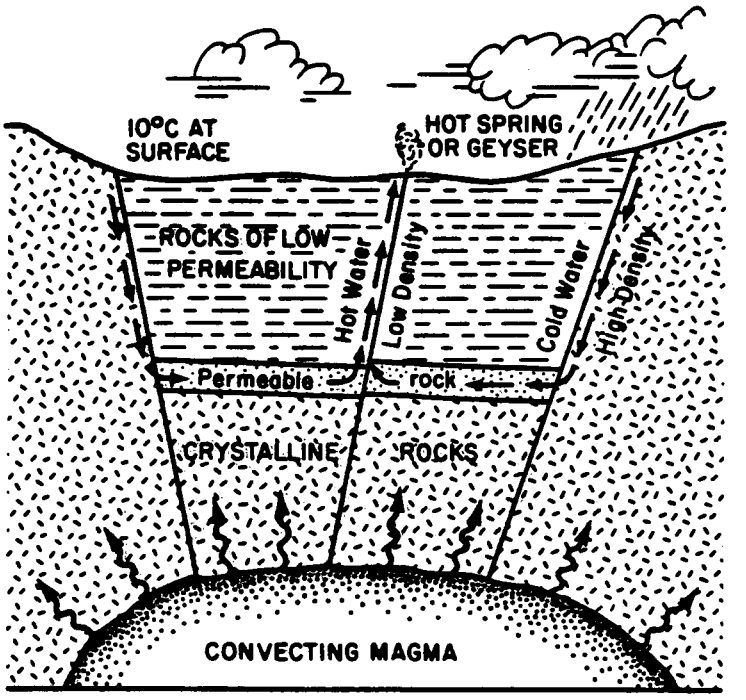

Figure 2. Conceptual reservoir model (after White, 1973).
[XBL 8111-4842]

impermeable caprock and bedrock and an adequate supply of water. The heat source (the magma body) is generally a magmatic intrusion. In most geothermal fields the depth or areal distibution of the intrusion is not known, but in a few fields geophysical methods have been successfully used to determine the dimensions of the intrusion and its location relative to the ground surface. For example, seismic microearthquake studies at the Krafla geothermal field in Iceland have identified a magma body located at a depth of 3-7 km [Einarsson, 1978].

In geothermal systems the heat is transported from the heat source to the aquifer by conduction and convection. In the aquifer convective heat transfer dominates due to the higher permeability of the rocks. The reservoir rocks in all presently known geothermal fields are volcanic, with the exception of the geothermal fields in the Salton Trough (e.g., East Mesa, Niland, and Cerro Prieto), and the Larderello field in Italy. Reservoir fluids are in liquid and/or vapor form. The caprock is often impervious, especially in vapor-dominated systems. However, surface manifestations are often present since fractures or faults extending to the surface allow leakage of the reservoir fluids. The schematic model shown in Fiqure 2 is valuable as a tool for explaining the characteristics of geothermal systems, but in reality geothermal reservoirs are more complex. Typically, a geothermal reservoir is fractured and possesses many aquifers located in heterogeneous reservoir rocks. This greatly complicates modeling of geothermal systems and the interpretation of field data.

CLASSIFICATION OF GEOTHERMAL FIELDS

Geothermal fields can be classified, according to the state (vapor or liquid) of the reservoir fluids, into vapor-dominated and liquid-dominated fields. In vapor-dominated fields the pressure gradient with depth is close to being vapor-static, whereas in liquid-dominated fields a near-hydrostatic pressure profile is observed. If only liquid water is present in the reservoir, the reservoir fluids are subcooled, and further classification according to its temperature is in order. High-temperature systems contain fluids above 150°C, intermediate-temperature systems have a temperature range of 90°-150°, and low-temperature systems are those of temperatures below 90°C. In vapor-dominated systems the fluid temperature is approximately 240°C and the pressure is around 35 bars, corresponding to the maximum enthalpy of saturated steam [James, 1968].

In addition to the above classification, geothermal reservoirs can be classified according to the flow characterisics of the in-situ rocks. Thus, there are porous media reservoirs (e.g., geothermal fields in the Salton Trough), and predominantly fractured reservoirs. This type of classification has little meaning when considering the fluid reserves in geothermal reservoirs, but in terms of the recoverable energy the two types of reservoir differ drastically. Because the recoverable energy indicates the power potential of a geothermal resource, this classification may be the most important one when considering the economic feasibility of a geothermal project.

METHODS OF ANALYZING GEOTHERMAL SYSTEMS

The primary objective of mathematical modeling of geothermal reservoirs is to obtain data that will assist the field developer in his decision-making process. The developer is interested in knowing the amount of energy that can be extracted from a reservoir in a given time period, and the most feasible method of exploitation. These are obviously very complicated problems, and it is questionable that the correct answer in technical and economical sense can be obtained, even when using the most complex mathematical tools. The complexity arises primarily because of the limited data that are generally available. The decision to build a power plant in the case of high-temperature application, or a space heating system in the case of a low-temperature geothermal field, is generally made early in the lifetime of the project, when data of the response of the reservoir under exploitation are not yet available. Relying on results of modeling studies performed under those conditions could prove disasterous. The logical way of developing a geothermal field is to increase the production in stages, using mathematical modeling at each stage to predict the future behavior of the field, after validation against the early-time data. Thus, mathematical modeling should be carried out continuously throughout the lifetime of the project.

Many mathematical models have been developed for the analysis of geothermal systems. Basically, these can be subdivided into three groups: (1) empirical methods, (2) analytical methods, and (3) numerical methods. Empirical methods involve obtaining analytical functions that fit

the data; a typical example is decline curve analysis. The theoretical foundation for the decline curve analysis was developed by Arps (1945, 1956). Later, Fetkovitch (1973) showed that the solution of Arps' equation corresponds to the long-time solution of the constant pressure production problem [van Everdingen and Hearst, 1949]. Studies of the extension of Arps' equation and the development of new decline equations have been carried out by a number of authors [Slider, 1968; Gentry, 1972; Gentry and McCray, 1978; Bodvarsson, 1977]. Application of empirical techniques to geothermal data has been rather limited to date. Rivera (1977, 1978) applied these techniques to data from wells at Cerro Prieto, Mexico, and obtained reasonably good matches. However, Zais and Bodvarsson (1980) could not reproduce Rivera's results. Zais and Bodvarsson applied various empirical equations to data from Cerro Prieto, Mexico; Wairakei, New Zealand; and other fields. Although they generally do not obtain very good matches with the data due to the scatter in the data, their comparison of the different methods is quite useful.

Analytical methods involve solutions of ordinary or partial differential equations constrained by initial and boundary conditions. These include the so-called "lumped-parameter" models, where the geothermal reservoir is characterized by one or a few homogeneous reservoir regions. As the rigorous mathematical equations that govern single- or two-phase flow in porous or fractured geothermal reservoirs are highly nonlinear, many simplifying assumptions must be made to a allow for a closed-form analytical solution to these problems. These include highly regular

geometries, constant rock and fluid properties, and constant or simple analytical functions representing the initial and boundary conditions. Analytical methods are quite useful in identifying parameters or groups of parameters that characterize a given system, but in general, as will be demonstrated in this dissertation, it is necessary to use distributed-parameter models for a complete, realistic solution to geothermal problems.

There are numerous available analytical solutions for natural convection in geothermal reservoirs. These are thoroughly summarized by Cheng (1978), and will therefore not be described here. Lumped-parameter models, in addition to distributed-parameter models, have been used for the simulation of geothermal fields under exploitation. There is presently some controversy regarding the applicability of lumped-parameter models to the simulation of geothermal systems, due to the coarse space discretization that is generally employed in these models. Distributed-parameter models, on the other hand, allow a much more detailed description of a reservoir system and the different flow regimes that occur in the system. Therefore, in this dissertation, emphasis is placed upon the development and use of distributed-parameter models for theoretical studies of geothermal systems as well as practical field applications. However, since it is important to fully understand the applicability and limitations of the mathematical tools available for geothermal reservoir simulations, a detailed comparison of the lumped- and the distributed-parameter methods is given in a later section (Field-wide modeling of the Baca field, New Mexico).

THE USE OF DISTRIBUTED-PARAMETER MODELS

Distributed-parameter models for the simulation of geothermal fields have only been developed during the last decade. Numerical simulators capable of modeling mass and heat transfer for single-phase liquid water were developed first, but only recently have simulators capable of two-phase fluid transport in geothermal reservoirs been developed. However, the rapid development of computer software for the solution of linear equations requires the continuous development and/or modification of numerical simulators for more efficient and accurate solutions of complex nonlinear problems.

Until recently geothermal developers have had little confidence in numerical simulators, and this has inhibited their application to geothermal fields. However, in light of the positive results obtained from a recent comparison of the different simulators [Stanford Geothermal Program, 1980], there is an increasing awareness of the usefulness of numerical simulators in the development of geothermal fields.

Numerical simulators can be used for theoretical studies of the physical behavior of geothermal systems, as well as for direct field applications. Although considerable work has been devoted to theoretical studies of geothermal systems, a basic understanding of their physical behavior is limited. This is especially true for the more complicated two-phase systems. However, fundamental studies that include well testing analysis, exploitation strategies, and injection problems of

geothermal systems can be found in the literature. These will be explored further in a later section.

The application of numerical simulators to specific geothermal fields can be of tremendous value to the field developers. Numerical simulators can be used, for example, to

(1) model a system in its natural (unexploited) state. This study aims at determining the heat flow, recharge rates, and the initial distribution of the fluid reserves in the hydrothermal system.

(2) study different exploitation alternatives. The appropriate production depths and rates can be determined.

(3) determine the appropriate well spacing, based upon a given generating capacity.

(4) predict the deliverabilities and the longevities of the production wells.

(5) determine the generating capacity and longevity of the field based on a given exploitation scheme.

(6) study different injection alternatives. Here one is concerned with the distance between the production and the injection wells, and the injection depths and rates.

(7) carry out sensitivity studies. The limited data generally available from geothermal fields require a complete sensitivity study. This should involve the most sensitive reservoir parameters, such as the permeability and the porosity, and also the recharge, reservoir dimensions, and the initial distribution of the reserves.

The above list clearly illustrates the potential of numerical simulators as tools for obtaining data that can greatly aid the field developer in his decisision-making process. Several important studies have addressed some of the problems listed above. Numerical simulation studies of the Wairakei geothermal field were carried out by Mercer et al. (1975), Pritchett et al. (1976), and Mercer and Faust (1979). Jonsson (1977) used a numerical simulator to study the Krafla geothermal field in Iceland, and Zyvolski and O'Sullivan (1978) studied the Broadlands geothermal field in New Zealand. Furthermore simulation studies of the Baca geothermal field, New Mexico, were carried out by Bodvarsson et al. (1980), the East Mesa anomaly was studied by Riney et al. (1979) and Morris and Campell (1979), and the Serrazzano geothermal reservoir in Italy was simulated by Pruess et al. (1980).

CODE DEVELOPMENT

During the last decade considerable efforts have been devoted to the development of numerical simulators for geothermal applications. As a result of this effort various groups have access to single- and two-phase simulators. However, with the rapid development of numerical techniques, and the software needed for efficient solution of sparse matrices, there is a continuous need to update these numerical codes in order to increase the capability to handle complex problems. In this section the present status of numerical modeling of geothermal systems is reviewed and the development of a new simulator is described.

BACKGROUND

In a broad sense, numerical models for the simulation of geothermal systems can be divided into two categories: (1) models developed for studies of the natural (unexploited) behavior of geothermal systems, and (2) models developed for studies of geothermal reservoirs under exploitation.

Many investigators have conducted numerical studies of natural convection in geothermal systems [e.g., Donaldson, 1970; Horne and O'Sullivan, 1974]. A thorough review of these studies is given by Cheng (1978), and since they are outside the scope of the present work, they will not be described here.

One of the first numerical models developed for studies of geothermal systems under exploitation was that of Sorey (1975). Sorey developed a

three-dimensional single-phase simulator for mass and heat transport in geothermal reservoirs. Using his model Sorey studied natural convection systems and modeled the Long Valley, California, hydrothermal system. Mercer et al. (1975) developed a single-phase finite-element code using pressure and temperature as dependent variables. They applied the code to the Wairakei system, and were able to match the field behavior up to 1962. At that time, the system had developed into a two-phase system, so their single-phase simulator was not applicable.

A number of papers addressing the problem of two-phase flow in geothermal reservoirs began to appear in the literature in 1975. Toronyi and Farouq Ali (1975) developed a two-phase, two-dimensional simulator coupled with a wellbore model. They used a finite-difference method with Newton-Raphson iteration to solve the equations for pressure and saturation. However, the simulator was only capable of calculating two-phase flow, and not the flow of superheated steam or subcooled liquid. At the Second United Nations Symposium, San Francisco, in 1975, three papers on the simulation of two-phase flow in geothermal reservoirs were presented [Faust and Mercer, 1975; Garg et al., 1975; Lasseter et al., 1975]. Each of these papers described a new two-phase code using the mathematical background given by Donaldson (1962), Mercer et al. (1974), and Brownell et al. (1975). Faust and Mercer (1975) solved for pressure and enthalpy using a Galerkin finite-element approximation in space and a finite-difference approximation in time. Garg et al. (1975) used the finite-difference method with fluid density and internal energy as dependent variables.

Lasseter et al. (1975) solved the equation for density and internal energy, but used the integrated finite-difference method for discretization of the flow regime and the formulation of the governing equations.

Faust and Mercer (1976) compared the finite-difference approach and the finite-element method for the simulation of geothermal reservoirs. They concluded that the finite-element method is better suited for liquid geothermal reservoirs due to reduced numerical dispersion, but that the finite-difference method is preferable for the simulation of vapor-dominated reservoirs because it conserves mass and energy better and exhibits less numerical oscillation.

Moench (1976) developed a finite-difference model for the simulation of vapor-dominated reservoirs. In his model liquid water may be present and evaporate into steam, but it is immobile at all times. Using this model, Moench studied superheating of discharging steam, conductive heat transfer, gravitational effects of a steam column, and energy effects due to compressible work.

The simulation of heat transport in fractured, single-phase geothermal reservoirs is addressed by O'Neill et al. (1976) and O'Neill (1978). O'Neill used the so-called double-porosity approach for developing the governing equations in terms of the pressure and temperature in the fractures and the porous blocks. He employed the finite-element approach in this three-dimensional nonisothermal model. Case studies using the model included hot water injection and the coupling of the temperature equations

in the fractures and the rock matrix. Thomas and Pierson (1976) developed a three-dimensional finite-difference model for the simulation of two-phase geothermal reservoirs. Pressure, temperature and saturation are used as dependent variables in the model, with implicit pressure and explicit saturation formulation.

Coats (1977) developed a three-dimensional finite-difference two-phase simulator using the Newton-Raphson iteration procedure. In contrast to most other models, Coats' model includes a well bore model. Lippmann et al. (1977) developed a three-dimensional integrated finite-difference model for single-phase geothermal simulations. Their model includes the one-dimensional consolidation theory of Terzaghi (1925) for compaction (subsidence) calculations. Two-phase finite-element simulators were developed by Huyakorn and Pinder (1977), and Voss (1978). These simulators were developed to illustrate that the finite-element technique could be used in the development of two-phase simulators [Pinder, 1979].

The simulators listed above represent the state of the art of the numerical simulation of geothermal systems. However, since their initial development, many of these simulators have been modified to improve their efficiency. An excellent example is the numerical simulator SHAFT. Initially developed by Lasseter et al. (1975) and Assens (1976), the code has in recent years been extensively redeveloped, using improved mathematical and numerical techniques [Pruess et al., 1979b; Pruess and Schroeder, 1980]. Recently, comparison studies between the various simulators

discussed above have been conducted [Stanford Geothermal Program, 1980; Pinder, 1979; Wang et al., 1980]. The results of these studies have illustrated that, although the various simulators differ in their applicability and flexibility, they generally give consistently reliable solutions to common problems in geothermal reservoir engineering.

NUMERICAL CODE

The recently developed numerical code PT (pressure-temperature) will be described in the following sections. This code is three-dimensional and solves numerically the mass and energy transport equations for a liquid-saturated medium, and uses the one-dimensional consolidation theory of Terzaghi (1925) for calculating the deformation of the medium. The model employs the Integrated Finite Difference Method (IFDM) for discretizing the saturated medium and formulating the governing equations [Edwards, 1972; Narasimhan and Witherspoon, 1976]. The sets of equations are solved by direct means, using an efficient sparse solver [Duff, 1977].

The code PT was developed from an older program CCC [Lippmann et al., 1977], but uses much more powerful mathematical and numerical techniques. In comparison to CCC, PT is 10 to 100 times more efficient for most problems.

Governing Equations

The governing equations employed in the model are the basic mass and energy balance laws. The mass flow equation (see Nomenclature) can be written in integral form as:

$$\int_V \frac{\partial}{\partial t}(\phi\rho)dV = -\int_A \rho\vec{v}_d \cdot \vec{n}dA + \int_V G_f dV \qquad (1)$$

Equation (1) applies to any control element of volume V and surface area A, containing solids and/or liquid water.

The energy equation can similarly be written in integral form as:

$$\int_V \frac{\partial}{\partial t}(\rho e_f)dV = \int_A \lambda\vec{\nabla}T \cdot \vec{n}dA - \int_A \rho c_f \delta T\vec{v}_d \cdot \vec{n}dA + \int_V G_h dV. \qquad (2)$$

where the term on the left-hand side is the accumulation term with e_f the internal energy of the fluid (liquid water). The first term on the right-hand side (RHS) represents heat transfer by conduction as expressed by Fourier's law, λ being the thermal conductivity of the rock-fluid system. The remaining terms on the RHS are the convective term and the source term, respectively. In the convective term, δT denotes the interface temperature.

Equations (1) and (2) are coupled through the pressure- and the temperature-dependent parameters, as well as through the convecting term. In the model, the fluxes are calculated using Darcy's law, which can be written as:

$$\vec{v}_d = -\frac{k}{\mu}(\vec{\nabla}P - \rho\vec{g}), \qquad (3)$$

where k is the absolute permeability, μ is the dynamic viscosity of the fluid and $\vec{g}$ is the acceleration due to gravity.

Equations (1) and (3) are nonlinear with pressure/temperature-dependent parameters ρ, k, μ, λ, and c. Furthermore, the parameters ϕ,

β_r and k are stress-dependent. The equation of state for water, which is used in the program, is given in Appendix B.

Deformation

The model employs the one-dimensional theory of Terzaghi to calculate the vertical deformation of the medium. The basic concept of the theory is the relationship between the effective stress σ' and the pore pressure P. For a saturated medium this expression can be written as:

$$\sigma' = \sigma_N - P, \tag{4}$$

where σ_N denotes the normal stress (overburden). The effective stress can easily be calculated from equation (4) at any time, given that the normal stress σ_N is known and remains constant.

The consolidation behavior of each material is described by the "e - log σ' curves," where e is the void ratio, related to the porosity ϕ by the expression:

$$\phi = \frac{1}{1 + e} \tag{5}$$

A typical consolidation curve is shown in Figure 3. It consists of a so-called virgin curve and a series of parallel swelling-recompression curves (the model neglects hysteresis between swelling and repression curves). When the rock is loaded to levels never before attained, the deformation is represented by the virgin curve, but for swelling or load levels below the preconsolidation stress, the deformation is represented by the swelling-recompression curves. In the model, the "e - log σ' curves" are generally approximated by straight lines, one of slope C_c

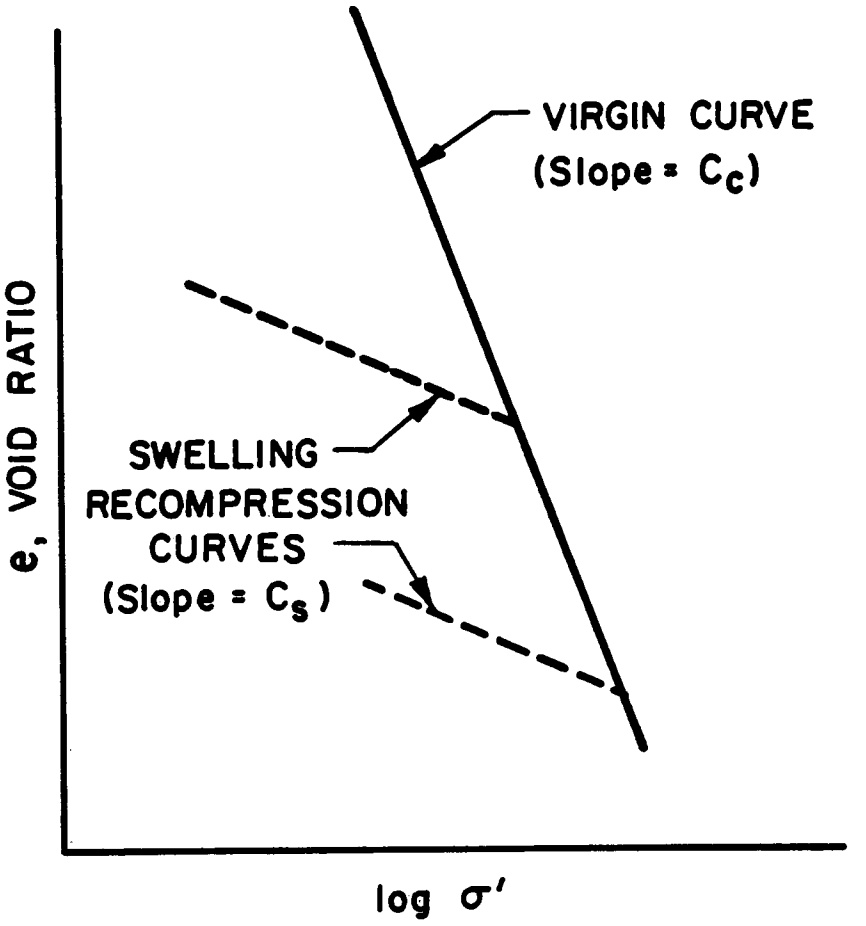

Figure 3. Typical consolidation curve. [XBL 773-5219]

(compression index) for virgin loading, and others of slope C_s (swelling index) for unloading/loading below the preconsolidated stress.

The stress-dependent parameters in equations (1) and (3), ϕ, β_r and k, can easily be calculated if the consolidation curves for each material are given. The porosity is computed using equation (5), and the rocks compressibility can be calculated using the following expression:

$$\beta_r = \frac{a_v}{e} \tag{6}$$

In equation (6), a_v is the coefficient of compressibility for the matrix, defined as [Narasimhan, 1975]:

$$a_v = -\frac{de}{d\sigma'} = \frac{C_c}{2.303\ \sigma'} \ . \tag{7}$$

In calculating the permeability k as a function of void ratio, the following empirical relation is used [Narasimhan, 1975]:

$$k = k_o \exp\left[\frac{2.303\ (e - e_o)}{C_k}\right] . \tag{8}$$

In equation (8), k_o and e_o are arbitrary reference values of the permeability and void ratio, respectively. For a given material, C_k is the slope of the best fitted line of void ratio (e) versus log k.

Assumptions

In the development of the mathematical model used in the computer code, the following primary assumptions have been employed:

(1) Darcy's law describes fluid movement through fractured and porous media.

(2) The rock and the fluid are in thermal equilibrium at any given time.

(3) Energy changes due to the fluid compressibility, acceleration and viscous dissipation are neglected.

These asumptions are generally employed in the numerical modeling of geothermal reservoirs.

Numerical Formulation

The model employs the Integrated Finite Difference Method (IFDM) to discretize the flow regime and to handle the spatial gradients. The flow regime is divided into arbitrarily-shaped polyhedrons, constructed by drawing perpendicular bisectors to lines connecting nodal points (Fig. 4). This permits easy evaluation of the surface integrals in equations (1) and (2). Except for the procedure used in evaluating the gradients, the Integrated Finite Difference Method (IFDM) and the modified Galerkin Finite Element Method (with diagonal capacity matrix) are conceptually very similar [Narasimhan and Witherspoon, 1976]. Both approaches derive their ability to handle complex geometries from the integral nature of the formulation. Detailed description of the IFDM are given by Edwards (1972), Sorey (1975), and Narasimhan and Witherspoon (1976). In numerical notation the governing equations can be written as follows:

mass balance:

$$(V\phi\rho)_n \left[\beta_t \frac{\Delta P}{\Delta t} - \alpha_t \frac{\Delta T}{\Delta t}\right] = \sum_m \left(\frac{k\rho A}{\mu}\right)_{n,m} \left[\frac{(P_m - P_n)}{D_{n,m} + D_{m,n}} - \eta_g \rho_g g\right] + (G_f V)_n \quad (9)$$

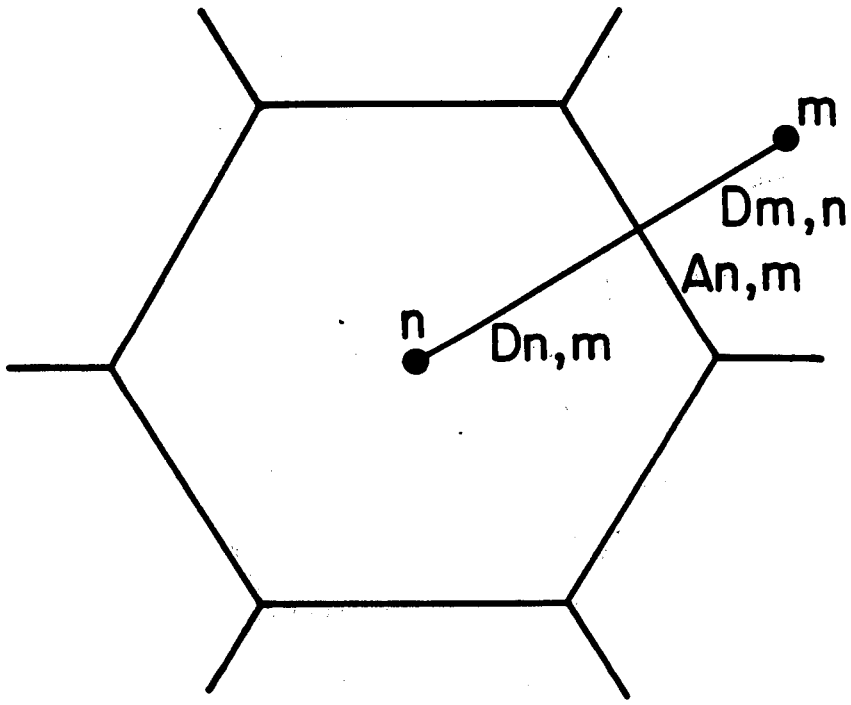

Figure 4. Typical node-connection network and nomenclature.
[XBL 804-7006]

energy balance:

$$[(\rho c)_M V]_n \frac{\Delta T_n}{\Delta t} = \sum_m \left\{ \frac{(\lambda A)_{n,m}}{D_{n,m} + D_{m,n}} (T_m - T_n) + \right.$$

$$\left. + \left(\frac{\rho c_f A k}{\mu}\right)_{n,m} (T_{m,n} - T_n) \left[\frac{P_m - P_n}{D_{n,m} + D_{m,n}} - \eta_g \rho_g g \right] \right\} + (G_h V)_n \qquad (10)$$

These equations are valid for an arbitrary node n connected to an arbitrary number of nodes m. The nodal point distances to the interface for node n and node m are represented by $D_{n,m}$ and $D_{m,n}$, respectively (Fig. 4). The quantity η_g is the direction cosine of the angle between the outward normal of node n and m.

In Equations (9) and (10), β_t and α_t represent the total compressibility and the total thermal expansivity, respectively, so that:

$$\beta_t = \beta_w + \beta_r \qquad (11)$$

$$\alpha_t = \alpha_w + \alpha_r \qquad (12)$$

Upstream Weighting

To evaluate the interface temperature $T_{n,m}$, the model employs an upstream weighting criterion:

$$T_{n,m} = dT_n + (1 - d)T_m \quad . \qquad (13)$$

where n is the upstream node and d, the upstream weighting factor, is restricted in value to the range 0.5 to 1.0 for unconditional stability.

Implicit Formulation

In the model, the equations are solved implicitly to allow for larger time steps to be taken. The implicit formulation is incorporated by means the following expressions:

$$
\begin{aligned}
T_n &= T_n^o + a_T \Delta T_n \\
T_m &= T_m^o + a_T \Delta T_m \\
P_n &= P_n^o + a_P \Delta P_n \\
P_m &= P_m^o + a_P \Delta P_m .
\end{aligned}
\tag{14}
$$

The weighting factor a is generally allowed to vary between 0.5 and 1.0 for unconditionally stable solutions, but it may also be specified as a constant. If a is specified to be zero during the simulation, a fully explicit solution scheme results (forward differencing) and time step is restricted to a critical stable value [Narasimhan, 1975]. If a = 0.5, the Crank Nicholson scheme results; for a = 1.0, a fully inplicit (backward differencing) scheme is employed.

Spatial Gradients

The spatial gradients between nodes are estimated by a linear approximation, i.e.,

$$
\vec{\nabla} P = \frac{P_m + P_n}{D_{n,m} + D_{m,n}} . \tag{15}
$$

The permeability and thermal conductivity of the matrix are evaluated using the harmonic mean to insure continuity of flux at the interface,

for example,

$$k_{m,n} = k_m k_n \frac{D_{n,m} + D_{m,n}}{k_m D_{n,m} + k_n D_{m,n}} \tag{16}$$

The density at the interface is calculated based on a simple weighted average:

$$\rho_{n,m} = \frac{D_{n,m}\ \rho_m + D_{m,n}\ \rho_n}{D_{n,m} + D_{m,n}} \tag{17}$$

However, in the gravity term, the fluid density is calculated assuming linear variations in temperature and pressure between grid blocks:

$$\rho_g = \frac{1}{2}\ [\rho_n + \rho_m] \tag{18}$$

Solution Technique

Equations (9) and (10) can be combined for simultaneous solution into a single matrix equation.

$$[A]\{X\} = \{b\} \tag{19}$$

The coefficients in the matrix [A] are in general a function of the temperature and pressure and therefore the equations are nonlinear. The vector {X} contains the unknowns (ΔP and ΔT) and the vector {b} represents the known explicit quantities.

The sets of nonlinear equations are solved using an efficient direct solver [Duff, 1977] and an iterative scheme for the nonlinear coefficients. Basically, the solver uses LU decomposition and a Gaussian elimination procedure to solve a set of linear equations.

The matrix of coefficients (the [A] matrix) is preordered using permutation matrices P' and Q' such that the resultant matrix is in block lower triangular form. Gaussian elimination is then performed within each diagonal block in order to obtain factorization into the lower triangular (L_k) and the upper triangular (U_k). Finally, the factorization is used to solve the matrix equations. In this solution package [Duff, 1977], no restriction is placed upon the characteristics of the matrix of coefficients; i.e., it need not be symmetrical or a specified degree of sparsity.

Program Structure

The structure of the program PT is shown in Table 1. It consists of a main program and eleven major subroutines. A brief description of the role of the major subroutines is also given in Table 1.

The input-output functions are handled by the subroutines INN and OUT, respectively. After the input data has been read in, the subroutine REFER is called for cross-referencing between nodes and connections. Then the subroutine TIMER is called and a time step is determined. THERM and FLUID are called for the determination of the rock and fluid properties, respectively, based on latest available pressures and temperatures, and GENER is called to determine the strength of sources and sinks. Then the subroutine SOLVER is called to set up the matrix coefficients and the known vector b. SOLVER then calls the linear algebra package MA 28 [Duff, 1977] for solution of the linear equations. If the Newton-Raphson option is specified, SOLVER will then call the subroutine ITER, which uses

Newton-Raphson iteration until convergence is achieved. If vertical deformation calculations are required, the subroutine COMPACT is called.

Finally, the subroutine TIMER is called, to up-date the pressures and temperatures of each mode, select the next time step, and call the subroutine OUT if an output is needed.

Table 1. Major Subroutines and Their Functions.

Subroutine	Function
PT	Main program
INN	Reads in input data
THERM	Provides solid properties
FLUD	Provides fluid properties
COMPACT	Calculates compaction
GENER	Determines strength of sources and sinks
SOLVER	Sets up matrix equations
ITER	Performs Newton Raphson iteration
TIMER	Selects time steps and determines if output is needed
REFER	Cross-references nodes and connections
MA28	Solves linear equations
OUT	Provides output

An input guide to the program PT is given in Appendix A. A general description of the basic characteristics of the code follows below.

Material Properties

At present the code allows specification of up to twelve (12) different materials. For each material the porosity, permeability, compressibility, thermal conductivity, heat capacity, and density of the solid must

be specified; thermal expansivity is optional. These parameters may be constant or may vary with temperature, and/or effective stress. The porosity and rock compressibility can vary with the effective stress, the permeability with both temperature and effective stress, and the thermal conductivity and heat capacity with temperature only. These relations are specified by tables, interpolated during each time step. Anisotropic permeability (and/or thermal conductivity) can be handled by orienting the interfaces parallel to the principal axes of anisotropy.

Fluid Properties

Input parameters are the fluid viscosity, heat capacity, density, expansivity, and compressibility of water. A constant value of the fluid heat capacity must be specified; other fluid properties may also be assumed constant. However, the code provides the option of specifying the viscosity as a function of temperature, and density as a function of temperature and pressure [Buscheck, 1980]. These functions are given in Appendix B.

Numerical Options

The program offers options of solving both the mass and the energy equation or only one of the two. If only one equation is solved, a smaller matrix is needed and therefore the calculation becomes more efficient. In the case of solving the energy equation only, steady mass flows for each connection must be specified. An option of using Newton-Raphson iteration is also included.

Spatial Grid

In the model there is no restriction upon choice of basic node shape or the numbering scheme of the nodes. The geometric configuration of the nodal elements can be arbitrary and the grid may be one-, two-, or three-dimensional, with rectangular, cylindrical, spherical symmetry, or it may be completely nonsymmetrical. The dimensions of the nodes and the connections between nodes are required input data. For complex problems, the design of the mesh may create the most difficulty in using the program. Auxiliary computer programs for mesh and input data generation have been developed for several grid systems, including the case with cylindrical or elliptical rings near a well which gradually change to rectangular nodes in the far field. This type of mesh is relevant for the simulation of horizontal or inclined fractures intersecting a well (cylindrical or elliptical cross sections) or intersecting other planar fractures within the rock mass (linear cross sections) and similar problems.

Sources and Sinks

Mass and energy sources and sinks may be specified for any node. The rate may be constant or vary with time.

Initial Conditions

Initial values of pressure, temperature and preconsolidation stress must be specified for each grid block. If the restart option is utilized, the specified initial values must correspond to the final values obtained in the previous run.

Boundary Conditions

In the model, prescribed constant potential or flux boundaries may be used. Finite capacity wells (wellbore storage) as well as a heterogeneous flow regime (fractures) can easily be simulated.

Time Steps

There are several options for selecting the time steps to be taken during the simulation. The maximum and minimum time steps may be specified, or the time steps may be automatically determined based upon the maximum desired pressure and/or temperature changes during a time step. The problem is ended when any one of several criteria is met. These include attainment of steady state, reaching the specified upper or lower limit for temperature and/or pressure, completing the required number of time steps, and reaching the specified maximum simulation time.

Output

Output is provided according to specified times or specified time steps. The pressure, temperature and first-order derivatives are printed for each node. The fluid and energy fluxes are given for each connection. The mass and the energy balance are also included in the output. A node may be specified, for which pressure and temperature are printed out after each time step.

Validation

In order to validate the program, several problems with known solutions were solved. A brief description of these problems and a comparison of the analytical solutions to the numerical solutions are given below.

The Theis Problem

Theis (1935) solved analytically for the pressure at a well produced at a constant rate in an infinite homogeneous, isotropic, aquifer of constant thickness. He obtained a closed-form solution in terms of an exponential integral. In simulating this problem, the code PT was used in its isothermal mode (e.g., only the mass conservation equation was solved). The mesh used consisted of logarithmically spaced elements around a well element of radius .1 m (approximately a 4-inch well). The fluids were produced at a constant rate from the well element (.1 kg/m·s). The comparison between the analytical and the numerical solution is shown in Figure 5. As the figure shows, the numerical results are almost identical to the analytical solution. In the simulation, a total of 80 elements were used, but a four-fold reduction in the number of elements will not alter the solution significantly. As isothermal calculations using the code PT are very cost-efficient, one generally does not need to worry about the number of elements, as long as the desired accuracy is obtained.

Constant Pressure Production

Jacob and Lohman (1952) solved analytically a problem identical to the Theis problem, but instead of a constant production rate, the well is

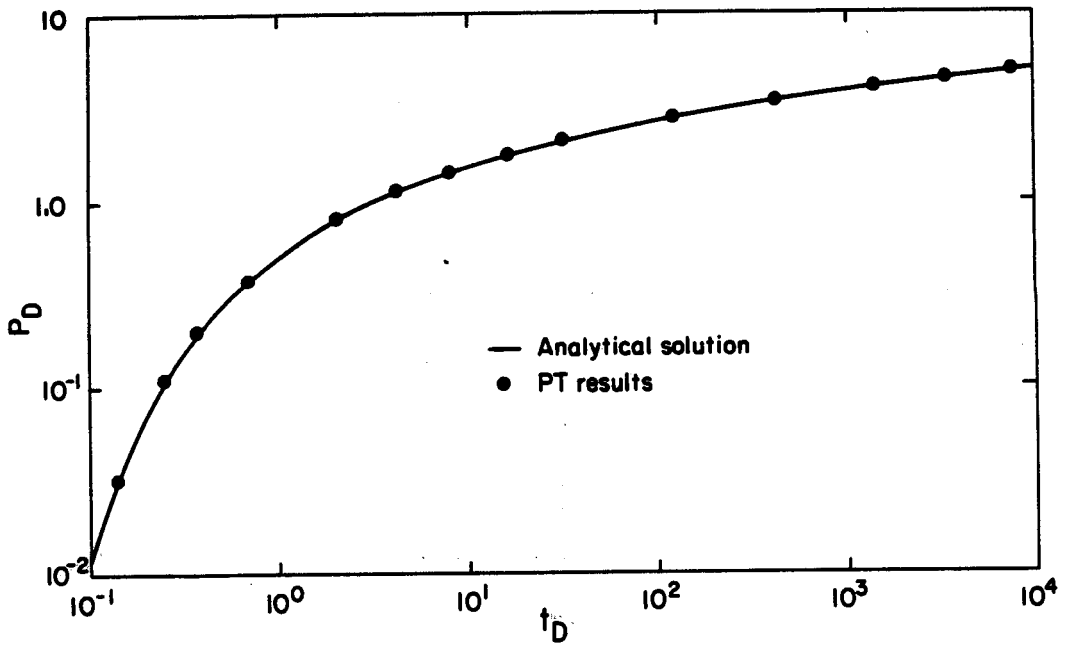

Figure 5. Comparison between analytical and numerical solution for the Theis problem. [XBL 8110-11682]

produced at a constant pressure. In this case, the flow rate at the well was monitored instead of the pressure. The solution was characterized in terms of dimensionless flow rate and a dimensionless time. The physical basis for the definition of the dimensionless flow rate stems from Darcy's law, as does the definition of the dimensionless pressure.

In simulating this problem, the mesh used must be carefully designed. Initially, when the pressure at the well is instantaneously changed from the average reservoir pressure to a lower production pressure, a sharp discontinuity in the pressure from the well to the reservoir prevails. This gives rise to enormous flow rates and sharp pressure gradients at early times. If an accurate simulation of the flow rate at early times is to be obtained, very small elements must be used close to the well. In the simulation, a wellbore radius of .1 m was used, but close to the well logarithmically spaced elements, starting with very small elements (10^{-5} m), were used. This enabled a near-perfect match with the analytical solution (Figure 6). If a coarser mesh had been employed, the numerical solution would have fallen below the analytical solution at early times, but the late time match would still have been satisfactory.

Conduction Problem

In order to check the conduction term in the energy balance equation, a simple conduction problem was solved. In this problem only two nodes were needed, with one connection between them. Initially, the nodes were at different temperatures; the temperature of nodes 1 and 2 were assigned as 25.664°C and 24.336°C, respectively. Very low values were assigned to

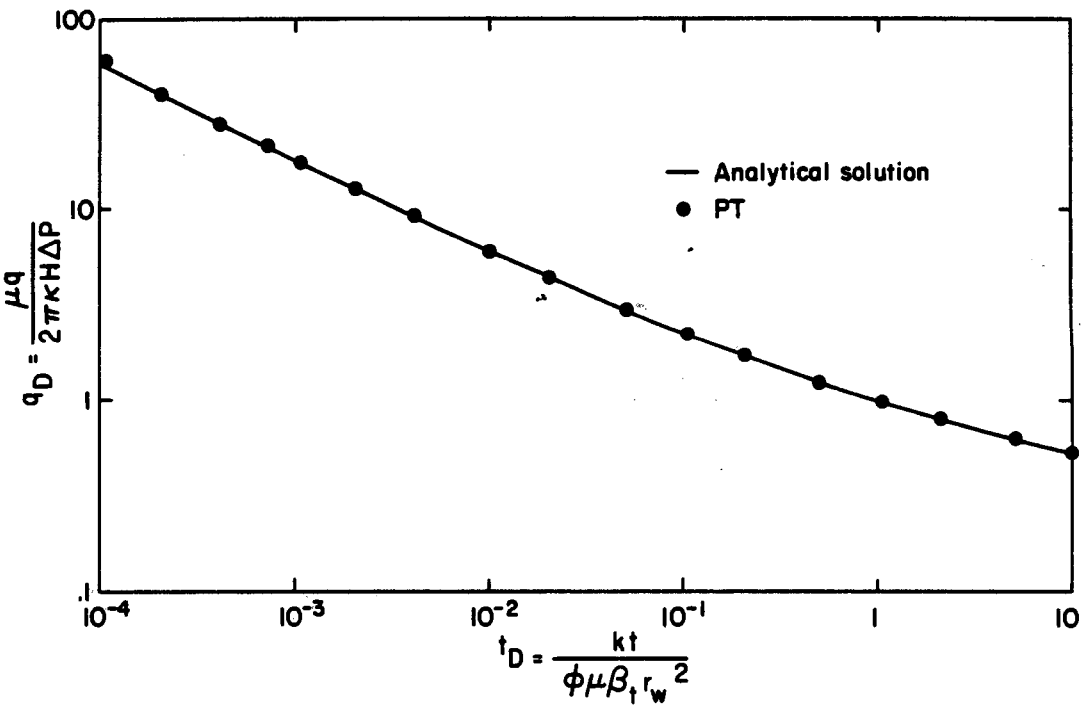

Figure 6. Comparison between analytical and numerical solution for the constant-pressure problem. [XBL 8110-11690]

the porosity and the permeability of the nodes, so that the temperature would equilibrate by pure conduction (convection becomes negligible). An expression for the temperature of node 2 as a function of time was easily derived as:

$$T_2 = (T_i - T_m) \exp - \left[\frac{2A\lambda}{D1 + D2} \frac{t}{\rho c V} \right] + T_m \tag{20}$$

where T_m is the average temperature of the two nodes (in this case 25°C) and D1 and D2 are the distances from the nodal points of nodes 1 and 2 to their common interface, respectively. Table 2 shows the comparision between the analytical solution and the numerical results. The table shows that a very good agreement was obtained. In solving this problem, a maximum temperature change of .002°C per time step was specified (TVARY = .002).

Table 2. Comparison of analytical and numerical solutions for the conduction problem.

Time (sec)	Analytical Solution (°C)	Numerical Solution (°C)
.1	25.5436	25.5437
.2	25.4451	25.4451
.3	25.3644	25.3645
.4	25.2984	25.2984
.5	25.2443	25.2444
.6	25.2000	25.2001
.7	25.1637	25.1638
.8	25.1341	25.1342
.9	25.1098	25.1099
1.0	25.0899	25.0900

Convection Problem

Another simple problem was solved to check the convection term in the energy equation. In this problem, two nodes and one connection were required, with a steady mass flow (q) going from node 1 to node 2. Initially, the temperatures of nodes 1 and 2 were 100°C and 200°C, respectively. Conductive effects were neglected. The solution for the temperature at node 2 was:

$$T_2 = (T_i - T_1) \exp - \left[\frac{qt}{\rho V}\right] + T_i \tag{21}$$

where T_i was the initial temperature of node 2. In solving this problem, the program PT with the option of solving only the energy balance equation (NOPT = 2) was used. A steady mass flux of 1.0 kg/s was specified in input block SPECS (QSTEADY), and since there was only one connection, the input block FLOWS was not necessary. When a minimum temperature change of 0.2°C per time step (TVARY = .2) was specified, a perfect agreement to within .01°C between the analytical solution and the numerical results was obtained. This is shown in Table 3. When the requirement of the maximum temperature change per time step was relaxed to 1.0°C, a maximum error of .23°C resulted after 1000 seconds of simulation.

Conduction and Convection Problem

In this problem, a heat regenerator consisting of a rectangular fluid duct and a rectangular solid was considered. At time zero, the system was at 0°C and fluid of 100°C temperature began flowing through the fluid duct. The mass flow rate was steady, and heat losses to the solid were specified in terms of an overall heat transfer coefficient.

Table 3. Comparison of analytical and numerical results for the convection problem.

Time (sec)	Analytical Solution (°C)	Numerical Solution (°C)
100	190.49	190.49
200	181.88	181.88
300	174.04	174.09
400	167.04	167.04
500	160.66	160.66
600	154.89	154.89
700	149.67	149.67
800	144.95	144.95
900	140.67	140.67
1000	136.80	136.80

A complete description of the parameters and the mesh used is given by Edwards (1972) and the analytical solution is given by Carslaw and Jaegar (1959).

Again the problem was solved using the steady flow option in the program PT (NOPT = 2). Comparison between the analytical and the numerical solution in the fluid duct, .3 cm from the inlet, is given in Figure 7. The slight discrepancy at early times is due to numerical dispersion, but the numerical results converge to the analytical solution at later times.

Horizontal Fracture Problem

Gringarten (1971) solved analytically the problem of isothermal fluid flow to a well intersecting a single horizontal fracture in a homogeneous

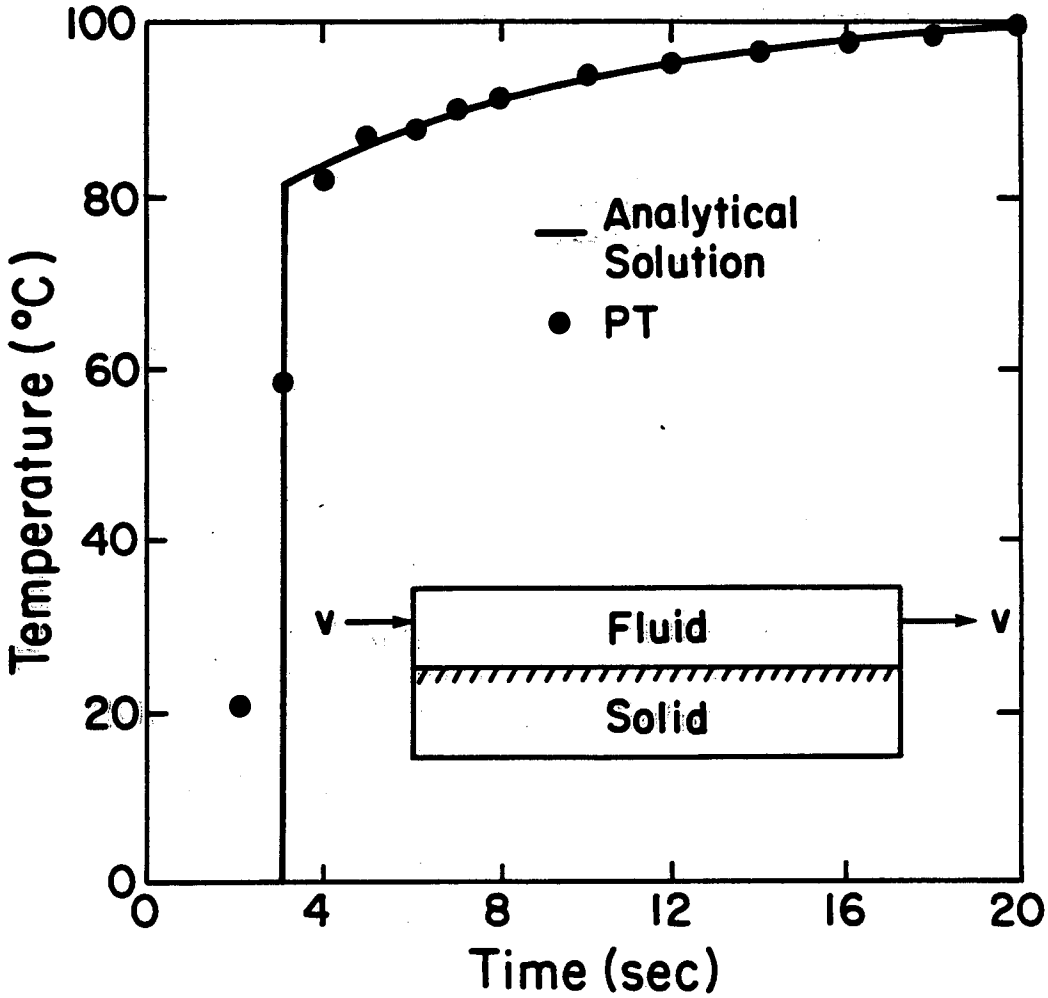

Figure 7. Comparison between analytical and numerical solution in the fluid duct. [XBL 8110-11680]

porous reservoir. In his analytical approach to the problem, Gringarten made three important assumptions:

(a) all of the flow to the well is through the fracture;

(b) the flow per unit area into the fracture is uniform across the fracture surfaces (uniform flux assumption);

(c) gravity effects are negligible.

Figure 8 shows the type curves developed by Gringarten.

To validate PT for flow through fractured media, Gringarten's problem was simulated using the mesh shown in Figure 9. Based on Gringarten's first assumption, it was not necessary to include a well element in the mesh. To satisfy the uniform flux assumption, sinks of variable strength were placed in the fracture elements. The strengths of the sources were determined by the surface area of the elements. All of the elements used in the simulation were placed at the same elevation to exclude gravity from the calculations. Two cases with different h_D ($h_D = (H/r_f)(\sqrt{k_r/k_z})$) values were studied. Figure 10 shows the comparison between the numerical and the analytical solutions for $h_D = 1$. Similarly, a good agreement was found for the case of $h_D = 4$.

Vertical Fracture Problem

The problem of a well intercepting a single vertical fracture in a porous media reservoir was solved analytically by Cinco-Ley et al. (1978). The primary assumptions used in their analytical approach were as follows:

(a) the produced fluids enter the well only through the fracture.

(b) gravity effects are negligible.

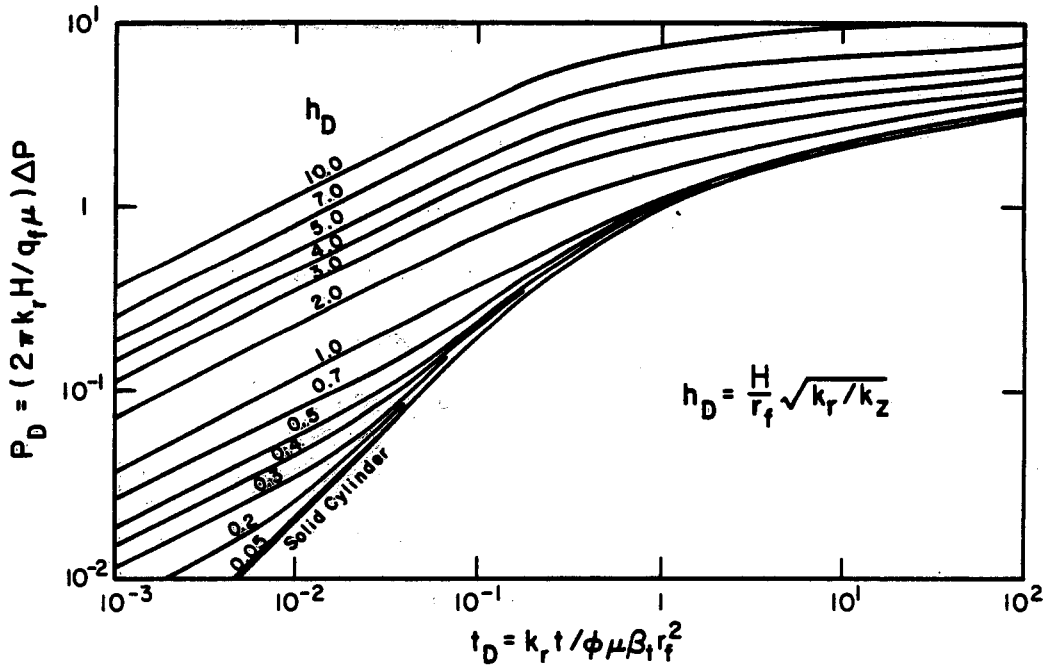

Figure 8. Type curves for horizontal fracture problem (after Gringarten, 1971). [XBL 804-7009]

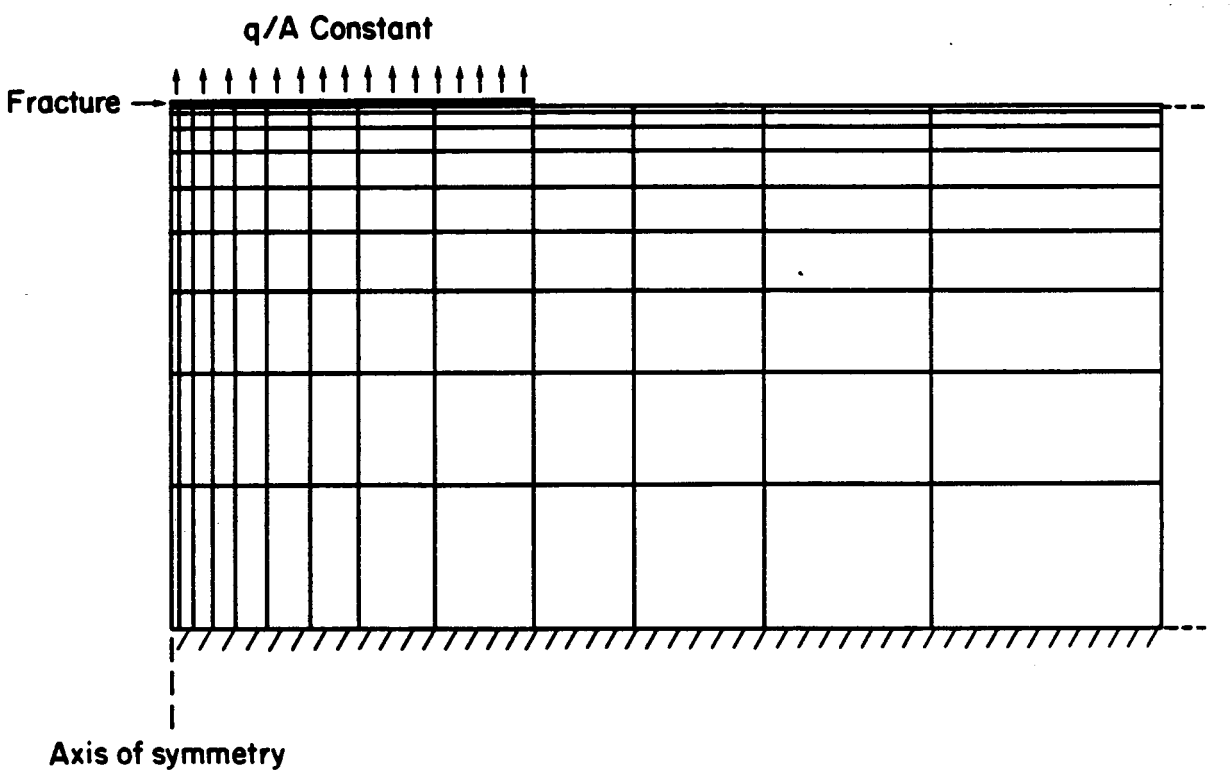

Figure 9. Mesh used for horizontal fracture problem. [XBL 8110-11679]

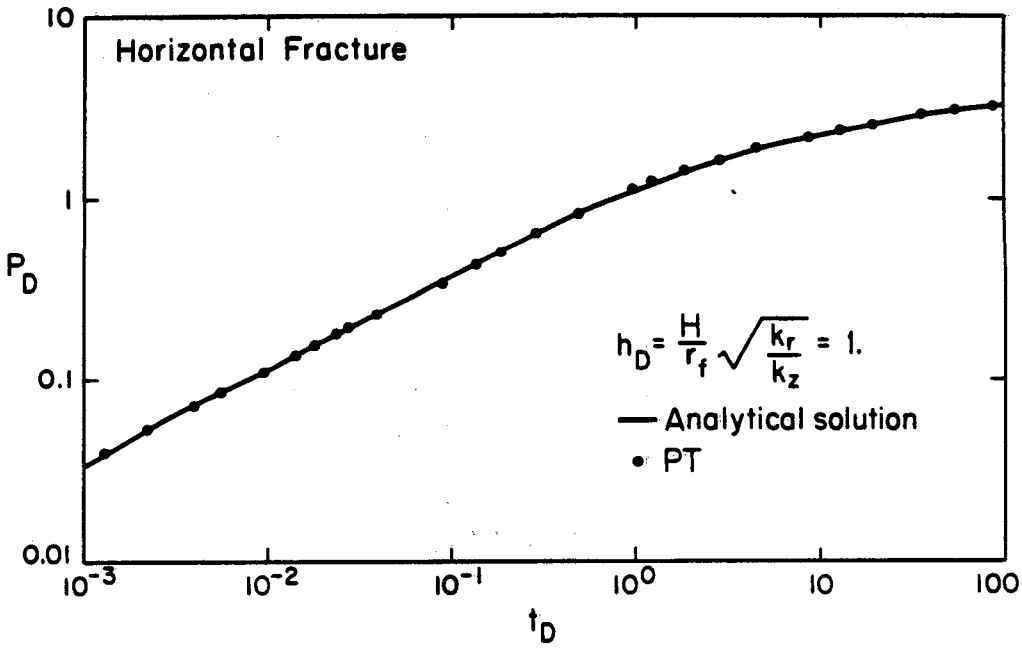

Figure 10. Comparison between analytical and numerical solution for $h_D = 1$. [XBL 802-6786A]

In the numerical simulation of this problem, the program was in its isothermal mode (NOPT = 1) and the mesh shown in Figure 11 was used. In order to satisfy the first assumption made by Cinco-Ley et al., the well element was connected only to the fracture elements, not to the elements representing the surrounding formation. Gravity was again excluded from the calculation by placing all of the nodes at the same elevation.

Using the mesh shown in Figure 11, the case of $C_r = 100$ ($C_r = bk_f/\pi k x_f$) was numerically simulated. Figure 12 shows the comparison between the numerical values obtained and the values given by Cinco-Ley et al. The excellent agreement obtained did not warrant any additional comparison.

Field Validation

PT was recently used for simulation of an aquifer thermal energy storage experiment conductred by Auburn University [Tsang et al., 1981]. Two injection-storage-production periods were simulated. The results of the simulation showed excellent agreement with the temperature distribution in the aquifer at various times and the energy-recovery factors. This validation of the code against field data illustrates its accuracy and flexibility.

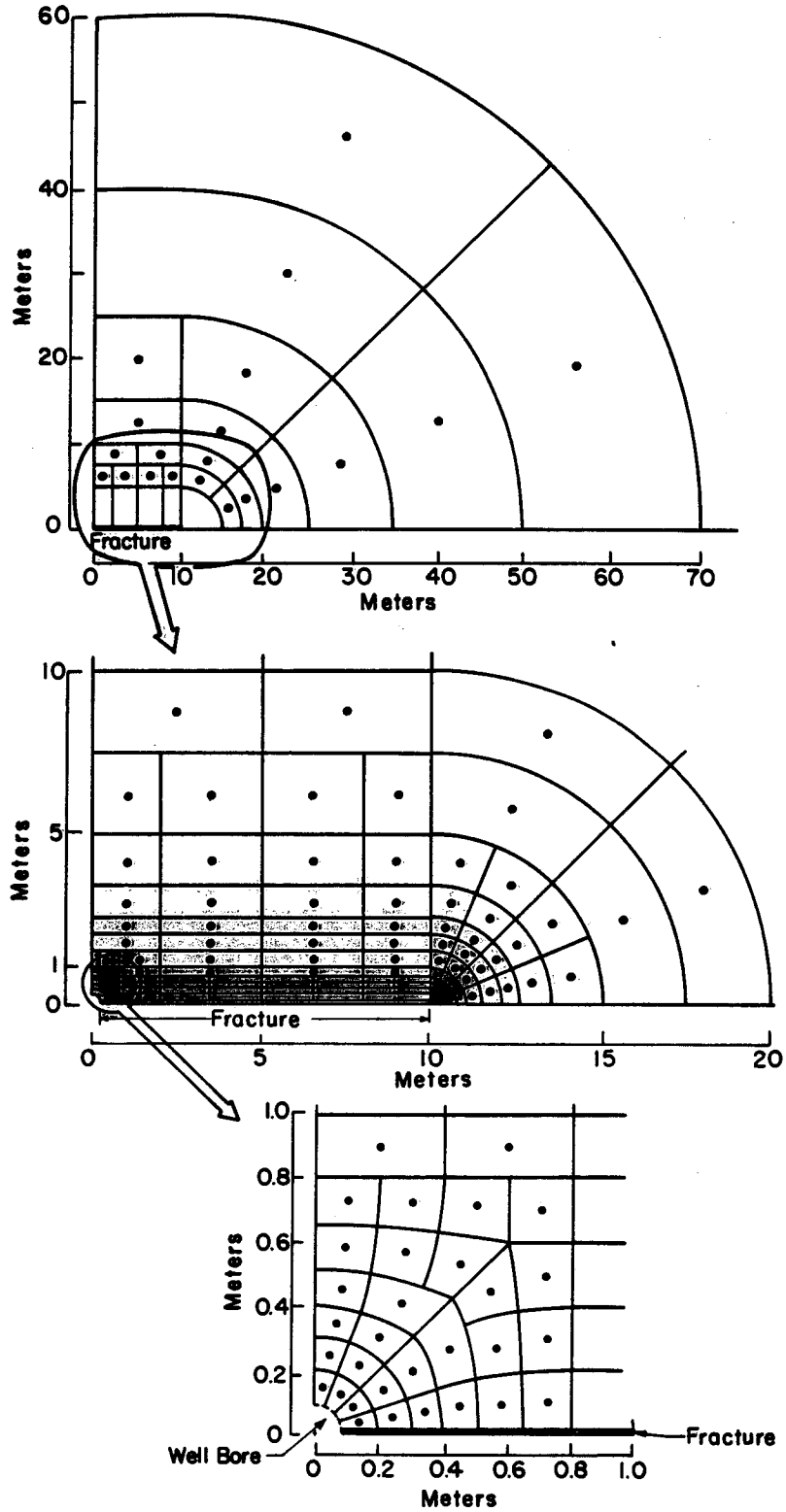

Figure 11. Mesh used for the vertical fracture problem (after Palen, 1980). [XBL 792-5744]

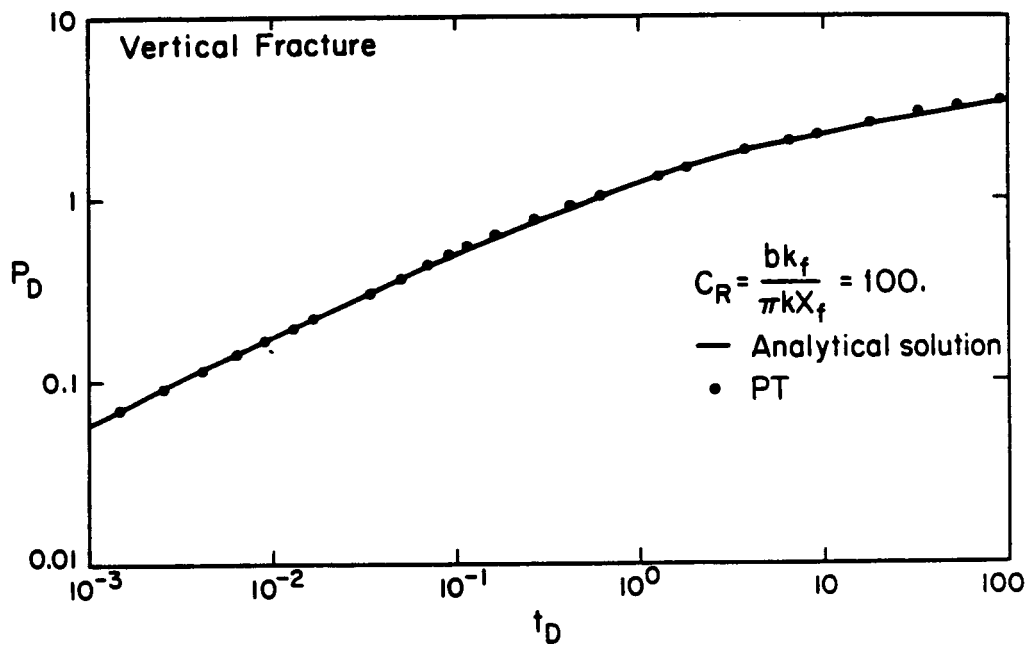

Figure 12. Comparison between numerical values obtained and values given by Cinco-Ley (1977). [XBL 802-6783]

SUMMARY OF CODE DEVELOPMENT

In this chapter the development of a new numerical simulator for modeling geothermal systems was described. The code is three-dimensional and capable of simulating the mass and heat transfer associated with the flow of single-phase liquid water through porous or fractured media. The model has been extensively validated against known analytical solutions for mass and heat transfer in porous and fractured rocks. Also in this chapter, a detailed description of the model in terms of its mathematical and numerical formulation was given and the basic capabilities of the code were illustrated. The input manual can be found in Appendix A.

THEORETICAL STUDIES OF GEOTHERMAL RESERVOIRS

In this chapter, some theoretical problems in geothermal reservoir engineering are addressed. These problems include analysis of well tests in single- and two-phase reservoirs, exploitation strategies for two-phase geothermal reservoirs, and the analysis of fault-charged geothermal reservoirs. As each of these problems is quite general, only the most important aspects of the present work are discussed. Emphasis is placed on identifying the problem and illustrating the insight gained through the present work.

In the analysis of these problems, various mathematical techniques were employed. Analytical methods were used to pose the problem and identify important parameter groups. However, for complex problems such as those considered here, numerical studies in addition to analytical work are necessary if a reliable solution is to be obtained. In the analytical work, many simplifying assumptions must be made. If the effects of these assumptions on the overall solution of the problem are not understood, one must be very cautious when applying the results to field problems. This type of integrated analytical-numerical approach is illustrated in a following section where the problem of injection into fractured geothermal reservoirs is addressed.

In many cases, however, the limited capability of the analytical approach does not allow an appropriate treatment of the problem. This is especially true in complex nonlinear problems such as nonisothermal or

two-phase flow. In these, and other cases where highly nonlinear behaviors are evident, only numerical methods can be applied. In this dissertation the newly developed simulator PT was used for these types of problems and, in special cases, the two-phase simulator SHAFT79 [Pruess and Schroeder, 1980].

ANALYSIS OF WELL TESTS IN GEOTHERMAL RESERVOIRS

Conventional well test analysis methods have been developed in the petroleum and groundwater literature and are of limited use for geothermal applications because they are generally based on the assumption of isothermal fluid flow. These are well summarized by Earlougher (1977) for the porous-media type reservoirs and Raghavan (1977) for reservoirs in which the wells intercept fractures. In geothermal reservoirs, problems caused by high temperatures and two-phase flow make well test data difficult to obtain, and complicate their analysis. The high temperatures encountered in geothermal reservoirs shorten the useful life of cables and electronic equipment. Therefore, presently, accurate downhole pressure data cannot be obtained in high temperature (>200°C) geothermal reservoirs [Schroeder et al., 1980].

The analysis of well test data from hot-water (single-phase) reservoirs is complicated primarily by the variable fluid properties (density and viscosity). On the other hand, little is known about the analysis of well test data from two-phase resevoirs. Papers addressing this problem have only appeared recently in the literature [Garg, 1978; Grant, 1978;

Moench and Atkinson, 1978; Grant, 1979b; Sorey et al., 1980; O'Sullivan, 1980]. The difficulty in analyzing data from two-phase reservoirs is due to the highly nonlinear two-phase compressibility effects, and the lack of knowledge of the relative permeability functions for porous and fractured geothermal reservoirs. A more detailed discussion of these problems is given in a later section.

Injection Testing of Hot-Water Reservoirs

In well test analysis of data from groundwater or petroleum reservoirs, the Theis solution [Theis, 1935] is frequently used. When a constant flow rate is used, the solution indicates that a plot of the pressure drop versus the logarithm of time asymptotes to a straight line after a short initial period. The slope of this straight line can be used to calculate the transmissivity (kH) of the reservoir whereas the intercept with the time axis will yield the total formation compressibility β_t.

Direct application of the Theis solution to well test data from hot-water reservoirs is questionable for the following three reasons:

(1) generally, the flow rate from/into a geothermal well is not constant but varies with time;

(2) usually, geothermal reservoirs exhibit areal and vertical temperature gradients and consequently the fluid properties will vary spatially;

(3) often, well tests in hot-water reservoirs are performed by injecting water rather than by producing it. The temperature of

the injected water is generally different from the undisturbed reservoir water and consequently gives rise to nonlinear fluid properties.

The variable flow rate can easily be handled by using superposition principles. Variable-rate programs using the superposition of the Theis solution with a least-squares statistical optimizer have been developed [McEdwards, 1981].

Effects of temperature variation on the pressure response at a well can be significant. Mangold et al. (1981) conducted a detailed study of nonisothermal effects due to areal variation in reservoir temperatures. They found that the pressure response can be significantly altered by these effects. However, the magnitude of these effects depends greatly on the temperature range, the extent of the temperature variations, and the size of the temperature anomaly. If the reservoir temperature anomaly extends over a considerable distance, it is unlikely that temperature effects will be observed in short-term production tests.

More significant thermal effects are observed during cold-water injection tests in hot-water reservoirs. As injection testing is currently being used at a number of geothermal fields (e.g., Krafla, Iceland; Olkaria, Kenya; Los Azufres, Mexico; Wairakei, New Zealand), a theoretical basis for analyzing such nonisothermal tests is greatly needed. The results of numerical simulation studies addressing this problem are discussed below.

During injection tests, water at a temperature lower than that of the reservoir water is injected into the geothermal aquifer. A temperature variation will develop in the reservoir, with colder water close to the injection well and hotter reservoir water farther away. This in turn creates differences in the density and viscosity of the fluid within the reservoir. In this study, the numerical simulator PT was used in its nonisothermal mode. In our numerical model the dependence of viscosity and density of the fluid on temperature is fully accounted for.

Problem and Approach. The problem considered is that of an injection well fully penetrating a horizontal homogeneous isotropic geothermal reservoir. The injected water is at a temperature of 100°C but the reservoir contains single-phase water at a temperature of 300°C. Actually, as will be seen later, the results obtained are valid for any temperature, if appropriate correction factors are used.

In the numerical simulation, a radial mesh (concentric circles) was used with fine elements close to the well covering the region with temperature variations. Farther away from the well, the mesh increased logarithmically. The reservoir was modeled as a single layer and thus buoyancy forces were neglected. Figure 13 shows a schematic of the model used; the parameters used in the simulation are given in Table 4.

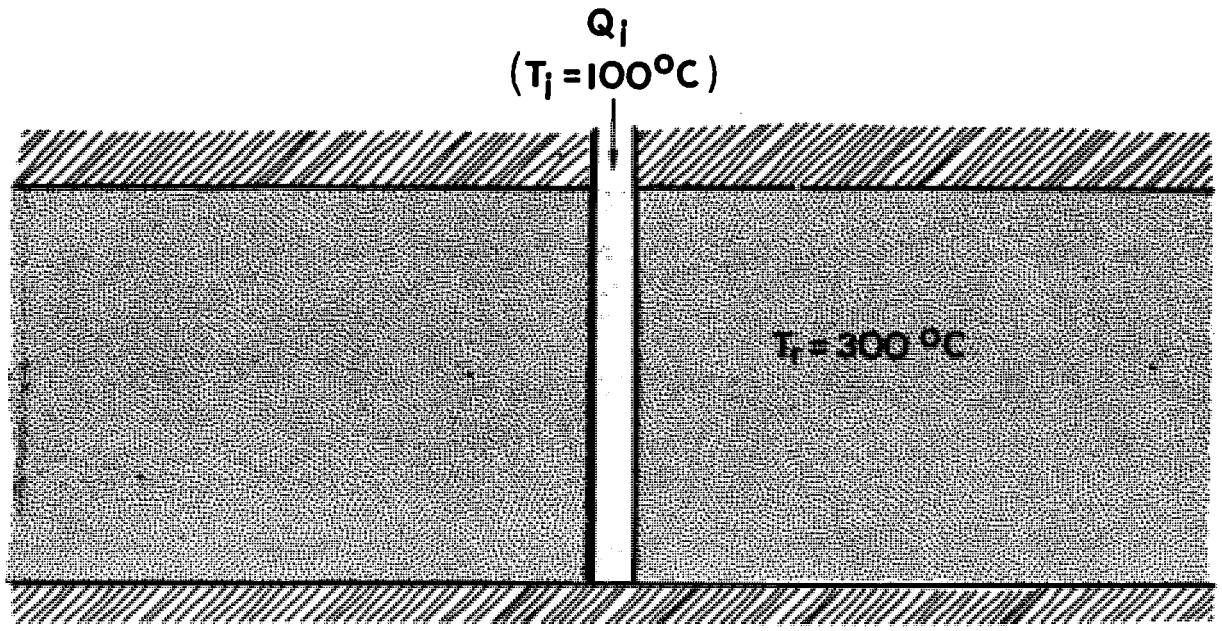

Figure 13. Model used in the study of injection into a porous media geothermal reservoir. [XBL 806-1241]

Table 4. Parameters used in the study of injection testing of porous geothermal reservoirs.

Flow rate (kg/s)	.200
Reservoir thickness (m)	1×10^{-3}
Permeability (m^2)	1×10^{-10}
Thermal conductivity (J/m.sec°C)	2.00
Density of solids (kg/m^3)	2650
Specific heat of solids (J/kg°C)	1000
Porosity (-)	.40
Specific heat of fluid (J/kg°C)	4200
Injection temperature (°C)	100
Reservoir temperature (°C)	300

Injection Tests. When 100°C water is injected into a hot (300°C) porous reservoir, initially at equilibrium, the pressure behavior shown in Figure 14 will result. At early times the pressure at the injection well will follow the Theis solution for the hot reservoir (300°C), but at later times, following a transition period, the pressure will follow a line that is parallel to the Theis solution for 100°C water. This behavior is caused by the differences in density and viscosity of the injected water and the reservoir water. Tsang and Tsang (1978) solved this problem analytically using the Boltzmann transformation and by approximating the parameter k/μ as a Fermi-Dirac function of r^2/t. Mangold et al. (1981) used a numerical simulator to study the pressure behavior at a production well located in a hot spot; i.e., the well is completely in a localized geothermal hot region with colder water farther away from the well.

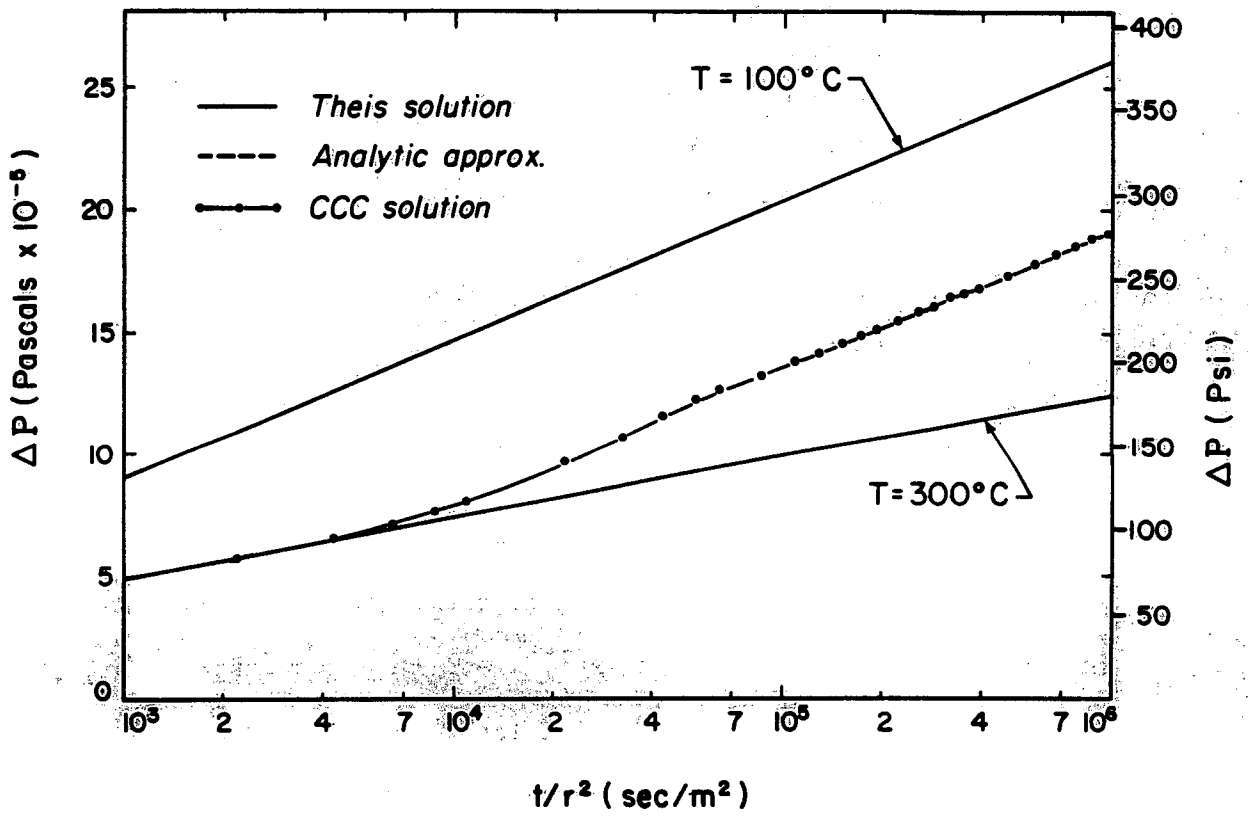

Figure 14. Pressure behavior at an observation well (r = 2.5 m) during cold water (100°C) injection into a 300°C geothermal reservoir. [XBL 799-2077]

Figure 15 shows how varying the permeability and storativity of the rock matrix affects the pressure behavior at the injection well. When the transmissivity and the permeability of the rock matrix are kept constant but the storativity is changed, the curves are just shifted along the time axis as predicted by the Theis solution. However, when the permeability is varied and the other two parameters kept constant, the time of deviation from the 300°C Theis-curve changes. This is consistent with the results by Tsang and Tsang (1978) who found that time of deviation is dependent on reservoir thickness as well as other parameters such as the flow rate and the reservoir and fluid heat capacities.

Injection-Rest-Injection Test. Figure 16 shows the results when there is initially a circular region of cold water (cold spot) around the well. The type of pressure response shown in Figure 16 should result when injection tests are performed soon after drilling is completed and before the well has been allowed to heat up. This kind of well test procedure is used in a number of geothermal fields (Krafla, Iceland; Olkaria, Kenya, etc.). The figure shows that at early times the pressure follows the 100°C Theis curve and then after some time, which depends upon the radius of the cold spot, the pressure increases along a line parallel to the 300°C Theis curve. At still later time another transition occurs and the pressure again starts increasing at a rate corresponding to the 100°C Theis-curve solution. These results indicate that by using an injection-rest-injection well test procedure, the radius of the cold spot generated by the first injection can be determined. This in turn allows the

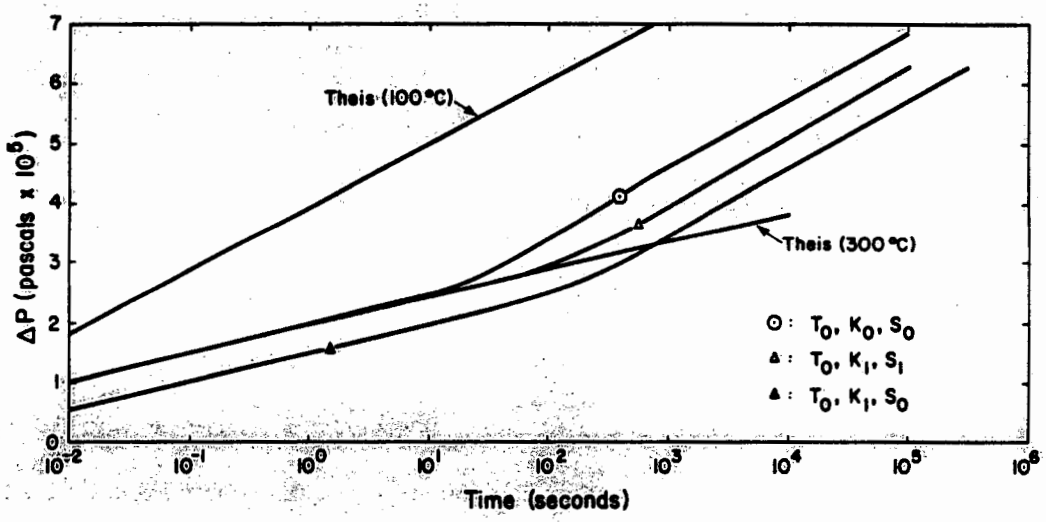

Figure 15. Transient injection pressure behavior, when 100°C water is injected into a 300°C reservoir, for different values of transmissivity and storativity of the reservoir.

[XBL 806-1328]

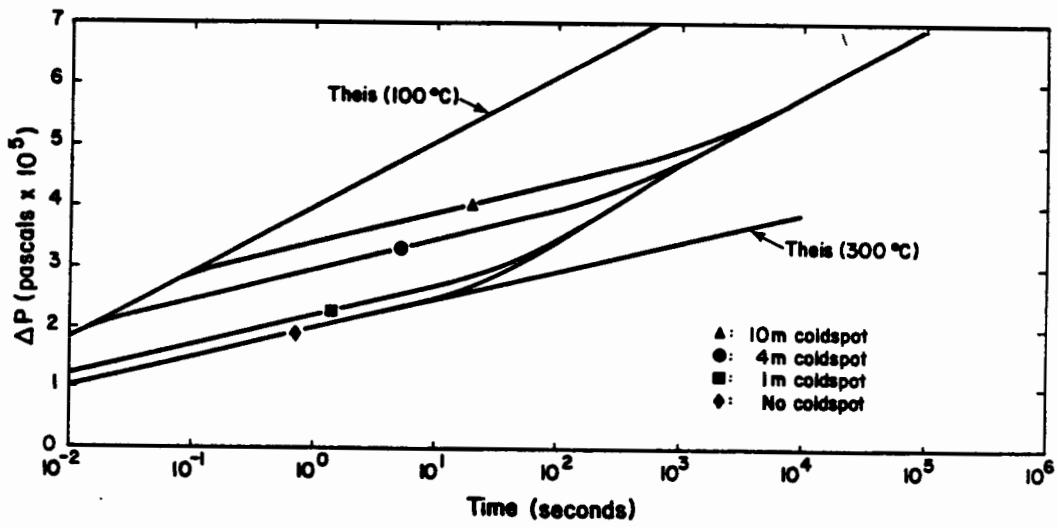

Figure 16. Injection pressure behavior, when 100°C water is injected into a well located in a cold-spot (lower temperature region).
[XBL 806-1329]

porosity to be approximated from equation 22, if the heat capacities of the reservoir solids and the water can be estimated.

$$\frac{v_T}{v_H} = \frac{\phi \rho_w c_w}{\rho_A c_A} \tag{22}$$

In equation (22), v_T is the velocity of the thermal front and v_H is the velocity of the hydrodynamic front.

Injection-Falloff Test. At the time when injection has just been terminated there is a pressure as well as a temperature gradient within the geothermal reservoir (Figure 17). If at this time a falloff test is performed, the pressure response shown in Figure 18 results. The pressure will initially decline at a rate corresponding to the 100°C Theis solution, but later a change in slope will occur and the 300°C Theis curve will be followed. These results are consistent with those obtained by Mangold et al. (1981).

Injection-Production Test. A case was studied where production immediately followed an injection period (that is, with reservoir initial conditions as shown in Figure 17). The calculated pressure behavior in the well, shown in Figure 19, is characterized by three distinct straight lines. At first the pressure decreases at a rate that corresponds to twice the rate given by the Theis solution for 100°C water. Later on the pressure decrease follows a slope that equals twice the slope given by the Theis solution for 300°C water. The reason for the doubled pressure decrease in comparison with the Theis solution is that two independent

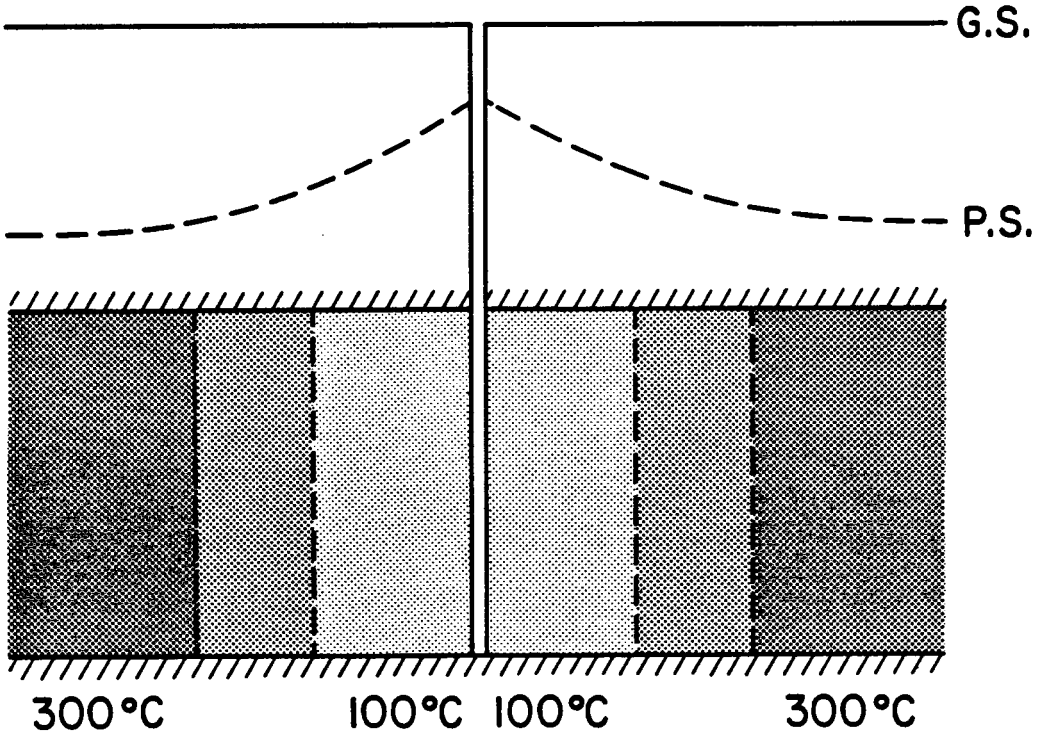

Figure 17. Schematic diagram showing reservoir conditions immediately after injection. [XBL 806-1330]

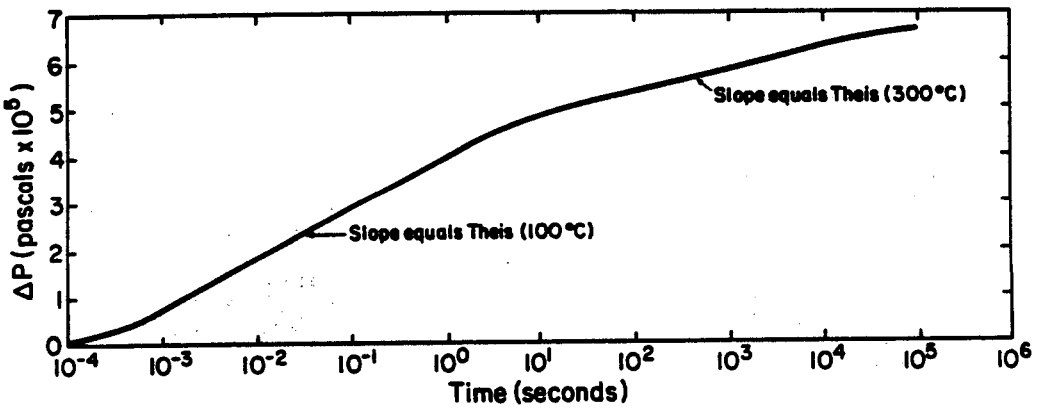

Figure 18. Pressure fall-off after 1.2 days of injection. [XBL 806-1331]

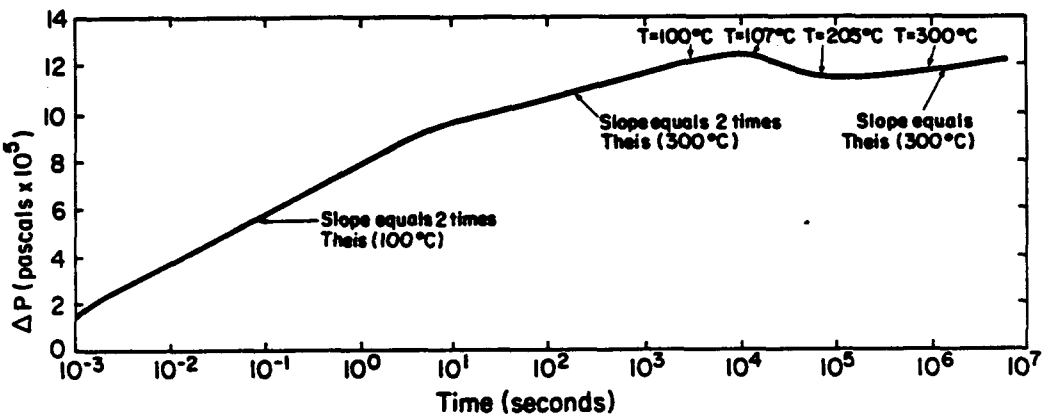

Figure 19. Pressure transient behavior during a production test, immediately following 1.2 days of injection. [XBL 806-1332]

forces control the drawdown, the constant withdrawal rate and the initial pressure falloff condition in the reservoir. Superposition of these two effects causes the double slopes.

After the two double slopes a transition occurs, following which the pressure starts declining at a rate corresponding to the Theis solution for 300°C water. During the transition the pressure in the well actually increased, probably due to rapid changes in the viscosity of the water. As shown in Figure 19, the temperature of the produced water changed from 100°C to 300°C during the transition, implying a more than threefold decrease in the viscosity of the water.

Discussion. Data from injection tests of porous media geothermal reservoirs show several linear segments on a pressure-log time plot. This behavior is due to the dependence of fluid density and viscosity on temperature. Our results indicate that when an injection-rest-injection procedure is employed, the radius of the cold spot resulting from the first injection period can be determined. Consequently an estimate of the effective porosity of the reservoir can be obtained.

An injection-production test can be advantageous because larger pressure changes can be observed (twice the rate predicted by the Theis solution). An observation of three different linear segments in the data may also lead to a better determination of the reservoir parameters. It must be noted, however, that other factors, such as boundaries and permeability variation within the reservoir, may cause a similar break in the

slope in the data shown in Figures 14-19. One must therefore be careful when analyzing injection test data. A knowledge of the temperature of the injected water and the reservoir fluids is essential for a proper determination of the reservoir hydraulic parameters.

Effects of Relative Permeability Parameters in Two-Phase Reservoirs

As previously mentioned, it is only recently that theoretical studies of well test analyses of two-phase geothermal systems have appeared in the literature. Moench and Atkinson (1978) numerically studied the pressure behavior of a well in a vapor-dominated reservoir with immobile liquid water. They found that pressure buildup exhibits an anomalous plateau caused by condensation effects in the reservoir near the well. Later Moench (1978) extended the model to include the effects of heat conduction. Garg (1978) developed an analytical solution for the pressure response of a well in a flashing or a two-phase reservoir produced at constant rate. He found that a plot of the downhole pressure versus the logarithm of time is a straight line, and the slope of the line is inversely proportional to the total kinematic mobility (to be defined later). Grant (1978) compared two-phase pressure gradients to single-phase gradients for geothermal wells. He found that the compressibility of a two-phase mixture is 10-10,000 times greater than the compressibility of single-phase steam or liquid water. The consequence is that while kH values remain unaffected, the $\phi\beta_t H$ values are affected by several orders of magnitude. Sorey et al. (1980) showed that the flowing enthalpy reaches a constant value when a well completed in a two-phase reservoir is produced at a constant rate. They also showed that during buildup the region around the well may reach higher liquid saturations than the undisturbed liquid saturation. They explain this phenomenon in terms of heat losses close to the well due to intensive boiling. Details of the mathematical approach taken by Sorey et al. are given by Grant (1979b).

O'Sullivan (1980) developed a semi-analytical similarity solution for well test analysis of two-phase geothermal reservoirs. A more detailed description of his approach is given in the following section.

One of the most fundamental problems in the analysis of well test data from two-phase reservoirs is the lack of understanding of the relative permeability functions for steam and liquid water. This also greatly affects the confidence in the numerical simulation of geothermal systems.

In two-phase flow in a porous material the mobility of each individual phase is retarded by the presence of the other. The degree of interference depends on the volumetric proportion of the two phases. This phenomenon is expressed mathematically by the saturation-dependent relative permeability functions k_{rl} and k_{rv}, for the liquid and vapor phases, respectively, which multiply the matrix permeability. Because the two phases move differentially, the mixture behaves like a fluid with a saturation-dependent "effective" or total kinematic viscosity ν_t given by:

$$\frac{1}{\nu_t} = \frac{k_{rl}}{\nu_l} + \frac{k_{rv}}{\nu_v} \tag{23}$$

where ν_l and ν_v are the kinematic viscosities of the liquid and vapor phases, respectively. Similarly, the enthalpy transported by the mixture depends on the relative permeability functions and is different from the in-place enthalpy. This "flowing" enthalpy h_f is given by:

$$h_f = \nu_t \left[h_l \frac{k_{rl}}{\nu_l} + h_v \frac{k_{rv}}{\nu_v} \right] \tag{24}$$

where h_l and h_v are the liquid and vapor enthalpies, respectively.

The movement of mass and energy in a geothermal reservoir is very strongly influenced by the magnitude of these two quantities, the total kinematic viscosity and the flowing enthalpy, which in turn, from equations (23) and (24), obviously depend on the nature of the relative permeability functions. Unfortunately the dependence of k_{rl} and k_{rv} on liquid saturation S_l is presently not known and is very difficult to deduce from laboratory experiments or field data.

Various investigators have reported on studies regarding the relative permeability functions. Experimental work on determining the relative permeability curves has been reported by Corey (1954), Chen et al. (1978), Counsil and Ramey (1979), and others. Grant (1977b) and Horne and Ramey (1978) used flowrate and enthalpy data from the Wairakei geothermal field in New Zealand to obtain information about the relative permeability parameters. Numerical modeling studies on the importance of the relative permeability curves have been reported by Jonsson (1978), Sun and Ershaghi (1979) and Bodvarsson et al. (1980). Finally, Sorey et al. (1980) illustrated effects of the relative permeability on the pressure drop and enthalpy variations during production from a single well by considering relative permeability curves suggested by Corey (1954) and Grant (1978).

In the present study, the sensitivity of ν_t and h_f to variations in the relative permeability functions is examined first. Then, the determination of ν_t and h_f from well-test results is discussed. A method of using these measurements together with theoretical plots of k_{rl} and k_{rv}

versus h_f to deduce the general shape of the relative permeability functions is suggested. Finally, the effects of the relative permeability functions on the pressure decline of flowing enthalpy build-up during a constant-rate production test is considered. It is shown that the characteristic rise in the flowing enthalpy from its initial value to a stable value after a moderate time is strongly influenced by dependence of h_f on S_l (and hence k_{rl} and k_{rv} on S_l).

Sensitivity study. Various relative permeability curves for steam-liquid water have been proposed in the literature [Corey, 1954; Chen et al., 1978; Horne and Ramey, 1978; and Counsil and Ramey, 1979]. However, since the curves that have been suggested are quite different from each other, the choice of relative permeability curves to be used in simulation studies of geothermal systems is rather arbitrary. Therefore at this stage it is important to identify which characteristics of the relative permeability curves are significant.

The relative permeability curves are characterized by the cutoffs where the steam or liquid becomes either fully mobile or immobile. A sensitivity study has been conducted to determine the relative importance of each of the cutoffs. The approach used is quite simple; for horizontal flow (no gravity) the relative permeability curves influence reservoir behavior only through the flowing enthalpy, h_f, and the total kinematic viscosity, ν_t. Therefore by observing the effect of the individual cutoffs on these quantities, their relative importance can be determined.

In the present study attention is given primarily to either Corey-type curves or straight line curves (see Figure 20). At present the Corey relative permeability curves are most widely used in reservoir numerical modeling. The curves, illustrated in Figure 20, indicate the two-phase conditions under which both phases are mobile; the mobility of each phase is severely retarded by the presence of the other. The sum of the individual relative permeabilities only reaches unity when one of the fluids is immobile. The other curves shown in Figure 20 are the "X" relative permeability curves, where the mobility of each phase is a linear function of the saturation and no cutoffs are present. The "X" curves represent the other extreme, where the phases are independent of each other and their mobilities are only a function of their volume fraction. Thus these relative permeability represent the likely extremes of what the real relative permeability functions may be.

The most important aspect of these curves is the "cutoffs" where steam or water becomes either fully mobile or immobile. In the following sensitivity study, five straight-line functions are considered: four possible curves each having one 30% cutoff, and what is referred to as the "X" curves, which correspond to the case with no cutoffs (broken lines in Figure 20).

Figure 21 shows the effect of the cutoffs on the flowing enthalpy. For comparison, the "X" relative permeability curve is shown as the thick solid line. The figure shows that when considering enthalpy, the immobile liquid cutoff is much more important than the other cutoffs.

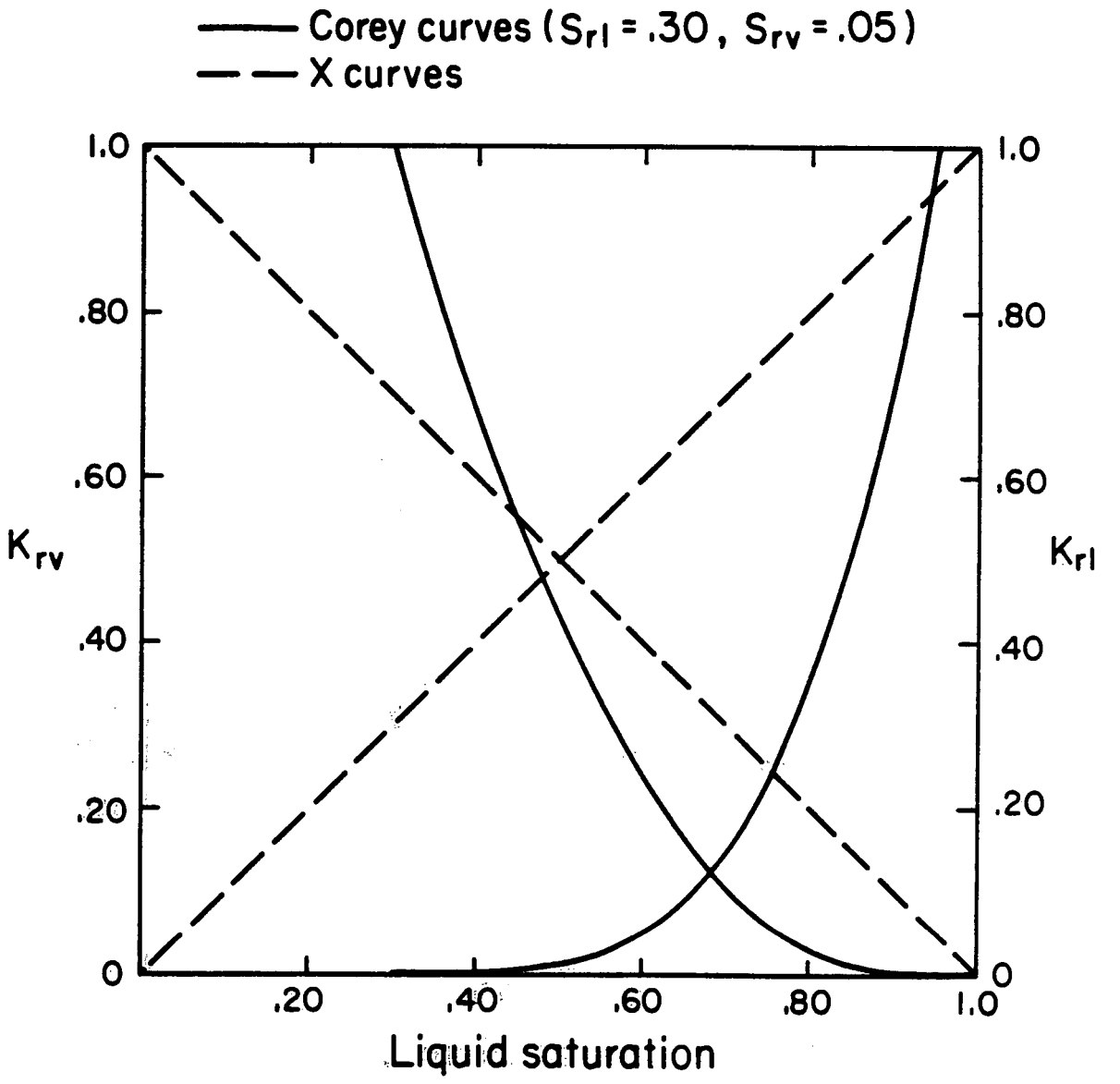

Figure 20. The Corey and the "X" relative permeability curves.
[XBL 8012-6556]

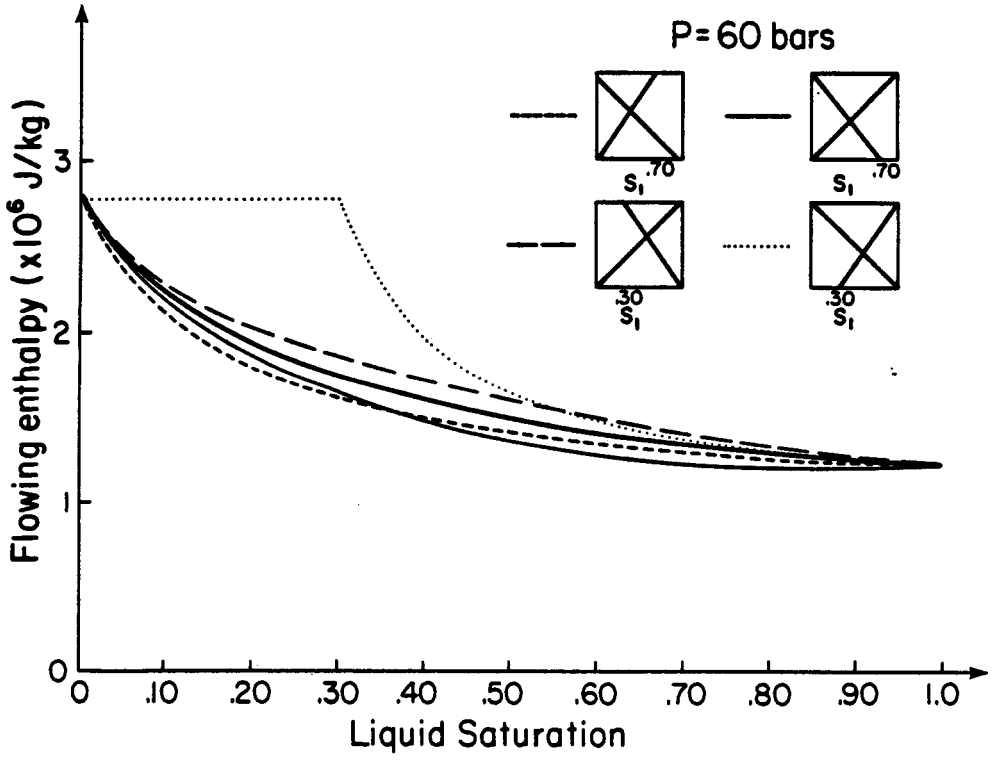

Figure 21. The relationship between flowing enthalpy and liquid saturation for linear relative permeability curves.

[XBL 8012-6540]

Figure 22 shows the effect of the cutoffs on the total kinematic viscosity (ν_t). Again the "X" relative permeability curves are included for comparison. In this case, both the liquid water cutoffs seem to be considerably more important than the vapor cutoffs. However, in terms of the percentage deviation from the "X" curve (the thick solid line), the importance of the immobile liquid water cutoff is considerably more than the fully mobile liquid water cutoff. The vapor cutoffs again are not very important. Similar conclusions regarding the importance of the cutoffs are obtained by Sun and Ershagi (1979), in considering the heat output from a one-dimensional system.

Well test data. During a well test in a two-phase reservoir, the downhole pressure follows a decline curve similar to that shown in Figure 23. The exact shape of the curve varies with reservoir conditions but in general it does not follow a straight line (Theis curve) because the mobility changes as the saturation changes near the well. Nevertheless, the slope of the decline curve (m) can be used to calculate the mobility at each pressure using the formula [Garg, 1978; Sorey et al, 1980; or O'Sullivan, 1980]:

$$\frac{kH}{\nu_t} = \frac{2.303q}{4\pi m} \tag{25}$$

The flowing enthalpy of the produced fluid typically follows a curve like that shown in Figure 24, rising from an initial value to a stable higher value after a moderate time. Simultaneous measurements of pressure and flowing enthalpy thus allow ν_t and h_f to be calculated provided kH is known (e.g., from an injection test).

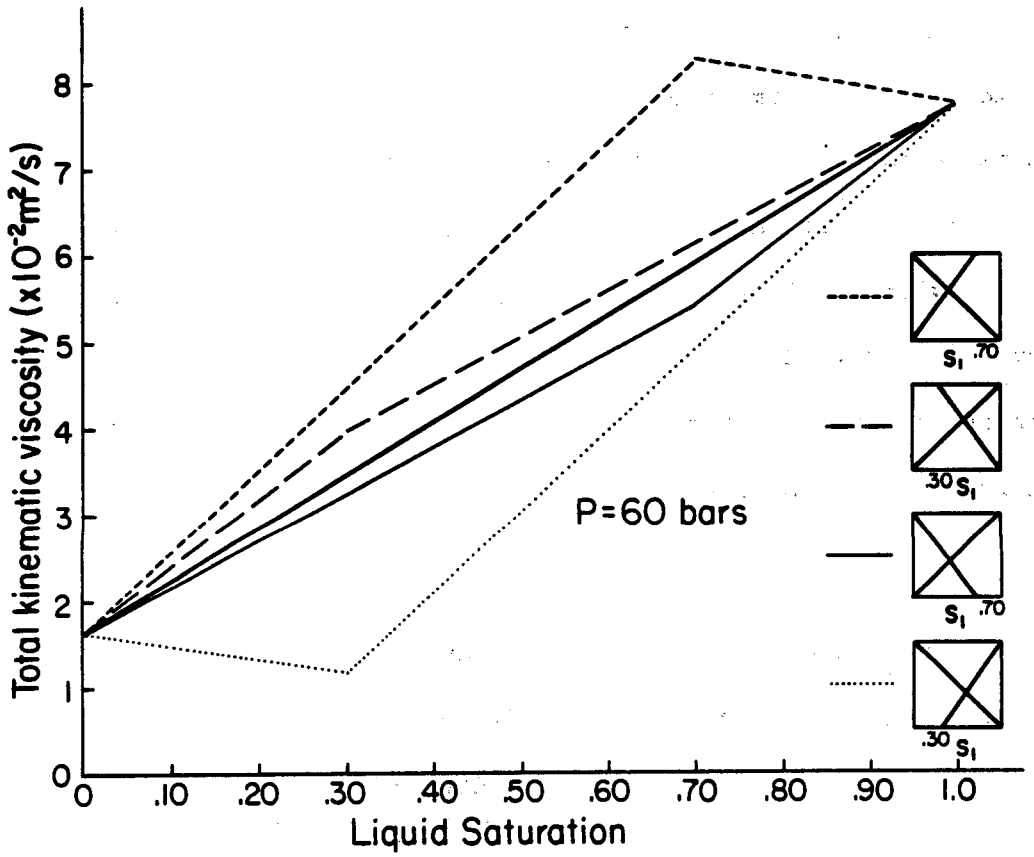

Figure 22. The relationship between kinematic viscosity and liquid saturation for linear relative permeability curves.
[XBL 8012-6541]

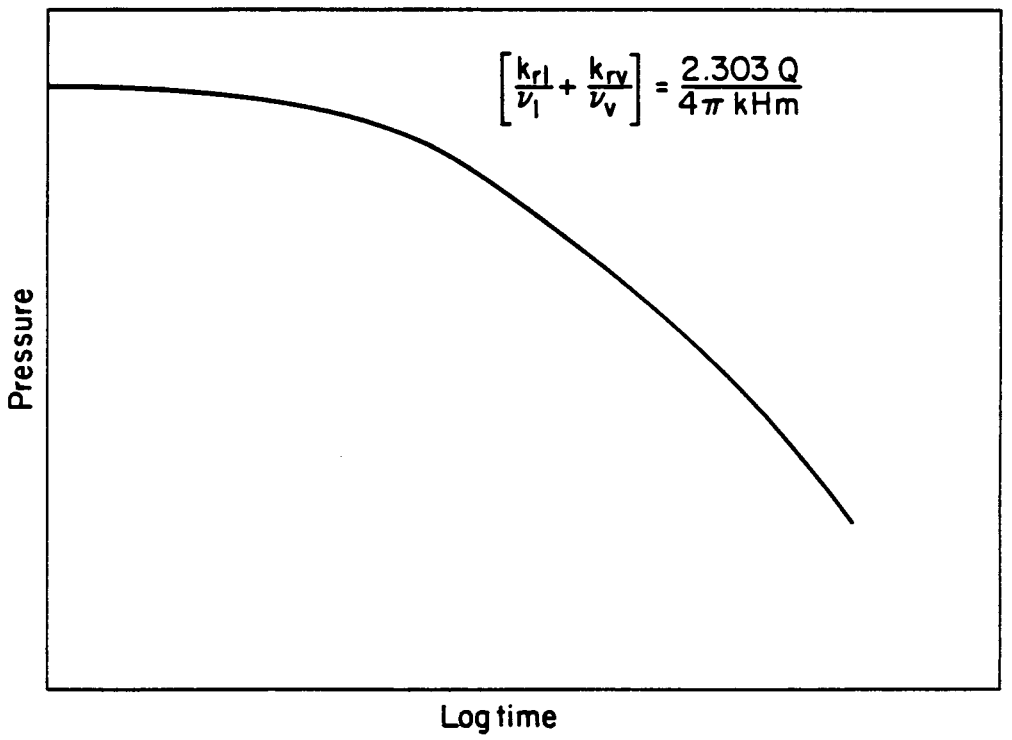

Figure 23. Pressure transient behavior during a well test in a two-phase reservoir. [XBL 8012-6538]

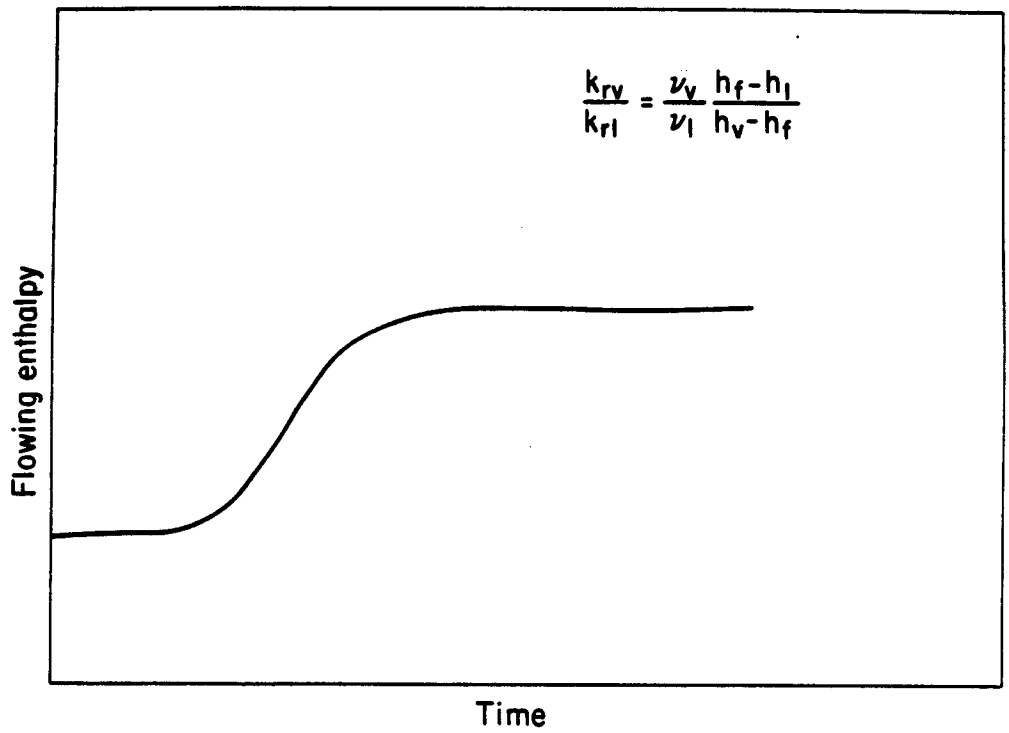

Figure 24. Flowing enthalpy during a well test in a two-phase reservoir. [XBL 8012-6539]

Using equations (23) and (24), k_{rv} and k_{rl} can then be calculated. By repeating this process at a number of values of flowing enthalpy (either at different times during the test or by using different production rates), plots of k_{rv} and k_{rl} versus h_f can be obtained. However, as the corresponding liquid saturation S_l is not known and cannot be measured satisfactorily, the required relative permeability curves cannot be obtained.

Although detailed relative permeability curves cannot be obtained, the plots of k_{rl} and k_{rv} versus h_f are useful. Theoretical plots of this type for the "X" curves and Corey curves (Figure 20) are shown in Figures 25 and 26. Figure 25 shows the flowing enthalpy as a function of the liquid relative permeability for the Corey and the "X" curves. The figure shows that although the two curves have distinctly different characteristics, they form a rather small zone of probable liquid relative permeability values. The vapor relative permeability when plotted against flowing enthalpy for the Corey and the "X" relative permeability curves (Figure 26) also illustrates the basic difference between the two cases, but the curves are further apart. A comparison of field results with those of Figures 25 and 26 should give a clear indication of whether the relative permeability curves at the geothermal field in question more closely resemble the Corey or the "X" relative permeability curves.

The rise in flowing enthalpy. As explained earlier, the flowing enthalpy in a constant-rate well test reaches a stable value after some time. Sorey et al. (1980) studied the rise in flowing enthalpy using an

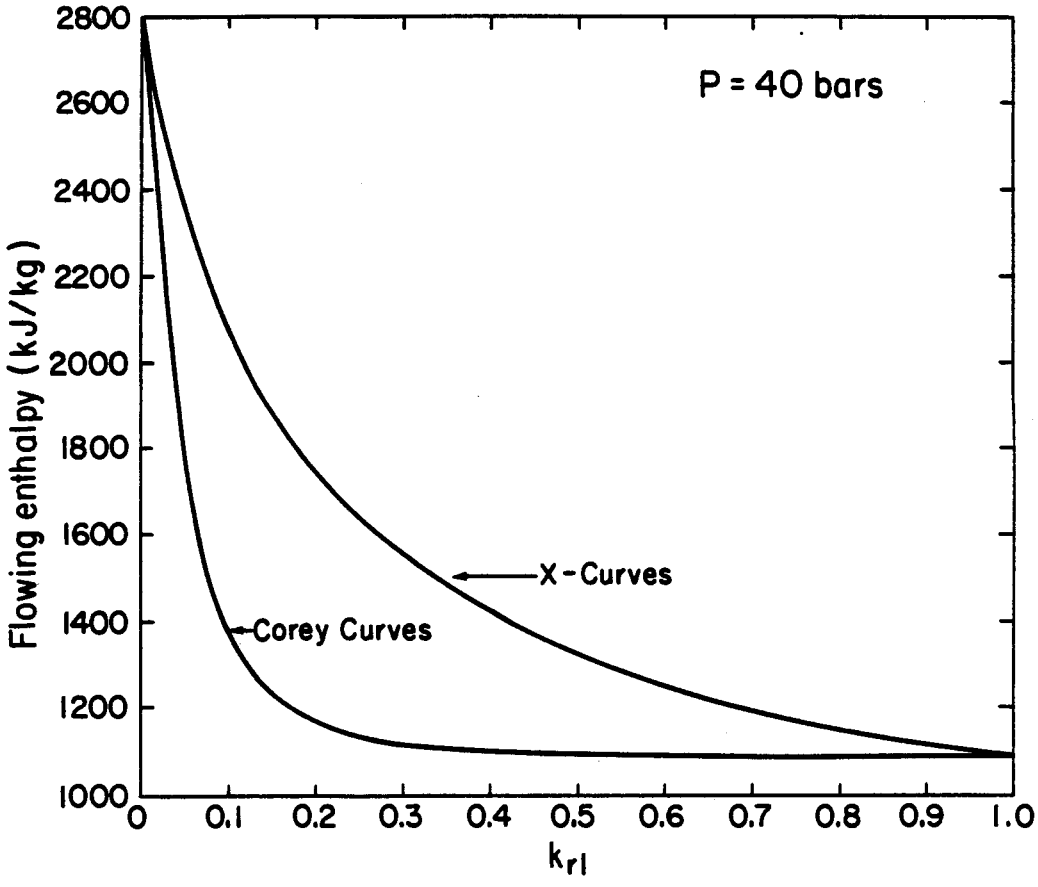

Figure 25. The relationship between flowing enthalpy and liquid relative permeability curves. [XBL 8012-6532]

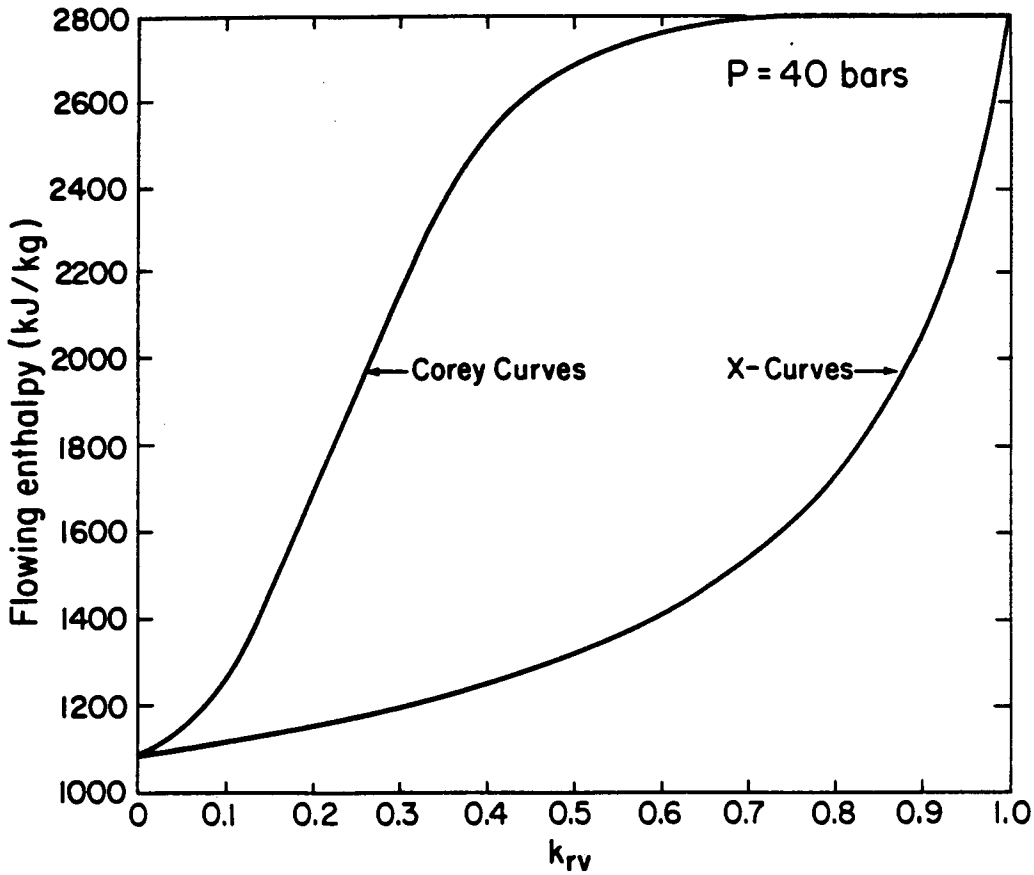

Figure 26. The relationship between flowing enthalpy and vapor relative permeability for Corey and "X" relative permeability curves. [XBL 8012-6533]

approximate analytical method and found a strong dependence on the relative permeability curves used. A semi-analytic technique developed by O'Sullivan (1980) has been used to study the effect of the relative permeability curves on the rise in the flowing enthalpy in more detail. In order to explain the main features of the results, a brief outline of the basic equations is required.

Basic Equations. Following O'Sullivan (1980) by using the transformation $\eta = r/\sqrt{t}$, the mass and the energy balance equations for a two-phase system can be written:

$$\frac{dQ_m}{d\eta} + \frac{\eta^2}{2}\frac{dA_m}{d\eta} = 0 \tag{26}$$

$$\frac{dQ_e}{d\eta} + \frac{\eta^2}{2}\frac{dA_e}{d\eta} = 0 \tag{27}$$

In equations (26) and (27), A_m and A_e are the mass and the energy accumulation terms, respectively,

$$A_m = \phi\rho \tag{28}$$

$$A_e = (1 - \phi)\rho_r c_r T + \phi(\rho h - P) \tag{29}$$

The density (ρ) and enthalpy (h) of the fluid mixture are defined as:

$$\rho = \rho_l S_l + \rho_v S_v \tag{30}$$

$$h_f = (\rho_l h_l S_l + \rho_v h_v S_v)/\rho \tag{31}$$

The mass (Q_m) and the energy (Q_e) fluxes can be written as (ignoring conduction):

$$Q_m = T_m \eta \frac{dP}{d\eta}, \tag{32}$$

$$Q_e = h_f Q_m, \tag{33}$$

where the mobility T_m is given by $T_m = k/\nu_t$. Using Q_m, P, and S_1 as independent variables, equations (26), (27), (32), and (33) can be combined to yield:

$$\eta \frac{dS_1}{d\eta} = - \frac{Q_m}{T_m} \left\{ \frac{Q_m \frac{dh_f}{dP} + \frac{\eta^2}{2} \left[\frac{dA_e}{dP} - h_f \frac{dA_m}{dP} \right]}{Q_m \frac{dh_f}{dS_1} + \frac{\eta^2}{2} \left[\frac{dA_e}{dS_1} - h_f \frac{dA_m}{dS_1} \right]} \right\} \tag{34}$$

Similarly, equations (26) and (27) can be combined to give:

$$Q_m \frac{dh_f}{d\eta} = - \frac{\eta^2}{2} \left[\frac{1}{\eta} \left(\frac{dA_e}{dP} - h_f \frac{dA_m}{dP} \right) \frac{Q_m}{T_m} + \left(\frac{dA_e}{dS_1} - h_f \frac{dA_m}{dS_1} \right) \frac{dS_1}{d\eta} \right]. \tag{35}$$

Equations (34 and 35) will be used as a basis in the following discussion

The phenomenon of stable enthalpy during a constant-rate well test has been observed in well data from Wairakei and during numerical simulations of well tests (Sorey et al., 1980 and O'Sullivan, 1980). Analytical verification of a long-time stable flowing enthalpy can be obtained by considering equation (35) in the limit as $\eta \to 0$ (large times) which yields simply:

$$\frac{dh_f}{d\eta} = 0 \qquad \text{or} \qquad h_f = \text{constant} \tag{36}$$

As $\eta \to 0$ and h_f approaches its constant value, equation (34) can be approximated by:

$$\eta \frac{dS_1}{d\eta} = - \frac{Q_m}{T_m} \frac{\frac{dh_f}{dP}}{\frac{dh_f}{dS_1}} \tag{37}$$

In the above derivations, the chain rule for partial differentation has been used in the formula:

$$\frac{dh_f}{d\eta} = \left(\frac{\partial h_f}{\partial S_1}\right)_P \frac{dS_1}{d\eta} + \left(\frac{\partial h_f}{\partial P}\right)_{S_1} \frac{dP}{d\eta} \tag{38}$$

The second term on the right-hand side of equation (38) is small and therefore this equation can be used in a discrete form to approximate the rise in flowing enthalpy as follows:

$$\Delta h_f \approx \left(\frac{\partial h_f}{\partial S_1}\right)_P \Delta S_1. \tag{39}$$

The accuracy of this formula is confirmed by independent calculations. In equation (39), ΔS_1 represents the total change in saturation up to the time when a stable value of the flowing enthalpy is reached. From equation (39) the strong dependence of Δh_f on the relative permeability curves is obvious. However, the saturation change ΔS_1, and therefore also Δh_f, is dependent upon several other factors, including initial conditions (T, S_1), porosity, mass flowrate and total kinematic mobility. The relationships between Δh_f and these parmeters must be established before Δh_f can be used to investigate the shape of the relative permeability curves.

Figure 27 shows the rise in flowing enthalpy versus the initial flowing enthalpy for three initial temperatures. The curves in Figure 27 show that the rise of flowing enthalpy is dependent upon the initial temperature and the initial flowing enthalpy in the reservoir. The dependence on the initial temperature can be explained by considering equations (34) and (39).

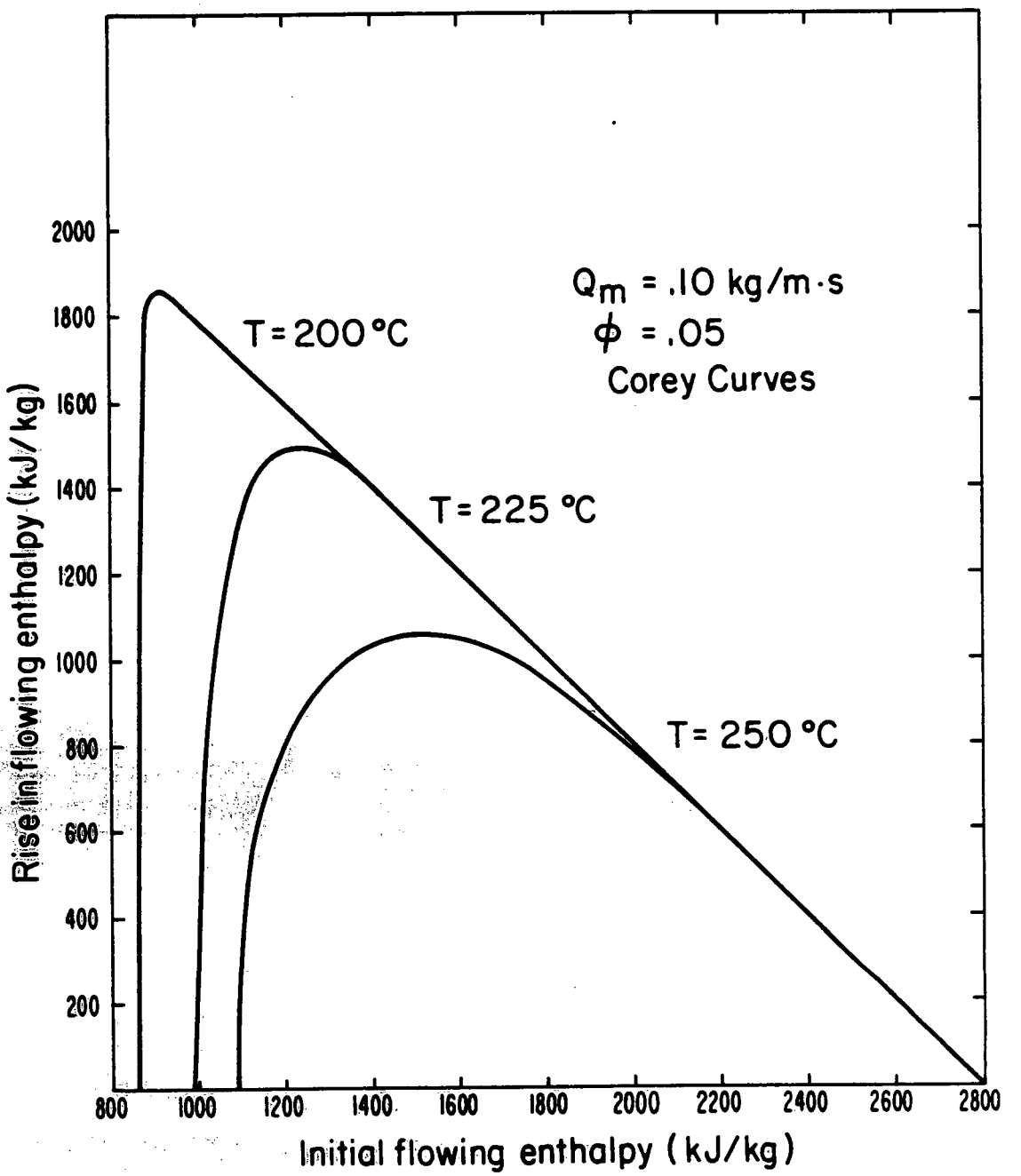

Figure 27. The relationship between the rise in flowing enthalpy and the initial flowing enthalpy for a porosity of ϕ = .05.
[XBL 8012-6536]

The saturation changes given by equation (34) are more pronounced at lower temperatures (or equivalently at lower pressures), primarily due to the lower total kinematic mobility (T_m) at lower temperatures. Consequently, the flowing enthalpy changes will be larger at lower temperatures (equation 39). The dependence of Δh_f on the initial saturation can be explained using Figure 28. For the Corey relative permeabilty curves, the change in flowing enthalpy is most pronounced at medium values of saturation and the rise in the flowing enthalpy is therefore largest at those initial saturation values.

The rise in flowing enthalpy also depends on the porosity ϕ and the mass flow rate Q_m. Figure 29 shows a plot similar to that in Figure 27, but a higher porosity was used in the simulation (ϕ = .25). Sorey et al. (1980) developed curves similar to the ones shown in Figures 27 and 29 using an approximate analytical procedure. Their curves in general show a considerably smaller rise in flowing enthalpy than the curves shown in Figures 27 and 29. The difference is due to the approximations involved in deriving the analytical expressions used by Sorey et al. The numerical method presented here does not necessitate the use of those approximations.

The relationship between the rise in flowing enthalpy and porosity is shown in Figure 30 for an initial temperature of 250°C and several values of initial saturation. In all of the cases, the lower the porosity, the greater the rise in flowing enthalpy. In cases of high initial liquid saturation, a linear relationship between the rise in flowing enthalpy and $(1 - \phi)/\phi$ was observed for porosity values higher than ϕ = .05.

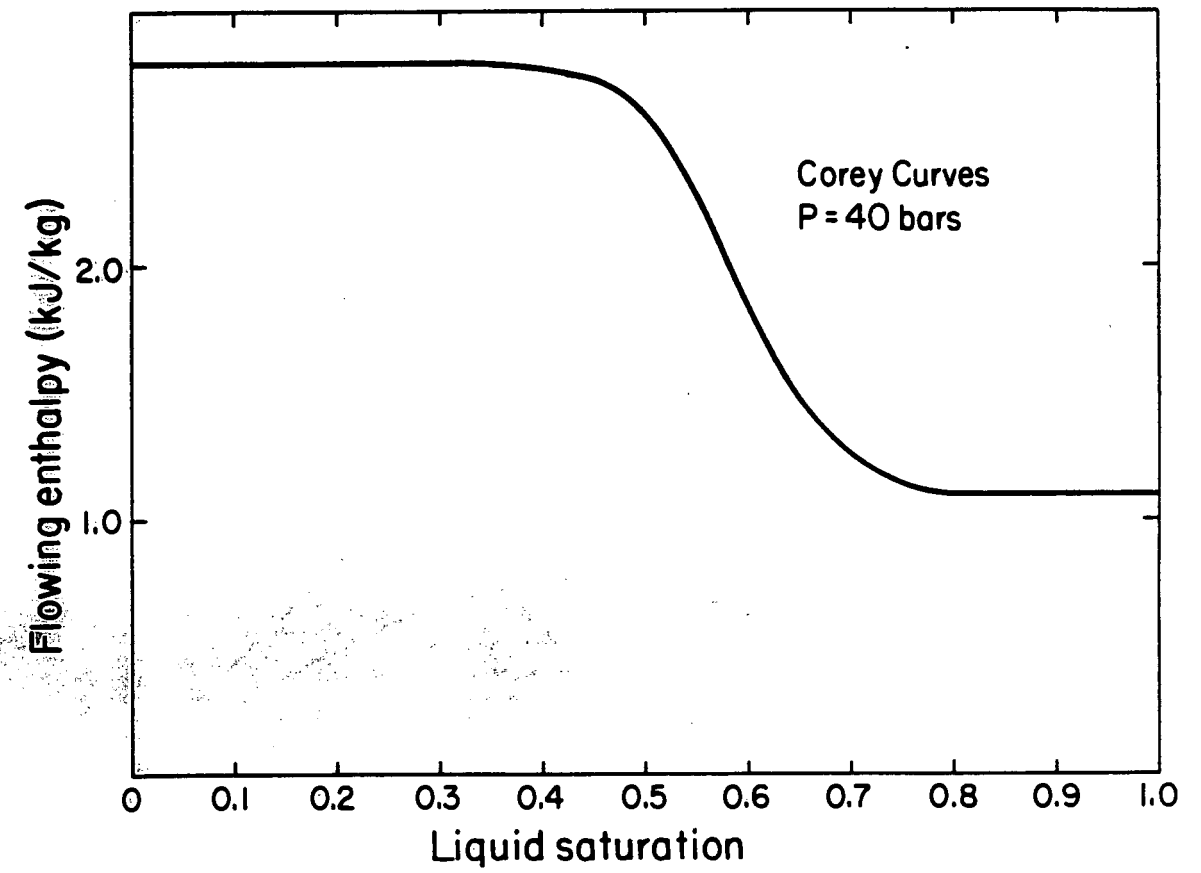

Figure 28. The relationship between flowing enthalpy and liquid saturation for the Corey relative permeability curves.
[XBL 8012-6546]

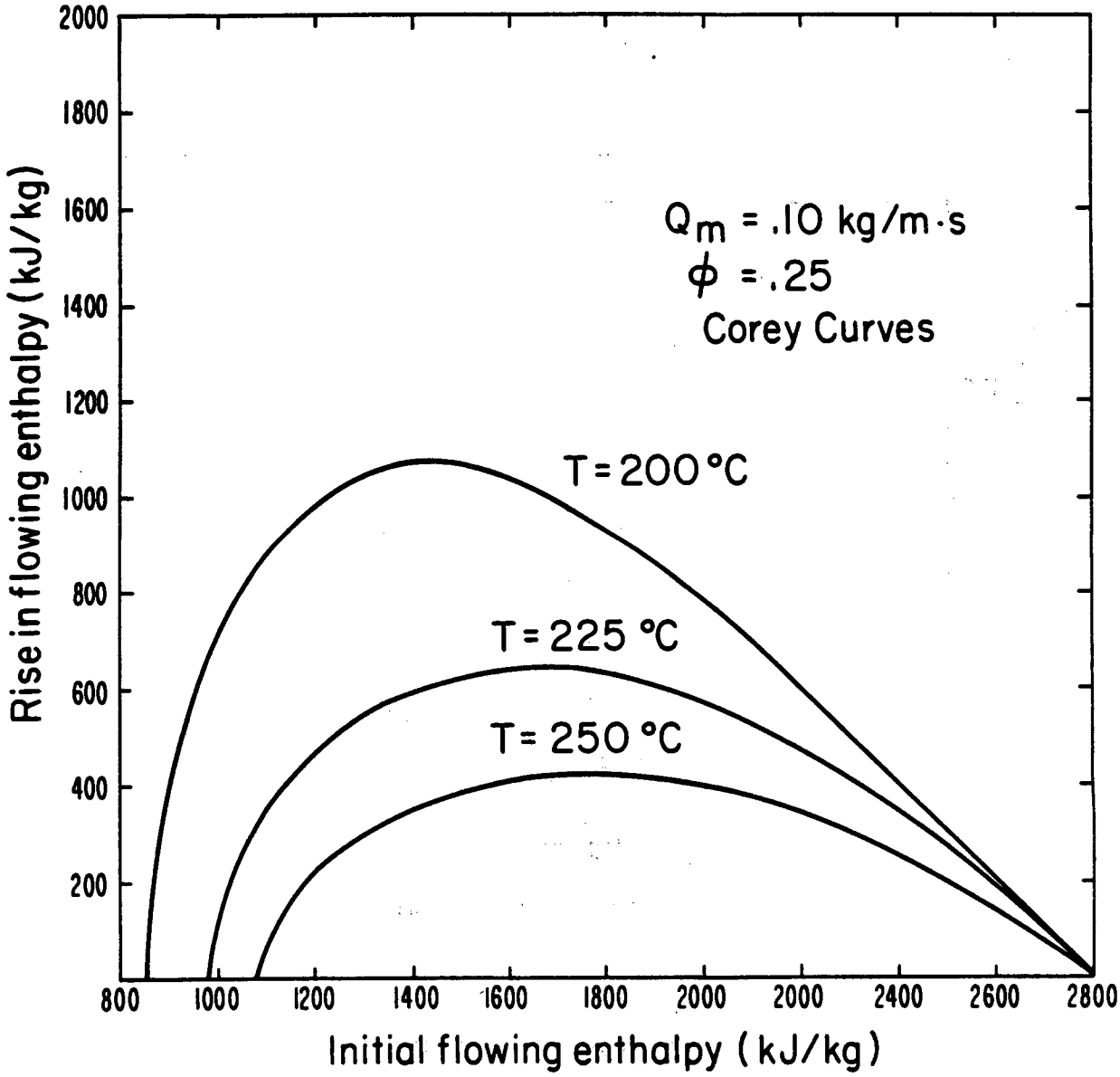

Figure 29. The relationship between the rise in flowing enthalpy and the initial flowing enthalpy for a porosity of ϕ = .25.
[XBL 8012-6537]

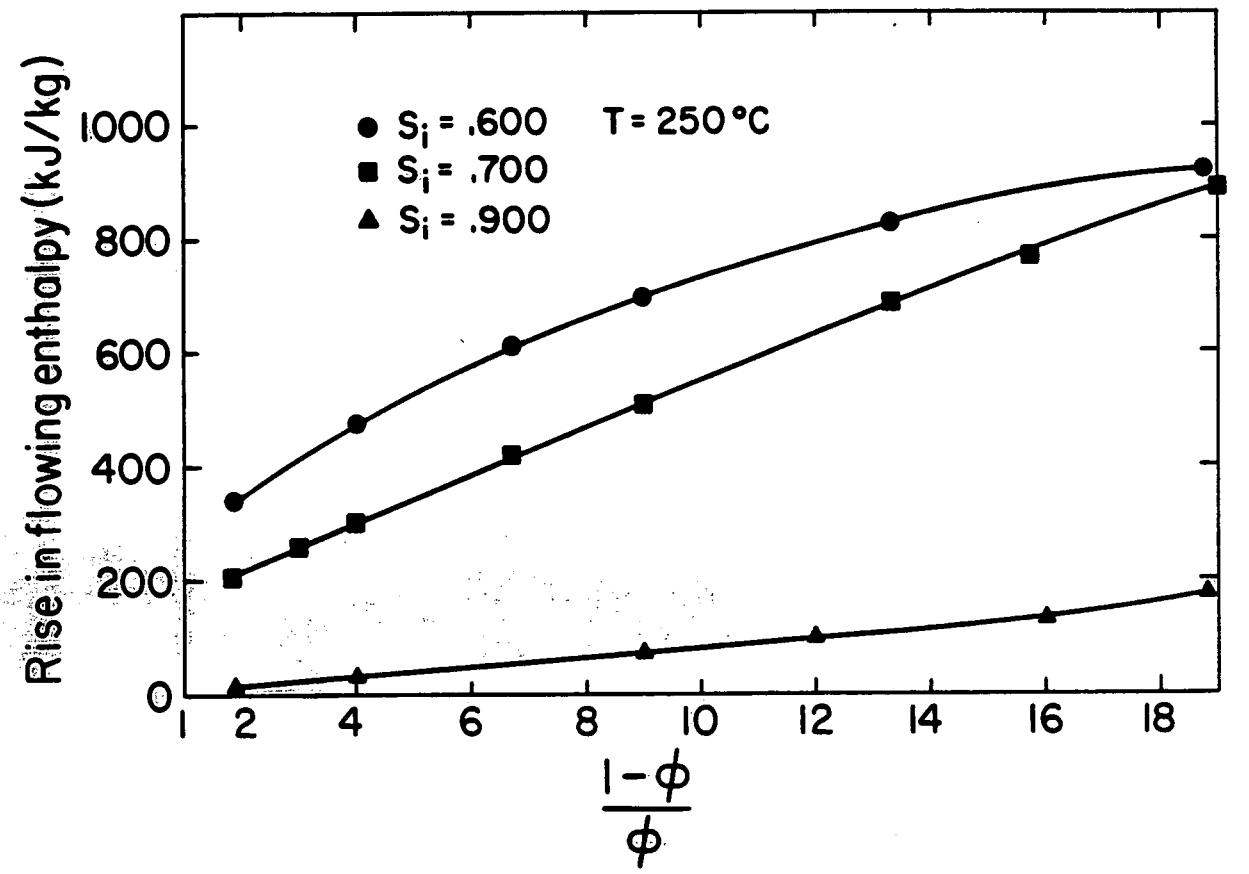

Figure 30. The relationship between porosity and the rise in flowing enthalpy. [XBL 8012-6535]

At lower initial liquid saturations the nonlinear effects are more pronounced. These results have been confirmed by an independent analytical study.

The relationship between the mass flowrate and the stable flowing enthalpy is shown in Figure 31. Three curves representing different values of the initial saturation are shown, but in all three cases, the initial temperature of 250°C and a porosity of 0.05 was used. The curves representing high initial saturation ($S_i > .80$) show an approximately linear relationship between the flowrate and the stable flowing enthalpy, but at lower initial saturations ($S_i = .64$) a more nonlinear behavior is observed. The near-linear relationship at high initial liquid saturations can be derived analytically by considering equations (34) and (39). At high initial saturations, the derivatives dh_f/dP and dh_f/dS_i are negligible for the Corey relative permeability curves (see Figure 27), and equation (34) can be written as:

$$\eta \frac{dS_1}{d\eta} = \frac{Q_m \left(\frac{dA_e}{dp} - h_f \frac{dA_m}{dP} \right)}{T_m \left(\frac{dA_e}{dS_1} - h_f \frac{dA_m}{dS_1} \right)} \tag{40}$$

The terms in the numerator and denominator of equation (40) are almost constant at higher initial liquid saturations. Consequently,

$$\Delta S_1 \; \alpha \; \frac{Q_m}{T_m} \tag{41}$$

and from equation (39),

$$\Delta h_f \; \alpha \; \frac{Q_m}{T_m} \; . \tag{42}$$

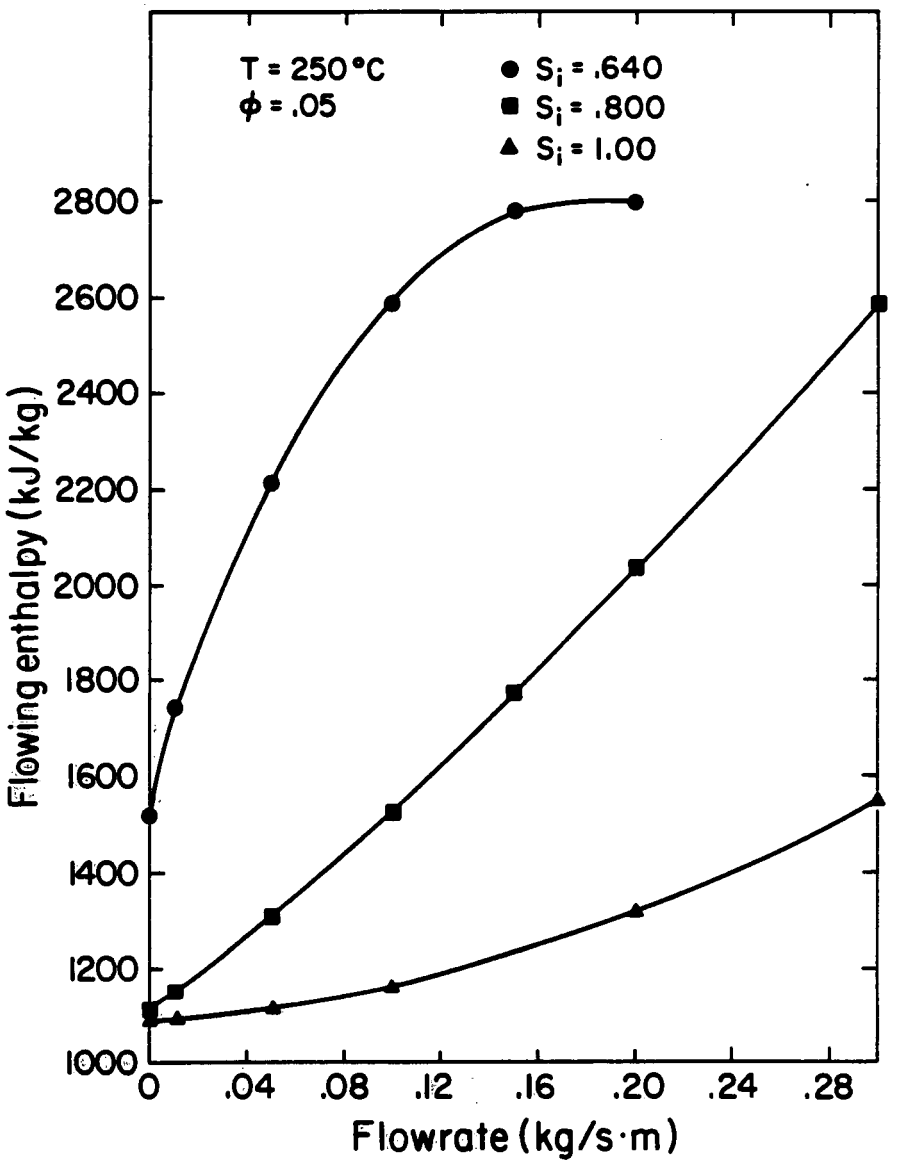

Figure 31. The relationship between flow rate and the rise in flowing enthalpy. [XBL 8012-6534]

The slight nonlinear effects in the high initial saturation curves shown in Figure 30 are probably due to the fact that T_m decreases slightly with pressure and saturation.

Sorey et al. (1980) observed a near-linear relationship between the flowing enthalpy and flowrate from wells in Wairakei, New Zealand. Their use of linear plots, such as the one shown in Figure 30, to obtain the initial resevoir enthalpy for the wells in New Zealand is well justified. However, in the case of a low initial saturation, linear approximations may be somewhat in error.

In light of the preceding discussion it is clear that the rise in flowing enthalpy is complicated by various factors, such as the porosity, flowrate, and the initial conditions. However if all of these factors are known, the change in saturation may be approximated and the slope of the h_f versus S_l curves (dh_f/dS_l) can be determined (equation 39). This in turn will yield information regarding the relative permeability parameters.

Conclusions. The primary results obtained in this study are as follows:

(1) The liquid cutoffs are the most important characteristics of the relative permeability curves, as they greatly affect the flowing enthalpy and the total kinematic mobility.

(2) The relative permeability parameters can be determined from field data in terms of the flowing enthalpy, and compared to

theoretical curves (e.g., Corey and "X" curves). This will enable an approximate determination of the conventional relative permeability curves in terms of saturation to be made.

(3) The rise in flowing enthalpy can give information regarding the relative permeability curves, provided that parameters such as kh and ϕ are known (e.g., from injection and interference tests). However, the rise in flowing enthalpy is complicated by many other factors, such as the porosity and the extraction rate.

RESERVOIR EXPLOITATION STRATEGIES

In the development of a geothermal resource, an appropriate production strategy must be selected. This includes determination of the optimal well spacing and completion depths. In many cases these decisions are based solely on achievable levels of power production, without giving due consideration to ultimate energy recovery. Thus, the production wells are often located very close to each other and the completion depth is determined based on available exploration data. This may lead to short-lived production wells and a low recovery ratio for the geothermal resource. Selection of an exploitation strategy should be based on appropriate reservoir engineering calculations that will result in an optimum balance between energy recovery and investment costs. Calculations aimed at optimizing field development were carried out by Morris and Campbell (1979) for the East Mesa geothermal field in the Imperial Valley, California.

The economic value of a geothermal well depends not only on its deliverability, as in the case of an oil well, but also on the enthalpy of the produced fluids. If there is a two-phase zone or a vapor zone present in the field (e.g., Baca, U.S.A.; Olkaria, Kenya; Broadlands, New Zealand), there is an incentive to produce from them, rather than from deeper liquid reservoirs, because fluids of higher enthalpy can be obtained. The short-term benefits are obvious, but in the long run, a lower energy recovery ratio from the field may result, as will be shown below.

Reservoir With a Steam Cap

In this study, the behavior of a liquid-dominated geothermal reservoir in response to production from different horizons is studied using numerical simulation methods. The Olkaria geothermal field in Kenya is used as an example where a two-phase vapor-dominated zone overlies the main liquid-dominated reservoir. One of the important questions arising in the development of the Olkaria field is from which zone is it most beneficial to produce. The present study is the first attempt to answer that question. The possibility of improving energy recovery from vapor-dominated reservoirs by tapping deeper horizons is also considered. The data used in the following discussion have been reported by Noble and Ojiambo (1975), U. N. Feasibility Reports (1976), McNitt (1977), and Bjornsson (1978).

Surface exploration of the Olkaria geothermal field started in 1956. Exploratory drilling began in 1973 and approximately 20 production wells have been drilled to date at the site. Resistivity surveys have indicated the presence of a large resource extending over an area of approximately 100 km^2. The wells are located within the lowest resistivity zone (<20 ohm-m), which covers an area of 12 km^2. The wells range in depth from approximately 1000 to 1700 m. The following reservoir model has been developed based on well data [Bjornsson, 1978].

At 700-800 m depth (below the caprock) the wells have penetrated a 50-150 m-thick vapor-dominated zone. The vapor zone is believed to contain 10-25% by volume immobile residual water. A thick water-dominated

reservoir underlies the vapor zone. Seismic data have indicated that the basement depth is approximately 3600 m, indicating that the thickness of the water zone is approximately 2700 m. The water reservoir is believed to be in a two-phase condition with steam saturation in the range of 10-25% by volume.

A pressure of 35 bars has been measured in the vapor zone, corresponding to a temperature of approximately 240°C. The pressure in the water zone is believed to follow the curve for boiling point versus depth [Truesdell and White, 1973]. This would indicate that the temperature of the basement rocks exceeds 360°C.

The reservoir rocks consist of acid lavas, tuffs, and agglomerates. The lava flows are typically on the order of 50 m thick. Well tests performed on the wells have indicated an average reservoir permeability of 10-20 md. This type of testing, in general, will reflect horizontal permeability of the reservoir rocks.

At Olkaria, if the fluid is produced mainly from contact zones between lava flows, the vertical permeability may be significantly lower than the horizontal permeability (10-20 md). Assessment of the producibility of the Olkaria reservoir must therefore include a thorough sensitivity analysis of the effects of anisotropic permeabilities.

Numerical Approach

The numerical simulations were carried out using the code SHAFT79 that was developed by Pruess and Schroeder (1980). The reservoir model

used in the numerical simulations is shown in Figure 32. The vapor zone is assumed to be 150 m thick, and underlain by a 2700 m-thick liquid-dominated zone. The caprock and bedrock are assumed to be closed to mass and heat flow.

The conductive heat flow through the basement and caprock, and the relatively small fluid discharge at the surface are neglected in the model. Due to the large production rate assumed in the calculations, these approximations should not significantly affect the computed response of the reservoir to exploitation.

The mesh used in the study consists of a total of 59 disk-shaped elements, varying in thickness from 10 to 200 m. The elements form a one-dimensional vertical column with the top 15 elements (a total of 150 m) representing the initial vapor zone. The remaining 44 elements represent the initial water zone, with fine (10 m-thick) elements close to the boundary between the vapor and the water zones, and thicker elements at greater depths.

The reservoir is assumed to cover a 12 km^2 area, which corresponds to that of the largest resistivity low at Olkaria. The present reservoir model ignores horizontal variations in reservoir properties and conditions. The four cases studied are shown schematically in Figure 32. In Case 1, it is assumed that the wells produce solely from the vapor zone. Case 2 considers production from the water zone only. In Cases 3 and 4,

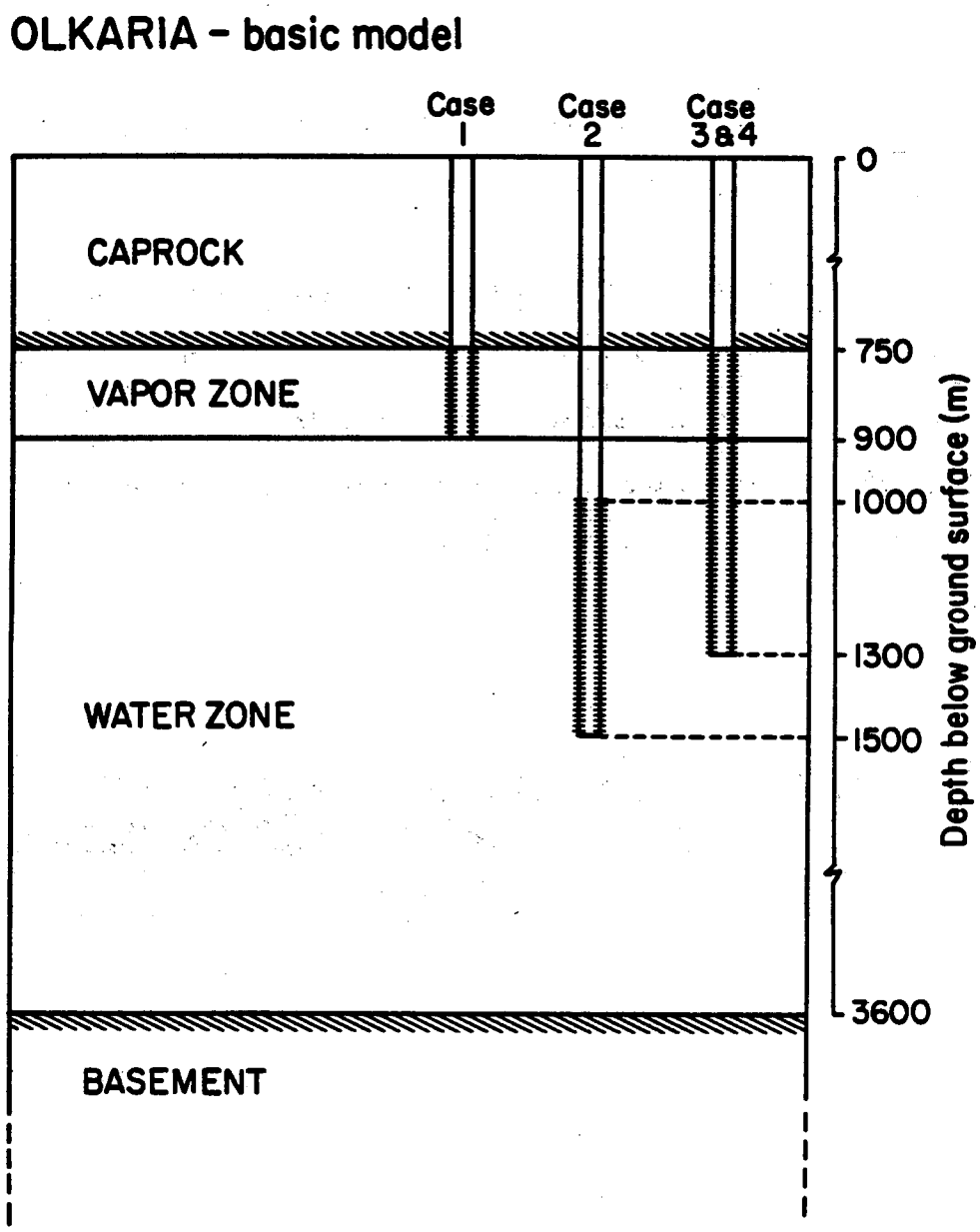

Figure 32. A schematic reservoir model of the Olkaria geothermal field.
[XBL 814-2914]

the fluids are produced from both the vapor and the water zones. The thickness of the production interval used in each case is shown in Figure 32.

The reservoir parameters used in the study are given in Table 5. It should be noted that in Case 4 smaller values were used for reservoir permeability (2 md) and porosity (5%). The initial pressure, temperature and vapor saturation profiles are shown in Figure 33. We neglect the small amount of steam that may be present in the water zone; it would have little impact on the simulated reservoir behavior. Below the vapor zone, the pressure and temperature follow the saturation curve.

Table 5. Parameters Used in the Study.

Parameters	Cases 1, 2, and 3	Case 4
Absolute permeability	20 md	1 md
Porosity	10%	5%
Heat capacity of rocks	1000	1000 J/kg°C
Density of rocks	2650	2650 kg/m^3
Thermal conductivity	2.0	2.0 J/m·s·°C
Relative permeabilities	Corey Equations (see equations 43 and 44)	
Residual (immobile) liquid saturation	0.35	0.35
Residual (immobile) vapor saturation	0.05	0.05

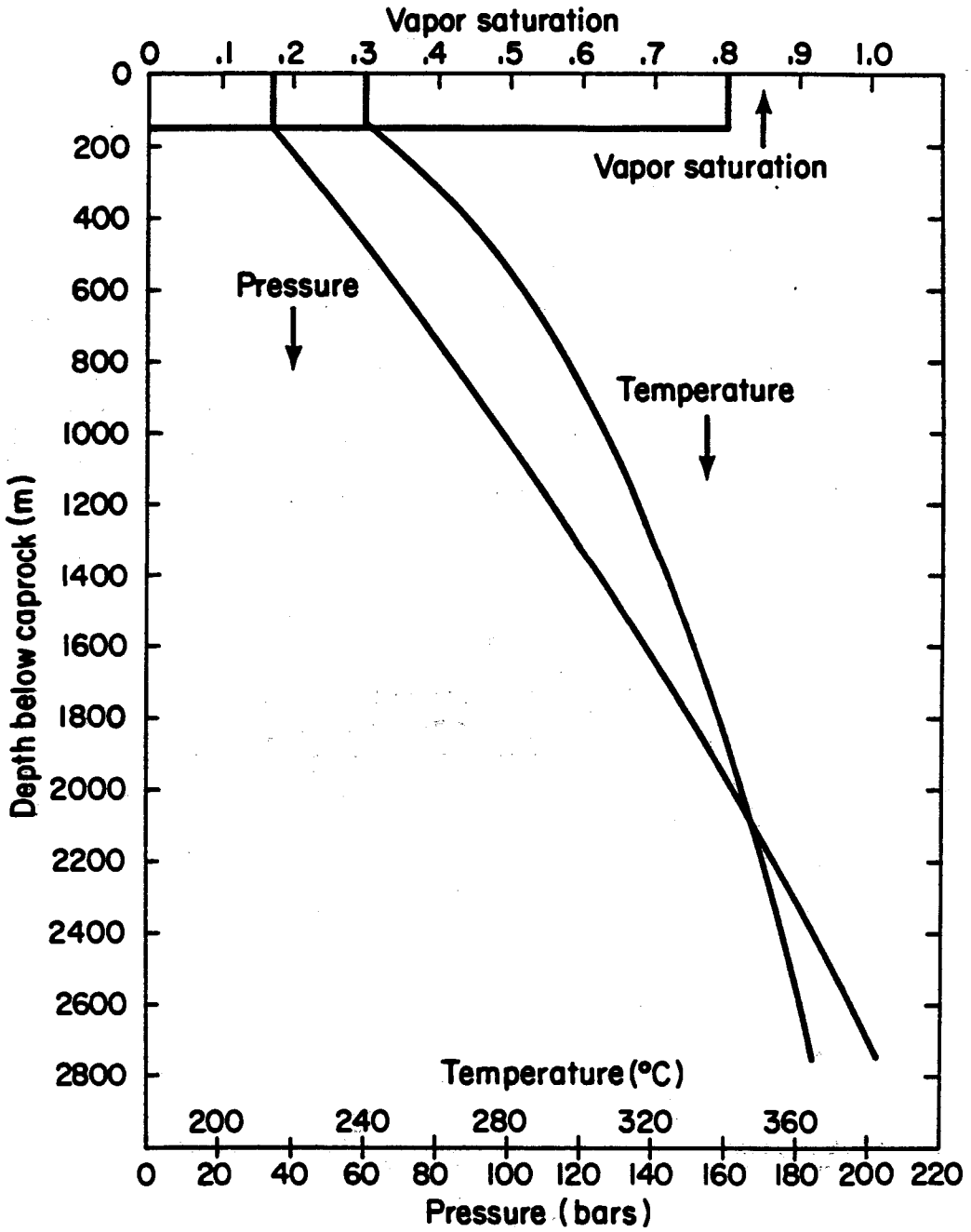

Figure 33. Initial reservoir conditions. [XBL 816-3205]

The relative permeability functions used were the 4th-order Corey Equations (see last section). These functions are illustrated in Figure 20 and can be expressed as:

$$k_{rl} = \begin{cases} [S^*]^4 & S < 1 - S_{rl} \\ 0 & S > 1 - S_{rl} \end{cases} \tag{43}$$

$$k_{rv} = \begin{cases} [1 - S^*]^2[1 - (S^*)^2] & S > S_{rv} \\ 0 & S < S_{rv} \end{cases} \tag{44}$$

where $S^* = \dfrac{1 - S_{rl} - S}{1 - S_{rl} - S_{rv}}$.

In this analysis, the specific relative permeability functions used are not of primary importance as the basic features of reservoir behavior are the same regardless of the assumed relative permeability curves.

The production strategy employed in the modeling studies was to produce the required steam supply for a 45 MW_e power plant. This requirement leads to variable mass flowrate with time. When the fluid is produced from the water zone, in comparison with production from the vapor zone, a considerably larger mass of fluid is needed to obtain the required steam supply (theoretically 120 kg/s of steam are needed for a 45 MW_e power plant). In order to satisfy the constant steam requirement criterion, the steam fraction in the separators must be calculated and the total flow rate at each time step adjusted accordingly. The following equations were incorporated into SHAFT79 to carry out the calculations:

$$H_w = S_q H_{sv} + (1 - S_q) H_{s1} \quad (45)$$

$$q_t = q_s / S_q \quad (46)$$

Equation (45) approximates the two-phase flow from the well bottom to the separators as an iso-enthalpic expansion. It was used to calculate the steam quality in the separators (S_q). The enthalpy values used in equation (45) were calculated based on an 8-bar separator pressure. Saturated steam enthalpy does not vary much with pressure, so that different separator pressure values will not significantly alter the results. The total mass flow rate (q_t) was calculated using equation (46).

In all of the cases studied, we assumed that the required steam supply was produced uniformly over the production interval. In other words, more mass of fluid was produced from a water-dominated element than from a vapor-dominated element. The amount of steam to be extracted from an element is proportional to the size (i.e., thickness) of the element.

Simulation Results

Case 1: Production From Vapor Zone Only

In this case, the fluid was produced solely from the vapor zone (see Figure 32). Figure 34 shows a plot of pressure versus depth at different times for this case. The inset in Figure 34 illustrates the production interval. The figure shows that during the 18.7 years of simulation, the pressure changed quite slowly in the system, but rather more rapidly in the vapor zone than in the underlying water reservoir. This is due to

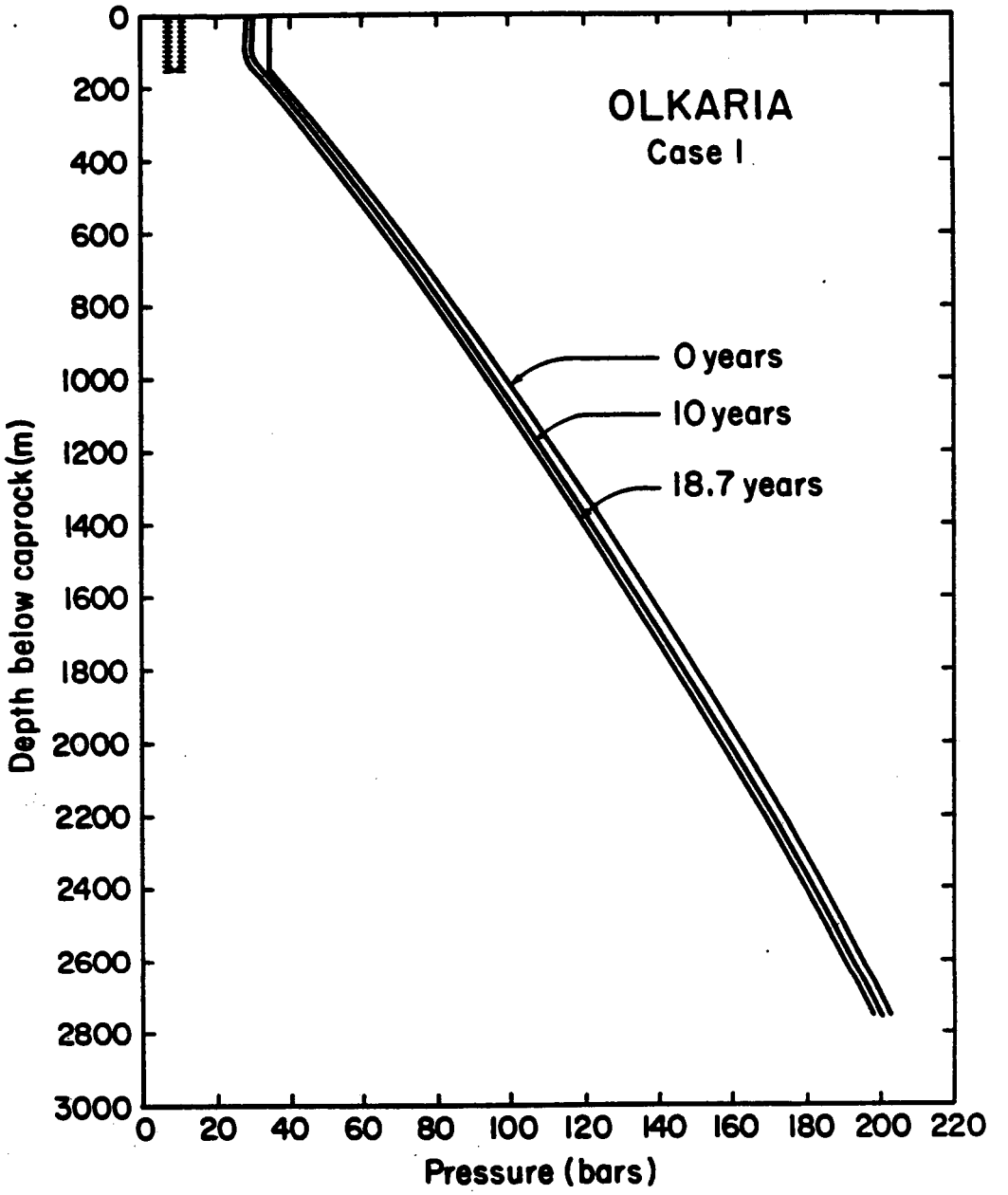

Figure 34. Pressure transients for Case 1. [XBL 814-2915]

the more intense boiling in the vapor zone than in the water reservoir. The pressure in the water zone changed only because the initial pressure was somewhat higher than the saturation pressure.

Figure 35 shows vapor saturation profiles at different times during the simulation. The boiling front advanced downwards with time, reaching a depth of 1000 m below the caprock at the end of the simulation (18.7 years). The vapor saturation in the upper portion of the vapor zone increased quite rapidly with time, due to boiling. In the lower portion of the vapor zone, the vapor saturation actually decreased at early times due to upflow of liquid water, but then the saturation gradually started building up again. The upflow of water occurred because of the extensive boiling and associated temperature and pressure decline in the vapor zone, resulting in pressure gradients that exceed the hydrostatic pressure gradient for liquid water. Later on, however, the water upflow ceased because the water mobility at the top of the water reservoir was steadily decreasing due to the increasing vapor saturation (relative permeability effects).

The total mass production rate is shown in Figure 36. The fluid was produced uniformly from the top 15 elements in the mesh, representing the vapor zone. Since all of the elements were equal in size, each produced 8.0 kg/s of steam. Figure 36 shows that initially 120 kg/s of steam-water mixture was produced, but the rate rapidly increased to 245 kg/s. The variations in the flow rate occurred because of the upflow of water into the vapor zone, as shown in Figure 35, by the decrease in vapor

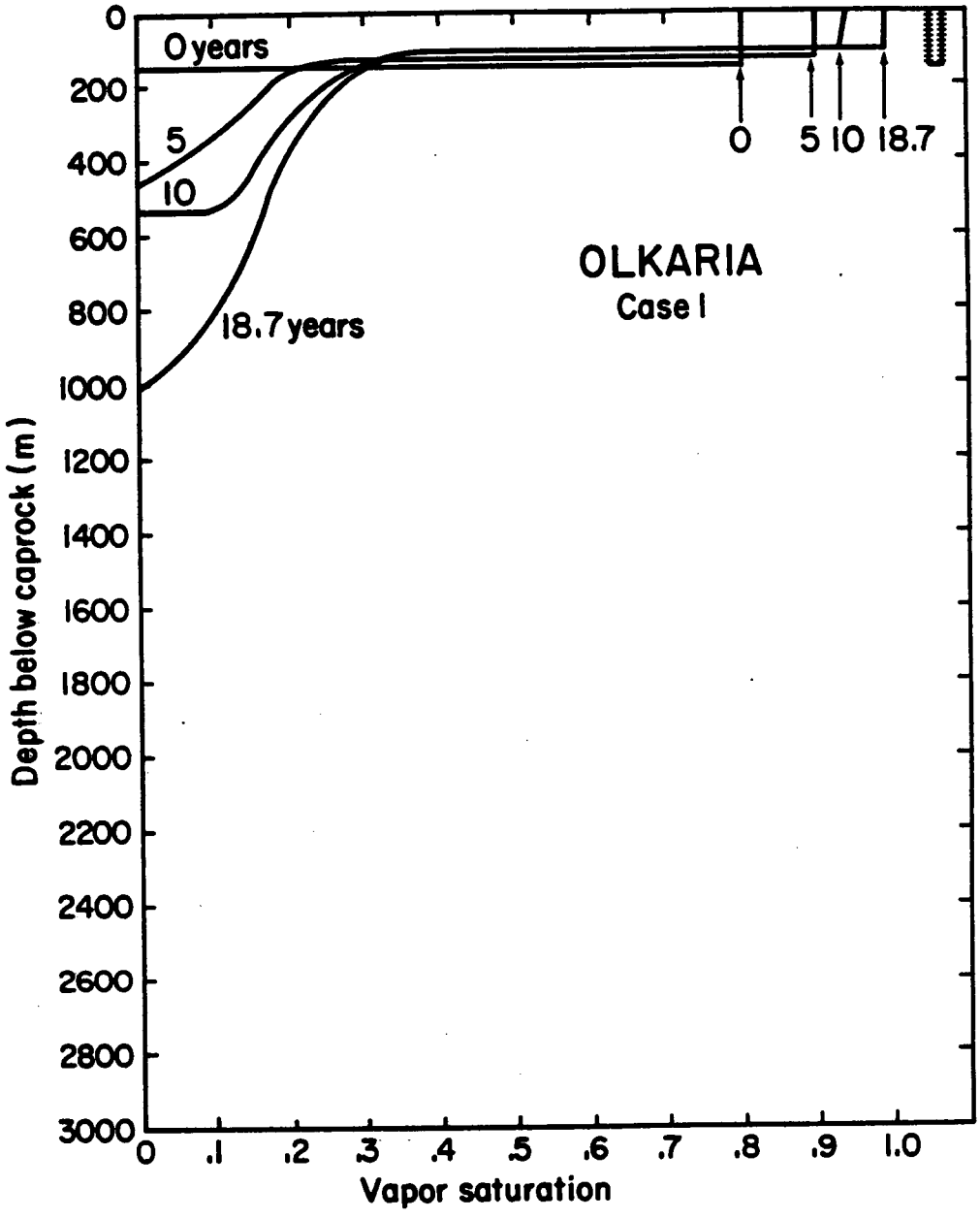

Figure 35. Changes in vapor saturation due to production from vapor zone. [XBL 814-2916]

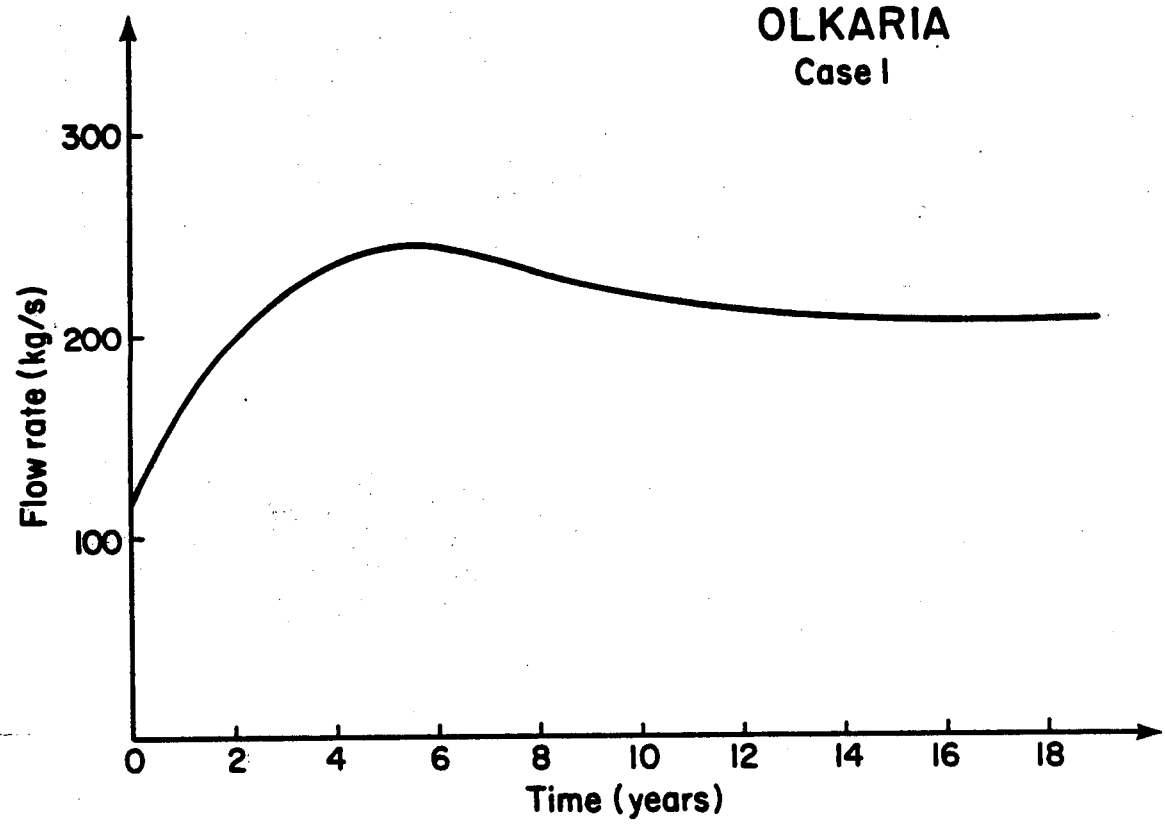

Figure 36. Changes in mass flow rate during production from vapor zone (Case 1). [XBL 814-2917]

saturation. During the simulation, the vapor elements close to the initial vapor-water interface decreased in vapor saturation. When the liquid saturation exceeded the immobile liquid saturation (in our case S_{rl} = .35), a mixture of liquid and vapor was produced. At that time, the mass of fluid produced had to be increased to satisfy the constraint of a constant steam withdrawal rate. As shown in Figure 36, the total flow rate declined again after 6 years because of an increasing vapor saturation in the steam elements.

Due to large computing costs, the simulations of Case 1 were terminated after 18.7 years. At this time, the top elements in the vapor zone had saturations close to 1.0 and the imminent phase transitions, with their associated large changes in pressures and flow rates, necessitated small time steps. In Case 1, boiling occurred only at the top of the reservoir (the vapor zone and the upper parts of the water zone) as the temperature changes in Figure 37 clearly show. Consequently the vapor elements increased rapidly in vapor saturation. Previous experience with this type of reservoir behavior indicates that very soon after the vapor elements make a transition to single-phase conditions, the pressure in the vapor zone will start to fall dramatically [Pruess et al., 1979a; Bodvarsson et al., 1980]. It is probable that the pressure will fall so rapidly in the vapor zone that production could not be sustained for more than 25 years.

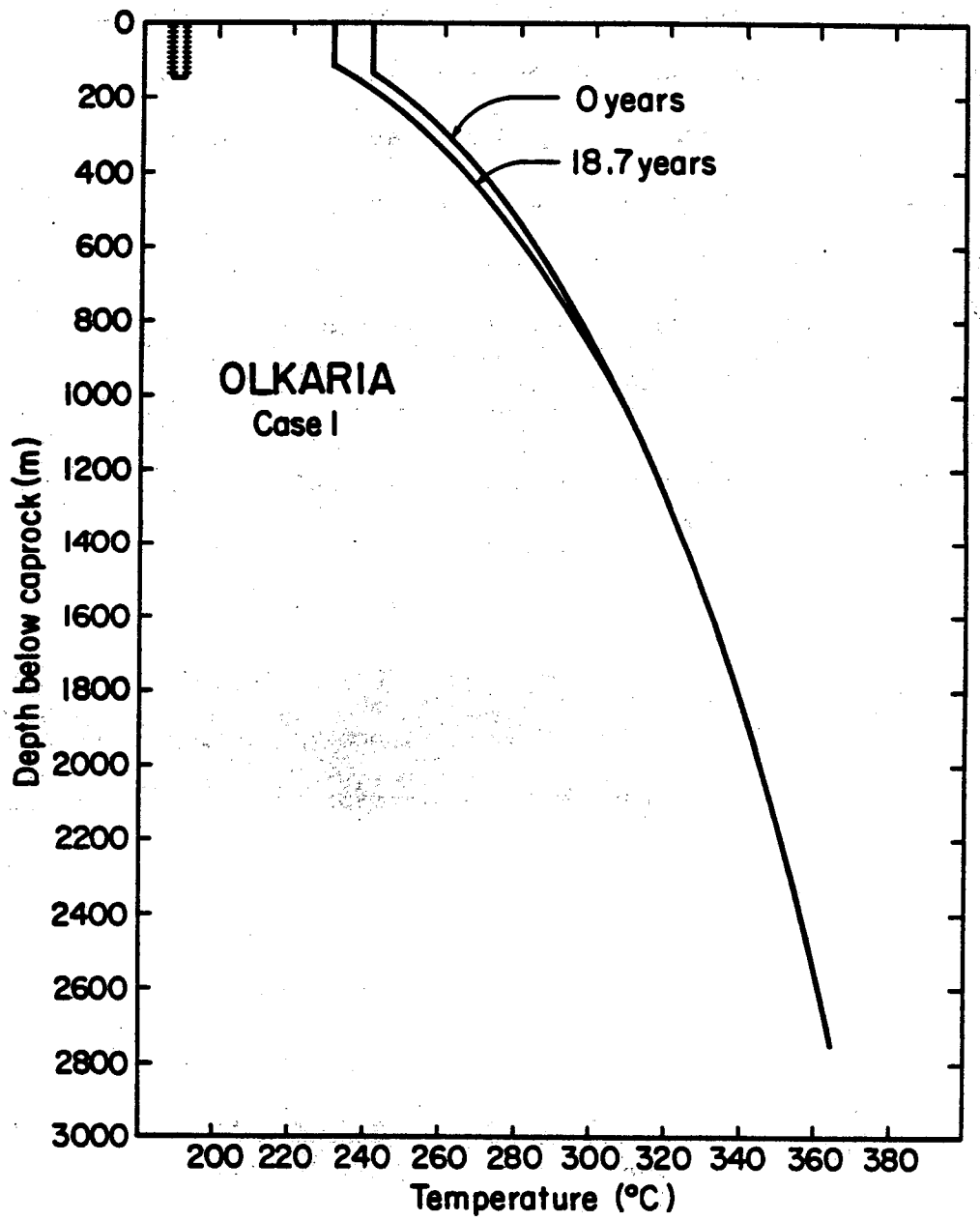

Figure 37. Temperature changes due to production from vapor zone (Case 1). [XBL 814-2918]

Case 2: Production From the Water Zone Only

In this case the fluids were produced from the water zone underlying the vapor cap (Figure 32). The vapor zone and the top 100 m of the water zone were cased off; however, the wells were perforated over a 500 m-thick interval in the water zone. This case gives rise to a rather remarkable and interesting depletion pattern, as will be discussed below.

Figure 38 shows the pressure variations in the reservoir at different times during the simulation. The initial pressure distribution is given for reference purposes. The figure shows that at early times the pressure decreased rather evenly in the water zone, but actually increased in the vapor zone. In the upper portion of the water zone, the pressure decreased along with the temperature due to boiling, but in the lower portions of the water zone, the pressure decrease was due to a steady upflow of water. In the vapor zone, however, pressures and temperatures increased because vapor, which had been mobilized by the boiling process, flowed up from depth and condensed near the top. The upflow of vapor replenished mass reserves near the production horizons, and gave rise to a very long reservoir life. The pressure gradients in the upper part of the system were lower than hydrostatic, thereby preventing upward flow of water. The pressure gradients were considerably higher than vaporstatic, however, which permitted mobile vapor to flow upward. This resulted in condensation in the upper part of the water zone as well as in the vapor zone.

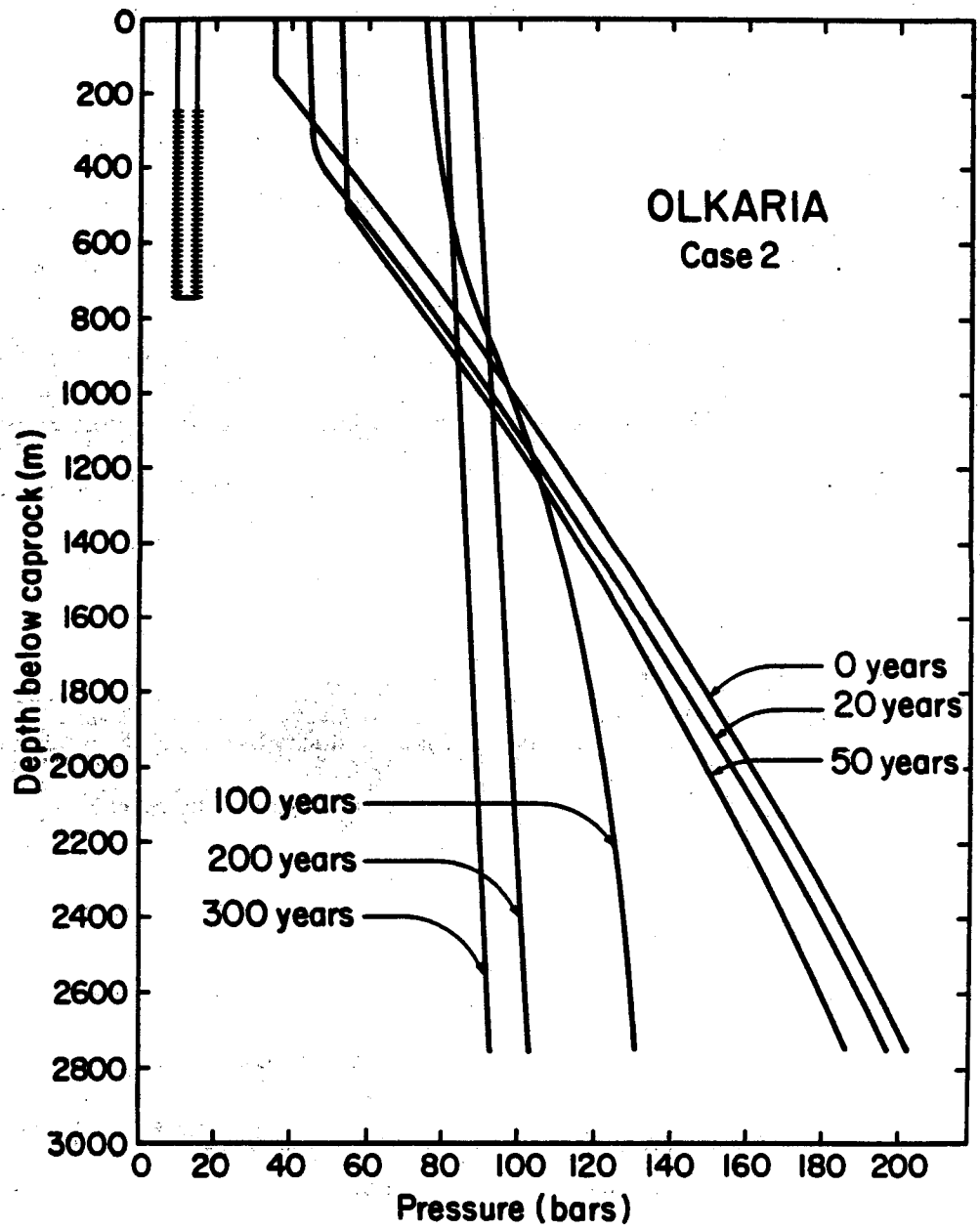

Figure 38. Pressure changes due to production from liquid zone (Case 2). [XBL 814-2919]

At later times, the boiling spread down to the deeper portions of the reservoir, creating upflow of vapor and condensation in the upper part of the water zone as well as in the vapor zone. These processes eventually gave rise to almost isothermal conditions and uniform boiling throughout the entire reservoir after 200 years of simulation. At that time the pressure had increased by 50 bars in the vapor zone and 35 bars in the production zone; in the liquid zone (2000 m below the caprock) the pressure had decreased by 50 bars (Figure 39).

The saturation profiles are shown for different times in Figure 40. The boiling front advanced rapidly downwards, reaching the bottom of the reservoir after less than 50 years. The vapor saturation in the vapor zone decreased during the first 100 years of simulation due to the upflow and condensation of steam from depth. After 50 years, the boiling was most pronounced near the bottom of the reservoir due to the large upflow of water and steam and the effect of the impermeable boundary at the bottom of the reservoir. This gave rise to relatively higher saturations at the bottom of the reservoir at large times, eventually leading to single-phase vapor conditions after little over 100 years. The saturation profiles show clearly the nearly uniform depletion process that took place in the reservoir, giving rise to a very long productive life of the reservoir [Pruess et al., 1979a].

The processes of production-induced boiling, upflow and condensation of steam, and subsequent increase in temperature and pressure at shallower

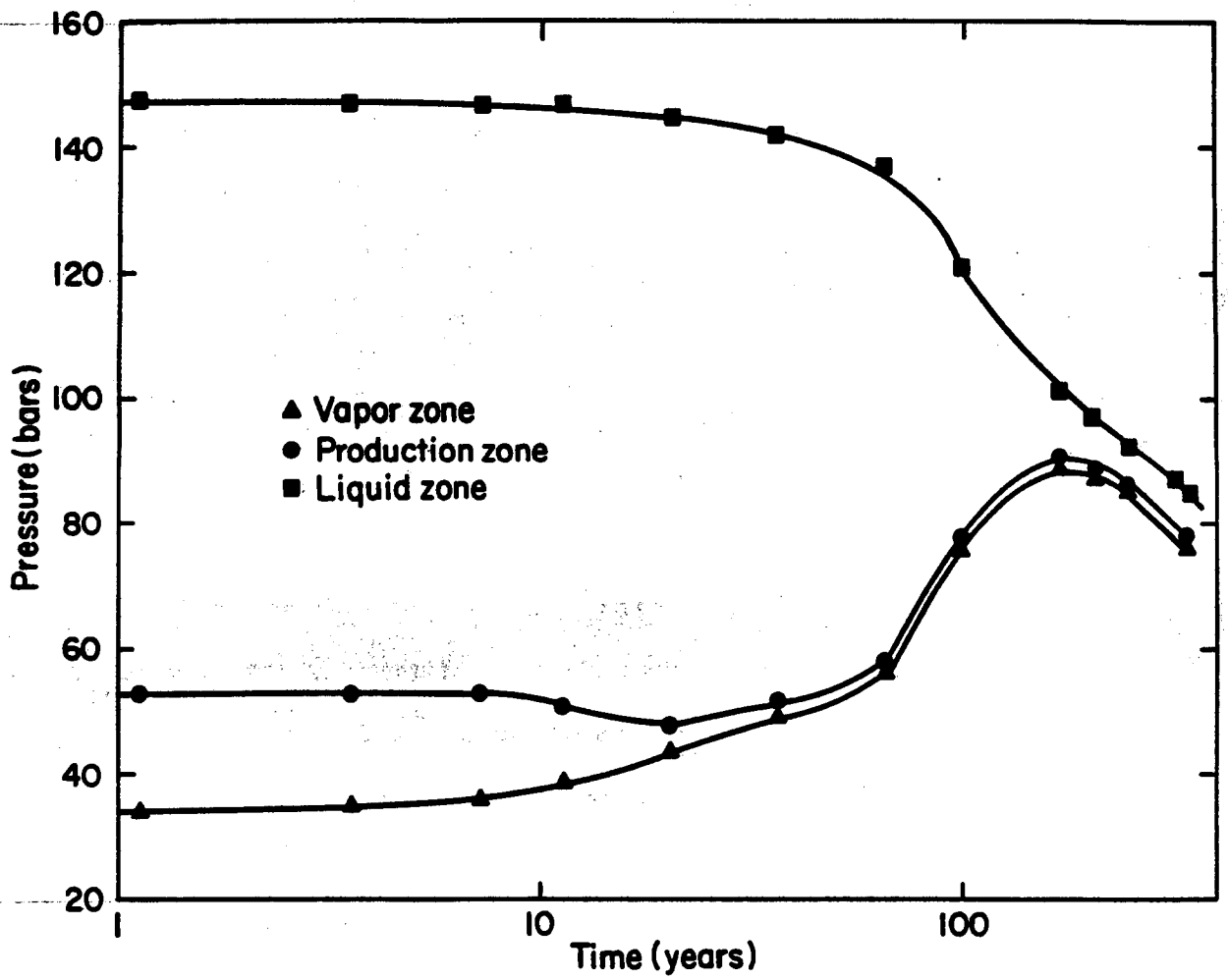

Figure 39. Pressure changes with time in three different parts of the reservoir (Case 2). [XBL 816-3206]

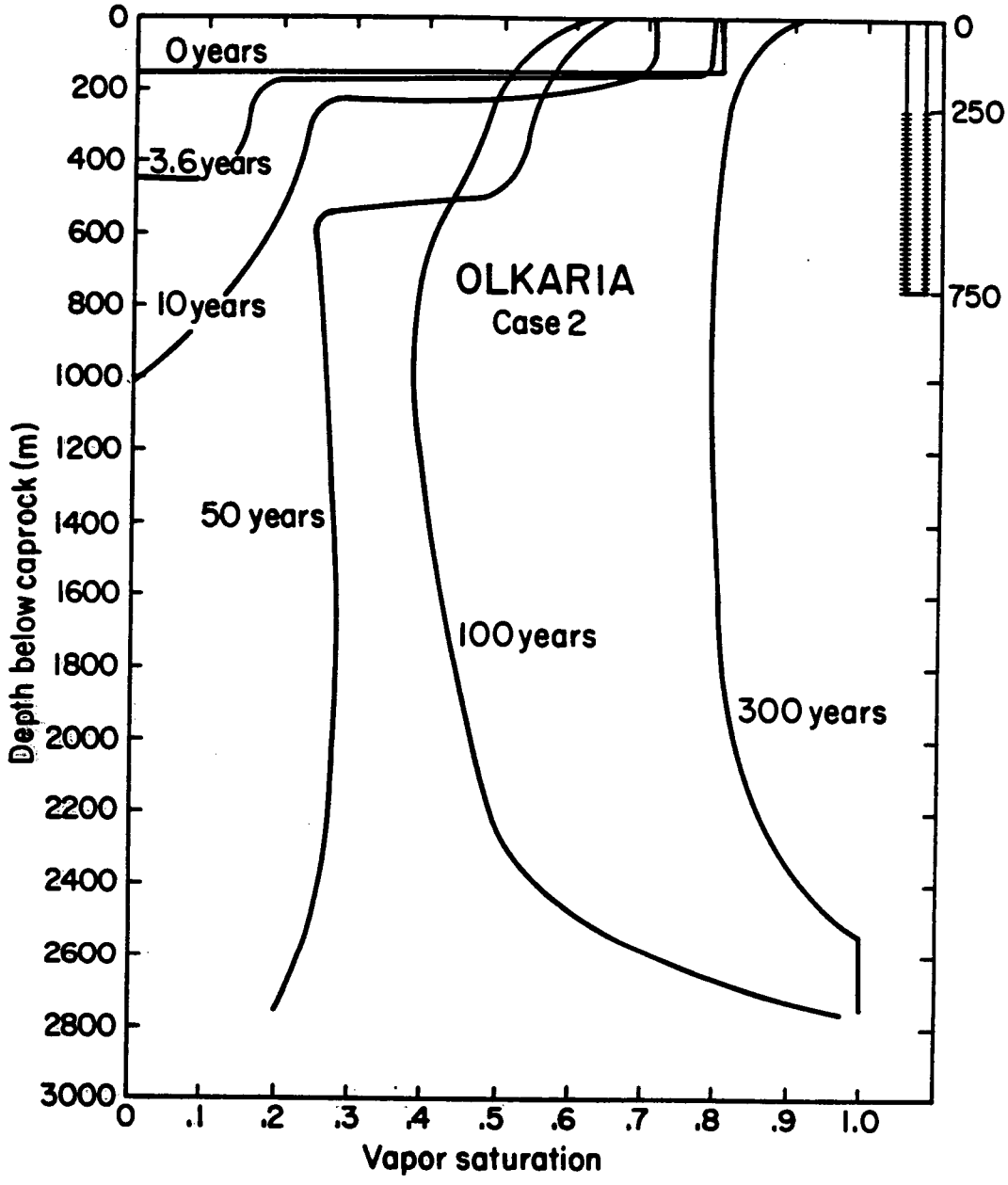

Figure 40. Vapor saturation changes due to production from liquid zone (Case 2). [XBL 814-2920]

depths which were noted in the present simulation actually have been observed in some water-dominated geothermal fields. Henley (1979) and Allis (1979) reported increases in the flow rates and temperatures of surface manifestations at the Wairakei and Tauhara geothermal fields after exploitation started. Similar effects have been observed at the Tongonan geothermal field in the Philippines [V. Stefansson, private communication, 1981].

Total fluid production to provide enough steam for 45 MW_e is shown as a function of time in Figure 41. Initially large amounts of liquid water were produced because of the low vapor saturation in the production nodes and from then on, a mixture of vapor and liquid water was produced. As the vapor saturation in the production nodes increased, the vapor quality in the separators increased and eventually, after 120 years, only steam was produced. At this time the liquid saturation in the production nodes had fallen below the immobile liquid saturation and the total flow rate produced corresponded to the theoretical steam requirement for a 45 MW_e power plant (120 kg/s).

Case 3: Production From Both Vapor and Liquid Zones

Figure 32 shows schematically the production interval used in Case 3. It was assumed that the wells are drilled to a total depth of 1300 m. The perforated interval was 550 m long and the wells were open both in the initial vapor zone and in the water zone.

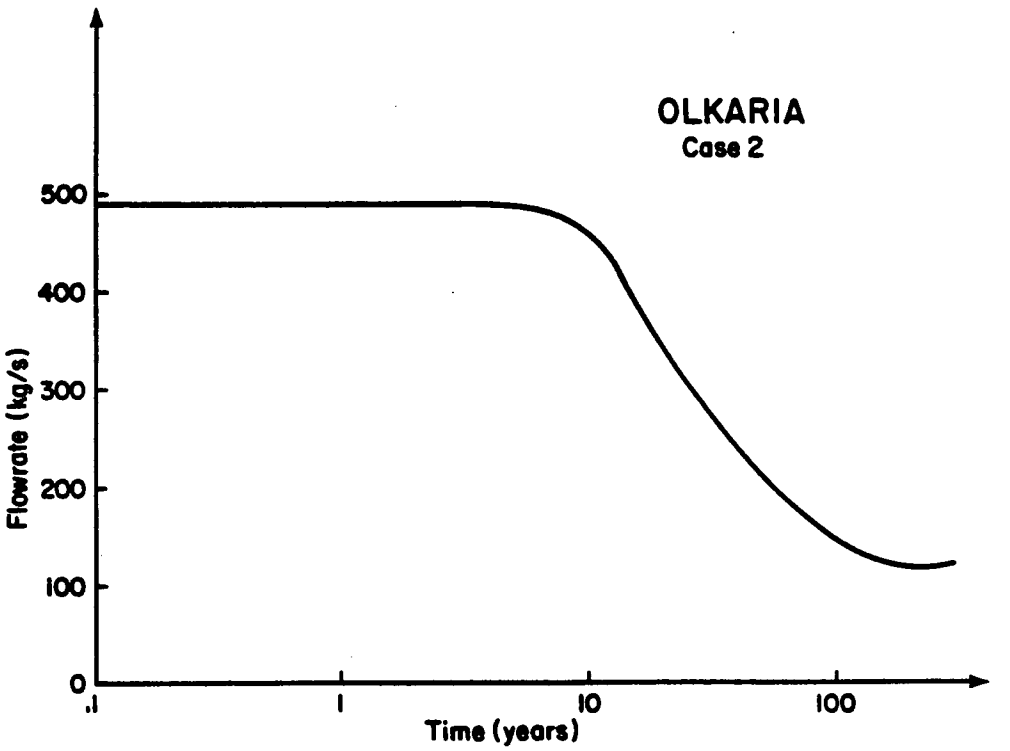

Figure 41. Flow rate changes due to production from liquid zone (Case 2).
[XBL 814-2921]

During the simulation, the pressure and saturation changes with time were very similar to those obtained in Case 2. Upflow and condensation of steam in the upper portions of the reservoir gave rise to a similar uniform depletion pattern as noted in Case 2. The reasons for this similarity are obvious; the high vapor saturation in the vapor zone and the long production interval (550 m) led to low production rates from the vapor zone. This in turn caused condensation to control the pressure changes in the vapor zone and the upper portion of the water zone. Comparison of this case with Case 1 illustrates clearly that high flowrates from the vapor zone will decrease the productive life of the reservoir considerably, whereas low to moderate production rates will enable production of high-enthalpy fluids, and also result in a longer reservoir life.

Comparison of Cases 2 and 3 show that in Case 3 the reservoir pressures were higher at all times. The reason for this is obvious when one compares the total mass withdrawn in the two cases (Figures 41 and 42). In Case 3, the fluids were produced from both the vapor and the water zones, resulting in higher average flowing enthalpy of the liquid-vapor mixture. This in turn, when compared with Case 2, resulted in a smaller fluid mass to be extracted from the reservoir at any given time.

Case 4: Production From Both the Vapor and the Water Zones, Assuming Low Vertical Permeability

The final case studied differed from Case 3 only in that lower reservoir permeability and porosity values were used in the simulation (Table 5). In this case, the permeability and porosity were reduced to

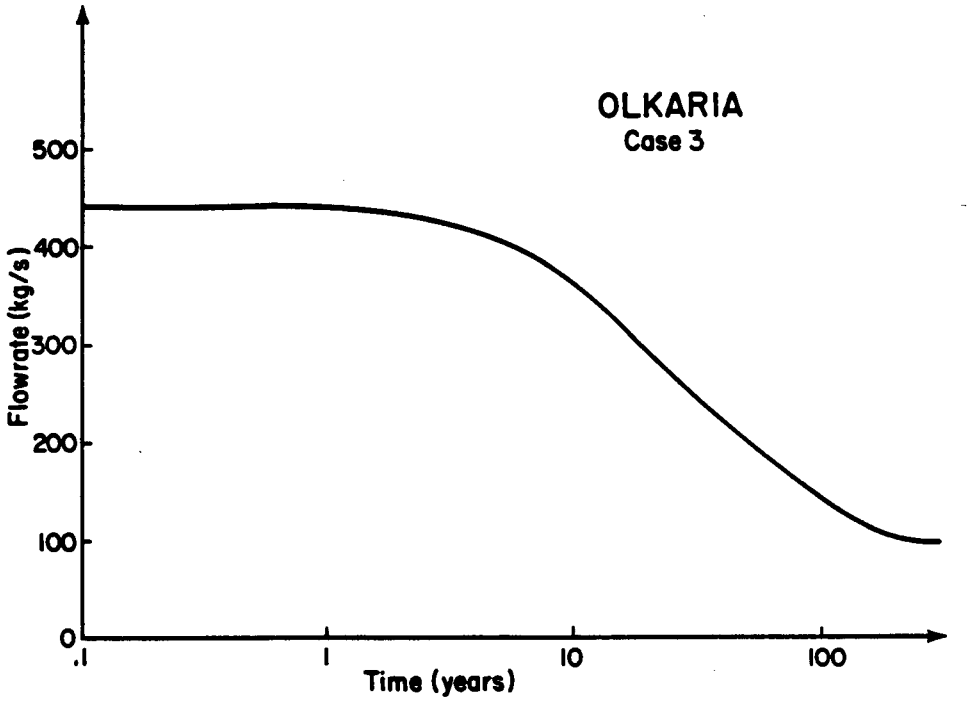

Figure 42. Flow rate changes during production from both vapor and liquid zones (Case 3). [XBL 814-2924]

2 md and 5%, respectively. The permeability of the Olkaria reservoir inferred from well tests is 10-20 md. This value essentially represents the average horizontal permeability of the reservoir. The geological characteristics of the Olkaria reservoir seem to indicate, however, that the vertical permeability may be considerably lower. Case 4 represents an attempt to study the sensitivity of our results to changes in vertical permeability. The average porosity of the Olkaria reservoir has been estimated as 5-10%; in this case the lower limit of 5% was used. This case should represent a more pessimistic outlook on the behavior of the Olkaria geothermal field under exploitation.

The pressure profiles at different times are shown in Figure 43. Although the total simulation time only slightly exceeded 70 years, the general depletion trend of the reservoir can be clearly seen. Figure 43 shows that the pressure decreased rather rapidly in the production region, but only slightly in the deeper portions of the reservoir. This shows that the boiling was confined to a rather small region around the production interval, due to the low permeability of the reservoir.

The vapor saturation profiles given in Figure 44 similarly show the slow advance of the boiling front during exploitation. A comparison with Case 3 shows that in Case 4, after 70 years, the boiling front had advanced only to a depth of 1600 m below the caprock, whereas in Case 3, the boiling front had advanced to the bottom of the reservoir (2850 m below the caprock) in less than 50 years. Also, it is of importance to note that the vapor saturation in the vapor zone always increased with

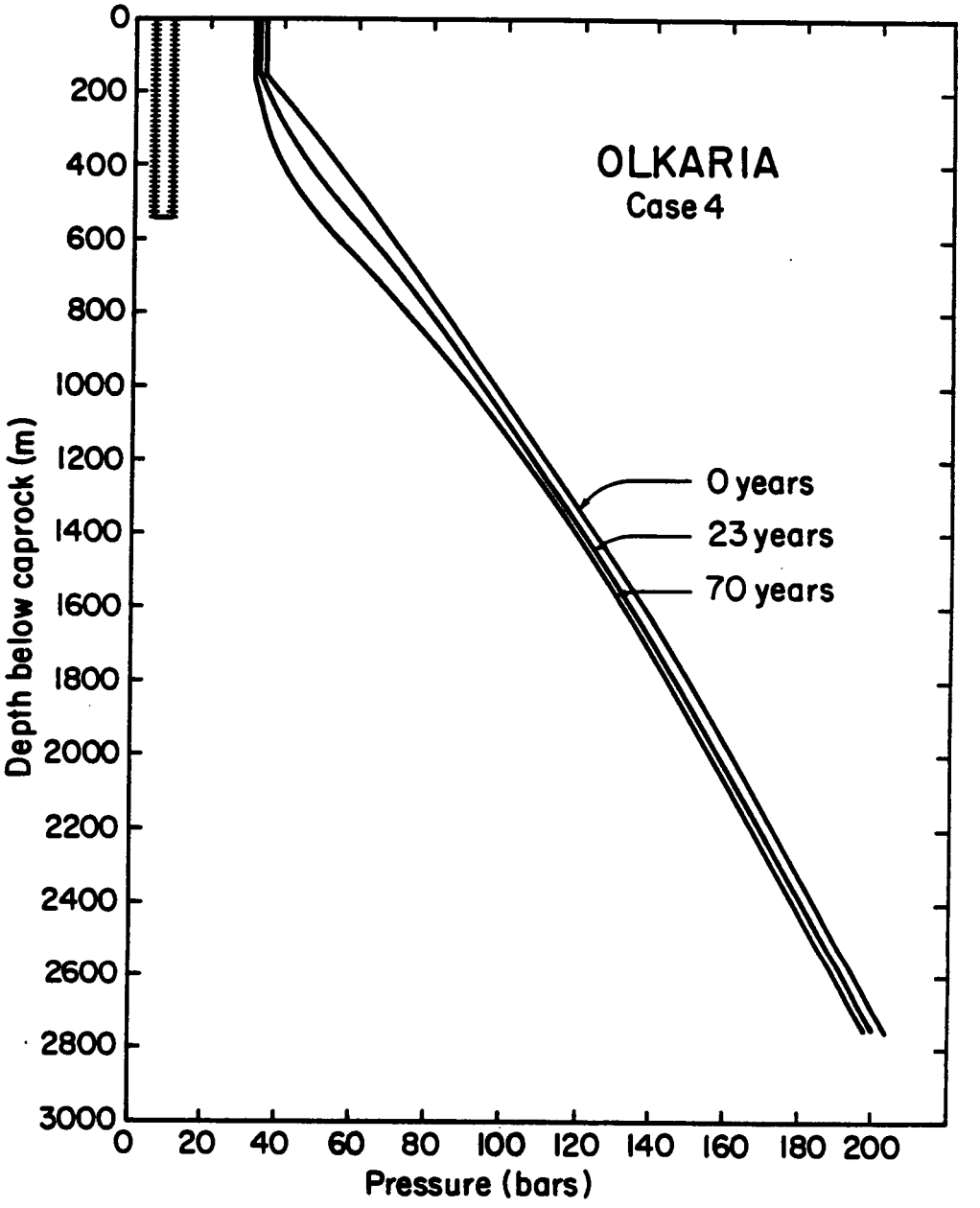

Figure 43. Pressure changes during simulation of Case 4. [XBL 814-2925]

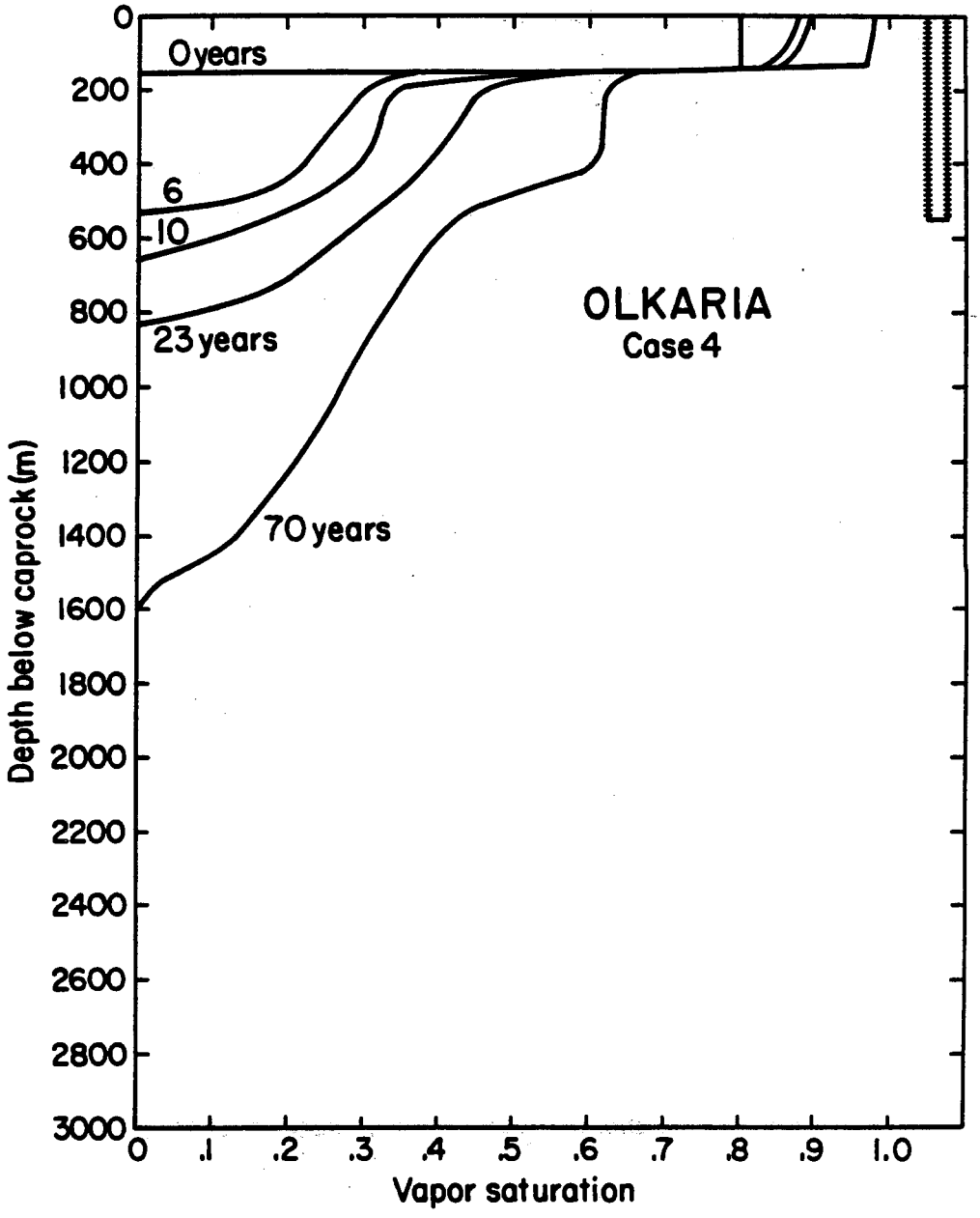

Figure 44. Vapor saturation changes during simulation of Case 4.
[XBL 814-2926]

time. This illustrates the effect of the lower permeability allowing less upflow of vapor and consequently less condensation in the vapor zone.

The total flow rate (q_t), as shown in Figure 45, was very similar to that of Case 3. However, at later times it was smaller due to the higher vapor saturation in the production nodes.

The results from this case show clearly that the vertical permeability is a very important factor in the determination of the longevity of a liquid-dominated reservoir.

Single-Phase Liquid-Dominated Reservoirs

The general results shown above for the Olkaria-type geothermal reservoir should also be applicable to liquid-dominated reservoirs without an initial steam cap (e.g. Salton Sea, U.S.A.; Cerro Prieto, Mexico; Krafla, Iceland). If the initial reservoir pressure is above the saturation pressure corresponding to the reservoir temperature, soon after exploitation starts the pressure will drop to the saturation pressure [Bodvarsson et al., 1980]. After that, a two-phase zone will develop in the upper portion of the reservoir and conditions similar to those presently found at Olkaria will result. Production-induced boiling has recently been observed at the Svartsengi geothermal field in Iceland [J. Eliasson, private communication, 1981]. Although the aquifer at Svartsengi initially contained only single-phase liquid water, a two-phase zone has recently been formed at the top of the aquifer. Note that

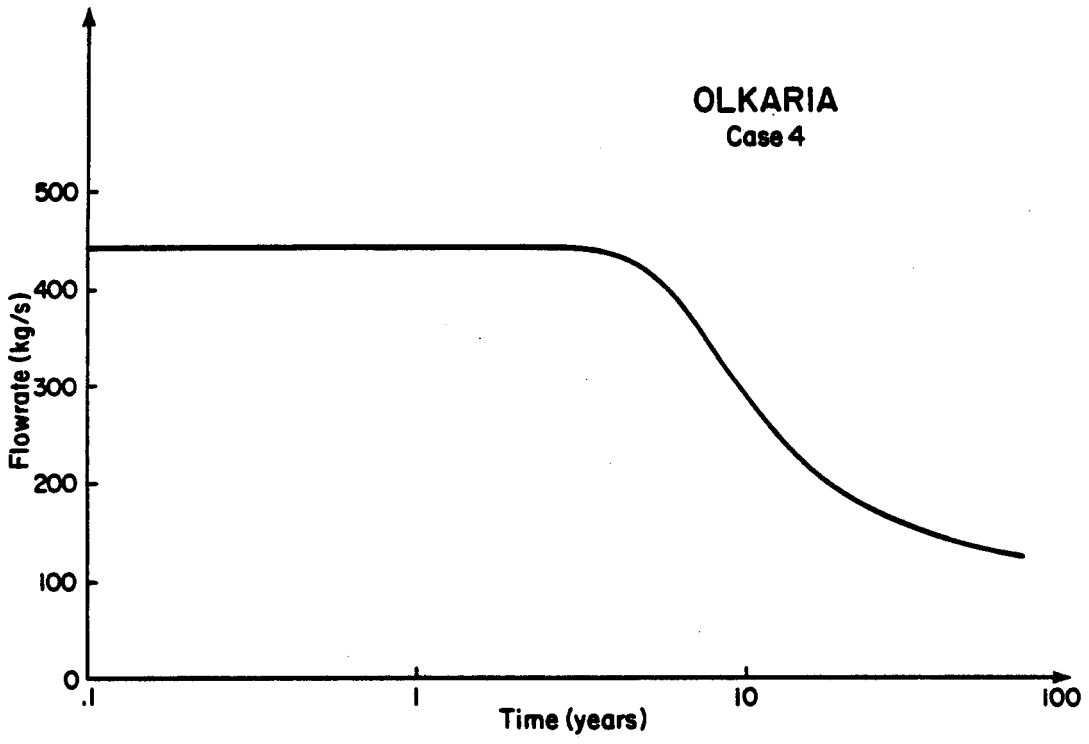

Figure 45. Flow rate changes during simulation of Case 4. [XBL 814-2927]

if the colder water recharge is significant, the two-phase zone could be restricted to the near-well regions, as in Cerro Prieto [Grant et al., 1981].

Vapor-Dominated Reservoirs

Let us now consider the question of whether production from deeper horizons in vapor-dominated reservoirs could give rise to effects similar to those discussed above. Two conditions must be met in order for production from depth to cause an increasing upflow of steam which would replenish mass reserves in shallower horizons and give rise to temperature and pressure increases due to condensation. First, the initial relative permeability for steam must be significantly less than 1 at depth so that production-induced increases in vapor saturation will result in a higher steam mobility; and second, vertical pressure gradients at depth must be substantially larger than vaporstatic, preferably approaching hydrostatic, so that mobile steam will actually be driven upward in significant amounts.

It is not known whether either of these conditions exist in vapor-dominated reservoirs. Both conditions could be met in a "deep water table," which, although never clearly identified, has for a long time been hypothesized to underlie vapor-dominated reservoirs [White et al., 1971; Weres et al., 1977]. Below a water table, pressure gradients would have to be close to hydrostatic, and vapor saturation presumably would be small or absent. At Larderello, Italy, there may be some evidence that vertical pressure gradients at depth significantly exceed vaporstatic values. However, published data for The Geysers, U.S.A. [Dykstra, 1981],

do not give any indication of large vertical pressure gradients at depth. Therefore, upflow of steam appears to be limited by pressure gradients so that any increase in mobility would only have small effects. Moreover, it appears doubtful whether the effective mobility for vertical steam flow could be significantly increased by a production-induced rise in vapor saturation. Recent work on vapor-dominated reservoirs, which has specifically addressed the effects arising from the fractured nature of these systems, indicates that the vertical flow of steam may be essentially unaffected by relative permeability [Pruess and Narasimhan, 1981]. The reason for this is that steam moves along vertical fractures which contain little or no water even in the pre-exploitation state, so that the relative permeability of the steam phase is 1. Production from depth would increase vapor saturation and mobility in the rock matrix, but this may have a negligible effect on the vertical flow because the matrix permeability is much smaller than the fracture permeability.

In summary, it is unlikely that conditions in vapor-dominated reservoirs are such that depletion at great depth could significantly replenish the fluid and heat reserves at shallow depth. But given the uncertainties about the liquid saturations in vapor-dominated reservoirs at depth, it may still be worth trying to tap deep horizons in an attempt to improve energy recovery.

Conclusions

Different reservoir exploitation strategies for a liquid-dominated geothermal reservoir with an overlying two-phase zone (Olkaria, Kenya) have been studied. The studies indicate that:

1. Production from depth can give rise to an optimal energy recovery of the reservoir. If the permeability is adequate, a remarkably uniform depletion process may result in which a counterflow of steam and liquid water results initially in the mining of heat and mass from lower portions of the reservoir while pressures are stable, or even increase, in the shallower portions. Later, uniform boiling will occur everywhere in the reservoir. Field data from Wairakei, New Zealand, have verified some of the mechanisms operative in this process.

2. Extensive production from the vapor zone may be advantageous in the short run, but in the long run, localized boiling will enhance single-phase vapor conditions in the production regions and will result in a short productive life for the reservoir.

3. The uniform boiling process described in (1) is very sensitive to the reservoir vertical permeability. If the vertical permeability is very low, upflow of significant mass of steam will not occur, and consequently the pressure increase due to steam condensation in shallow regions of the reservoir will not result.

4. The results discussed above should be applicable to other liquid-dominated reservoirs, regardless whether or not a shallow two-phase zone is present initially.

5. It is questionable whether production from the deeper regions will enhance production in shallow regions of vapor-dominated reservoirs. Due to the uncertainties regarding the liquid saturations of those systems at depth, such a possibility cannot be ruled out at present.

In assessing the results from this section, one must bear in mind that a simple reservoir model was used, which was not expected to quantitatively account for field behavior. Future investigations should employ a more detailed model to determine the sensitivity of the results to reservoir geometry, horizontal and vertical variations in reservoir properties, and different relative permeability curves. This, of course, will mean using a distributed-parameter model that is appropriately designed for the problem at hand.

INJECTION INTO FRACTURED GEOTHERMAL RESERVOIRS

Reinjection of geothermal wastewater is gradually becoming a preferred means of waste disposal. At present, continuous reinjection is practiced at The Geysers, California [Chasteen, 1975; Kruger and Otte, 1973]; Ahuachapan, El Salvador [Einarsson et al., 1975; Cuellar, 1975], Mak Ban, Philippines [Horne, 1981], and five Japanese geothermal fields (Otake, Onuma, Onikobe, Hatchobaru, and Kakkonda) [Horne, 1981; Kubota and Aosaki, 1975; Hayashi et al., 1978]. Small-scale reinjection tests have been reported at a number of geothermal fields, e.g., Baca, New Mexico [Chasteen, 1975], East Mesa, California [Mathias, 1975; Benson et al., 1978], Larderello, Italy [Pruess, private communication, 1981], Cerro Prieto, Mexico [Cortez, 1981], Broadlands, New Zealand [Brixley and Grant, 1979]; and Tongonan, Philippines [Studt, 1980]. The increasing interest in reinjection undoubtedly results from growing environmental concerns regarding toxic minerals (e.g., boron, arsenic) present in geothermal wastewater.

Although reinjection is currently employed mainly as a means of wastewater disposal, it can greatly enhance the energy recovery from a geothermal field. The operators of The Geysers geothermal field are considering increasing the amount of injected water by using imported water, thereby attempting to take advantage of this important benefit of reinjection [Pruess, private communication, 1981]. A number of investigators have produced theoretical and numerical studies on the effect of reinjection on energy recovery from geothermal fields [Kasameyer and Schroeder,

1975; Pritchett et al., 1977; Lippmann et al., 1977; O'Sullivan and Pruess, 1980; Schroeder et al., 1980]. Reinjection also aids in maintaining reservoir pressures. This has been illustrated at the Ahuachapan geothermal field, where direct correlation between the percentage of produced water injected and the reservoir pressure decline was found [Witherspoon, private communication, 1981].

The danger in employing reinjection is the possibility that the colder water will prematurely break through from its zone around the injection well into the production region, thus drastically reducing the efficiency of the operation. The movement of the cold water (thermal front) in porous-media reservoirs is fairly well known from theoretical studies by various investigators [Lauwerier, 1955; Bodvarsson, 1972; Gringarten and Sauty, 1975; Lippmann et al., 1980; Tsang et al., 1978]. However, fluid movement in most geothermal reservoirs (except those in the Imperial Valley and perhaps Larderello, Italy) is controlled by fractures, a more complicated situation. It is generally believed that the cold water will advance very rapidly through the fractures and prematurely break through at the production wells.

The objective of this section is to investigate the advancement of the thermal front during injection into a fractured reservoir system. A reservoir system consisting of equally spaced horizontal fractures intersecting an injection well is considered. Analytical and numerical studies are carried out, addressing the important question of how

fractures affect the movement of the thermal front during injection. Fundamental studies related to this problem have been reported by various researchers [Kasameyer and Schroeder, 1975; Romm, 1966; Bodvarsson, 1969, Gringarten et al., 1975; Bodvarsson and Tsang, 1980b].

The experience gained from the large-scale reinjection experiments indicates that the advancement of the thermal front depends to a great extent on the geologic conditions that prevail at each geothermal site. Horne (1981) reports thermal interference in four of the five Japanese geothermal fields where reinjection is practiced (Onuma, Onikobe, Hatchobaru, and Kakkonda). However, at the Otake geothermal field, where reinjection has been employed since 1972 [Cuellar, 1975], no thermal effects from reinjection have been observed. At Ahuachapan, premature thermal breakthrough has not occurred, although the water was injected at high flow rates for five years through an injection well located only 150 m away from a good producer [Witherspoon, private communication, 1981]. These examples illustrate the basic need to study the advancement of the thermal front through fractured media so that criteria can be established for determining injection-well locations and flow rates based on some general geologic conditions. In the present study, such a criterion is developed for geothermal systems with horizontal fractures or layered reservoirs.

Basic Model

The physical model considered is shown in Figure 46. The model consists of an injection well fully penetrating a reservoir with a number, n, of equally spaced horizontal fractures. The fractures are all identical with a constant aperture, b, and all extend to infinity. The injection rate, q_t, is assumed to be constant and the same fluid mass flow rate, q, enters each fracture ($q_t = n \cdot q$). Gravity effects are neglected and therefore, due to symmetry, only the basic section shown in Figure 46 needs to be considered.

In this study, the problem is approached using both analytical and numerical techniques. In the analytical work, the rock matrix associated with the fracture was assumed to be impermeable and therefore only the effects of thermal conduction were present. In the numerical study, most of the simplifying assumptions in the analytical work were relaxed and cases where the rock matrix is permeable were considered.

Analytical Approach

Mathematical Model

As illustrated in Figure 47, only one fracture from the general problem illustrated in Figure 46 was considered in the analytical study. Besides the general assumptions discussed above, the following additional assumptions were made:

(1) The flow in the fracture is steady and purely radial, with the well located at r = 0. The fracture of aperture b is at an

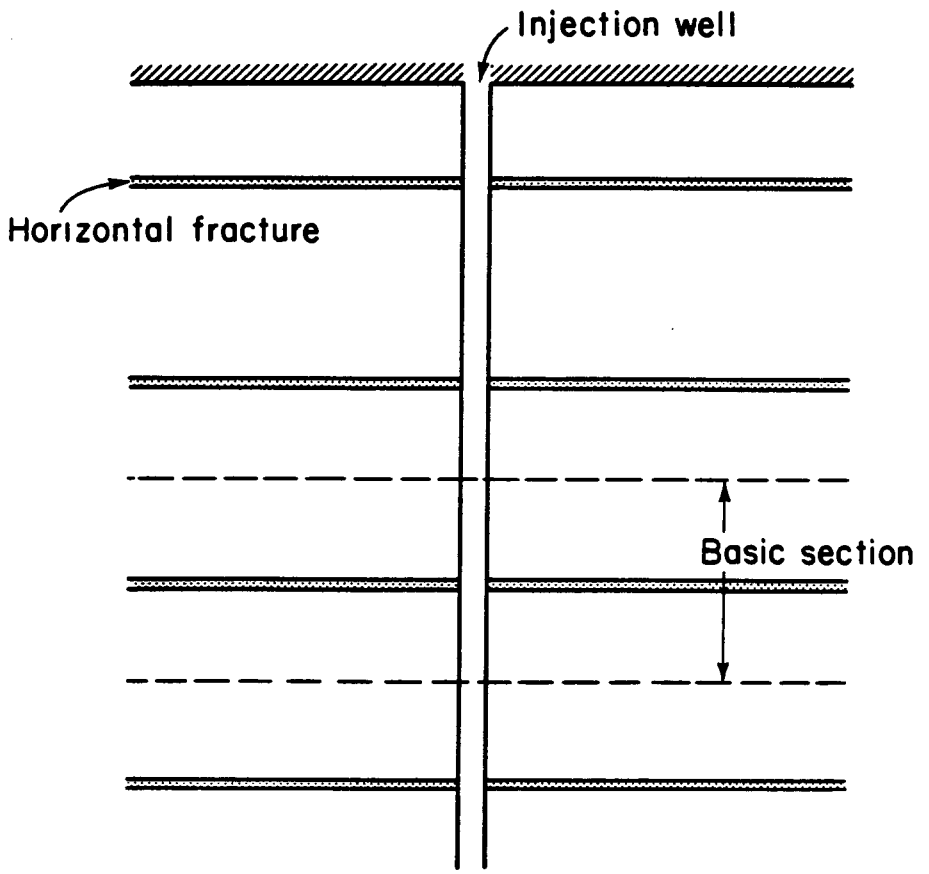

Figure 46. Basic model of an injection well penetrating a reservoir with equally spaced horizontal fractures. [XBL 805-7081]

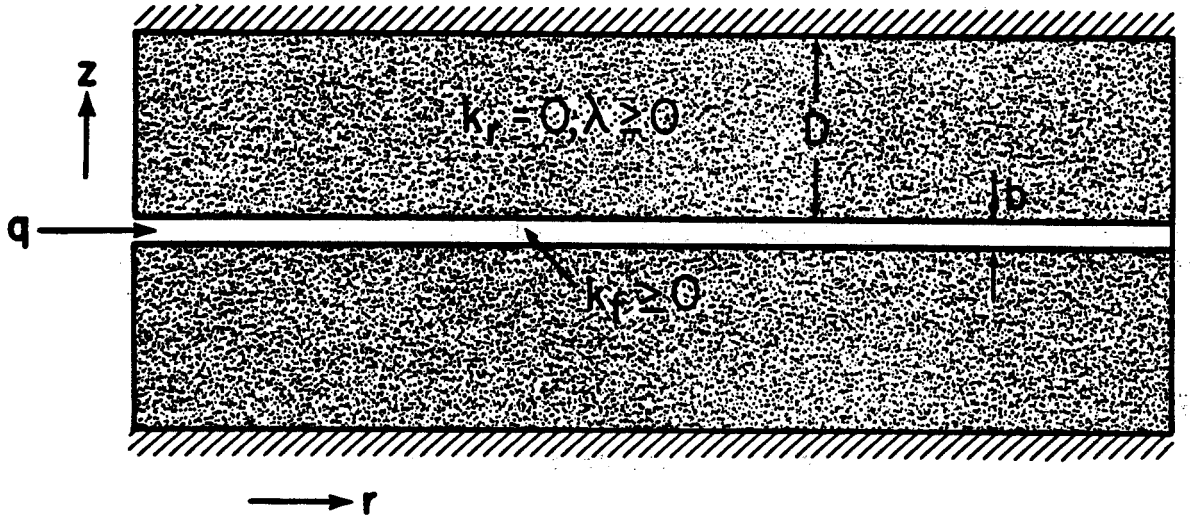

Figure 47. Schematic of analytical model. [XBL 815-2968A]

elevation of $z = 0$ with the rock matrix extending vertically to $z = \pm D$.

(2) Initially, the temperature is T_o everywhere in the system, but at $t = 0$, the temperature of the injected water is fixed at T_i.

(3) The fracture may contain some solids ($\phi_f < 1$) and an instantaneous thermal equilibrium between the fluid and the solids in the fracture is assumed. Furthermore, in the fracture, horizontal conduction is neglected and a uniform temperature in the vertical direction is assumed (infinite vertical thermal conductivity).

(4) The rock matrix above and below the fracture is impermeable. Horizontal conduction is neglected and the vertical thermal conductivity is finite. Heat flow boundaries at $z = \pm D$ are assumed to be perfectly insulated (no heat flow).

(5) The energy resistance at the contact between the fracture and the rock matrix is assumed to be negligible (infinite heat transfer coefficient) and therefore the fracture temperature is equal to the rock matrix temperature at the contact points ($z = \pm 0$).

(6) No nonlinearities are allowed; i.e., the density and heat capacity of the fracture fluids and solids, as well as the density, heat capacity, and thermal conductivity of the rock matrix are assumed to be constant.

The differential equation governing the fluid temperature in the fracture can be derived by performing an energy balance in a control volume within the fracture. The derivation is similar to those reported

by Lauwerier (1955), Bodvarsson (1969), and Gringarten et al. (1975). The fracture equation is:

$$\frac{1}{2\pi r}\frac{\rho_w c_w q}{b}\frac{\partial T_f}{\partial r} + \rho_f c_f \frac{\partial T_f}{\partial t} - \frac{2\lambda}{b}\frac{\partial T_r}{\partial z}\bigg|_{z=0} = 0 \tag{47}$$

where T_f is the temperature of the fluid in the fracture and T_r is the temperature in the rock matrix. The temperature in the rock matrix is governed by the one-dimensional heat conduction equation:

$$\frac{\partial^2 T_r}{\partial z^2} = \frac{\rho_r c_r}{\lambda}\frac{\partial T_r}{\partial t} . \tag{48}$$

The initial and boundary conditions can be expressed as:

$$T_f(r,0) = T_r(r,z,0) = T_o, \tag{49}$$

$$T_f(0,t) = \begin{cases} T_o & t < 0, \\ T_i & t > 0, \end{cases} \tag{50}$$

$$T_f(r,t) = T_r(r,0,t), \tag{51}$$

$$\frac{\partial T_r}{\partial z}\bigg|_{z=D} = 0. \tag{52}$$

The dimensionless parameters ξ, τ, η, θ and T_D are defined as:

$$\xi = \frac{\lambda \pi r^2 (2 + \theta)}{\rho_w c_w q\ D} , \tag{53}$$

$$\tau = \frac{\lambda t}{\rho_r c_r D^2} , \tag{54}$$

$$\eta = \frac{z}{D} , \tag{55}$$

$$\theta = \frac{\rho_f c_f}{\rho_r c_r}\frac{b}{D} , \tag{56}$$

$$T_D = \frac{T - T_o}{T_i - T_o} \, . \tag{57}$$

Substituting equations (53)-(57) into equations (47) and (48) yields:

Fracture:

$$(2 + \theta) \frac{\partial T_{D_f}}{\partial \xi} + \theta \frac{\partial T_{D_f}}{\partial \tau} - 2 \left. \frac{\partial T_{D_r}}{\partial \eta} \right|_{\eta=0} = 0. \tag{58}$$

Rock:

$$\frac{\partial^2 T_{D_r}}{\partial \eta^2} = \frac{\partial T_{D_r}}{\partial \tau} \, . \tag{59}$$

The initial conditions and the boundary conditions become:

$$T_{D_f}(\xi,0) = T_{D_r}(\xi,\eta,0) = 0, \tag{60}$$

$$T_{D_f}(0,\tau) = \begin{cases} 0 & \tau < 0, \\ 1 & \tau \geq 0, \end{cases} \tag{61}$$

$$T_{D_f}(\xi,\tau) = T_{D_r}(\xi,0,\tau), \tag{62}$$

$$\left. \frac{\partial T_{D_r}}{\partial \eta} \right|_{\eta=1} = 0. \tag{63}$$

Equations (58) and (59) along with the constraints given by equations (60)-(63) form a coherent, self-sufficient set of equations. The simultaneous solution of the equations using the Laplace transformation is derived in Appendix C. In the Laplace domain the solutions for the fracture and the rock temperatures are:

Fracture:

$$u = \frac{1}{p} \exp - \frac{[\theta p + 2\sqrt{p} \tanh \sqrt{p}]\xi}{(2 + \theta)} \quad . \tag{64}$$

Rock:

$$v = \frac{1}{p} \exp - \frac{[\theta p + 2\sqrt{p} \tanh \sqrt{p}]\xi}{(2 + \theta)} \cdot \{\cosh \sqrt{p}\, \eta - \sinh \sqrt{p}\, \eta \tanh \sqrt{p}\}. \tag{65}$$

where p is the Laplace parameter. Unfortunately, equations (64) and (65) are difficult to invert analytically from the Laplace domain so a numerical inverter was used. The inverter was developed by Stehfest (1979) and for this problem it gave results accurate within 0.7%.

Results of the Analytical Studies

The Thermal Diffusion Process. In the following discussion, the concept of a "thermal front" will frequently appear. Although conventionally "front" refers to a sharp discontinuity moving through matter, here the definition of the term "thermal front" will be based on the following expression:

$$R^2 = \frac{2}{T_i - T_o} \int_0^\infty (T_f(r) - T_o)\, r dr. \tag{66}$$

In equation (66), R denotes the radial distance from the injection well to the location of the thermal front in the fissure. The definition given by equation (66) is derived on the basis of energy balance considerations so that, if diffusion is neglected, the location of the resulting sharp front will at any time be given by Equation (20). In the

analytical work, the location of the thermal front is approximated as the location of the isotherm representing the average of the temperatures of the injected water and the initial reservoir temperature ($T_{TF} = [T_i + T_o]/2$). Similarily, in the rock matrix the location of the thermal front is taken as the average isotherm.

Figures 48 and 49 show the thermal diffusion from the fracture to the rock matrix for $\theta < 10^{-2}$ and $\theta > 100$, respectively. The dimensionless parameter, θ, represents the ratio of the energy content of the fracture to that of the rock. Low values of θ indicate a negligible energy content in the fracture while large values correspond to a negligible energy content in the rock. For the problem at hand, θ will most likely be less than 10^{-2} for all practical purposes.

In Figures 48 and 49, each plotted line indicates the location of the thermal front at the specified dimensionless time. The figures show that during cold water injection into the fractured rock, the thermal front will advance very rapidly along the fracture at early times, as only a small amount of heat is obtained from the rock. Later on, however, as the available surface area for heat transfer from the rock to the fracture increases, the rate of advancement of the thermal front along the fracture decreases and the cold front starts to penetrate the rock matrix. Eventually, the thermal front in the rock matrix catches up with the thermal front in the fracture at a time corresponding to $\tau \approx 1.0$, and after that a uniform energy-sweeping mechanism will prevail.

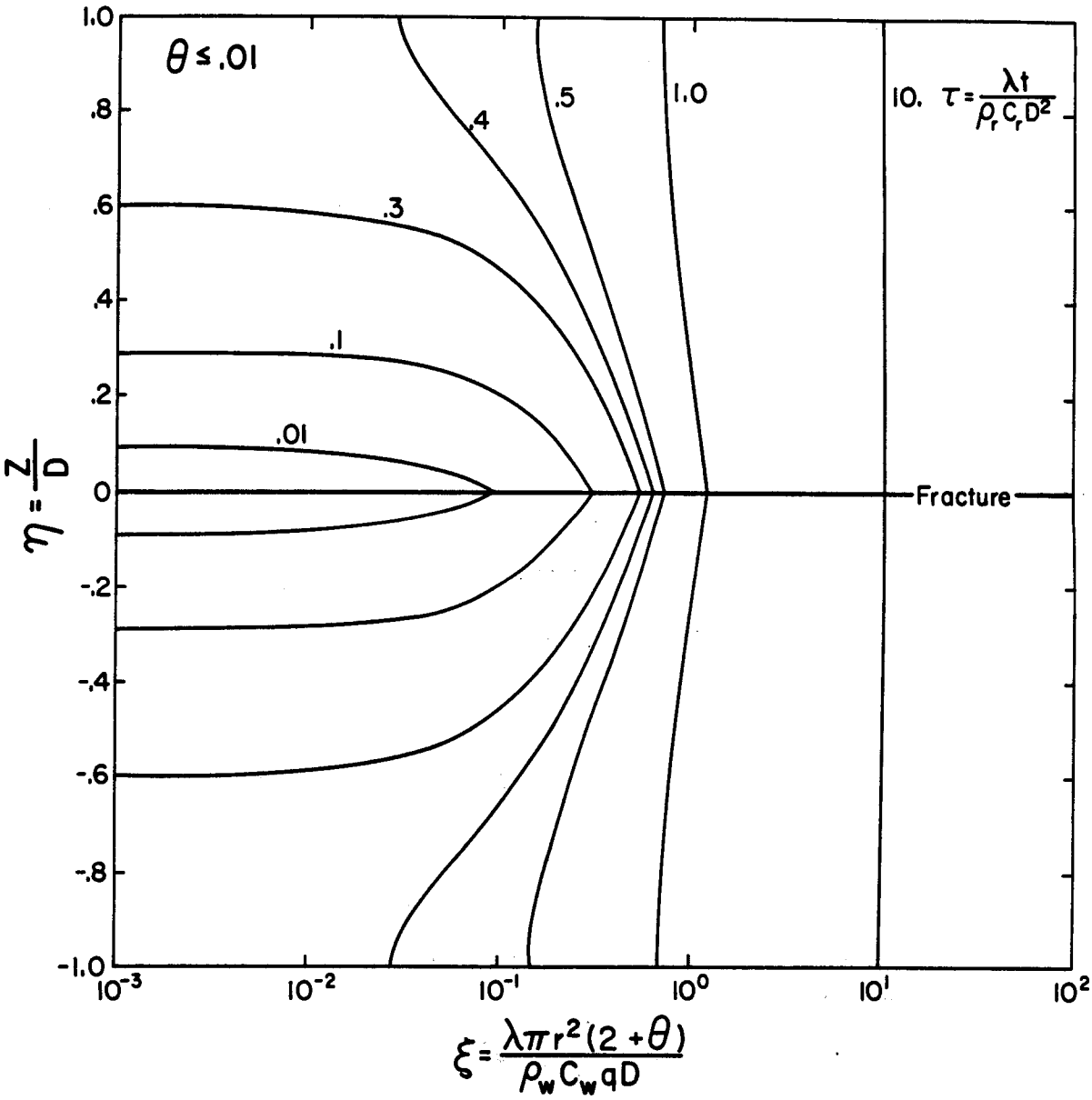

Figure 48. Plots of thermal fronts at various dimensionless times, τ for $\theta < 0.01$; η is dimensionless vertical distance and ξ is dimensionless advancement along the fracture. [XBL 815-2951]

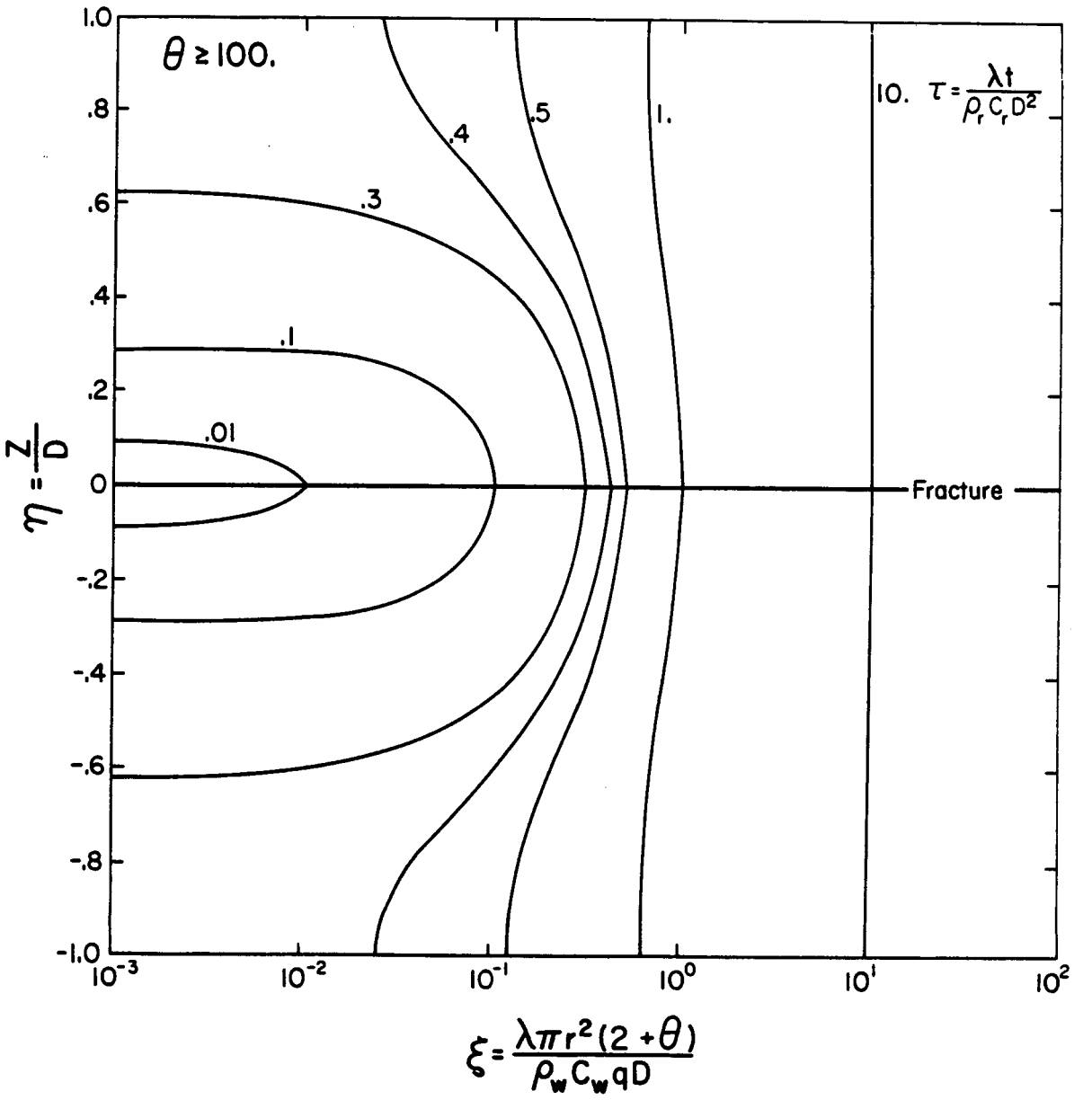

Figure 49. Plots of thermal fronts at various dimensionless times τ for $\theta < 100$. [XBL 815-2952]

This particular diffusion process emerged from numerical studies performed earlier [Bodvarsson and Tsang, 1980a], which led to the present analytical work.

It is interesting to compare Figures 48 and 49. The primary difference is that the dimensionless advancement (ξ) of the thermal front along the fracture at any given dimensionless time (τ) is always less in the case of large θ (Figure 49). For large θ, the rock matrix does not affect the movement of the thermal front along the fracture, so that the location of the thermal front along the fracture at any given time is governed by the following expression:

$$\frac{t}{r^2} = \frac{\pi b}{q} \frac{\rho_f c_f}{\rho_w c_w} . \tag{67}$$

Equation (67), derived by Bodvarsson (1972), applies to a single-layer radial system with insulated upper (caprock) and lower (basement) boundaries. This expression will be discussed further below.

Advancement of the Thermal Front Along the Fracture. The rate of water advancement along the fracture is of course one of the major concerns in the present problem. In Figure 50, type curves representing the movement of the thermal front in the fracture ($\eta = 0$) are given for various values of θ. The characteristics of the curves are such that subdividing the discussion into three subsections--early, intermediate, and late-time behavior--is warranted.

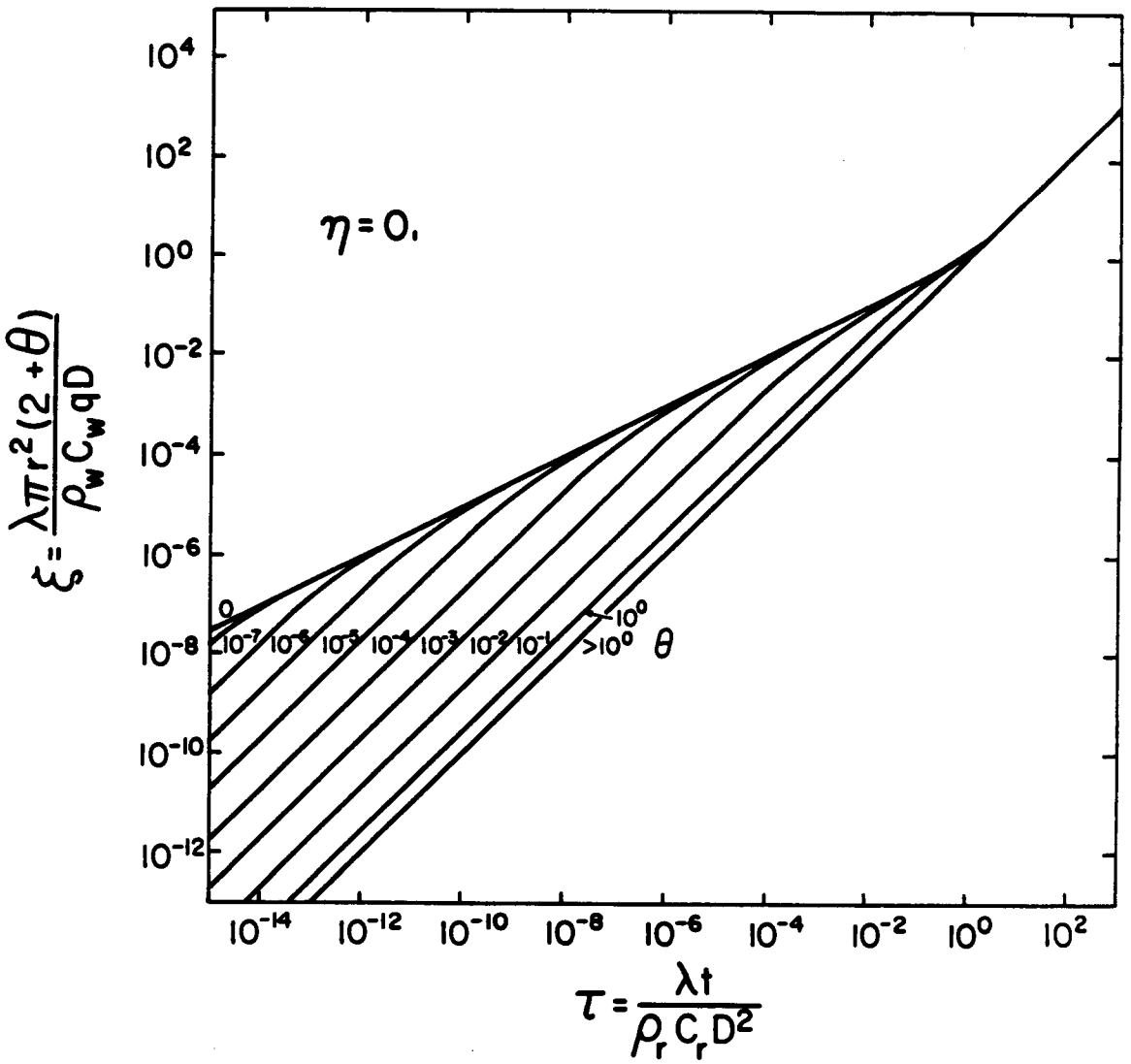

Figure 50. Type curves for the movement of the thermal front in the fracture for various values of θ. [XBL 815-2950A]

At early times, for a given value of θ, the relationship between the dimensionless distance ξ and the dimensionless time τ is:

$$\tau = \frac{\theta}{2 + \theta} \xi. \tag{68}$$

Equation (68) is derived in Appendix C. Substitution of the physical quantities for the dimensionless variables (equations 53-57) yields equation (67). This indicates that at early times, the cold-water front (thermal front) will advance along the fracture as if no rock matrix is present.

At intermediate times, the rock will start to conduct heat to the fracture and consequently slow down the advancement of the cold-water front along the fracture. This is evident in Figure 50 by the convergence of each θ curve to the locus ($\theta = 0$).

At intermediate times the relationship between the dimensionless distance ξ and the dimensionless time τ can be expressed as [Bodvarsson and Tsang, 1980b]:

$$\tau = \frac{4.396}{(2 + \theta)^2} \xi^2. \tag{69}$$

Substitution of equations (53)-(57) into equation (69) yields:

$$t = 4.396 \frac{\lambda \rho_r c_r}{(\rho_w c_w)^2} \left(\frac{\pi r^2}{q} \right)^2. \tag{70}$$

Equation (70) corresponds to the Lauwerier equation [Lauwerier, 1955] as expressed by Bodvarsson and Tsang (1980b). The problem solved by

Lauwerier is identical to the present problem, except that Lauwerier assumed an infinite outer rock boundary condition, which is a special case of our solution ($D \to \infty$). Equation (70) shows that the time, τ, is proportional to the radial distance to the fourth power. This indicates the power of the heat conduction and how it effectively retards the advancement of the thermal front along the fracture.

The transition between the early-time behavior and intermediate-time behavior occurs at dimensionless time and dimensionless distance given respectively by:

$$\tau = \frac{\theta^2}{4.396}, \tag{71}$$

$$\xi = \frac{\theta(2 + \theta)}{4.396} . \tag{72}$$

Equations (71) and (72) are derived by equating equations (68) and (69). Equations (71) and (72) seem quite reasonable, since a large fracture aperture and consequently a large θ, limits and retards the effects of conduction.

In the case of fractured reservoirs, equations (71) and (72) may not have much practical value, because the transition occurs after such a short time. However, when injection into layered reservoirs is considered, these equations may be useful. Rewriting equations (71) and (72) in terms of real variables (equations (53)-(57)) yields:

$$t = \frac{b^2}{4.396} \frac{(\rho_f c_f)^2}{\lambda \rho_r c_r}, \tag{73}$$

$$r = \sqrt{\frac{q}{4.396 \cdot \pi \cdot b} \frac{\rho_w c_w \rho_f c_f}{\rho_r c_r \lambda}} \, . \tag{74}$$

As evident in Figure 50, at large dimensionless times the θ dependence no longer exists and the following simple relation between the dimensionless time τ and the dimensionless distance ξ results:

$$\tau = \xi, \tag{75}$$

Equation (75) is derived in Appendix C and holds for both the fracture and the rock matrix. Substituting real variables for the dimensionless ones in equation (75) yields:

$$\frac{t}{r^2} = \frac{\pi(2\rho_r c_r D + \rho_f c_f b)}{\rho_w c_w q} \, . \tag{76}$$

As is to be expected, equation (76) is equivalent to equation (67), but with combined fracture and rock matrix thermal parameters. Equation (76) can be further simplified in cases of very large or very small θ as follows:

$$\frac{t}{r^2} = \begin{cases} \dfrac{2\pi\rho_r c_r D}{\rho_w c_w q} & \theta \ll 2 \\[2ex] \dfrac{\rho_f c_f}{\rho_w c_w} \dfrac{\pi b}{q} & \theta \gg 2 \end{cases} \tag{77}$$

For fractured reservoirs, the first expression ($\theta \ll 2$) would apply, whereas the second expression ($\theta \gg 2$) may be useful in cases of stratified reservoirs with relatively small shale breaks (e.g., Cerro Prieto, Mexico).

The transition from the intermediate-time solution to the long-time solution occurs when the conductive heat flow from the rock matrix to the fracture becomes affected by the no-heat-flow boundary condition at $\eta = 1$ (insulated at $z = D$). The transition occurs at the time and location given by the following equation:

$$\tau = \xi = \frac{(2 + \theta)^2}{4.396} . \tag{78}$$

Equation (78) is obtained by equating equations (69) and (75). Substitution of equations (53)-(57) into equation (78) yields:

$$t_c = \frac{\rho_r c_r D^2}{4.396\lambda} \left(2 + \frac{\rho_f c_f b}{\rho_r c_r D}\right)^2 , \tag{79}$$

$$r_c = \sqrt{\frac{\rho_w c_w q\ D}{4.396 \cdot \pi \cdot \lambda} \left(2 + \frac{\rho_f c_f b}{\rho_r c_r D}\right)} , \tag{80}$$

where t_c and r_c denote the time and radial distance from the injection well when a uniform energy sweep is achieved. Again, for very large or very small values of θ, equations (79) and (80) can be simplified as follows:

$$t_c = \begin{cases} \dfrac{2\rho_r c_r D^2}{4.396\lambda} & \theta \ll 2.0. \\[2ex] \dfrac{b^2(\rho_f c_f)^2}{4.396\rho_r c_r \lambda} & \theta \gg 2.0. \end{cases} \tag{81}$$

$$r_c = \begin{cases} \sqrt{\dfrac{2\rho_w c_w q \cdot D}{4.396 \cdot \pi \cdot \lambda}} & \theta \ll 2.0. \\[2ex] \sqrt{\dfrac{q \cdot b \cdot \rho_w c_w \rho_f c_f}{4.396 \cdot \pi \cdot \rho_r c_r \lambda}} & \theta \gg 2.0. \end{cases} \tag{82}$$

Note that for a small θ, the time of uniform energy sweep depends only on the thermal properties of the rock matrix and the distance to the insulated boundary [(D)], but not on the flow rate, the fracture aperature and width, or thermal parameters.

Advancement of the Thermal Front in the Rock Matrix

Figures 51 and 52 show the advancement of the thermal front in the rock matrix for small and large values of θ, respectively. The graphs show that the lower the value of η ($\eta = z/D$), the earlier the curve converges to the $\eta = 0$ curve which represents the thermal front along the fracture. This relationship is certainly reasonable since the lower the value of η the closer the observation point is to the fracture. The curves in Figures 51 and 52 also show that, at low values of ξ, the dimensionless parameters ξ and τ behave independently (τ does not change with changes in ξ). This behavior can be explained in terms of Figures 48 and 49. At early times during injection, the isotherms in the rock matrix close to the injection well (small ξ) are parallel to the fracture (pure vertical heat flow). The horizontal temperature gradient is practically negligible. Therefore, for a given η, the thermal front will arrive at the same dimensionless time regardless of the value of ξ.

Temperature Distribution in the Fracture and the Rock Matrix

The temperature distribution in the system at various dimensionless times is shown in Figure 53. In the plots, temperature contours for T_D varying from 0.1-0.9 are shown in steps of 0.1. [The temperature contours representing the temperature of the injected water ($T_D = 1.0$) and the

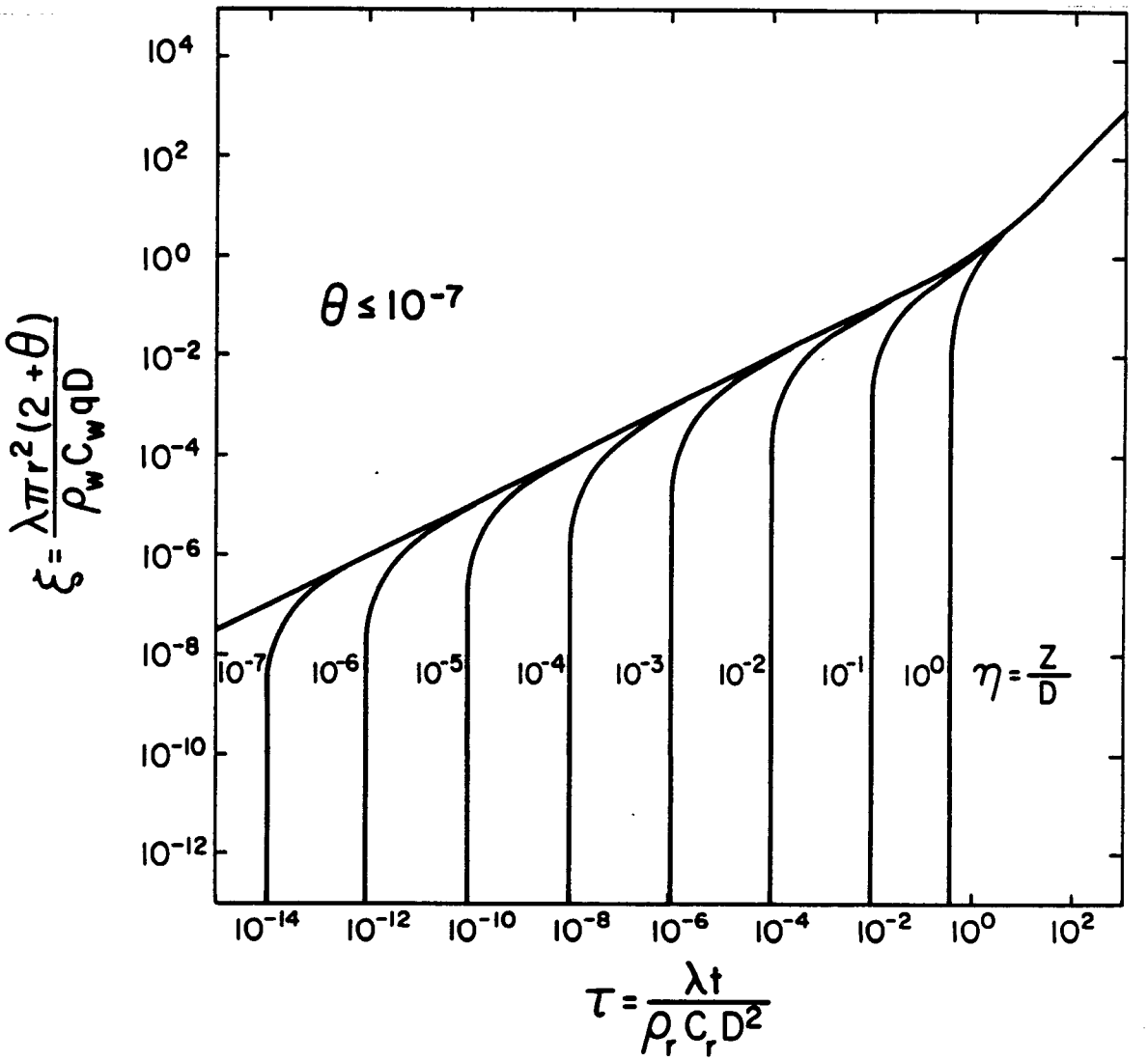

Figure 51. Advancement of the thermal front in the rock matrix for small values of θ. [XBL 815-2949]

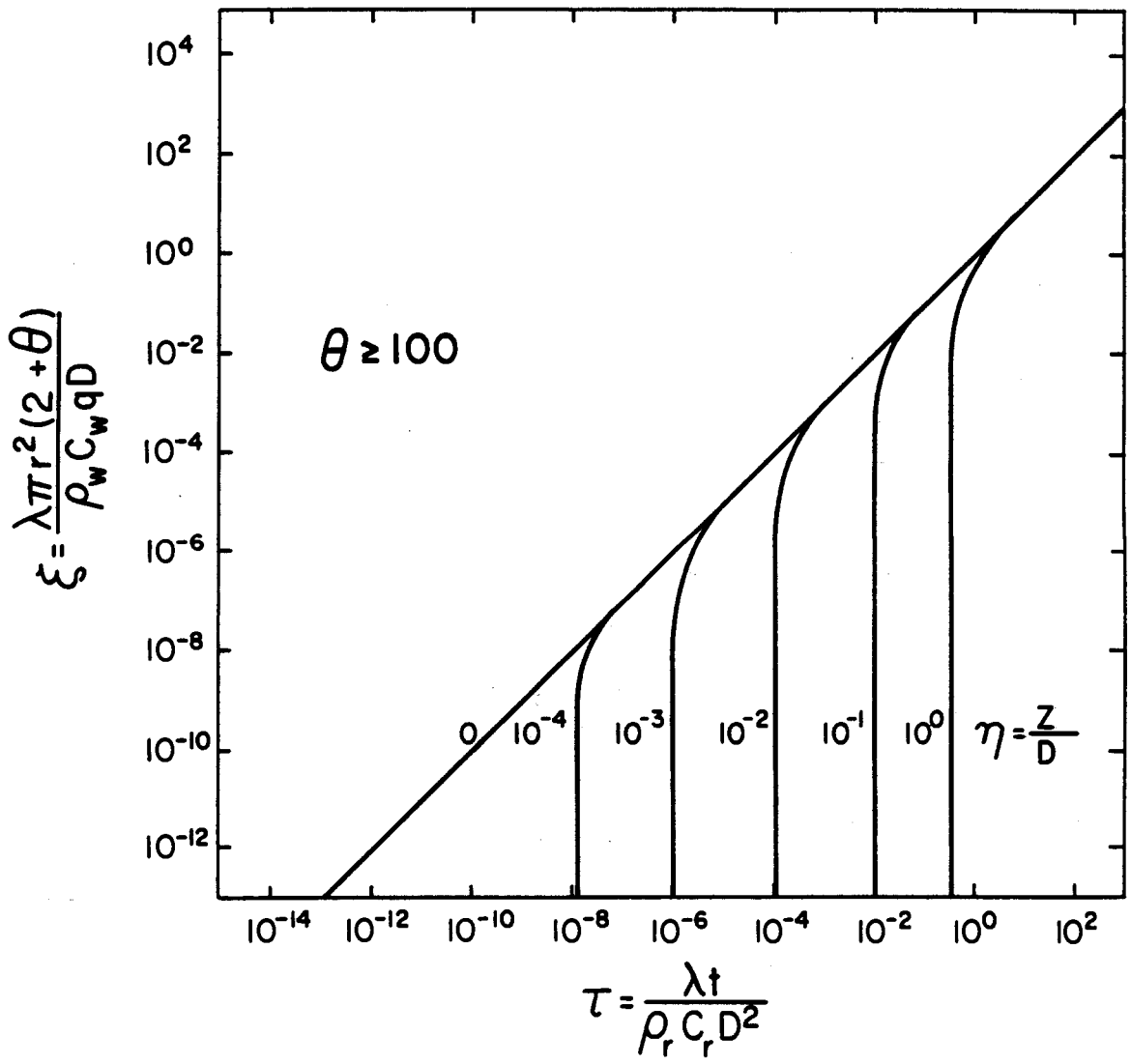

Figure 52. Advancement of the thermal front in the rock matrix for large values of θ. [XBL 815-2948]

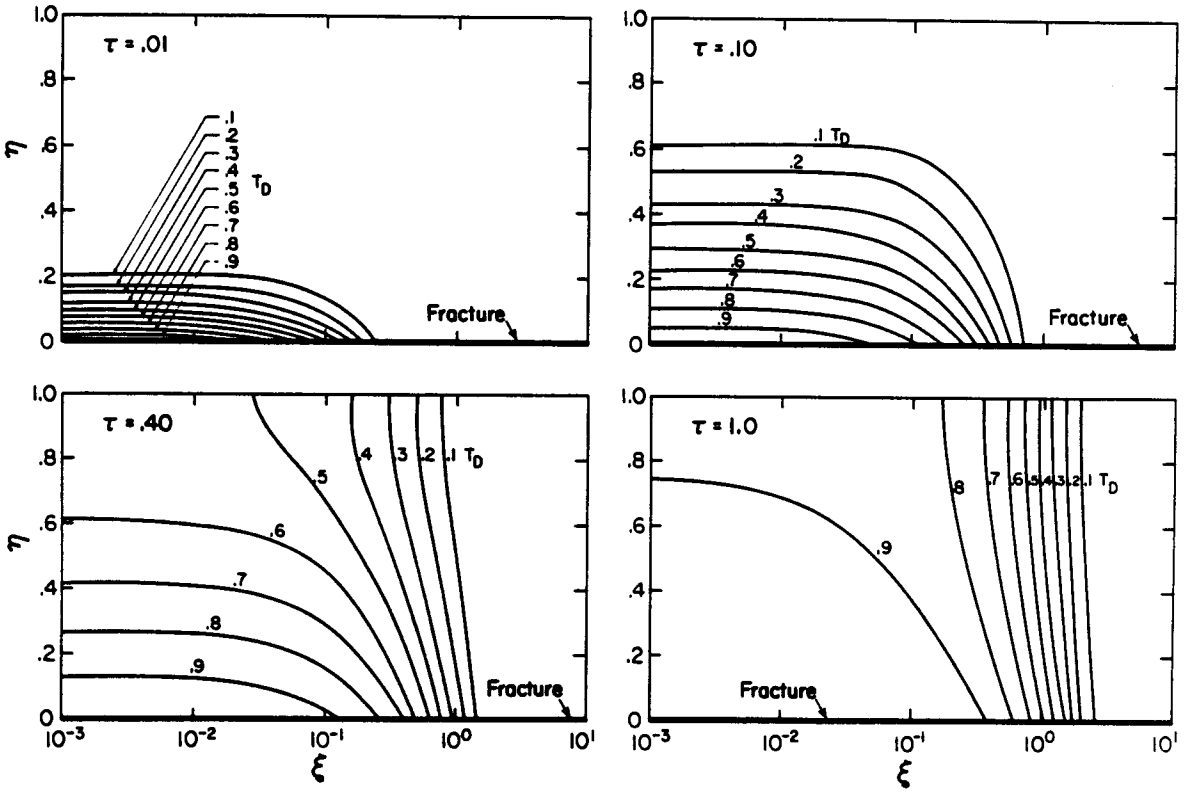

Figure 53. Temperature distribution in the fracture and rock matrix at various dimensionless times. [XBL 815-2953]

temperature of the native reservoir water ($T_D = 0.0$) are not shown, due to difficulties in tracing them with the numerical inverter.] Although the basic phenomenon explaining the behavior shown in Figure 53 has already been discussed (with reference to Figures 48 and 49), the graphs in Figure 53 can be quite useful in determining thermal transients from injection. Furthermore, the data plotted in Figure 53 may aid in estimating the recoverable energy from a geothermal system, given the exploitation scheme (well spacing, flow rates, etc.).

The temperature distribution along the fracture is shown in Figures 54 and 55 for intermediate and late times, respectively. At early times, that is, at times before the influence of the rock matrix is felt, the thermal front in the fracture is sharp since horizontal conduction in the fracture is neglected. The thermal front, however, becomes diffuse as the energy flow between the fracture and the rock matrix begins. Figure 54 shows how diffuse the thermal front becomes during intermediate times (after the rock matrix starts to contribute significant energy but before the no-heat-flow boundary condition is felt at $\eta = 1$). The curve is characterized by a rather sharp front but a very diffuse tail. The temperature distribution in the fracture and in the rock matrix (i.e., for all values of η) at late times is shown in Figure 55.

In the reverse case, with injection of hot water into a colder reservoir, the late-time behavior is illustrated in Figure 56. The figure shows that a hot zone corresponding to the temperature of the injected water has developed, with a transition zone further away from

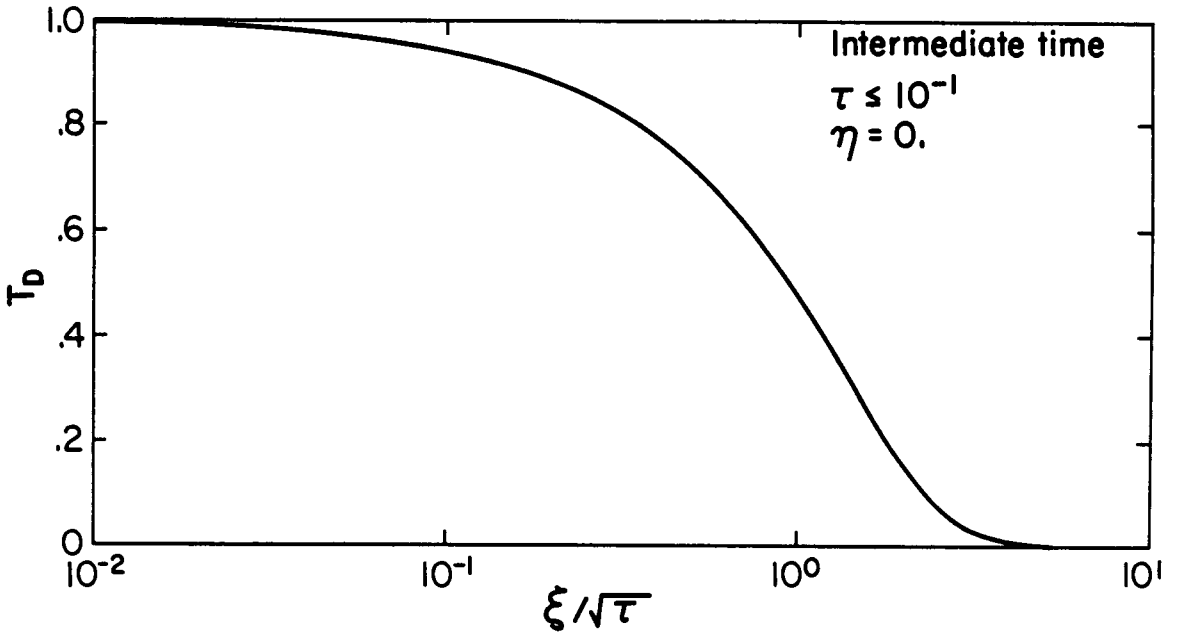

Figure 54. Diffuseness of the thermal front at intermediate times.
[XBL 815-2954]

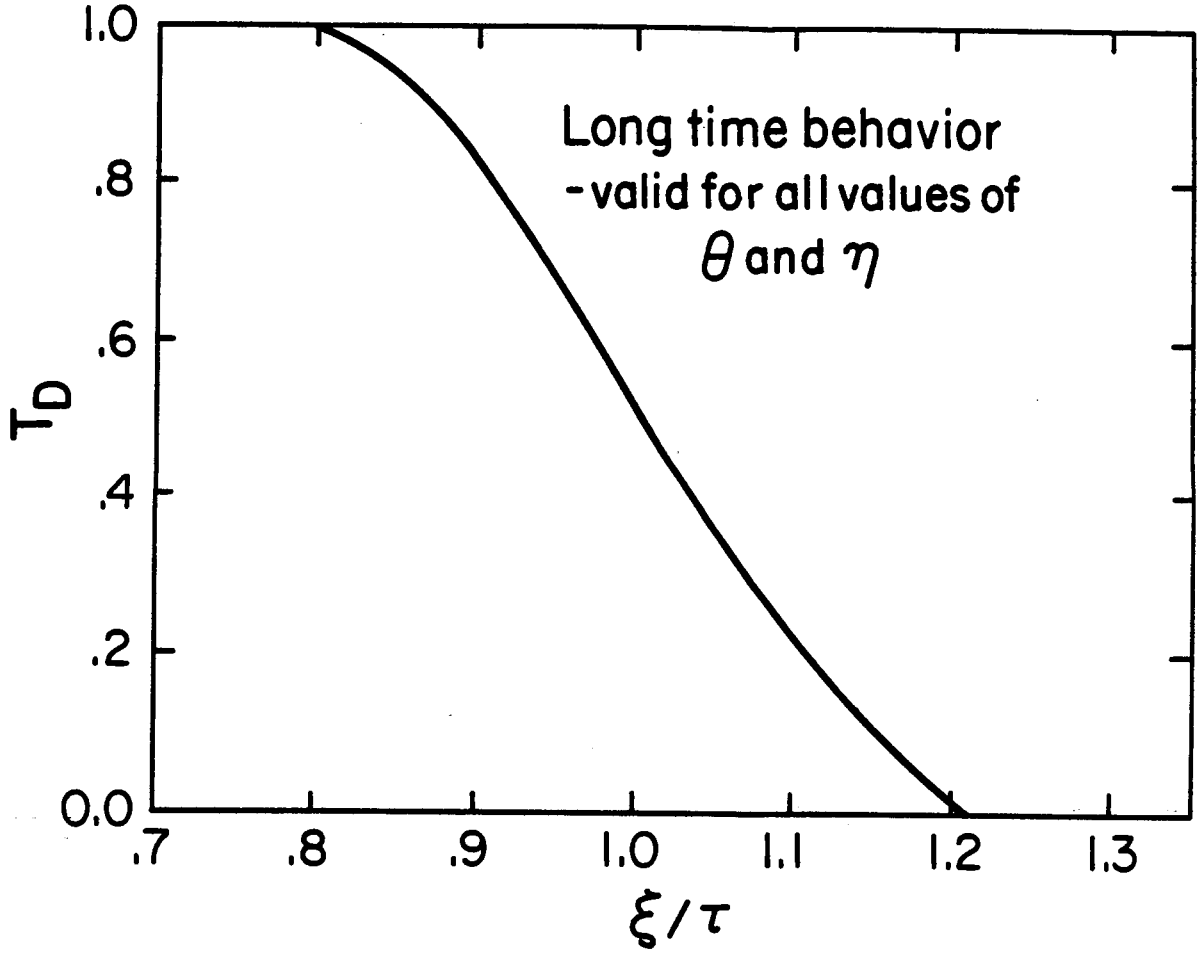

Figure 55. Diffuseness of the thermal front at late times.

[XBL 815-2955]

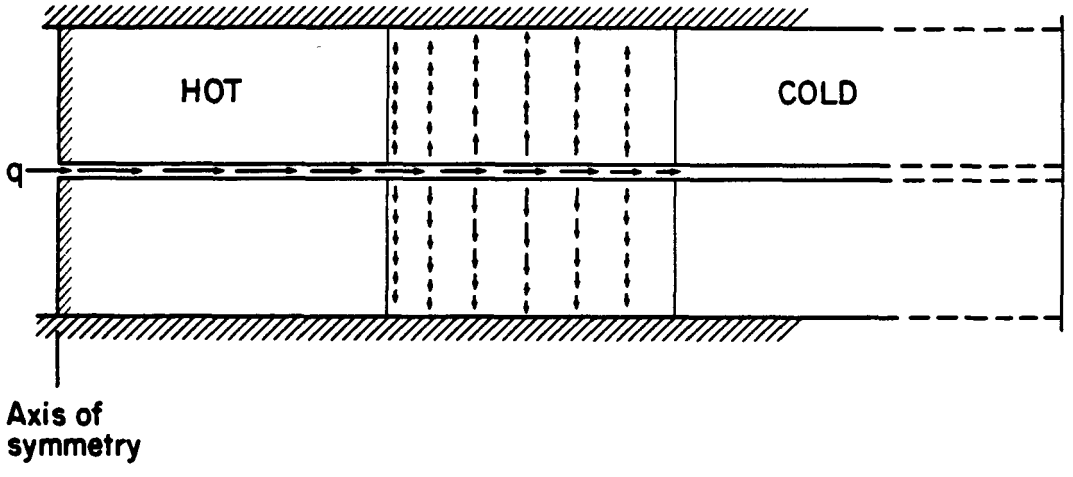

Figure 56. The heat transfer mechanism in the system at late times for the reverse case - hot-water injection into a colder reservoir. [XBL 815-2956]

the injection well and a cold water zone still further away. The heat is transported by convection along the fracture until the transition zone is reached. In the transition zone, the heat is conducted vertically into the rock matrix, with a heat flux density as shown in Figure 57. The parameter Q_d represents a dimensionless energy loss from the fracture to the rock matrix. Q_H is the energy flux calculated by means of the Fourier law of heat conduction:

$$Q_H = \lambda \cdot A \left.\frac{\partial T}{\partial z}\right|_{z=0} . \tag{83}$$

As Figure 57 shows, the maximum energy loss occurs at $\xi/\tau \simeq 1$; that is, at the radial distance from the well corresponding to the location of the thermal front (see equation (75)). Since θ is less than 0.01, practically all of the injected energy will be conducted to the rock matrix (the energy potential of the fracture is negligible compared to that of the rock matrix) and consequently the area under the curve in Figure 57 will equal unity.

As Figure 56 illustrates, in the analytical solution developed in this study, horizontal conduction was neglected. This assumption caused the concentrated area of heat transfer shown in Figure 57 and the resulting sharp front (Figure 55). The importance of this assumption is discussed below.

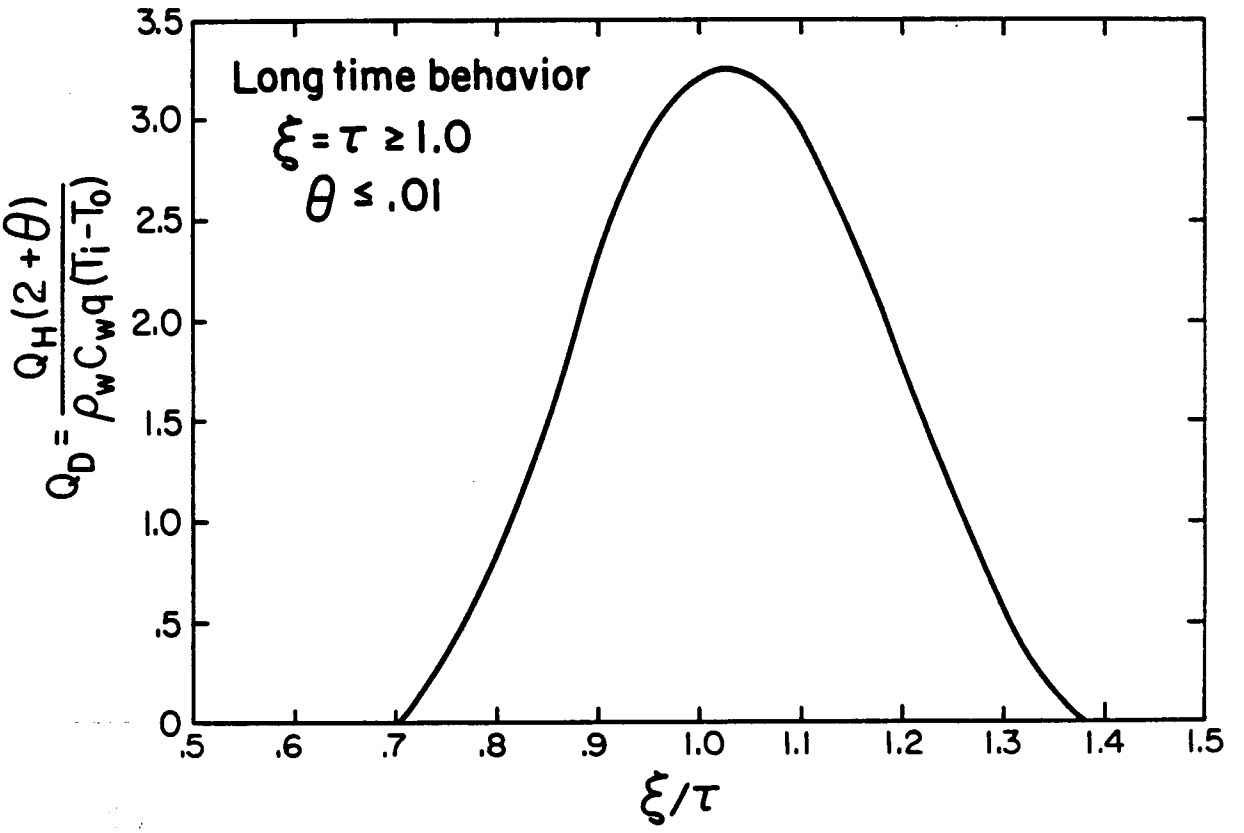

Figure 57. Heat flux density along the fracture at late times. The parameter Q_d represents dimensionless energy loss from fracture to rock. [XBL 815-2957]

Numerical Studies

In addition to the analytical work discussed above, parallel numerical studies were carried out. The objective of the numerical studies is twofold:

(1) to study the importance of the assumptions made in the analytical work; and

(2) to extend the analytical work to cases where the rock matrix is permeable in order to understand the importance of fluid movement into the rock matrix.

In this study the recently developed numerial code PT was used (see section on code development, page 18).

Comparison of Analytical and Numerical Results

As a first step, the problem considered in the analytical work was solved using the numerical code and applying the same assumptions as in the analytical work. Figure 58 shows a schematic view of the mesh used; because of symmetry, only half of the basic section shown in Figure 47 was modeled. The fracture elements (bottom layer) were connected to two constant-pressure, constant-temperature boundary elements (large nodes) to insure constant mass flow and a constant injection temperature T_i.

The vertical lines dividing the rock mass into elements are dotted to illustrate that there are no horizontal connections between the rock elements and subsequently no horizontal conduction in the rock matrix. The fracture elements were connected to enable a steady mass flow, but

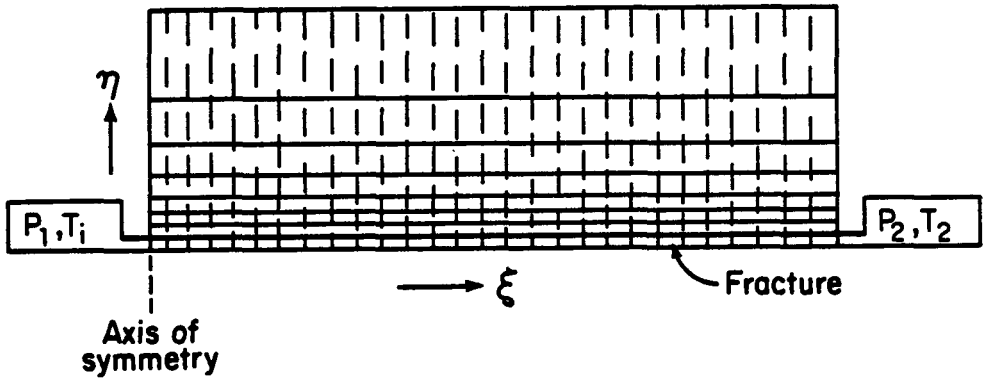

Figure 58. Schematic of the mesh used in the numerical calculations.
[XBL 815-9258]

the thermal conductivity of the fracture elements was set to zero. The nodal points of the fracture elements were placed at the rock-fracture boundary to satisfy the boundary condition that the temperature of the rock at $z = 0$ ($\eta = 0$) is identical to the fracture temperature. Finally, a very high rock thermal conductivity was used so that only small temperature gradients would develop in the rock matrix and therefore minimize the space discretization errors. The fracture aperture of 10^{-4} m was arbitrarily selected and a fracture spacing (2xD) of 0.02 m was used. Fixing all volumetric heat capacities as unity ($\rho_w c_w = \rho_f c_f = \rho_r c_r = 1$), a value of $\theta = 0.01$ resulted.

Figure 59 shows the comparison between the analytical and the numerical results for $\theta = 0.01$. The figure shows an excellent agreement between the analytical and the numerical results. However, although equation (66) was always used to determine the location of the thermal front, the equivalent isotherm was not always T_{TF}, the average of the temperature of the injected water and the initial reservoir temperature. In the case of the early-time simulation ($\tau < 10^{-4}$), T_{TF} is the proper isotherm, as the thermal front becomes diffuse due to numerical dispersion but remains symmetrical (see Figure 60). However, in the simulations representing intermediate ($10^{-4} < \tau < 1.0$) and late times ($\tau > 1.0$), heat transfer between the fracture and the rock matrix is present. This and the associated numerical dispersion yields a nonsymmetrical thermal front. In these cases, the proper isotherm representing the thermal front was selected by using graphical integration as illustrated in Figure 61

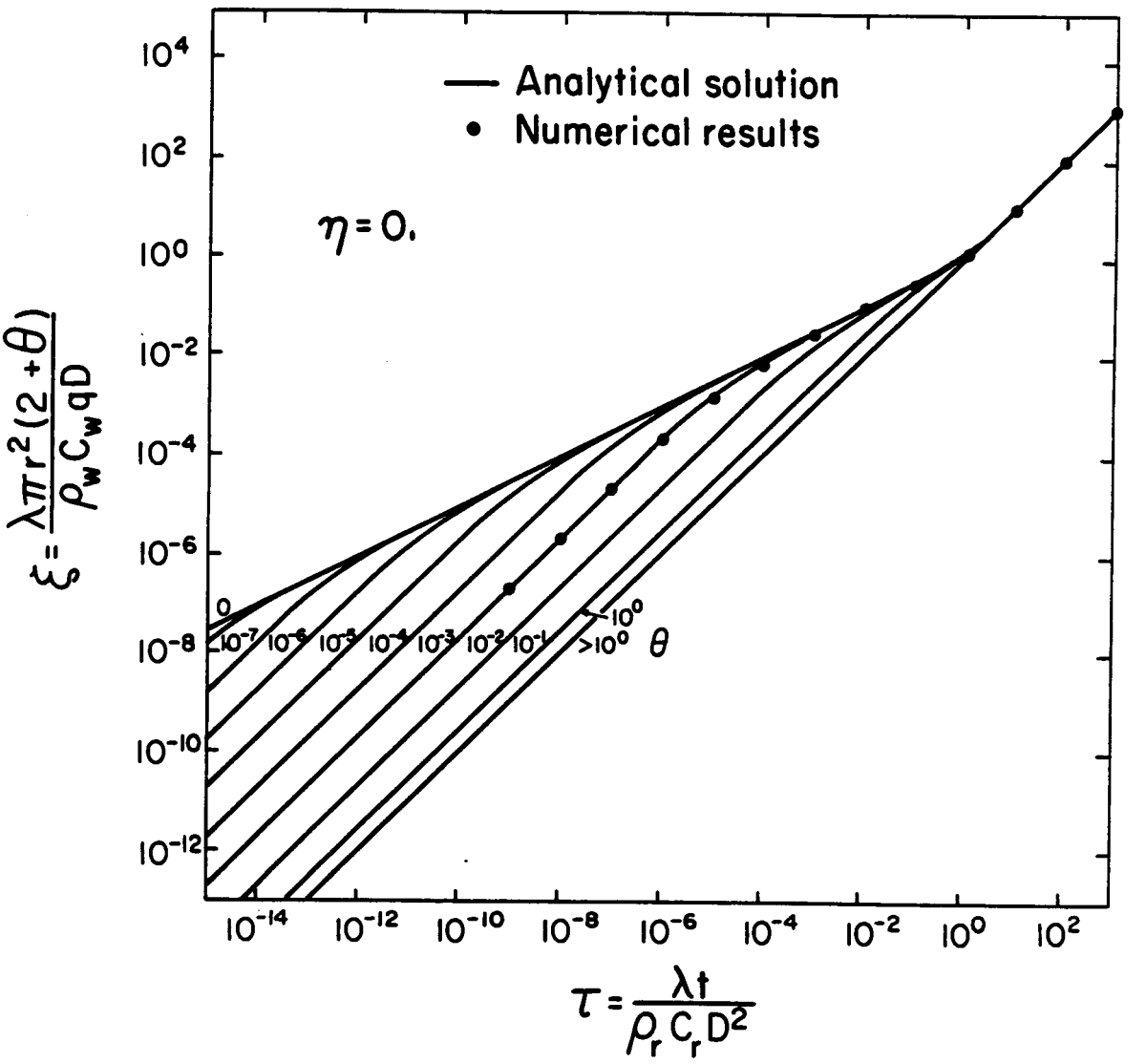

Figure 59. Comparison of the analytical and numerical results for $\theta = 0.01$. [XBL 815-2950]

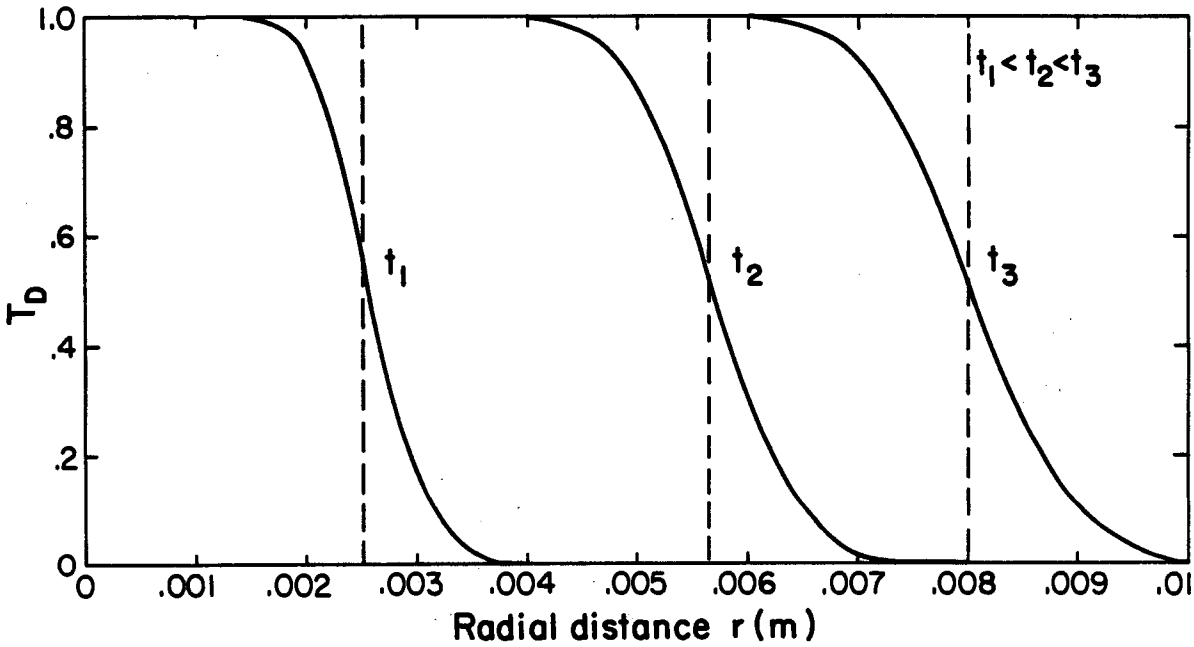

Figure 60. The effects of numerical dispersion on the thermal front at various times. [XBL 815-2960]

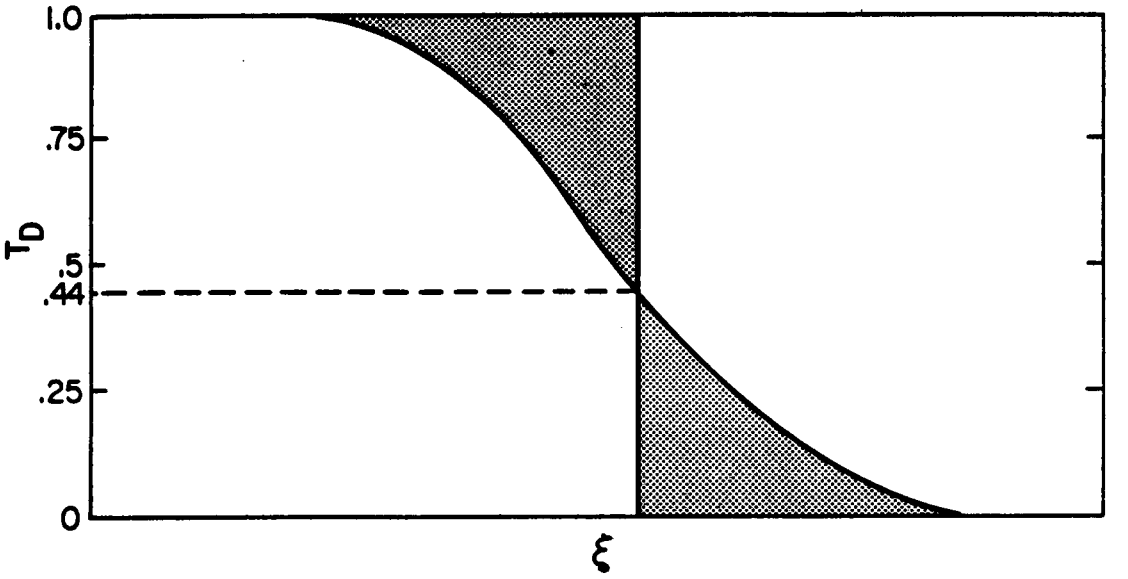

Figure 61. Graphical integration showing an intermediate-time thermal front isotherm as T_D = 0.44. [XBL 815-2961]

(equating the areas of the two shaded portions). Using this approach, the thermal front for the intermediate-time simulation was selected as $T_D = 0.44$. At later times, when the thermal front became more diffuse, the appropriate value was $T_D = .33$.

Importance of Assumptions Employed in Analytical Approach

In order to understand the importance of the assumptions employed in the analytical work, a number of computer runs using the numerical code PT were made. In these simulations some of the more critical assumptions listed on page 128 were relaxed. Thus, a transient mass flow is considered with variable fluid properties $\rho(P,T)$ and $\mu(T)$, and horizontal conduction both in the fracture and the rock matrix is allowed. The results show that the steady-state mass-flow assumption is indeed very reasonable and does not lead to significant errors in the thermal field. When considering only the location of the thermal front, the assumption of no horizontal conduction in the rock matrix is also reasonable. Figure 62 shows the comparison between the analytical results and the numerical results (with transient mass flow and horizontal conduction) for the advancement of the thermal front along the fracture for the case $\theta = .01$.

At late times, however, horizontal conduction will become the dominant means of heat transfer, both in the rock and in the fracture. Figures 63 and 64 show the thermal diffusion into the rock matrix at various times for the cases of no horizontal conduction and with horizontal conduction, respectively. The parameters and the mesh used in the simulation are given in Table 6. The figures show that before the thermal front in

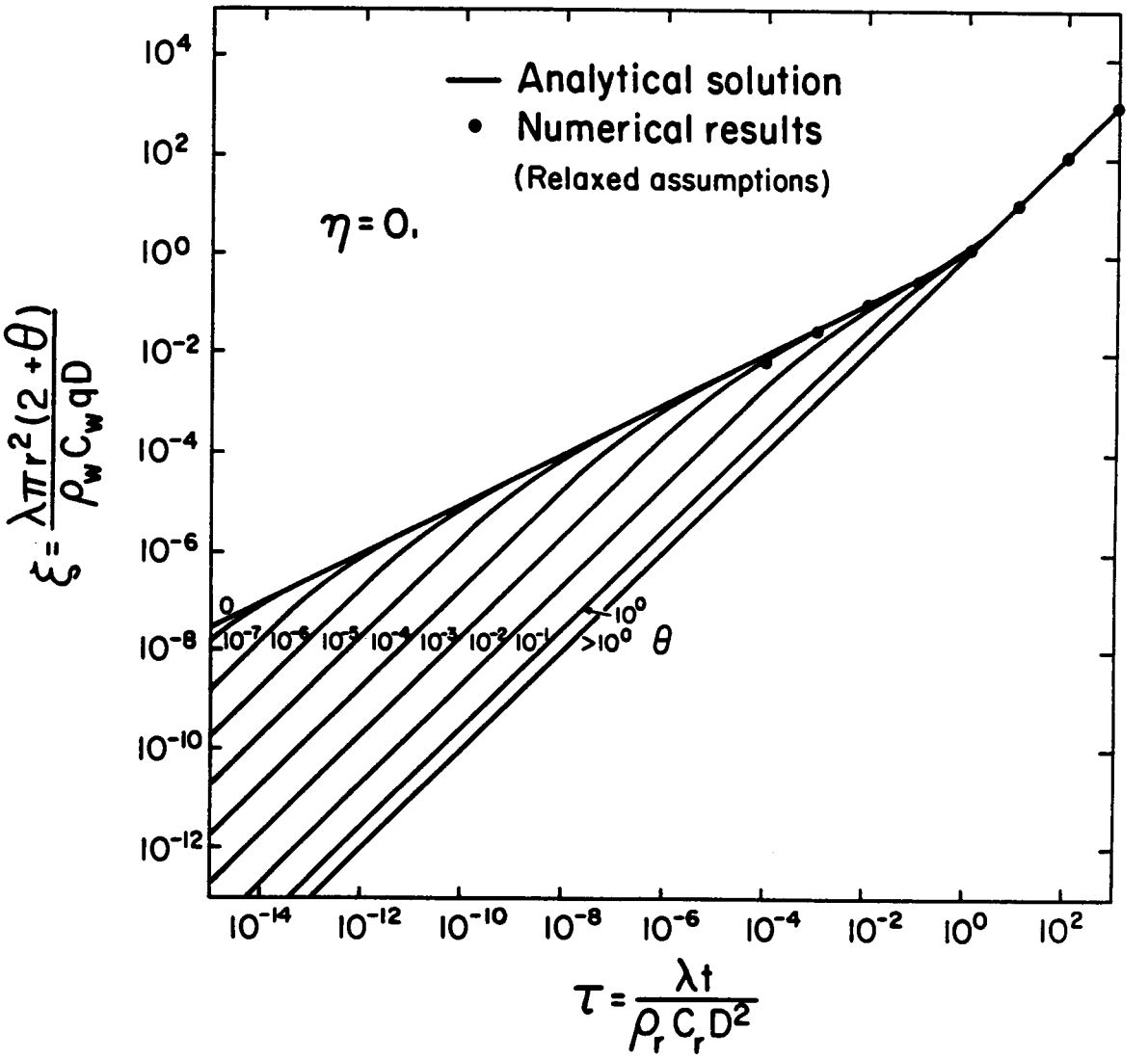

Figure 62. Comparison of analytical and numerical results (with relaxed assumptions) for advancement of the thermal front along the fracture. [XBL 815-2967]

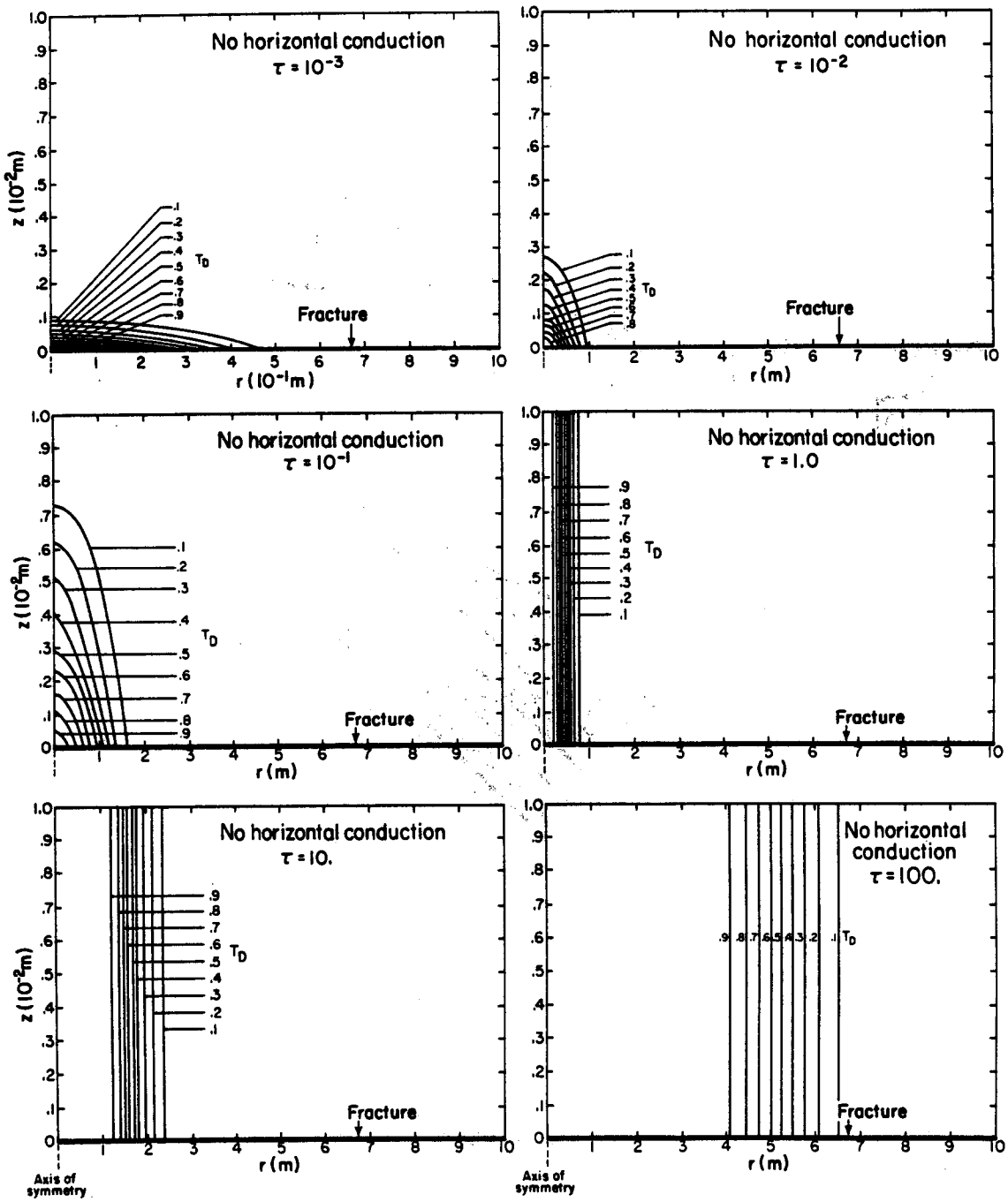

Figure 63. Temperature distribution in the rock matrix at various times; no horizontal conduction. [XBL 815-2975A]

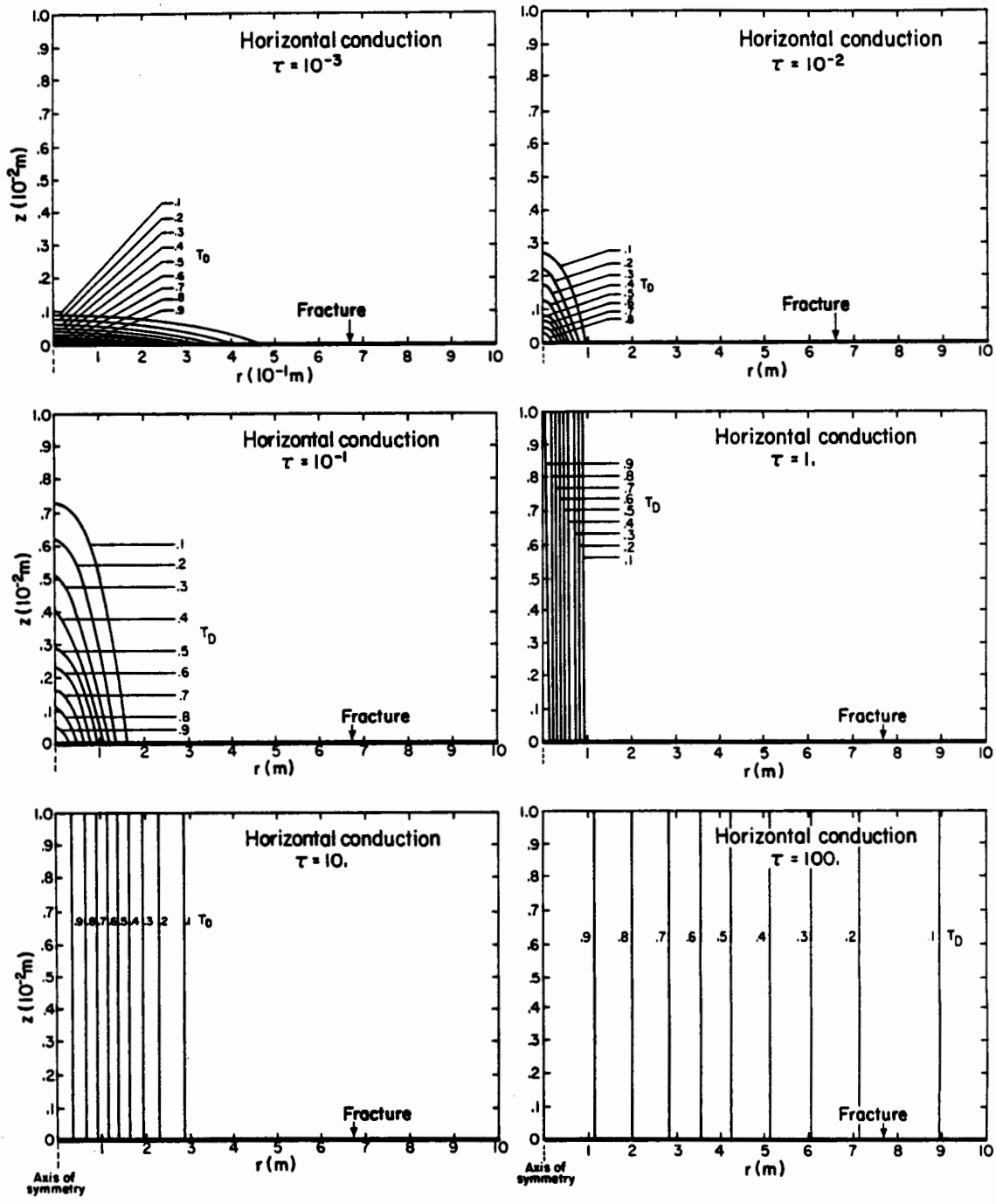

Figure 64. Thermal diffusion into the rock matrix at various times; horizontal conduction. [XBL 815-2966A]

Table 6. Parameters used in the study of the effects of horizontal conduction.

Parameters	Fracture (fluid)	Rock Matrix
Thermal conductivity, λ(J/m•s•°C)	1.0	10.0
Density, ρ(kg/m^3)	1000.0	1000.0
Specific heat, C(J/kg•°C)	1000.0	1000.0
Porosity, ϕ (-)	1.0	.001
Fracture aperture b	10^{-4} m	
Fracture spacing 2D	0.02 m	
Flow rate q	1×10^{-2} m^3/s	
Mesh:		
(a) Radial spacing	10 x 0.1 m, 20 x 1 m, 2, 3, 7, 8, 10, 15, 20, 60, 90, 150, 250, 350 m.	
(b) Vertical spacing	5×10^{-5}, 1×10^{-5}, 3×10^{-5}, 1×10^{-4}, 3×10^{-4}, 1×10^{-3}, 3×10^{-3}, 5.556×10^{-3} m.	

the rock catches up with the thermal front in the fracture ($\tau < 1.0$), the effects of horizontal conduction are negligible. This is reasonable, since at early times the vertical temperature gradients are orders of magnitude larger than the horizontal gradients (see Figure 53). However, after uniform sweeping conditions prevail, the horizontal conduction dominates and eventually, when the fluid velocity in the fracture becomes very small (radial effects), the thermal front will advance purely through conduction. This mechanism is shown schematically in Figure 65.

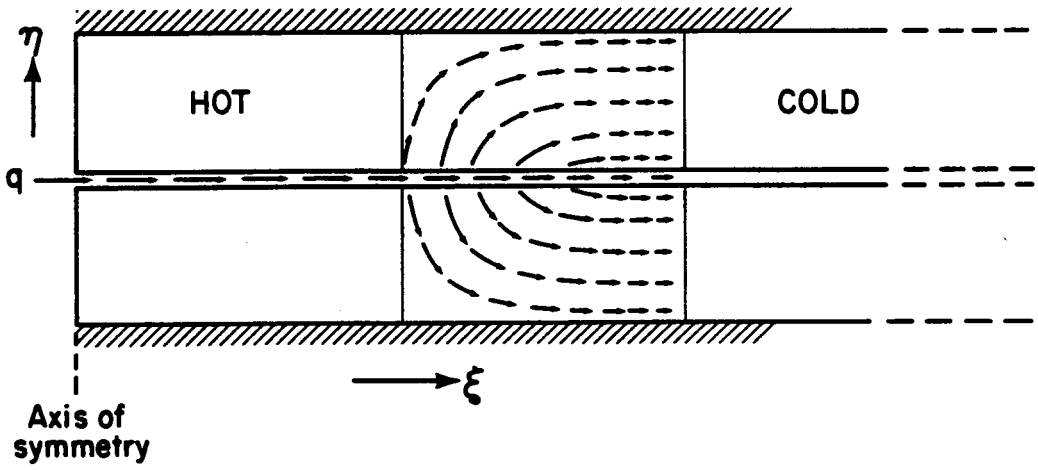

Figure 65. The late-time heat transfer mechanism for the rock-fracture system when horizontal conduction is considered.

[XBL 815-2977]

The importance of horizontal conduction when uniform sweep conditions are reached clearly indicates that the present analytical solution cannot be used to calculate the temperature distribution at late times. An approximate solution can, however, be obtained using the constant-pressure solution for flow to a well of finite radius by van Everdingen and Hurst (1949). After adapting the solution to the present problem, it becomes:

$$T_D(r_D,t_D) = \frac{2}{\pi} \int_0^\infty \frac{[1 - \exp(-u^2 t_D)][J(u)Y_o(ur_D) - (Y_1(u)J_o(ur_D)]du}{u^2[J_1{}^2(u) + Y_1{}^2(u)]} \tag{84}$$

$$\text{where } T_D = \frac{T - T_i}{T_o - T_i}, \qquad t_D = \frac{\lambda(t - t_c)}{\rho_r c_r r_c{}^2}, \qquad r_D = \frac{r}{r_c} \tag{85}$$

The symbol r_c denotes the radial distance from the injection well to the location where uniform sweep begins and can be calculated using equation (80); t is the time since injection began, and t_c is the time uniform sweep conditions start and can be calculated using equation (79). The primary assumption made when the temperature distribution is calculated using equation (84) is that a sharp front exists at $r = r_c$. At time $t = t_c$, the front is actually not very diffuse, as illustrated in Figure 55, and the assumption is probably reasonable, especially at late times ($t \gg t_c$). Equation (84) may be useful in estimating the temperature at the production well in cases of thermal breakthrough. In the present problem, the common approach of modeling the fractures as parallel plates has been employed (Hele Shaw approach). It is however, well

known that fracture apertures and consequently fingering and dispersion effects will occur [Maini, 1977; Neuzil and Tracy, 1981]. Dispersion in thermal flow is an interesting area for further research. However, our preliminary considerations indicate that its main effect is to increase thermal front smearing and may have less effect on the thermal front movement.

Importance of Permeability in Rock Matrix

In the analytical work, the assumption of an impermeable rock matrix was made. When the rock is permeable, heat transfer by convection between the fracture and the rock matrix will take place in addition to the conductive heat transfer. The thermal front along the fracture (Figure 50) will therefore advance more slowly than the analytical solution predicts. In addressing this problem, the following approach was taken:

(1) The nonisothermal mode of program PT was used to calculate the advancement of the thermal front in the fracture with time for several values of $k_D = k_f/k_r$, where k_f is the permeability of the fracture and k_r is the permeability of the rock matrix.

(2) By assuming that conduction is negligible compared to the convective heat transfer between the fracture and the rock matrix, the location of uniform sweep conditions could be calculated, based on steady-state flow patterns.

Convection and Conduction. As a first effort in examining the effects of conduction and convection, a finite permeability was assigned to the rock elements, while cold water was injected into the fracture

elements. Only the most general case was studied, taking into account:

(1) transient mass flow

(2) horizontal and vertical conduction in the rock matrix and horizontal conduction in the fracture

(3) horizontal and vertical permeability in the rock matrix, of equal magnitude (no anisotropy)

(4) nonconstant fluid parameters $\rho = f(P,T)$ and $\mu = f(T)$.

The parameters used in the study are listed in Table 7 along with the grid spacings. In general, a uniform spacing is used in regions where temperature changes are expected and logarithmic spacing is used in regions of the rock where isothermal flow is anticipated. The computer runs were made using only one set of geometric parameters, $\theta = 10^{-2}$, but a number of different values of dimensionless permeability k_D were used. The results for the advancement of the thermal front in the fracture are shown in Figure 66.

The results show that the rock permeability can have a large effect on the movement of the thermal front, and understandably, at any given time the higher the permeability of the rock matrix, the more the movement of the thermal front in the fracture will be retarded. The results in Figure 66 also indicate that if the permeability ratio k_D is greater than 10^4 the effect of the convective heat transfer is negligible. However, one must bear in mind that these results are only valid for the set of parameters listed in Table 7, although they are expressed in a

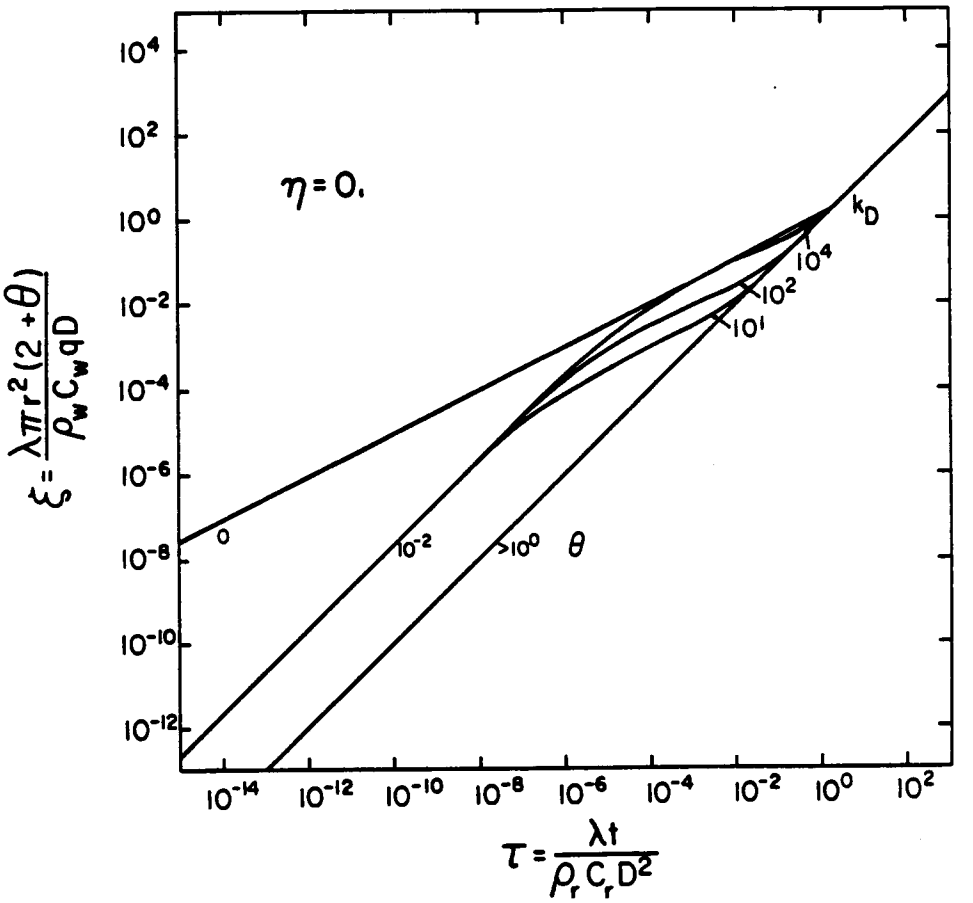

Figure 66. Effect of permeable rock matrix on the advancement of the thermal front along the fracture. [XBL 815-2984]

Table 7. Parameters and grid spacing used in the nonisothermal permeable rock study.

Parameters	Fracture Fluid	Fracture Rock
Thermal conductivity, λ(J/m·s·°C)	1.0	2.0
Density, ρ(kg/m^3)	1000.0	2650.0
Specific heat, C(J/kg·°C)	4200.0	1000.0
Porosity, ϕ (-)	1.0	.01
Permeability k(m^2)	1×10^{-9}	$1 \times 10^{-9} - 1 \times 10^{-16}$
Compressibility C(Pa^{-1})	5×10^{-10}	5×10^{-10}
Fracture aperture b	10^{-4} m	
Fracture spacing 2D	0.02 m	
Flow rate q	1×10^{-2} m^3/s	
Mesh:		
(a) Radial spacing	5 x 0.02, 17 x 0.5, .3, 0.5, 0.7, 0.8. 1.0, 1.0, 1.5, 1.5, 2, 6, 15, 25, 35, 60, 90, 150, 250, 350 m, etc.	
(b) Vertical spacing	5×10^{-5}, 1×10^{-5}, 3×10^{-5}, 1×10^{-4}, 3×10^{-4}, 1×10^{-3}, 3×10^{-3}, 5.56×10^{-3} m.	

dimensionless form in Figure 66. For any arbitrary set of parameters independent calculations are required.

Convection Dominated Systems. The above results show that convection due to a permeable rock matrix can have considerable effect on thermal diffusion into the rock during injection. It is therefore of interest to examine the case where the heat transfer between the fracture and the rock matrix is dominated by convection. By neglecting conduction, one only needs to follow the fluid paths to find out where the heat is being transported.

In this study, the fracture model shown in Figure 67 was used. As before, this model is valid for any number of equally spaced fractures. The following assumptions were employed:

(1) The water is injected into the fracture at $r = 0$.

(2) The mass flow is steady, and all fluid and rock parameters are constant.

(3) In the fracture only radial flow is considered; in the rock matrix both radial and vertical flow are considered.

(4) A constant pressure boundary is located at $r = R_o$. Otherwise, the geometry of the problem is identical to the problem discussed in the analytical work.

(5) The fracture has a permeability k_f and the rock matrix has a permeability k_r in both r and z directions (no anisotropy).

Based on the model shown in Figure 67 and the above assumptions, mass balance on elements in the fracture and the rock matrix yields the following equations:

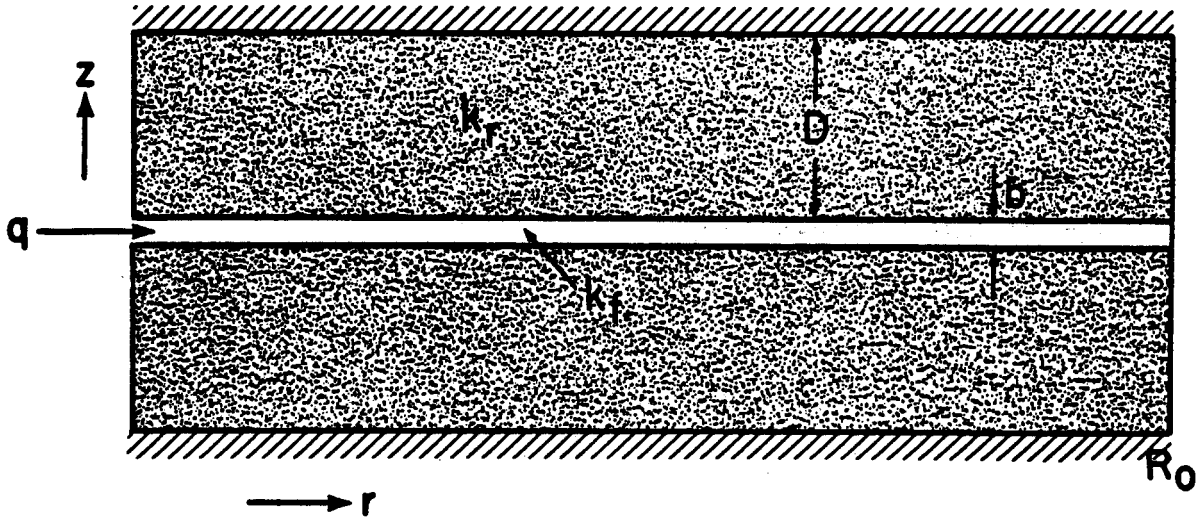

Figure 67. Schematic model of convection-dominated rock/fracture system. [XBL 815-2968]

Fracture:

$$\frac{\partial^2 P_f}{\partial r^2} + \frac{1}{r}\frac{\partial P_f}{\partial r} + \frac{2k_r}{bk_f}\frac{\partial P_r}{\partial z}\bigg|_{z=0} = 0. \tag{86}$$

Rock Matrix:

$$\frac{\partial^2 P_r}{\partial r^2} + \frac{1}{r}\frac{\partial P_r}{\partial r} + \frac{\partial^2 P_r}{\partial z^2} = 0. \tag{87}$$

The boundary conditions can be expressed mathematically as:

$$P_f(R_o) = 0, \tag{88a}$$

$$\lim_{r\to 0} r\frac{\partial P_f}{\partial r}\bigg|_{r=0} = \frac{q\mu}{2\pi k_f b} \tag{88b}$$

$$P_f(r) = P_r(r,0) \tag{88c}$$

$$\frac{\partial P_r}{\partial r}\bigg|_{r=0} = 0 \tag{88d}$$

$$\frac{\partial P_r}{\partial z}\bigg|_{z=D} = 0 \tag{88e}$$

$$P_r(R_o,z) = 0 \tag{88f}$$

Now the following dimensionless parameters are introduced:

$$r_D = \frac{r}{D} \tag{89a}$$

$$\eta = \frac{z}{D} \tag{89b}$$

$$R_D = \frac{r}{R_o} \tag{89c}$$

$$\omega = \frac{D}{b}\frac{k_r}{k_f} \tag{89d}$$

$$P_D = \frac{2\pi k_f b}{q\mu} P \tag{89e}$$

Substituting equations (89) into equations (86) and (87) yields:

Fracture:

$$\frac{\partial^2 P_{D_f}}{\partial r_D^2} + \frac{1}{r_D}\frac{\partial P_{D_f}}{\partial r_D} + 2\omega \left.\frac{\partial P_{D_r}}{\partial \eta}\right|_{\eta=0} = 0 \tag{90}$$

Rock Matrix:

$$\frac{\partial^2 P_{D_r}}{\partial r_D^2} + \frac{1}{r_D}\frac{\partial P_{D_r}}{\partial r_D} + \frac{\partial^2 P_{D_r}}{\partial \eta^2} = 0 \tag{91}$$

The boundary conditions given by equations (88) become:

$$P_{D_f}(R_D = 1) = 0 \tag{92a}$$

$$\lim_{r_D \to 0} r_D \frac{\partial P_{D_f}}{\partial r_D} = 1 \tag{92b}$$

$$P_{D_f}(r_D) = P_{D_r}(r_D, 0) \tag{92c}$$

$$\left.\frac{\partial P_{D_r}}{\partial r_D}\right|_{r_D=0} = 0 \tag{92d}$$

$$\left.\frac{\partial P_{D_r}}{\partial \eta}\right|_{\eta=1} = 0 \tag{92e}$$

$$P_{D_r}(R_D = 1, \eta) = 0 \tag{92f}$$

The above equations were solved numerically using the computer code PT in its isothermal mode. The mesh used is shown in Figure 68. The main

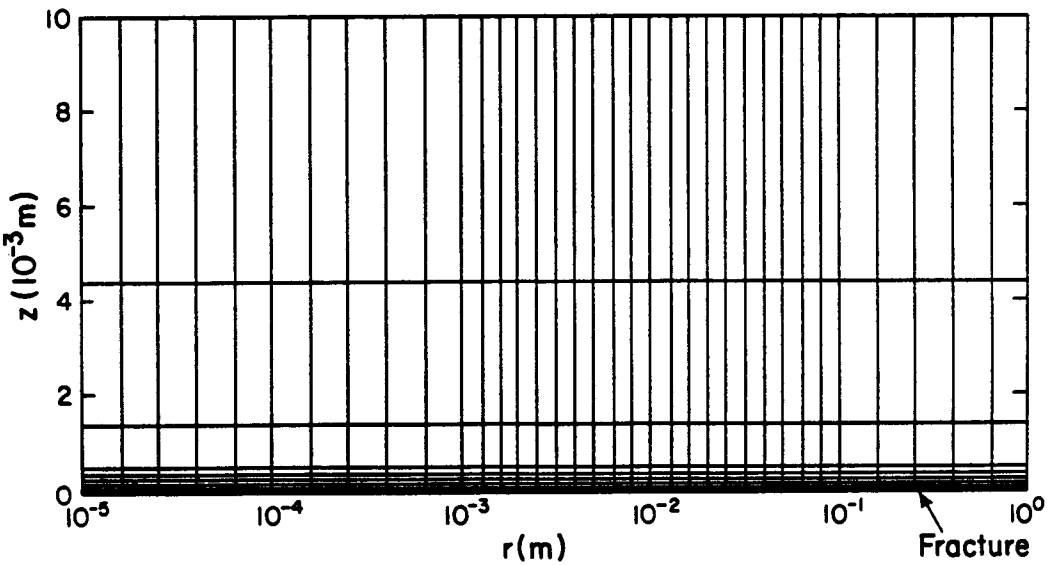

Figure 68. Mesh used in the study of convection-dominated systems.
[XBL 815-2969]

characteristics of the mesh are that it is logarithmically spaced both radially and vertically, and the nodal points are located at the log-mean center of the nodes. This type of grid setting has proven to be most accurate for diffusive-type problems. The grid was tested by running the Theis problem [Theis, 1935] with a constant pressure boundary (the solution is given by Witherspoon et al., 1967) and the results were within 1% of the analytical solution.

The pressure distributions along the dimensionless radial coordinate r_D are shown in Figures 69-71 for $\omega < .01$, $\omega = 1$, and $\omega > 100$, respectively. In all cases the distance to the constant pressure boundary R_o was very large. This parameter has no significant effects on the results if it is specified large enough so as not to affect the fluid flow near the well. The parameter $P_o\ (1 + 2\omega)$ was used in the figures because the curves converge at large dimensionless radii.

The curves in Figures 69-71 show a number of interesting characteristics. First, in all cases the curves converged at approximately $r_D = 1.0$. This indicates that at radial distances from the well greater than that corresponding to $r_D = 1$ no vertical pressure gradient exists and consequently, no flow between the fracture and the rock matrix takes place. Figures 69-71 also show that close to the well (r_D is small) there is no radial (horizontal) pressure gradient in the rock matrix (this is a consequence of equation 92d). In explaining these characteristics, it is helpful to consider the fluid flow in the system. Figure 72 shows the dimensionless flow along the fracture with q_{HD}, defined as:

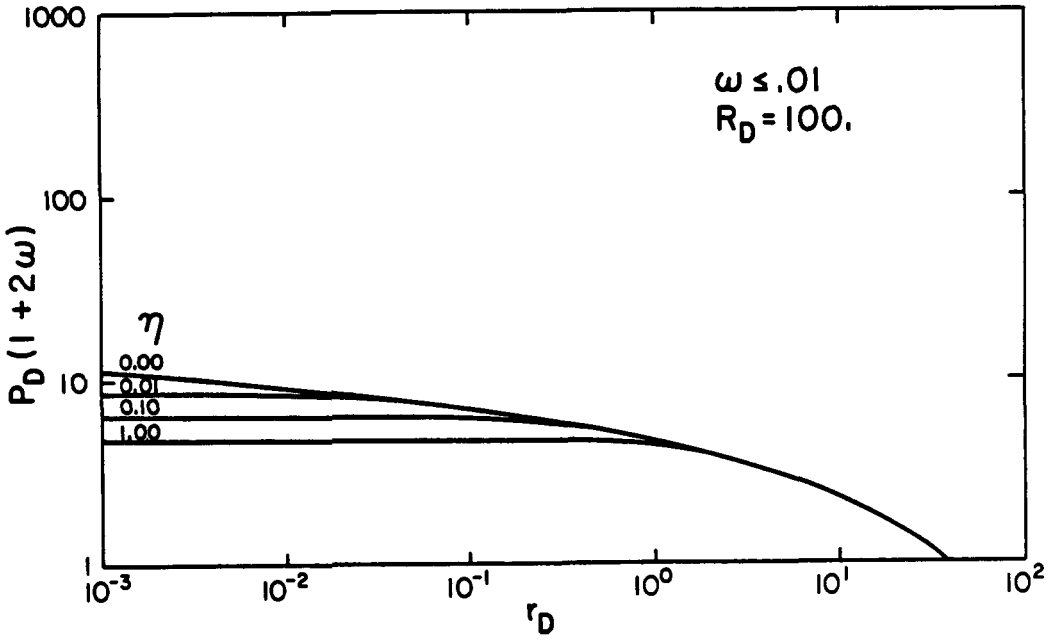

Figure 69. Pressure distribution along the dimensionless radial coordinate r_D for $\omega \leq 0.01$. [XBL 815-2978]

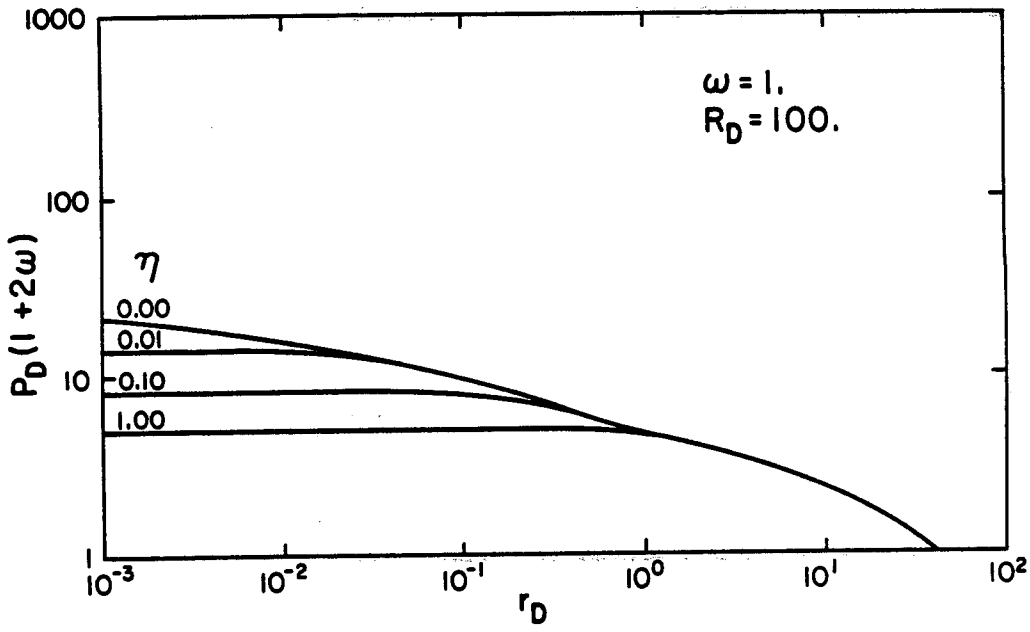

Figure 70. Pressure distribution along the dimensionless coordinate r_D for $\omega = 1$. [XBL 815-2979]

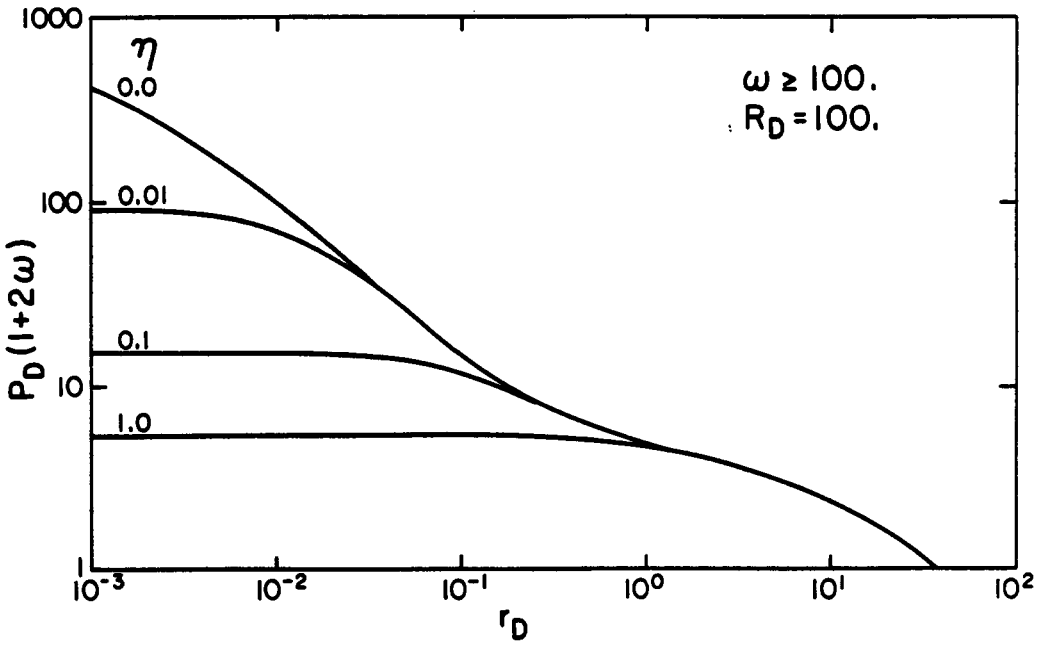

Figure 71. Pressure distribution along the dimensionless radial coordinate r_D for $\omega > 100$. [XBL 815-2980]

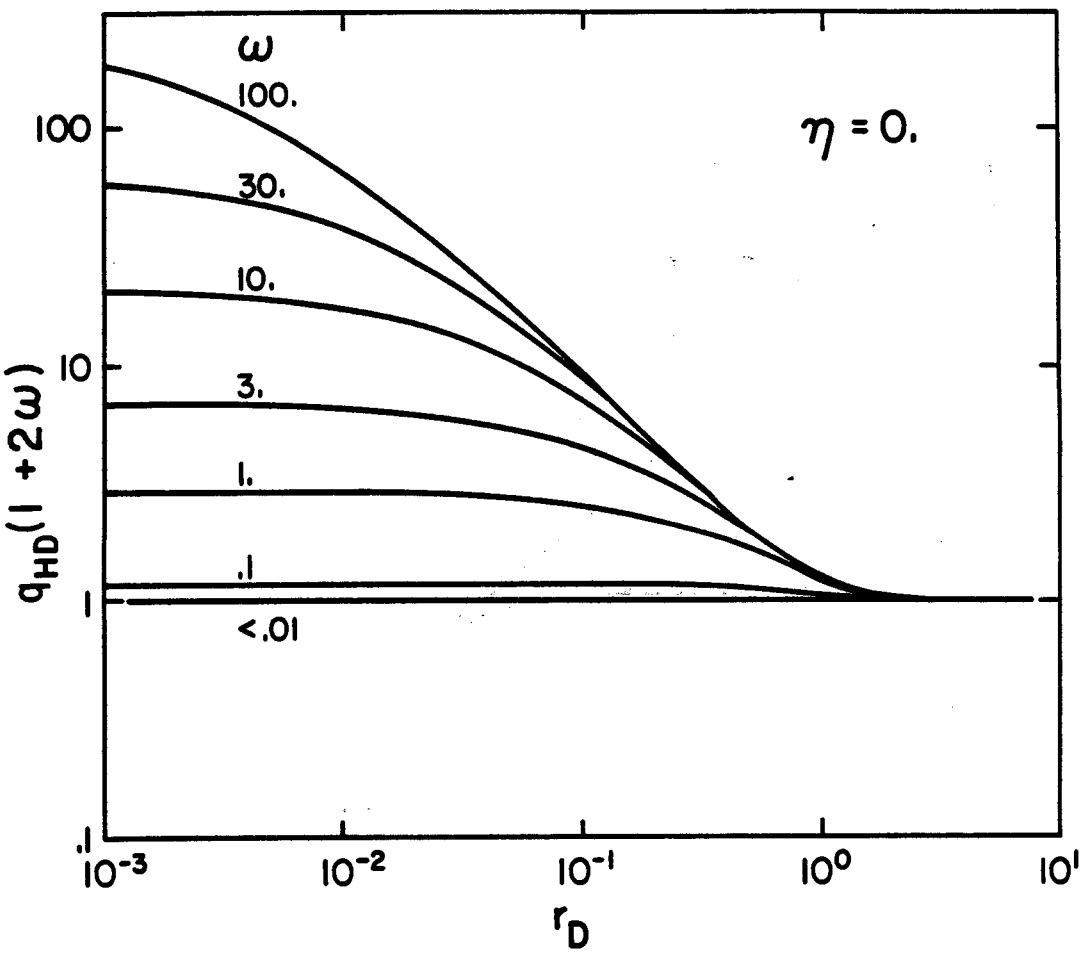

Figure 72. Dimensionless fluid flow along the fracture q_{HD}.
[XBL 815-2981]

$$q_{HD} = \frac{q_{FH}(r)}{q} \tag{93}$$

where $q_{FH}(r)$ is the flow along the fracture, and q is the total flow. In this plot all of the curves also converge at $r_D \sim 1.0$ to a single curve that can be represented by the equation:

$$q_{HD}(1 + 2\omega) = 1. \tag{94}$$

Expanding equation (93) by using Darcy's law and rearranging, yields:

$$q_{HD} = \frac{-\frac{k_f}{\mu} 2\pi rb \left(\frac{\partial P}{\partial r}\right)_f}{-\frac{k_f}{\mu} 2\pi rb \left(\frac{\partial P}{\partial r}\right)_f - \frac{k_r}{\mu} 4\pi rD \left(\frac{\partial P}{\partial r}\right)_r} = \frac{1}{1 + 2\omega} . \tag{95}$$

It is obvious that equation (95) is satisfied only when:

$$\left(\frac{\partial P}{\partial r}\right)_f = \left(\frac{\partial P}{\partial r}\right)_r , \tag{96}$$

which is exactly the behavior shown in Figures 69-71. In other words, the flow from the fracture to the rock matrix takes place close to the well ($r_D < 1.0$); further away the flows in the fracture and the rock are governed only by their transmissivities ($k_f b$ and $k_r D$).

The data plotted in Figure 72 also shows that very close to the well the flow in the fracture is constant and equal to the injection rate. Although the fluid flow from the fracture to the rock matrix per unit area is largest close to the well, the surface area there is small and consequently the total flow is small. The cumulative flow from the fracture to the rock matrix is plotted in Figure 73. Note that the horizontal axis is now defined as $r_D(1 + \omega)$. In Figure 73, there are two limiting curves

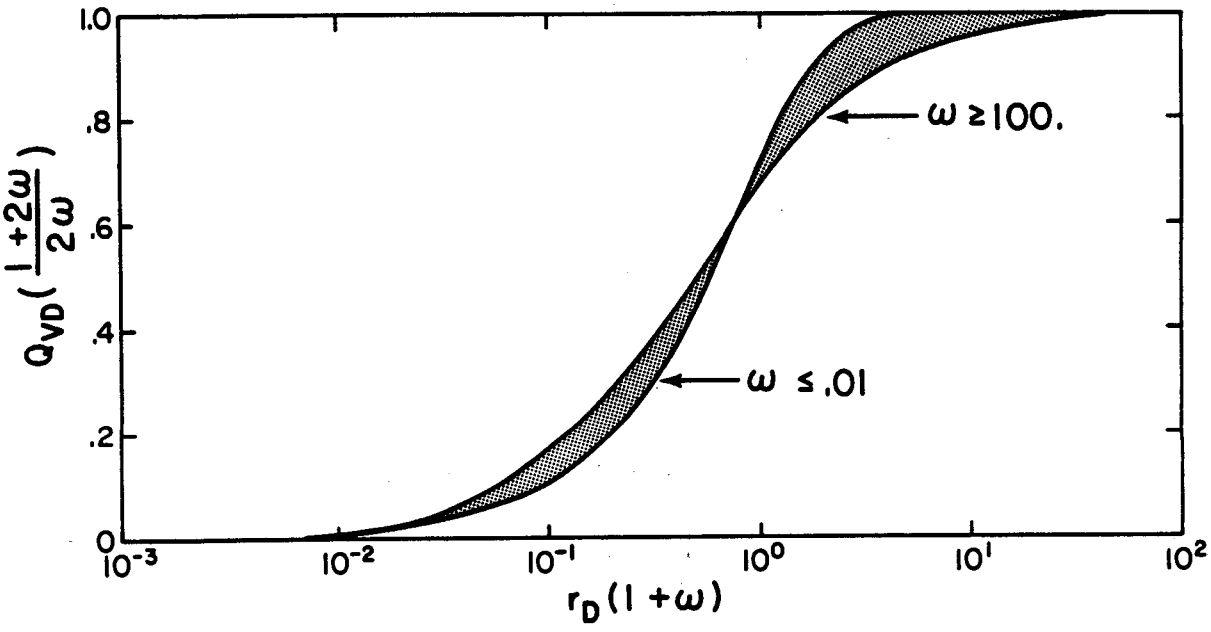

Figure 73. Cumulative flow from fracture to rock matrix. [XBL 815-2982]

representing high and low values of ω or equivalently high and low rock transmissivity. The figure shows that most of the flow between the fracture and the rock matrix takes place over the interval

$$10^{-2} < r_D(1 + \omega) < 10 \tag{97}$$

The scaling of the dimensionless radial coordinate with the dimensionless parameter ω, is due to the fact that the higher the rock permeability, the closer to the well where significant vertical flow will occur.

The implications for the cold-water injection problem are quite obvious. Figure 72 shows that all of the fluid flow from the fracture to the rock matrix will take place within the dimensionless distance $r_D = 1$ from the well. This indicates that if conductive heat transfer is negligible, all of the heat exchange from the fracture to the rock matrix will occur within $r_D = 1$ from the well. Therefore, in cases where the rock-matrix permeability is not negligible, this can be used as a constraint on the basic type curves shown in Figure 50. This will be illustrated in a numerical example in the following section. It should, however, be emphasized that this constraint can only be used in cases where $\omega > 10.0$, since ω represents the ratio of the convective heat flows in the rock and in the fracture. For example, if ω is 1.0, only 50% of the injected fluid will enter the rock matrix and consequently only 50% of the energy will enter the rock matrix. The remaining 50% will be contained in the fluid flowing along the fracture.

Application to Field Examples

In many geothermal fields the major fluid conduits in volcanic rocks are the contacts between subsequent lava layers [Fridleifsson, 1975; Newcomb et al., 1972; O'Brien et al., 1981; Benson et al., 1981]. These contacts may extend over a large area and behave hydrologically as horizontal fractures of large areal extent. For example, consider a 1000 m-thick geothermal reservoir consisting of six rather impermeable layers with the contact points between the layers being the principal fluid conduits. The number of high-permeability contact zones is not precisely known but a spinner survey indicates the presence of two to five major zones. An abandoned production well is located 250 m away from the nearest producer. If it is used as an injection well, the field developer is interested in knowing when the injected water will break through at the production well. The fluid and reservoir data needed for calculations are shown in Table 8. Using the parameters in Table 8 and the type curves in Figure 50, the curves in Figure 74 were developed. To account for the effect of the production well on the velocity field, the injection rate was doubled before the data shown in Figure 74 were calculated. Now using a well spacing of 250 m, the thermal front will reach the production well in 13 and 65 years for two and five fractures, respectively. Since the planned life of the project in question is assumed to be 15 years and since the approach to the problem is conservative (no rock permeability, etc.), the developer is reasonably certain that premature thermal breakthrough will not occur.

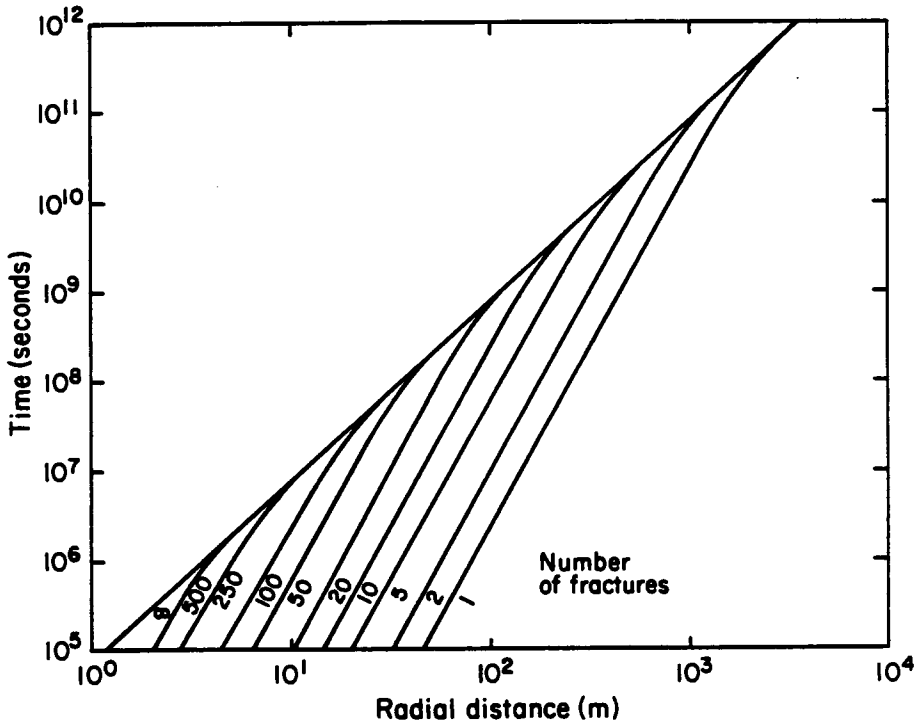

Figure 74. Location of the thermal front in the fractures versus time for different fracture spacing. [XBL 815-2983]

Table 8. Parameters used in multifractured reservoir.

Flowrate, q,	(kg/s)	10.0
Thermal conductivity, λ,	(J/m•s•°C)	2.0
Fluid density, ρ_w,	(kg/m^3)	1000
Fluid specific heat, c_w,	(J/kg•°C)	4000
Rock density, ρ_r,	(kg/m^3)	2500
Rock specific heat, c_r,	(J/kg•°C)	1000
Fracture porosity, ϕ,	(-)	1.0
Fracture aperture, b,	(m)	1×10^{-4}

As another field example, consider a simplified reservoir model of the Cerro Prieto field reported by Tsang et al. (1979) and shown in Figure 75. In this case, the aquifers were assumed to be the major fluid conduits and the shale breaks the low permeability layers. The injection well was assumed to fully penetrate both of the aquifers and to supply the same quantity of cold water to each. Neglecting gravity, or assuming strong anisotropy, fixing the injection rate as 20 kg/s, and using the same rock and fluid thermal properties as are shown in Table 8, the advancement of the thermal front in the aquifers with time was calculated. In this case, $\theta = 4.0$. In order to calculate when all of the energy from the shale layers can be extracted, equation (79) was used to yield

$$t \approx 400 \text{ years.} \tag{98}$$

This is the time when uniform energy sweep occurred. The radial distance to the point of uniform sweep was calculated using equation (80) as

$$r = 1635 \text{ m.} \tag{99}$$

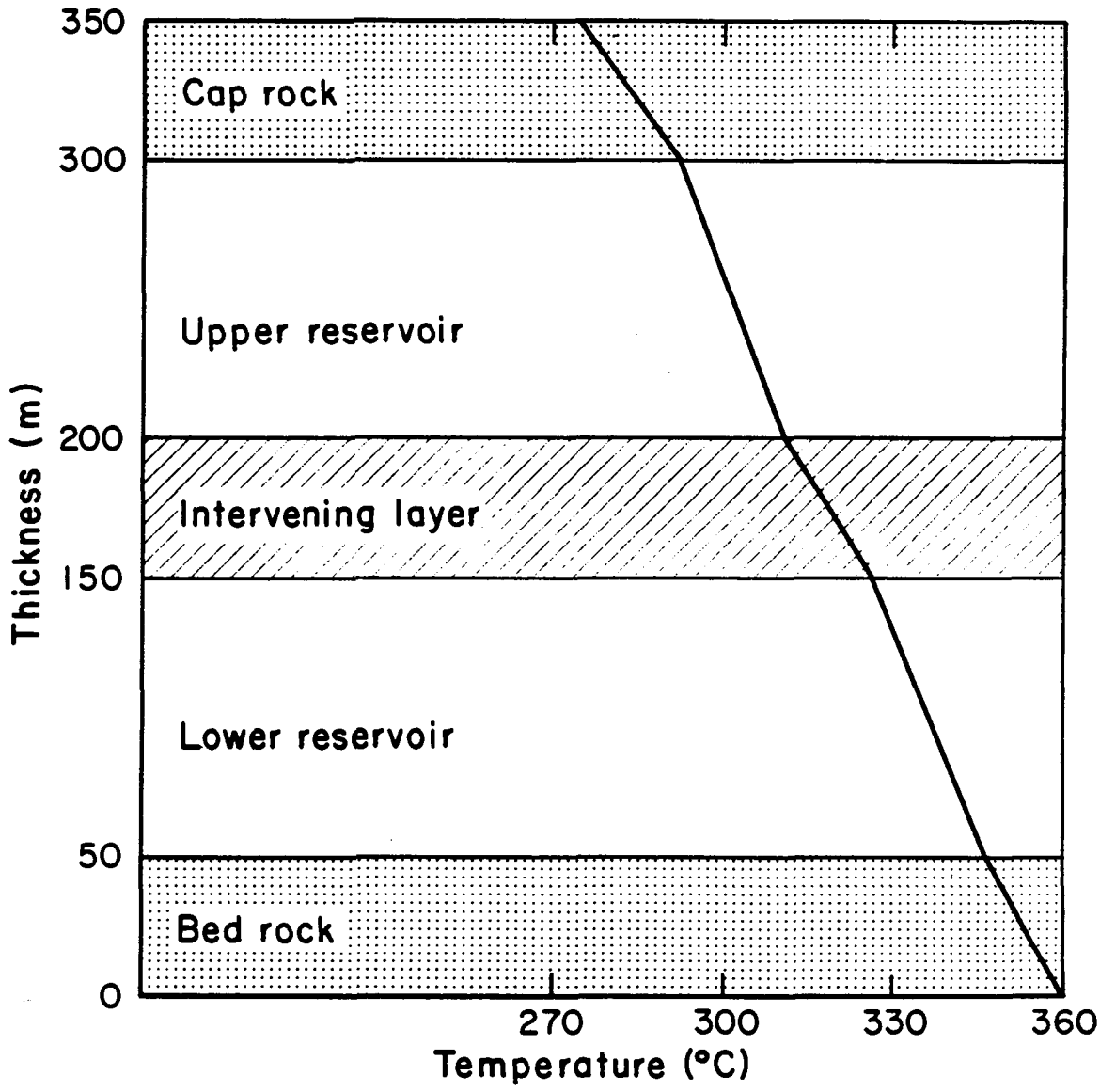

Figure 75. Geological model of the Cerro Prieto geothermal field (after Tsang et al., 1979). [XBL 803-6829]

If the geothermal project is planned for 30 years, the cold water front will only have advanced 240 m away from the injection well.

Now let us consider the case of two horizontal fractures in the aquifers in Figure 75. In this case, D = 50 m, and if the fracture aperture is 10^{-4} m, a fracture permeability of 8.33×10^{-10} m^2 can be calculated based on the cubic law [Witherspoon et al., 1980]:

$$k_f = \frac{b^2}{12} . \tag{100}$$

The permeability of the Cerro Prieto aquifers has been reported as approximately 6.5×10^{-14} m^2 [Tsang et al., 1979] and therefore $\omega \simeq 40$. Recognizing that earlier analysis of the permeable rock matrix can be used, providing $\omega > 10$, a critical radius of 50 m is calculated. Since the fractures will not affect the thermal front 50 m away from the well, our earlier calculation of 240 m in thirty years is valid in spite of the presence of the fractures in the reservoir.

Conclusions

In this study, the thermal behavior during cold-water injection into fractured geothermal reservoirs has been considered. The model used consisted of an injection well fully penetrating a geothermal reservoir with horizontal fractures. The approach employed in the study was twofold; first, a rather simple mathematical model was developed and solved analytically; second, numerical calculations were carried out in order to investigate the importance of the assumptions employed in the analytical study and to extend the applicability of the results.

The results from the analytical work were given in the form of type curves that can be used to design the locations of the injection wells with reference to the production wells and the injection rate. The type curves can also be used to predict the time of thermal breakthrough in existing injection/production systems. A number of curves showing the thermal contamination in the impermeable rock matrix (or adjacent layers) may be useful in calculating the recoverable energy in a reservoir system for given well locations and rates.

In the numerical study, the importance of the more critical assumptions employed in the analytical work were studied. The assumption of steady-state mass flow was found to be reasonable whereas the assumption of no-horizontal conduction in the rock matrix (adjacent layer) gave erroneous temperature distributions at very late times. A method of approximating the temperature distribution at late times was suggested.

Extension of the analytical work to include permeable rocks was studied numerically. A mathematical model was developed and key dimensionless parameters identified. The primary assumption used in this part of the work is that the conductive heat transfer is negligible compared to the convective heat transfer (high Peclet number). This enables one to consider only the stream lines under steady-state conditions. The problem was solved numerically using the computer code PT in its isothermal mode. The results obtained indicate that at radial distances from the injection well larger than the thickness of the rock matrix, uniform

energy-sweep conditions will develop. In certain cases ($\omega > 10$) this result can be used as a constraint on estimates obtained with the developed type curves.

Finally, two simple numerical examples using a hypothetical doublet and the Cerro Prieto geological model were given. In the doublet case, a reservoir with 2 to 5 fractures was considered and breakthrough times of 13 and 65 years, respectively, were calculated. Using typical injection rate and the Cerro Prieto geological model, our calculations indicated that the thermal front would have advanced only 240 m away from the injection well after 30 years of injection. It was further illustrated that this estimate was independent of fractures in the reservoir.

FAULT-CHARGED GEOTHERMAL RESERVOIRS

One of the most important tasks in geothermal reservoir engineering is to predict the useful lifetime of the resource for a given exploitation scheme. In order to make these predictions, reliable estimates must be available of the amount of hot water in place, the rate at which it can be extracted (transmissivity of the reservoir), and the rate and extent of hot-water recharge into the system. The first two estimates can often be readily obtained from simple volumetric calculations and well-test data, respectively; reliable estimates of the recharge are much more difficult to evaluate. In this section a simple model for calculating the rate of recharge into a fault-charged hydrothermal reservoir is developed.

All geothermal reservoirs are controlled to some extent by faults and fractures; in some, however, a single fault or the intersection of two or more major faults is believed to act as the main conduit for recharge. High-temperature examples of such fault-charged systems are Roosevelt Hot Springs, Utah, and East Mesa, California. Low to moderate-temperature systems of this type are Klamath Falls and Vale, in Oregon, and Susanville, California. In this section the model developed for evaluating such systems is first described and then applied to the Susanville, California, geothermal resource, a shallow, low-temperature hydrothermal system.

In contrast to the temperature logs from most geothermal wells, those from wells in fault-charged geothermal reservoirs often display anomalous behavior. One such profile, shown in Figure 76, was obtained from a well in the "steamer district" of the Klamath Falls KGRA (O'Brien et al., 1981). The profile shows the typical linear characteristics associated with conductive heat transfer in the top 200 ft, then a typical convective type profile down to 250 ft. At a depth of 250 ft the profile displays a definite reversal, and below this level the temperature profile reflects downflow in the well. One possible explanation for this atypical behavior is that a fault recharges an aquifer located at a depth of 200-250 ft below the ground surface. The relatively hot water travels up the fault until it intersects the permeable aquifer; it is then transported laterally in the aquifer. As the hot water moves through the aquifer, heat is lost mainly via conduction to the overlying and underlying strata. Variations in the temperature profiles between wells at different distances from the recharging fault can be used to estimate the recharge rate.

Various mathematical models applied to fault-charged hydrothermal systems are cited in the literature. Kilty et al. (1978) and Goyal and Kassoy (1981) developed two-dimensional models (semi-analytic solutions) of the East Mesa, California, field and the Monroe, Utah, hydrothermal system, respectively. Sorey (1975) and Riney et al. (1979) applied numerical models to the Long Valley and East Mesa, California, systems, respectively.

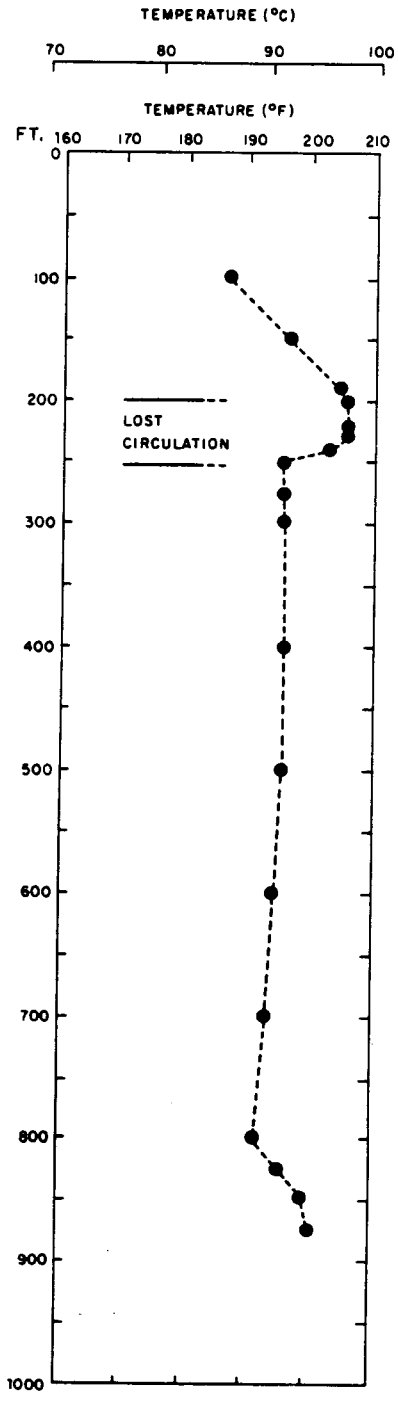

Figure 76. Temperature profile from a well at Klamath Falls, Oregon (after O'Brien et al., 1981). [XBL 8011-2979]

In contrast to these models, we will not consider vertical temperature variations within the aquifer, but accurately will model the transient heat losses to the caprock and bedrock. The model may therefore be quite useful in analyzing relatively young fault-charged thin hydrothermal systems, where transient heat losses are important, as well as in theoretical studies of the evolution of such systems.

Mathematical Model

Figure 77 shows the reservoir system on which the mathematical model is based. Hot water flows up the fault and feeds a shallow aquifer. The fault is shown by broken lines to illustrate that no heat losses are considered when the fluid is flowing up the fault. Initially the temperature in the system is linear with depth (normal geothermal gradient) as controlled by the constant-temperature boundaries at $z = D$ (ground surface) and $z = -H$. At time $t = 0$ hot water starts to flow into the reservoir at a temperature T_f. The primary assumptions employed are listed below:

(1) The mass flow rate is steady in the aquifer, horizontal conduction is neglected, and temperature is uniform in the vertical direction (thin aquifer). Thermal equilibrium between the fluid and the solids is instantaneous at each location.

(2) The rock matrix above and below the aquifer is impermeable, and horizontal conduction in the rock matrix is neglected.

(3) The energy resistance at the contact between the aquifer and the rock matrix is negligible (infinite heat transfer coefficient).

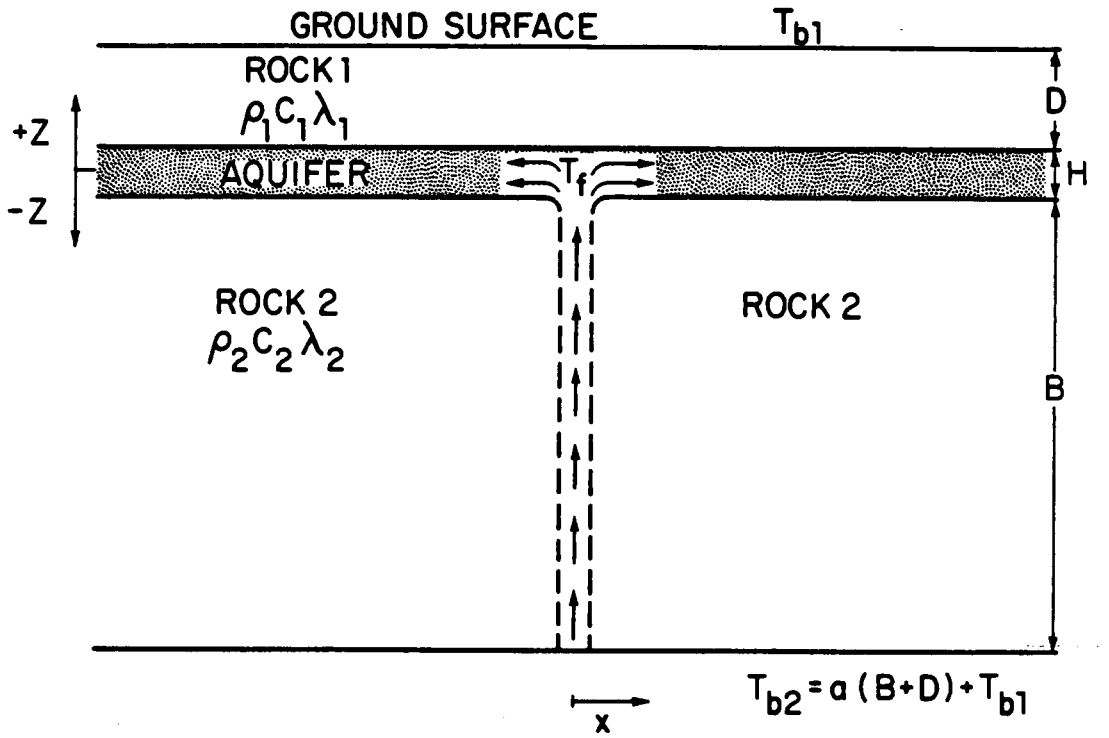

Figure 77. The mathematical model considered for fault problem.
[XBL 816-3178]

(4) The thermal properties of the formations above and below the aquifer may be different, but all thermal parameters for the liquid and the rocks are constant.

The differential equation governing the temperature in the aquifer at any time t can readily be derived by performing an energy balance on a control volume in the aquifer:

$$z = 0: \quad \frac{\lambda_1}{H} \frac{\partial T_1}{\partial z}\bigg|_{z=0} - \frac{\lambda_2}{H} \frac{\partial T_2}{\partial z}\bigg|_{z=0} - \frac{\rho_w c_w q}{H} \frac{\partial T_a}{\partial x} - \rho_a c_a \frac{\partial T_a}{\partial t} = 0. \tag{101}$$

In the caprock and the bedrock, the one-dimensional heat-conduction equation controls the temperature:

$$z > 0: \quad \lambda_1 \frac{\partial^2 T_1}{\partial z^2} = \rho_1 c_1 \frac{\partial T_1}{\partial t}, \tag{102}$$

$$z < 0: \quad \lambda_2 \frac{\partial^2 T_2}{\partial z^2} = \rho_2 c_2 \frac{\partial T_2}{\partial t}. \tag{103}$$

The initial conditions are:

$$T_a(x,0) = T_1(x,z,0) = T_2(x,z,0) = T_{b1} - a(z - D). \tag{104}$$

The boundary conditions are:

$$T_a(0,t) = T_f \qquad t > 0, \tag{105a}$$

$$T_a(x,t) = T_1(x,0,t) = T_2(x,0,t), \tag{105b}$$

$$T_1(x,D,t) = T_{b1}, \tag{105c}$$

$$T_2(x,-B,t) = T_{b2} = T_{b1} + a(B + D). \tag{105d}$$

The following dimensionless parameters are introduced:

$$\xi_1 = \frac{\lambda_1 x}{\rho_w c_w q D} \tag{106a}$$

$$\tau_1 = \frac{\lambda_1 t}{\rho_1 c_1 D^2}, \tag{106b}$$

$$\theta_1 = \frac{H}{D}\frac{\rho_a c_a}{\rho_1 c_1}, \tag{106c}$$

$$\eta = \frac{z}{D}, \tag{106d}$$

$$\gamma = \frac{\rho_2 c_2}{\rho_1 c_1}, \tag{106e}$$

$$\kappa = \frac{\lambda_2}{\lambda_1}, \tag{106f}$$

$$T_D = \frac{T - T_{b1}}{T_f - T_{b1}}, \tag{106g}$$

$$T_g = \frac{aD}{T_f - T_{b1}}, \tag{106h}$$

$$\sigma = \frac{B}{D}. \tag{106i}$$

Substitution of equations (105a)-(105i) into equations 101-103 yields:

$$\eta = 0: \quad \left.\frac{\partial T_{D_1}}{\partial \eta}\right|_{\eta=0} - \kappa \left.\frac{\partial T_{D_2}}{\partial \eta}\right|_{\eta=0} - \frac{\partial T_{D_a}}{\partial \xi_1} - \theta_1 \frac{\partial T_{D_a}}{\partial \xi_1} = 0, \tag{107}$$

$$\eta > 0: \quad \frac{\partial^2 T_{D_1}}{\partial \eta^2} = \frac{\partial T_{D_1}}{\partial \tau_1}, \tag{108}$$

$$\eta < 0: \qquad \frac{\partial^2 T_{D_2}}{\partial \eta^2} = \frac{\gamma}{\kappa} \frac{\partial T_{D_2}}{\partial \tau_1} . \tag{109}$$

The initial conditions become:

$$T_{D_a}(\xi_1,0) = T_{D_1}(\xi_1,\eta,0) = T_{D_2}(\xi_1,\eta,0) = -T_g(\eta - 1). \tag{110}$$

The boundary conditions become:

$$T_{D_a}(0,\tau_1) = 1, \ \tau_1 > 0, \tag{111a}$$

$$T_{D_a}(\xi_1,\tau_1) = T_{D_1}(\xi_1,0,\tau_1) = T_{D_2}(\xi_1,0,\tau_1), \tag{111b}$$

$$T_{D_1}(\xi_1,1,\tau_1) = 0, \tag{111c}$$

$$T_{D_2}(\xi_1,-\sigma,\tau_1) = T_g(\eta + 1). \tag{111d}$$

The solution of equations (107)-(111) can be obtained in the Laplace domain (see appendix D) as the following set:

$$\eta = 0: \qquad u = \frac{1}{p}[1 - T_g] \exp - \left[\theta_1 p + \frac{\sqrt{p}}{\tanh\sqrt{p}} + \frac{\kappa\sqrt{\frac{\gamma}{\kappa} p}}{\tanh\sqrt{\frac{\gamma}{\kappa} p}}\right]\xi_1 + \frac{T_g}{p} . \tag{112}$$

$$\eta > 0: \qquad v = \left[u - \frac{T_g}{p}\right]\cosh\sqrt{p}\eta - \frac{\left[u - \frac{T_g}{p}\right]}{\tanh\sqrt{p}} \sinh\sqrt{p}\eta - \frac{T_g}{p}(\eta - 1). \tag{113}$$

$$\eta < 0: \qquad w = \left[u - \frac{T_g}{p}\right]\cosh\sqrt{\frac{\gamma}{\kappa} p}\eta + \frac{\left[u - \frac{T_g}{p}\right]}{\tanh\sqrt{\frac{\gamma p}{\kappa}}\,\sigma} \sinh\sqrt{\frac{\gamma p}{\kappa}}\eta - \frac{T_g}{p}(\eta - 1). \tag{114}$$

In equations (112)-(114), u, v, and w represent the temperatures in the Laplace domain of the aquifer, the rock above the aquifer, and the rock below the aquifer, respectively.

As equations (112)-(114) cannot easily be inverted from the Laplace domain, the numerical scheme developed by Stehfest (1979) was used. The results are discussed below.

Evolution of fault-charged hydrothermal systems

The model has been employed to study the evolution of fault-charged hydrothermal systems. Figure 78 shows a plot of dimensionless temperature T_D versus depth at a given location for several different values of dimensionless time τ_1. The figure shows that initially ($\tau_1 = 0$) the system is in equilibrium with a linear geothermal gradient. At $\tau_1 = 0$ the hot water starts to flow into the permeable aquifer; in the early stages of development, only the aquifer is being heated. Later on, however, the conductive heat transfer between the aquifer and the adjacent rocks increases, causing the surrounding rock to be heated and the temperature in the aquifer to stabilize.

The temperature in the aquifer and the caprock reaches steady state at a dimensionless time τ, between 1 and 10. At this time the temperature in the rock formation below the aquifer is nowhere near a steady-state condition. The high value of $\sigma = 30$ shows that the constant-temperature boundary at the ground surface is much closer to the aquifer than the deep boundary and should therefore control the thermal response.

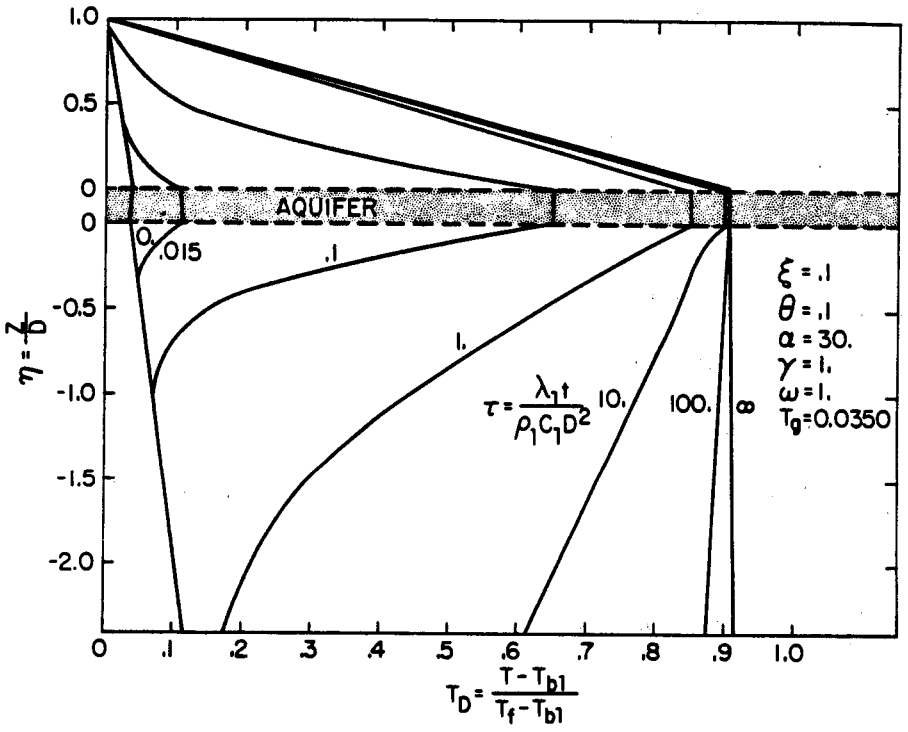

Figure 78. Evolution of a fault-charged hydrothermal system for $\xi_1 = 1.0$.
[XBL 816-3179]

In the example shown in Figure 78, the steady-state temperature of the aquifer at the location in question is approximately $T_D = 0.91$.

Similar development of the thermal field is observed at other locations away from the fault (different ξ_1). In Figure 79 the thermal evolution is shown at a location further away from the fault ($\xi_1 = 1.0$); all other parameters remain the same. In this case the steady state dimensionless temperature in the aquifer reaches a lower value and consequently the temperature gradient in the caprock is not as sharp. Similarly, closer to the fault ($\xi_1 < .1$) the aquifer will be fully heated to the temperature of the injected water ($T_D = 1.0$). In order to fully understand the behavior of the analytical solution (equations (112)-(114)), this discussion is divided into early time, intermediate time and late-time behavior.

Early-time behavior

At early times the solution for the temperature in the aquifer simplifies considerably, so that inversion into real space is possible (see Appendix D). The solution in real space is

$$T_{D_a} = [1 - T_g]\ U\ [\tau_1 - \theta_1 \xi_1] + T_g \tag{115}$$

where U denotes the unit function. Equation (115) shows that when the dimensionless time τ_1, is less than $\theta_1\ \xi_1$, the initial temperature T_g prevails. However, in the thermal region, when τ_1 is greater than $\theta_1\ \xi_1$, the aquifer temperature equals the temperature of the fault water. No temperature changes occur in the caprock and the bedrock at early times.

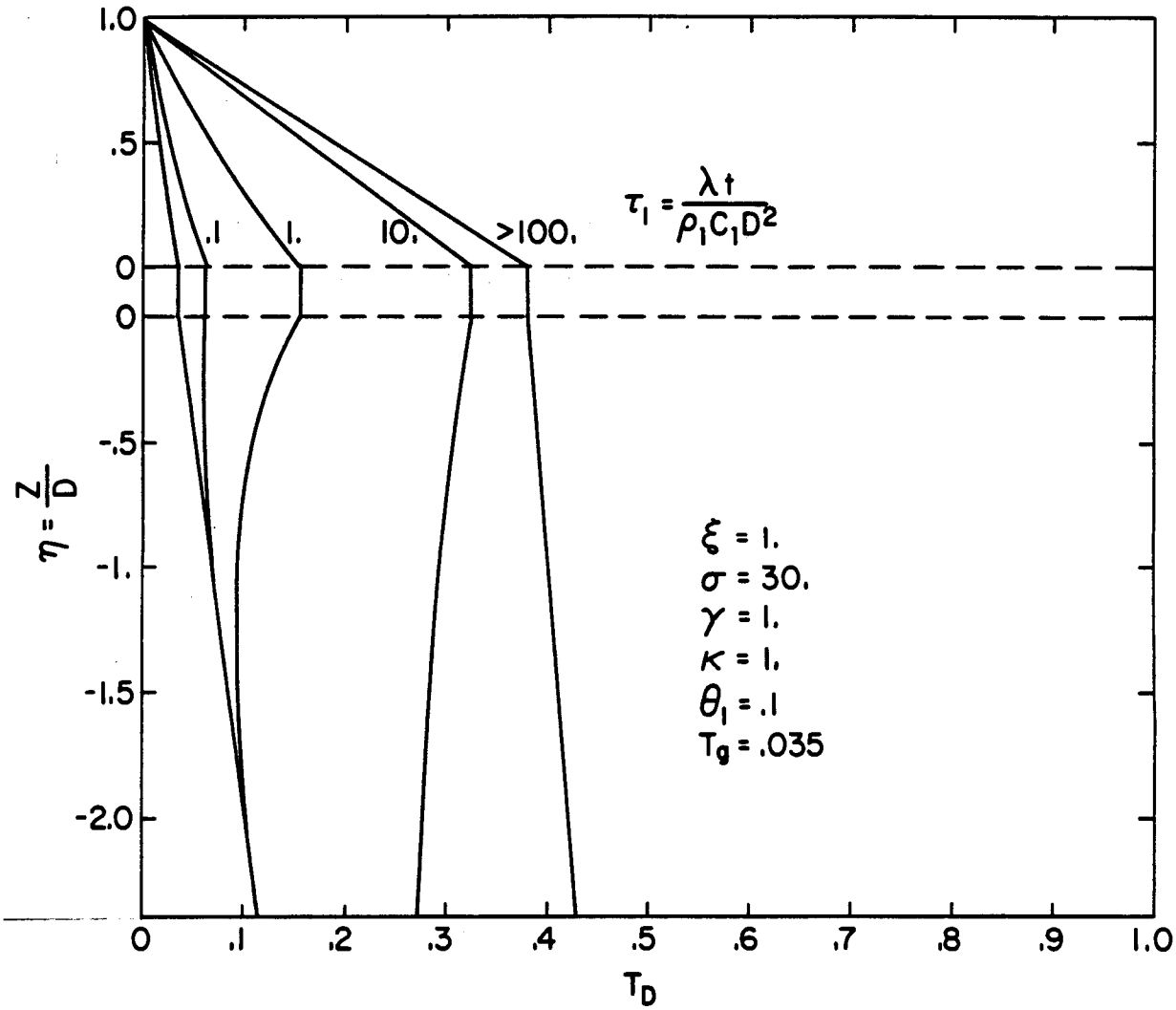

Figure 79. Evolution of a fault-charged hydrothermal system for ξ_1 = 1.0.
[XBL 819-11662]

Intermediate-time behavior

At intermediate times, before the boundary conditions at $z = D$ and $z = -(B + D)$ are felt, the present solution is identical to the Lauwerier (1955) solution except for the initial geothermal gradient and the different rock properties in the caprock and the bedrock. Thus, the Lauwerier solution is also a special case of the present solution. In order to check the validity of the present solution and the accuracy of the numerical inverter, this model was compared to the Lauwerier solution (Figure 80). For this comparison the geothermal gradient was neglected ($T_g = 0$) and the rock properties in the bedrock and the caprock were identical ($\gamma = 1.0$, $\kappa = 1.0$). As Figure 80 shows, a near-perfect match was obtained thereby verifying the accuracy of the present model and the numerical inverter. It should be noted, however, that the parameters associated with the Lauwerier solution in Figure 80 are as defined by Lauwerier (1955).

Late-time behavior

At late times the solutions for the temperatures in the Laplace domain (equations (112-114)) also simplify to the extent that inversion to real space is possible. In real space the solutions become (see Appendix D):

$$\eta = D: \quad T_{D_a} = [1 - T_g] \exp - \left[1 + \frac{\kappa}{\sigma}\right] \xi_1 + T_g \tag{116}$$

$$\eta > T_{D_1}: \quad T_{D_1} = [1 - T_g][1 - \eta] \exp - \left[1 + \frac{\kappa}{\sigma}\right] \xi_1 - T_g(\eta - 1) \tag{117}$$

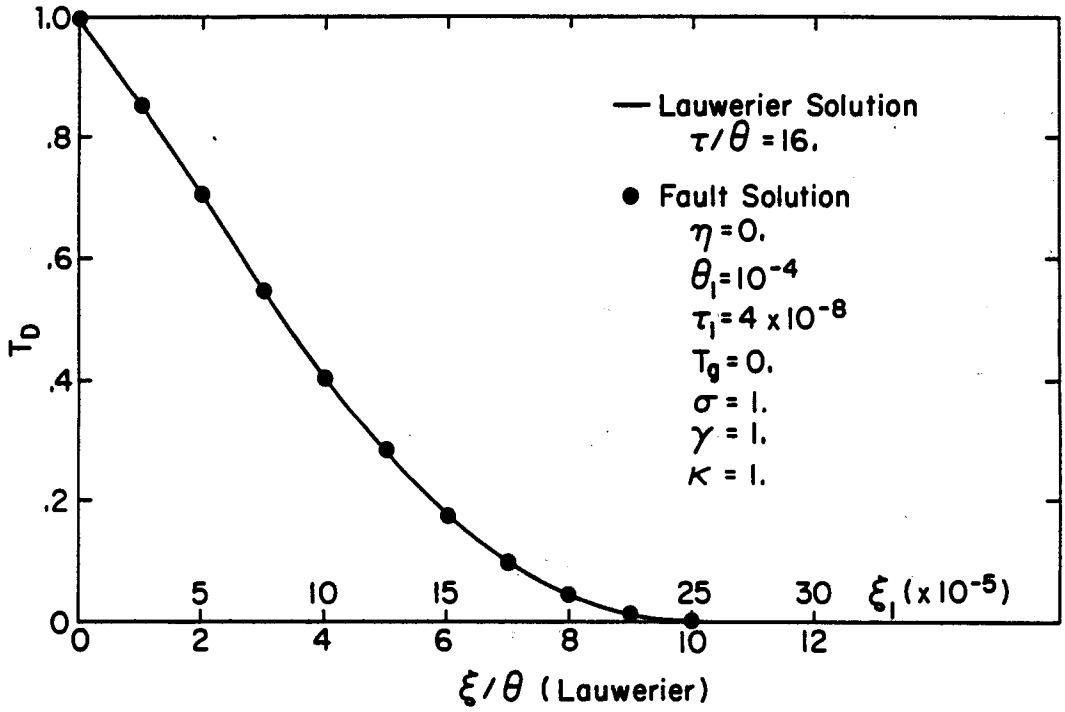

Figure 80. Comparison between the present solution and the Lauwerier solution. [XBL 819-11661]

$$\eta < T_{D_2}: \quad T_{D_2} = [1 - T_g] \left[1 + \frac{\eta}{\sigma}\right] \exp - \left[1 + \frac{\kappa}{\sigma}\right] \xi_1 - T_g(\eta - 1) \qquad (118)$$

Equations (116)-(118) show that the steady-state temperature profiles are independent of θ, as well as the heat capacities of the caprock and the bedrock γ. Further analysis of equations (116)-(118) is given below.

Evolution of thermal field in the aquifer

Figure 81 shows the evolution of the thermal field in the aquifer for $\theta_1 = .005$ and other parameters as specified in the figure. It shows that close to the fault (small ξ_1) the temperature rises almost immediately to the temperature of the recharging water. The figure also shows that a steady-state thermal field is reached shortly after dimensionless time τ_1, exceeds 1.0. Although the steady-state thermal field is independent of θ_1 (see equations (116-118)), the transient development of the thermal field is greatly affected by θ_1. This is illustrated in Figures 82-84. In general, the figures show that for any given dimensionless time, the smaller θ_1 is, the further away from the fault the thermal front has advanced. This is reasonable since θ_1 represents the heat capacity of the aquifer normalized to that of the caprock. Thus, the higher the value of θ_1 the greater the heat capacity of the aquifer and consequently the less portion of the aquifer can the recharged (hot) water heat up. Also, Figures 82-84 show that for higher values of θ_1, the location of the thermal front ($T_D = .50$) can be expressed by the simple relation,

$$\tau_1 = \theta_1 \xi_1 \qquad (119)$$

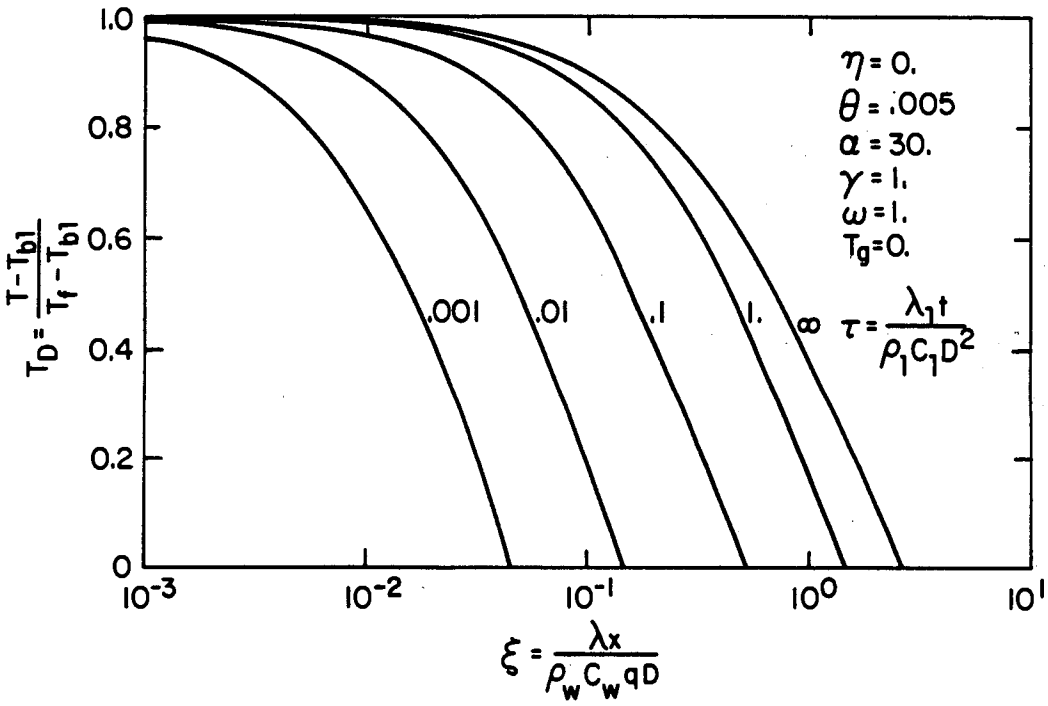

Figure 81. Evolution of the thermal field in the aquifer. [XBL 816-3180]

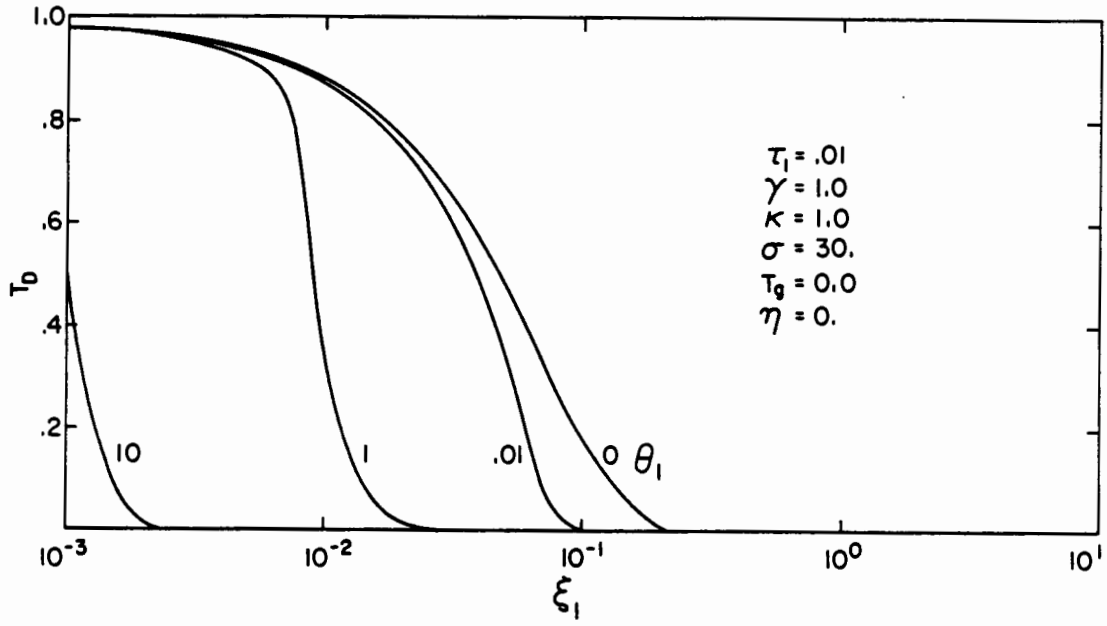

Figure 82. θ_1-dependence of the temperature profile along the aquifer for τ_1 = .01. [XBL 8110-11676]

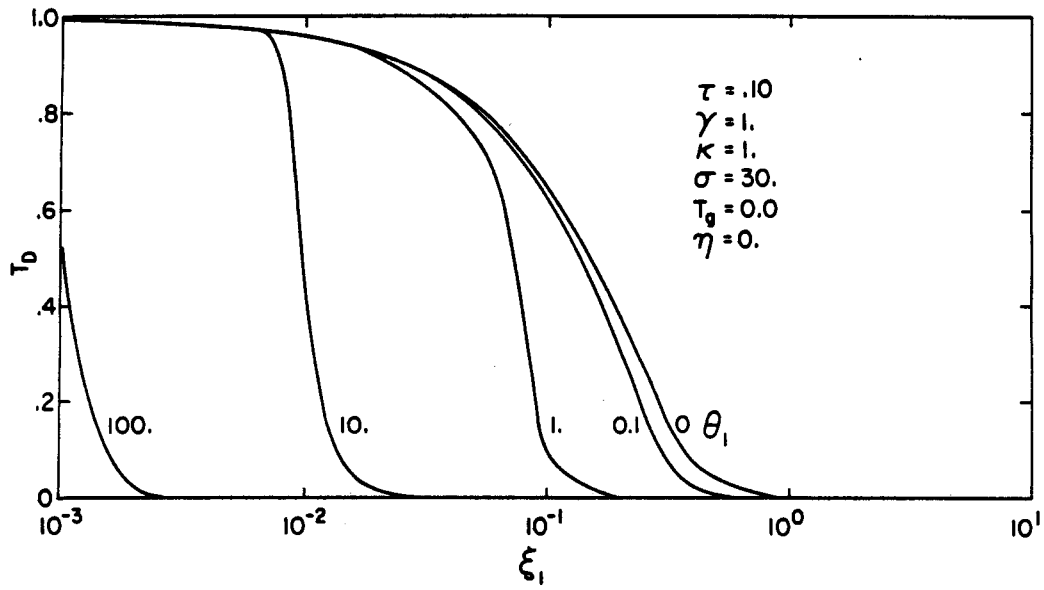

Figure 83. θ_1-dependence of the temperature profile along the aquifer for τ_1 = .10. [XBL 8110-11677]

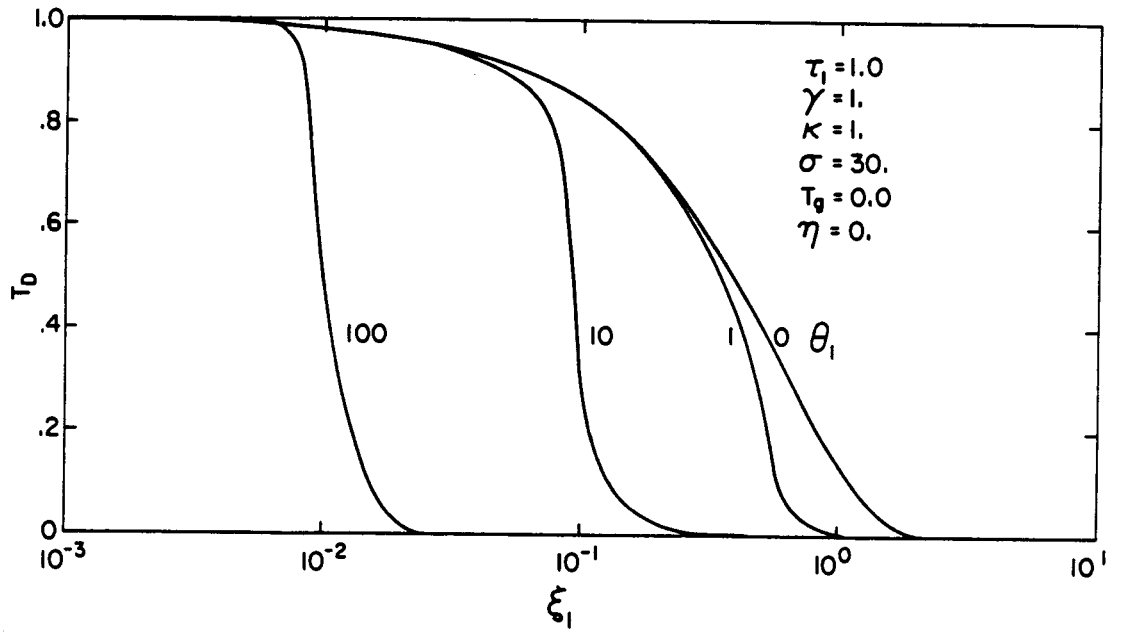

Figure 84. θ_1-dependence of the temperature profile along the aquifer for $\tau_1 = 1.0$. [XBL 8110-11678]

This has also been found earlier (see equation 68). Equation (119) does not hold for low values of θ_1 at the dimensionless times shown in Figures 82-84, since low values of θ_1 imply low aquifer heat capacity, and consequently significant heat conduction losses to the caprock and bedrock will occur at these dimensionless times.

Heat losses from the aquifer

Heat losses from the aquifer to the caprock and bedrock can be calculated at any given time by the Fourier law of heat conduction (see equation (83)). In terms of dimensionless parameters the Fourier law of heat conduction can be written as

$$Q_{D_t} = \frac{Q_D}{A\lambda_1(T_i - T_{b1})} = \left.\frac{\partial T_{D_1}}{\partial \eta}\right|_{\eta=0} + \left.\frac{\partial T_{D_2}}{\partial \eta}\right|_{\eta=0} \qquad (120)$$

where the first and the second terms on the right-hand side represent the heat losses to the caprock and the bedrock, respectively. Thus, Q_{D_t} represents the total heat loss to the caprock and the bedrock.

The heat losses from the aquifer to the caprock and bedrock for a given location away from the fault (ξ_1 = .10) are shown in Figure 85. The figure shows that at early times there are no heat losses to the caprock or the bedrock as the thermal front has not arrived. Later on, the heat losses increase to a maximum at $\tau_1 \simeq .10$, but after that decrease rapidly. At $\tau_1 \simeq 1.0$, the heat losses to the caprock stabilize but those to the bedrock continue to decrease and eventually become negative (i.e., heat flows from the bedrock into the aquifer) at very large times. This

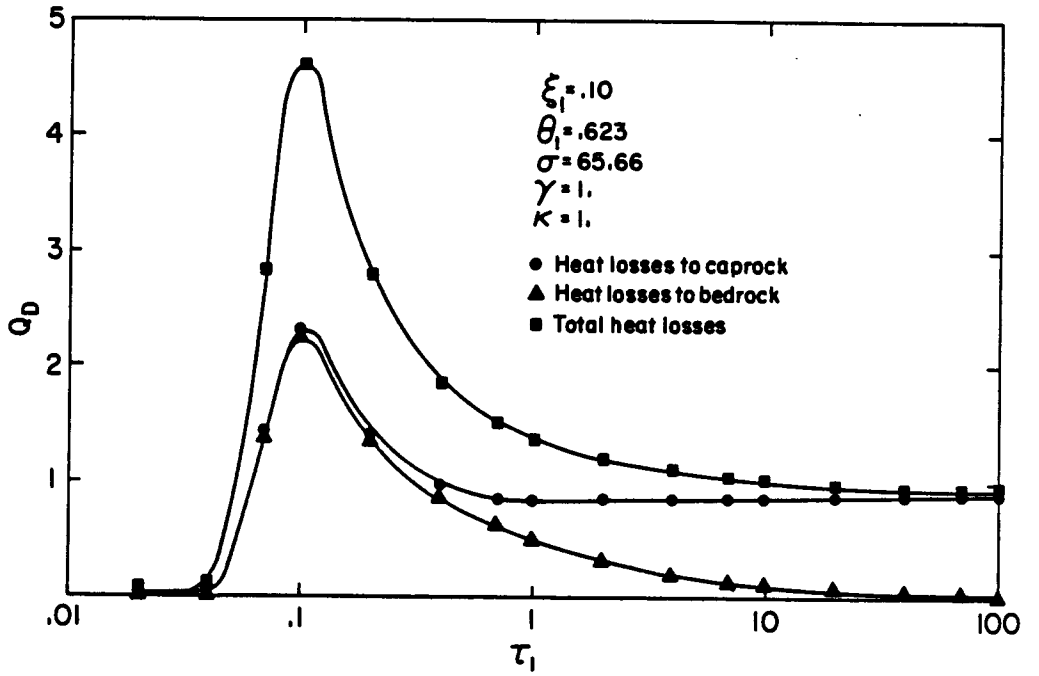

Figure 85. Dimensionless heat loss (Q_D) from the aquifer to the caprock and bedrock. [XBL 8110-11670]

behavior can be readily explained, when Figures 78 and 79 are considered. The heat losses from the aquifer to the caprock stabilize when the constant temperature boundary at $z = D$ is felt (approximately at $\tau_1 = 1.0$), and a steady linear gradient is established. However, due to the constant temperature boundary at $z = -(B + D)$, a linear, steady temperature gradient (positive with depth and therefore results in negative heat losses) is only achieved at late times as the bedrock is being heated. The total heat losses from the aquifer stabilize at the approximate value of 1.0 at late times.

The total heat losses from the aquifer, Q_{D_t} versus dimensionless distance ξ_1 at various dimensionless times for different values of θ_1 are shown in Figures 86-89. The figures show that at early times very large heat losses occur close to the fault (small ξ_1). However, the heat flux close to the fault decreases logarithmically with time. It can be shown mathematically that the heat losses close to the fault will decrease with time as specified by the following expression (Carslaw and Jaeger, 1959):

$$Q_{D_t} = \frac{2}{\sqrt{\pi \tau_1}} \, . \tag{121}$$

Equation (121) is valid only if $\kappa = \gamma = 1.0$, and at times before the constant-temperature boundary at $z = D$ is felt.

Another interesting characteristic of the curves shown in Figures 86-89 is that they can be enclosed by a single line, representing the area of heat losses at any given dimensionless time τ_1. The reason for this

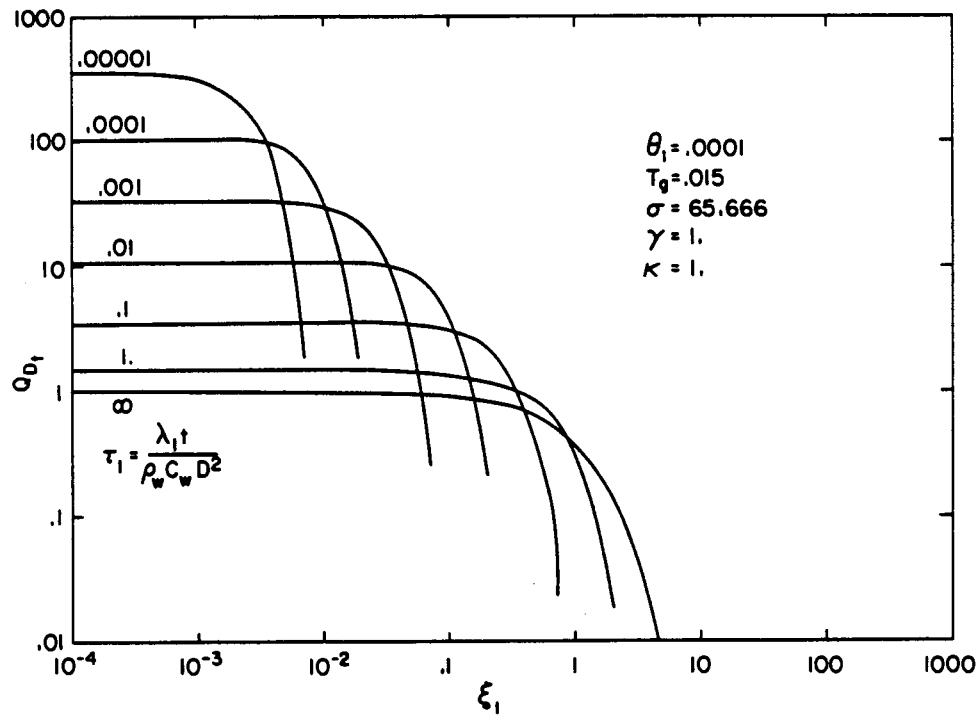

Figure 86. Total dimensionless heat losses (Q_{D_t}) from the aquifer for θ_1 = .0001. [XBL 8110-11663]

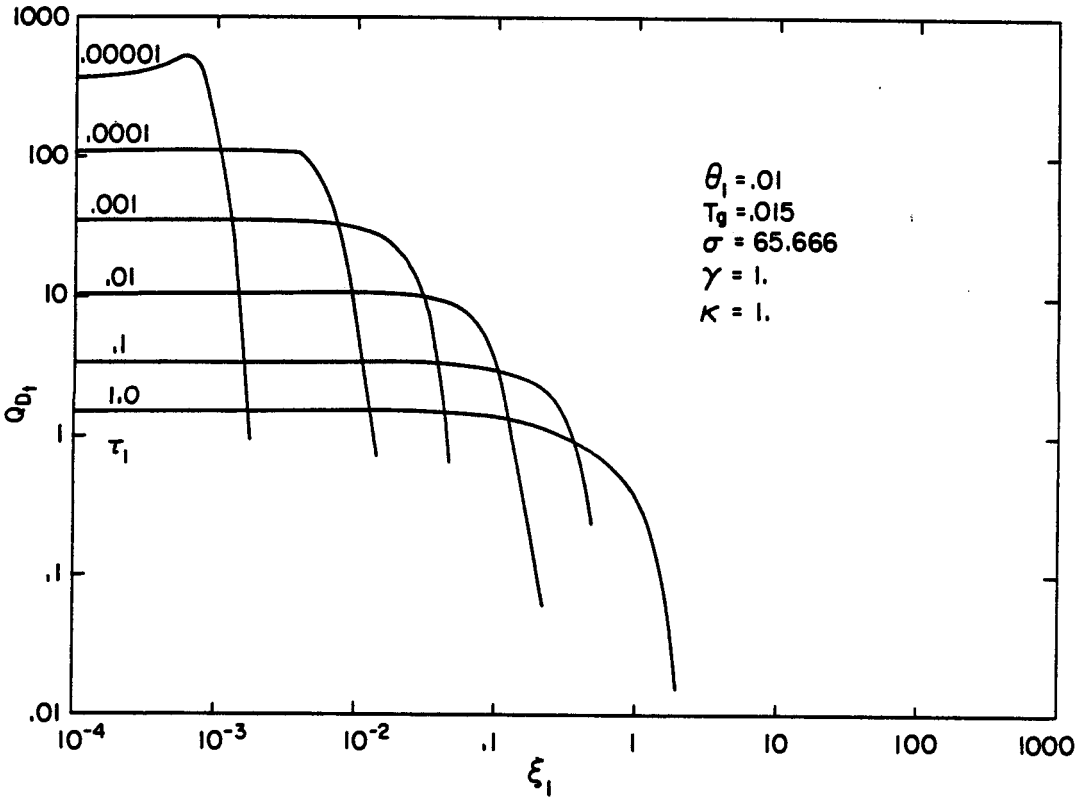

Figure 87. Total dimensionless heat losses (Q_{D_t}) from the aquifer for θ_1 = .01. [XBL 8110-11664]

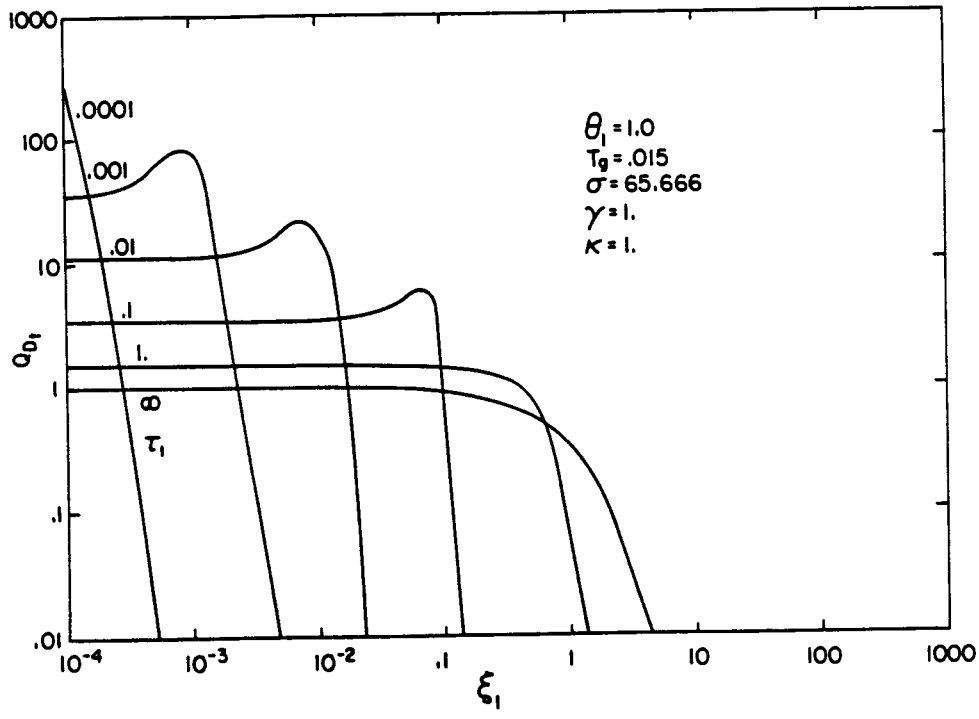

Figure 88. Total dimensionless heat losses (Q_{D_t}) from the aquifer for $\theta_1 = 1.0$. [XBL 8110-11667]

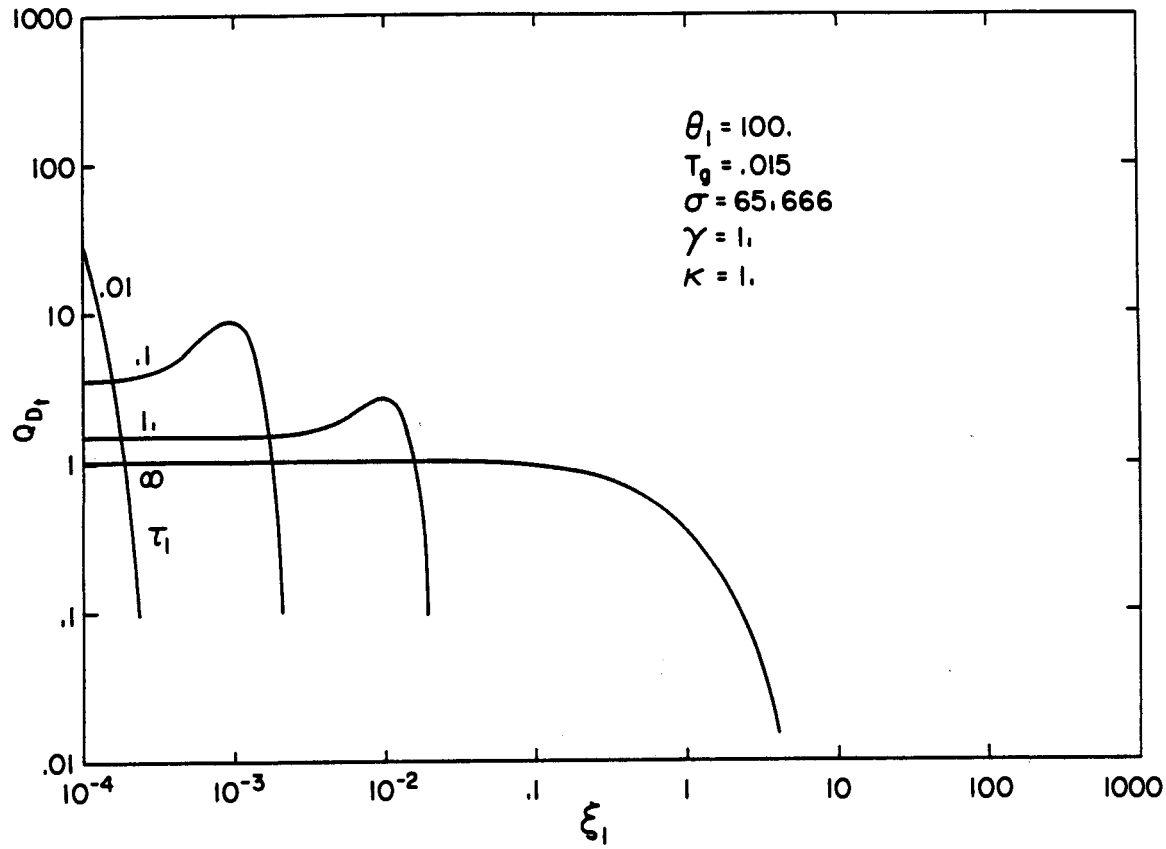

Figure 89. Total dimensionless heat losses (Q_{D_t}) from the aquifer for $\theta_1 = 100.$ [XBL 8110-11668]

is that the advancement of the thermal front along the aquifer is linearly related to the dimensionless time. Also, the steady-state curves in Figures 86-89 are identical; this again illustrates that the steady-state temperature distribution is independent of θ_1. The peculiar maxima in the heat loss curves for large values of θ_1, are probably artifacts created by the numerical inverter. There does not seem to be a theoretical basis for these maxima.

Heat losses at the surface

The heat losses at the ground surface can also be calculated using the Fourier law of heat conduction, and evaluating the derivative at the surface (z = D). Figure 90 shows the heat losses at the surface versus distance from the fault (ξ_1), for a given set of parameters. The figure shows that the thermal front reaches the surface close to the fault at a dimensionless time of $\tau_1 = .001$. The heat flux at the surface increases steadily with dimensionless time to a steady state value of 1.0 at dimensionless time $\tau_1 > 10$. For the parameters shown in Figure 90, the anomalous heat fluxes at the surface due to the fault-charged aquifer beneath extends to a dimensionless distance of approximately $\xi_1 = 10$. Further away from the fault, normal heat losses due to the normal geothermal gradient prevail.

Steady-state conditions

Equations (116-118) give the steady-state temperatures in the aquifer, caprock, and bedrock. Figure 91 shows the steady-state temperature distribution in the aquifer for various values of κ/σ. The figure shows

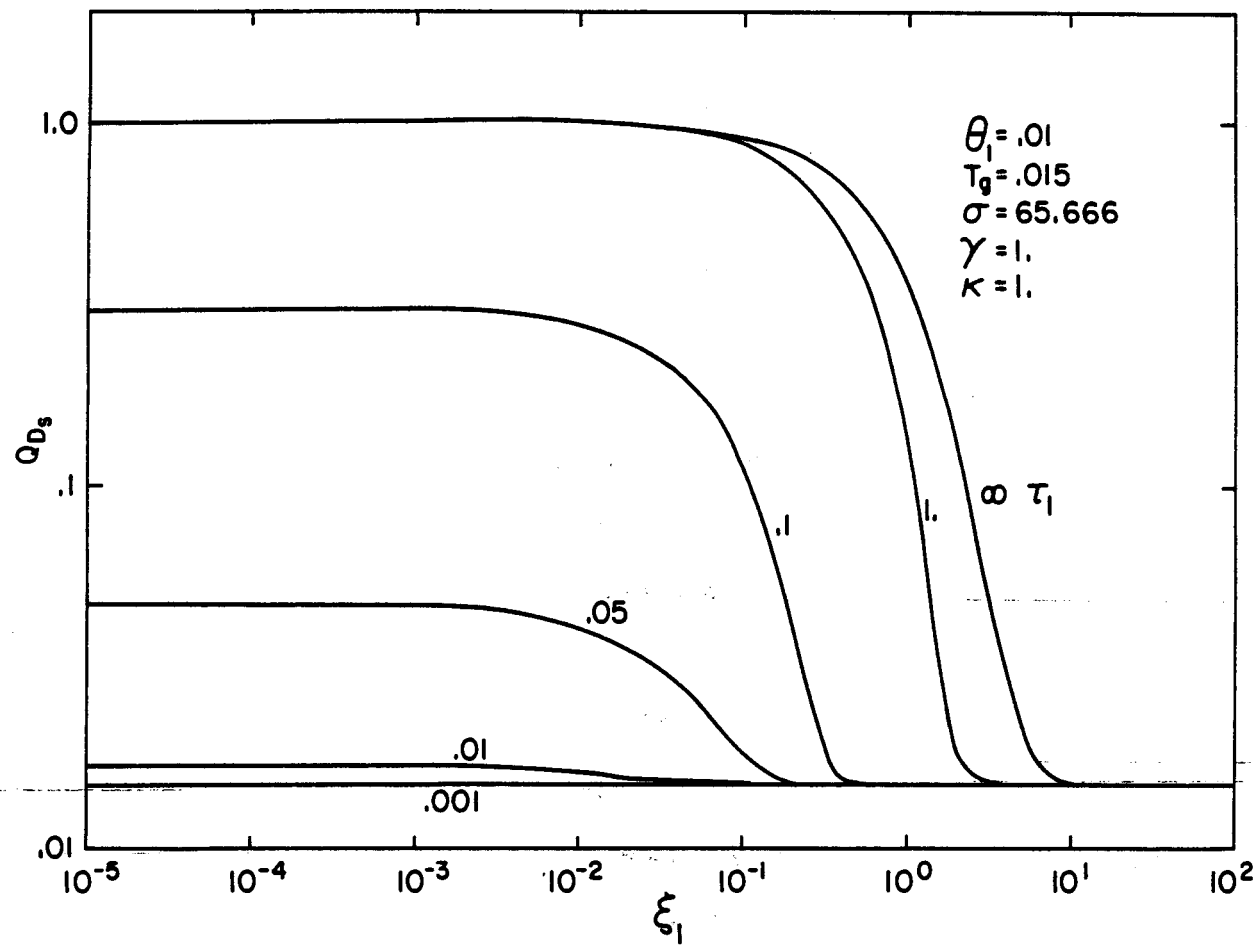

Figure 90. Heat losses at the ground surface. [XBL 8110-11673]

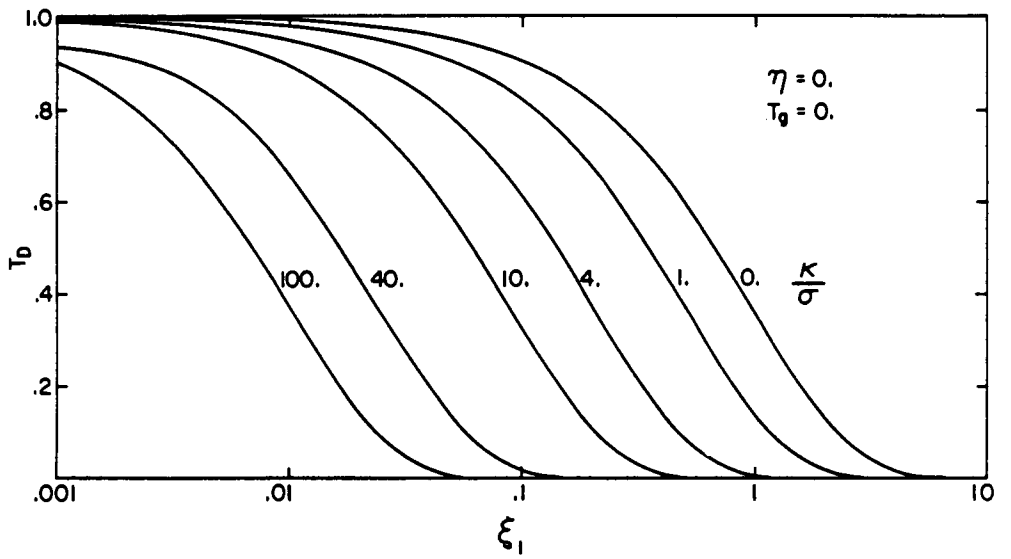

Figure 91. Steady-state temperature distribution in the aquifer for various values of κ/σ. [XBL 8110-11674]

that the smaller the value of κ/σ, the further away from the fault the thermal field extends. The parameter κ/σ represents the heat losses to the bedrock, with high values indicating either that the thermal conductivity of the bedrock is high, or that the lower constant-temperature boundary is close to the aquifer (small B).

The steady-state heat losses from the aquifer can easily be derived using equations (116)-(118). The expression for the steady heat losses is (see Appendix D):

$$Q_{D_t} = [1 - T_g] \left[1 + \frac{1}{\sigma}\right] \exp - \left[1 - \frac{\kappa}{\sigma}\right] \xi_1 \qquad (122)$$

The total steady heat losses from the aquifer versus the distance from the fault are shown in Figure 92 for various values of σ. In this case the geothermal gradient is specified as zero and κ is fixed at 1.0. The figure shows that the lower the value of σ, the higher the heat losses close to the fault and the shorter the extent of the thermal field from the fault. This behavior is reasonable as σ is inversely related to the steady heat losses to the bedrock. For very large values of σ the heat losses to the bedrock are negligible and consequently the total heat losses from the aquifer equal the heat flux at the ground surface.

Application to Susanville Geothermal Project

As a first attempt to validate this model for fault-charged hydrothermal systems, it was applied to data from the geothermal system at Susanville, California. The more than 20 exploration wells in Susanville

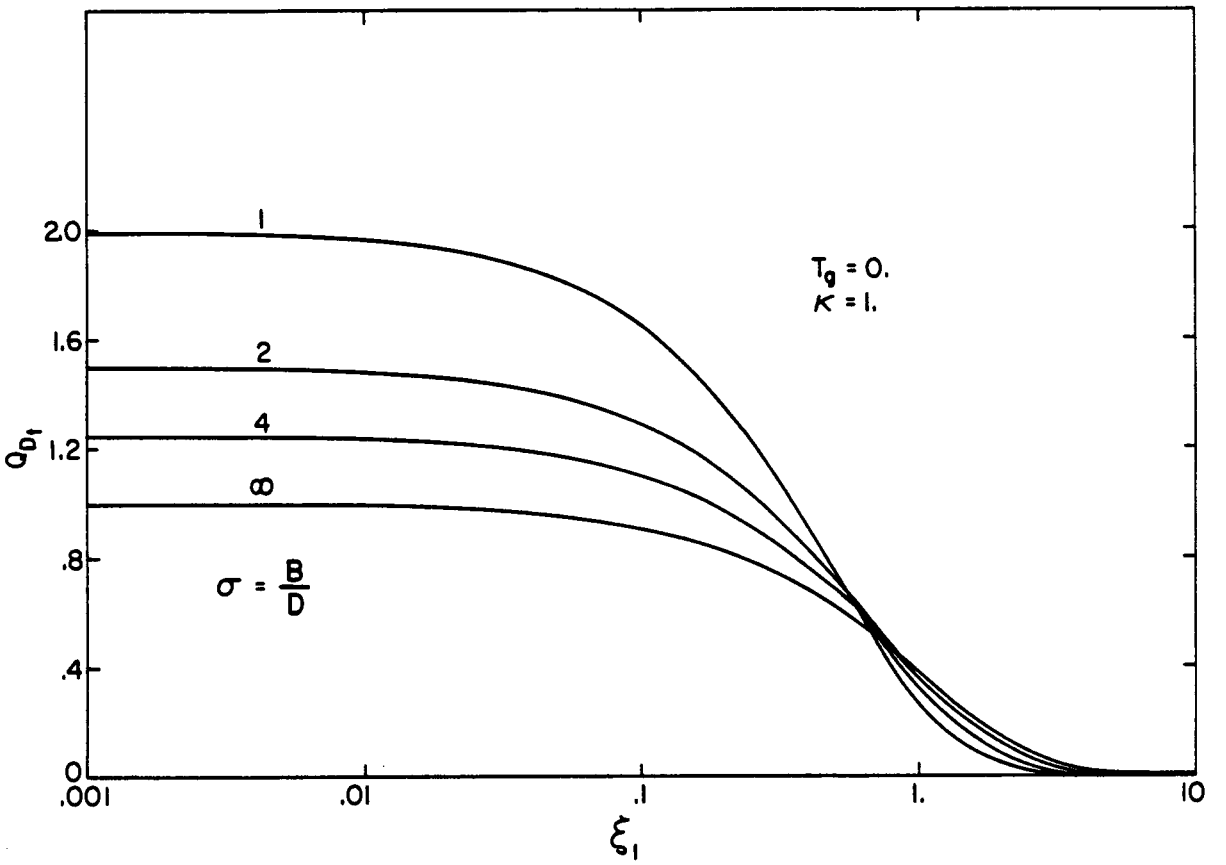

Figure 92. Steady-state heat losses from the aquifer for various values of σ. [XBL 8110-11675]

have located a low-temperature (< 80°C), shallow geothermal aquifer of limited areal extent [Benson and O'Brien, 1981]. Figure 93 shows the location of the wells and the temperature contours at an elevation of 1150 m, which corresponds to a depth of 125 m, where the primary aquifer is found. The temperature contours shown in Figure 93 suggest that the reservoir is charged by a fault with a NW strike; the fault being located slightly west of a line intersecting well S-9 and the Davis well. The steep temperature gradients to the west of the proposed fault illustrate that it is recharging the aquifer only to the east. Temperature contour maps at different depths show fault-related characteristics similar to those shown in Figure 93. Furthermore, many of the wells at Susanville show a reversal with depth similar to that shown in Figure 76 for the Klamath Falls well.

One potential use for the hydrothermal energy at Susanville is space heating. However, the limited areal extent of the hydrothermal system (Figure 93) indicates that the mass of hot water (the limiting temperature taken as 60°C) amounts to only 1-3 x 10^7 m^3 (depending upon the aquifer thickness selected). Current plans (U.S. Department of Energy, 1980) call for an extraction rate of approximately 0.035 m^3/s (550 gpm) for space heating of 14 public buildings. If recharge is neglected, this corresponds to a lifetime of 9-27 years. If the project is intended for 20 years, its success will depend greatly upon the recharge rate. A reliable estimate of the recharge into the Susanville hydrothermal system is therefore of considerable economic interest. Application of our model

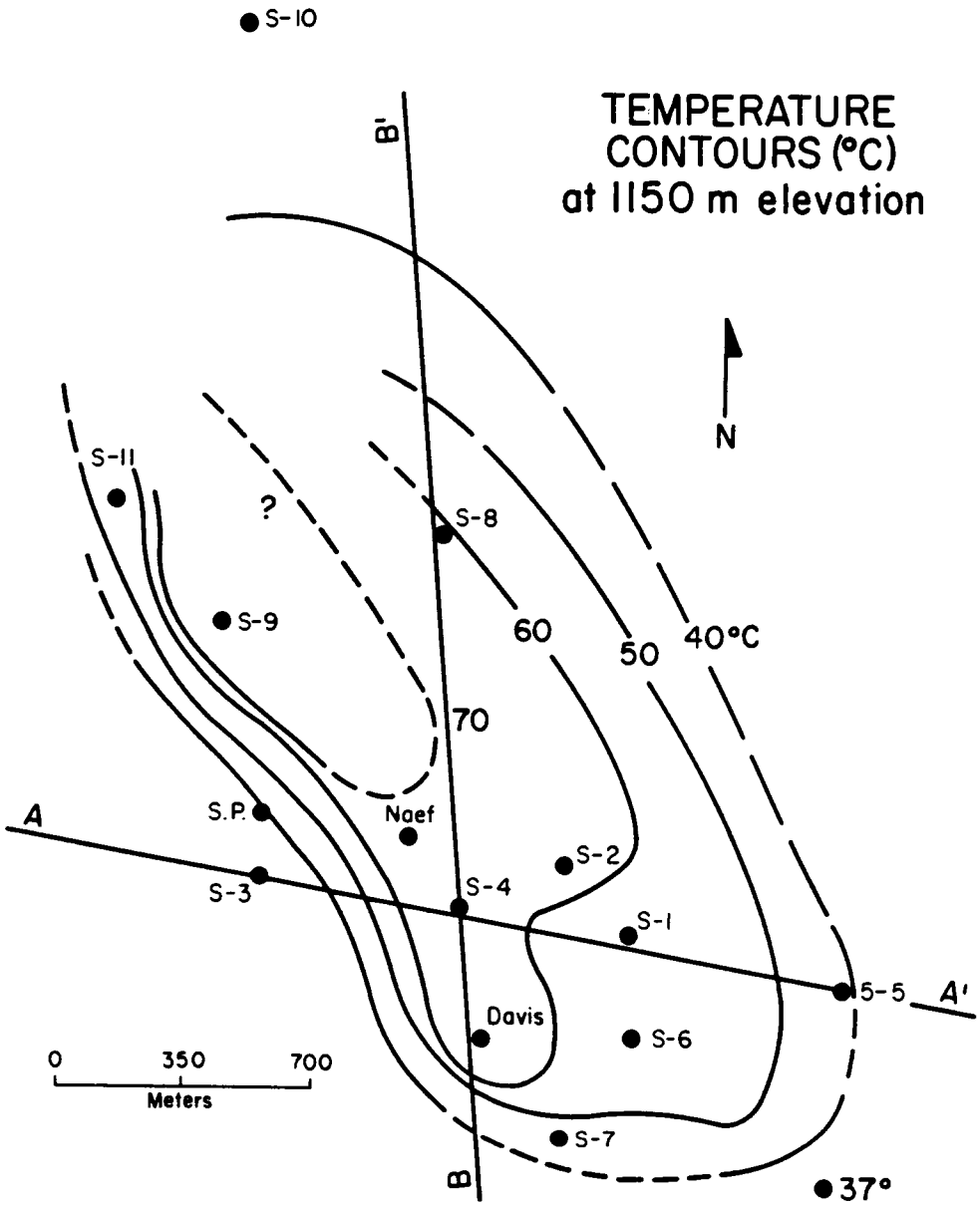

Figure 93. Temperature contours at 1150 m elevation at Susanville (after Benson et al., 1981). [XBL 807-7247]

to the Susanville anomaly can give the first estimate of the recharge rate.

Table 9 shows the parameters selected from the well data. The maximum temperature measured in the field is approximately 80°C in well S-9, which is located very close to the proposed fault (see Figure 93). The temperature of the water recharging the aquifer is therefore fixed at 80°C. Picking 60°C as the average aquifer temperature, the fluid parameters can be obtained, ρ_w = 983 kg/m^3, c_w = 4179 J/kg °C. It is now possible to determine that the appropriate value of θ_1 = 0.31 (equation (106c)).

Table 9. Parameters used for the Susanville model.

Parameter	Value
Aquifer thickness, b	35 m
Depth to aquifer, D	125 m
Aquifer porosity, ϕ	0.2
Thermal conductivity of rock, λ_1	1.5 J/m·s·°C
Rock heat capacity, c_1	1000 (J/kg·°C)
Rock density, ρ_1	2700 (kg/m^3)

The objective of this exercise is to use the model to match the temperature contour data shown in Figure 93 and the temperature profiles from individual wells in an attempt to estimate the hot water recharge. After a number of computer runs, the match shown in Figures 94 and 95 was obtained. As Figure 94 shows, the calculated temperature contours compare

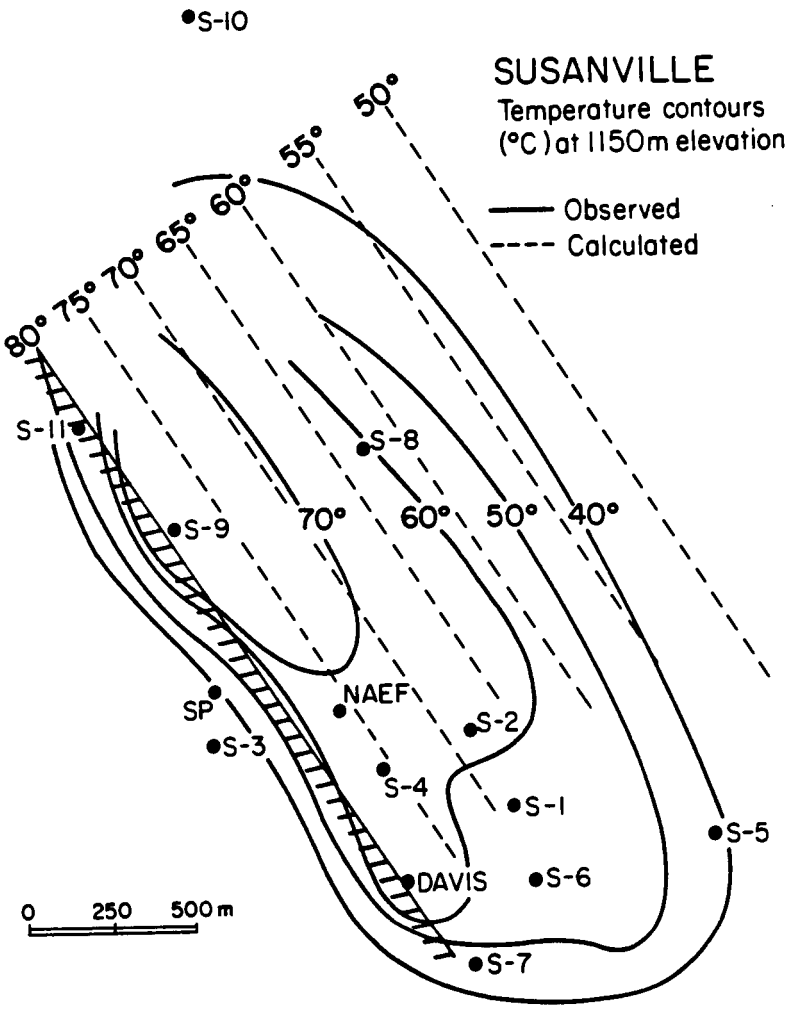

Figure 94. Comparison between observed and calculated temperature contour data. [XBL 816-3183]

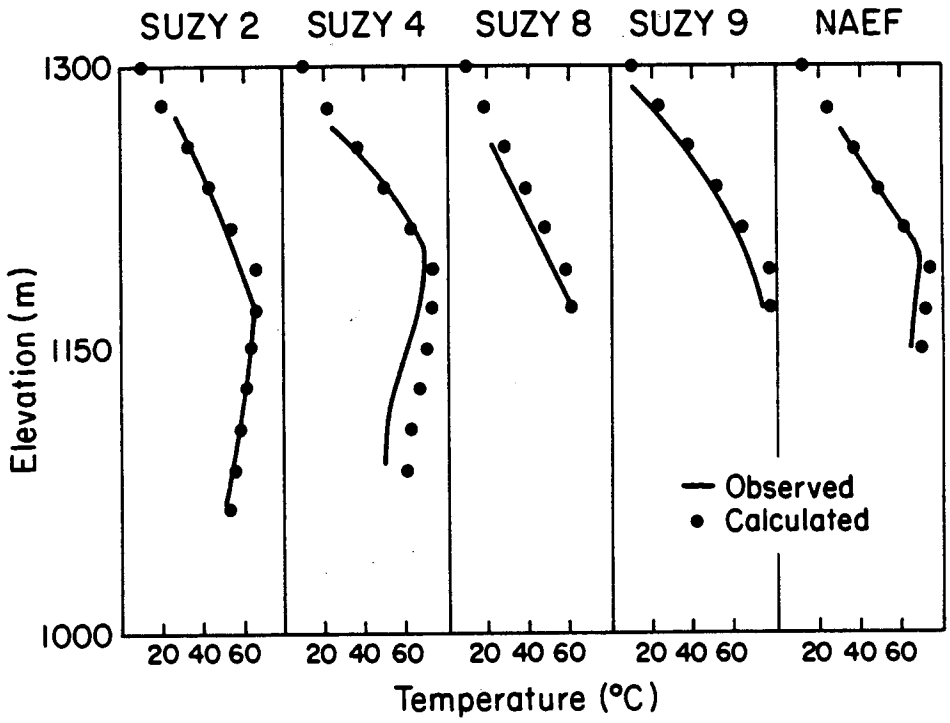

Figure 95. Comparison between calculated and observed temperature profiles in wells. [XBL 816-3181]

very well with the observed ones in the hottest region of the field, close to the proposed fault. Further away, however, there are large differences between the calculated and the observed temperatures. There are several possible reasons for the discrepancy. First, only limited data are available away from the fault (only wells S-5 and S-10), so that temperature contours are not accurately known. Second, evidence shows that there is a high regional flow of ground-water towards the southeast and that mixing of the colder shallow groundwater with the hot fluids is taking place. Third, the subsurface geology is considerably more complex than can be accounted for by the simple model we have used here. In any case, the model matches the temperature profiles of wells close to the proposed fault very well, as shown in Figure 95.

The match shown in Figures 94 and 95 was obtained using two different sets of parameters. First, if the lower constant temperature boundary is placed very deep ($H \gg D$), the parameters obtained indicate that the hydrothermal system has been under development approximately 2000 years and that the fault charges the system at a rate of 9×10^{-6} $m^3/s \cdot m$. Second, a very similar match is obtained if the constant temperature boundary is placed at a depth of about 400 meters ($\sigma = 2.0$); in this case the parameters obtained show that steady-state temperature conditions are reached (consequently the evolution time cannot be determined except that it exceeds 10,000 years) but the calculated recharge rate is the same as in the first case (9×10^{-6} $m^3/s \cdot m$). If one considers the age of the subsurface formations at Susanville, the second case seems more likely.

Also it is not unlikely that a deeper permeable aquifer with circulation of colder water is present at the site, and this would act as a constant temperature boundary.

Anyway, the accuracy of the calculated recharge rate is of more concern to the developers of the Susanvillle hydrothermal system than the time of evolution. If the heat losses from the aquifer are controlled by heat conduction as we have assumed in the present model, the calculated recharge rate should be reasonably accurate. However, in the model horizontal conduction is neglected in the model, and this may make the actual recharge rate greater than what we have calculated.

If we assume that the calculated recharge rate is correct and that the fault recharges over a distance of 2500 m, the total rate of recharge is approximately 0.0225 m^3/s. This recharge rate corresponds to approximately 70% of the proposed extraction rate; consequently a project lifetime of 25-75 years could be expected, or approximately three times the longevity if no recharge is considered. It should be emphasized, however, that the simplicity of the present model does not warrant definite conclusions. The results presented here should be considered as rough first estimates.

Unfortunately, detailed heat flow data over the Susanville anomaly are not available at present; such data would have been useful in confirming the accuracy of the model. Figure 96 shows the calculated heat flow values plotted against distance from the proposed fault.

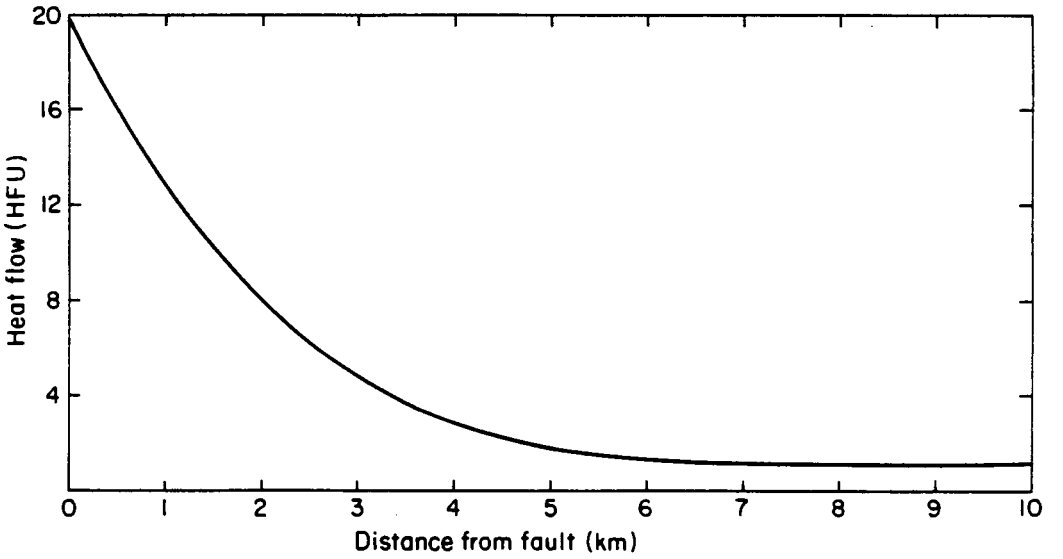

Figure 96. Calculated heat flows at Susanville. [XBL 816-3182]

Conclusions

A simple two-dimensional model for fault-charged hydrothermal systems has been developed and used in theoretical studies of such systems. The results obtained indicate that the evolution of the thermal field is greatly dependent on θ_1, a parameter denoting the ratio of the heat capacity of the aquifer to that of the caprock. The lower the value of θ_1 the greater the heat losses from the aquifer to the caprock and bedrock. A steady-state thermal field in the caprock is established at dimensionless time of $\tau_1 = 1\text{-}10$. The steady-state temperature field is greatly dependent on the distance to the constant temperature boundary condition at the ground surface ($z = D$). The constant temperature boundary condition below the bedrock ($z = -(D + B)$) has negligible effects, as long as the bedrock is much thicker than the caprock ($D \ll B$). Consequently the heat losses from the aquifer are primarily governed by the constant temperature condition at the ground surface.

The model has been applied to the hydrothermal system at Susanville, California. A reasonable match with the areal temperature distribution in the primary aquifer, and the temperature profiles of individual wells was obtained. This allowed an estimate of the recharge rate from the fault into the hydrothermal system to be obtained. As the calculated recharge rate into the Susanville hydrothermal system proved to be quite significant, a threefold increase in the potential of the Susanville hydrothermal anomaly for space heating purposes is predicted.

SUMMARY OF THEORETICAL STUDIES

In this chapter a few important geothermal reservoir engineering problems have been addressed. The studies of well test analysis of geothermal reservoirs showed that the conventional isothermal methods can be applied to well test data from hot water geothermal reservoirs, if the appropriate values of the fluid properties are used. Furthermore, two or more linear segments in the pressure transient data can be identified and consequently, averaged reservoir parameters can be obtained.

Analysis of well-test data from two-phase geothermal reservoirs is much more complex than that of single-phase reservoirs. Since under two-phase conditions, the fluid pressure is dependent on the fluid temperature the pressure drop in the reservoir is indirectly related to the extent and rate of boiling. The problem is further complicated by the relative permeability functions, which at present are unknown. In fact, these functions may differ from reservoir to reservoir and even from well to well. In the present study it was found that the immobile liquid cut-off is the most important characteristic of the relative permeability functions. Furthermore, it is shown that the relative permeability parameters can be determined as functions of the flowing enthalpy, from pressure and enthalpy transient data.

Presently, it is commonly believed that the production of high-enthalpy fluids from two-phase zones is more beneficial than the production from liquid-dominated zones. However the present studies of

exploitation strategies from two-phase geothermal reservoirs such as Olkaria showed, that in the long run, production of lower-enthalpy fluids from deeper horizons may be more beneficial as a more uniform depletion process results. Production from deeper horizons may greatly enhance the energy recovery from two-phase geothermal systems.

In the studies of injection into fractured geothermal reservoirs, it was found, that fractures may not cause premature breakthrough of the colder waters into the production region, as commonly has been believed. Although the fractures are the primary fluid conduits, conductive heat transfer from the rock matrix into the fractures causes drastic reduction in the velocity of the thermal front along the fractures. Thus, after a period of time, the thermal front in the fractures will advance at the same rate as the thermal front in the rock matrix, and consequently a uniform energy sweep will result. Type curves illustrating the advancement of the thermal front along the fractures, relative to that of the rock matrix, have been developed.

A simple model for fault-charged geothermal reservoirs has been developed. The results obtained using the model indicate that most of the heat losses from the aquifer are due to the constant temperature boundary condition at the ground surface. The temperature profiles can be used to estimate the recharge rate into such systems. Application of the present model to the hydrothermal system at Susanville, California, demonstrates that the calculated recharge rate significantly increases the potential of the resource for space heating applications.

FIELD APPLICATIONS

In an earlier section, a list of possible applications of numerical simulators to field data were given. These applications can basically be subdivided into two categories:

(1) simulations of individual wells, and

(2) field-wide simulation studies.

In this chapter, the application of numerical simulators to the Krafla geothermal field in Iceland, and the Valles Caldera (Baca) geothermal field in New Mexico is illustrated. At Krafla, injection tests are used to obtain the transmissivity and storativity of the reservoir. These tests are performed using variable flow rates, and much colder water than the undisturbed reservoir water is injected. The applicability of conventional type curve matching techniques to the data is therefore questionable. The data is analyzed using the numerical simulator PT.

Data from the Baca geothermal field have been used for a field-wide simulation study using the numerical simulator SHAFT79 [Pruess and Schroeder, 1979]. The approach taken is to use the existing geological, geophysical, and well data to estimate the reservoir capacity for the field. The reservoir model developed is then used to estimate the longevity of the reservoir based on a 50 MW_e power production. As the data from the field are limited, a very simple hydrological model is used in the simulations. However, the study illustrates how numerical simulations can aid the field developer in the decision making process.

MODELING OF WELL TESTS AT KRAFLA, ICELAND

The Krafla geothermal field is located in the neovolcanic zone in northeastern Iceland (Figure 97). The neovolcanic zone is charactertized by fissure swarms and central volcanoes. The Krafla geothermal field is located in a caldera (8 x 10 km), with a large central volcano, also named Krafla (Figure 98). As shown in Figure 97, one of the large fissure swarms goes right through the caldera. Detailed descriptions of the regional geological characteristics of the Krafla field are given by Saemundsson (1974), Bjornsson et al. (1977), Jakobsson et al. (1978), Saemundsson (1978), and Bjornsson et al. (1979).

The fissure swarms in the Krafla area are volcanically active. In 1975 a rifting episode occurred at Leirhnjukur (east of the main field) and since then several surface volcanic episodes have occurred [Bjornsson et al., 1977; Bjornsson et al., 1979]. Along with these episodes, a rise and fall of the ground surface has been experienced [Bjornsson et al., 1977]. The ground surface rises gradually with time as magma is accumulating in chambers below the ground surface, but periodically falls rapidly as magma is released into the fissure swarms to form dykes or penetrates all the way to the surface. Several large magma chambers have been located at depths of 3 to 7 km below ground surface using seismic studies [Einarsson, 1978].

Surface geophysical exploration at Krafla was initiated in 1970. In 1974, two exploration wells were drilled, and the subsurface data

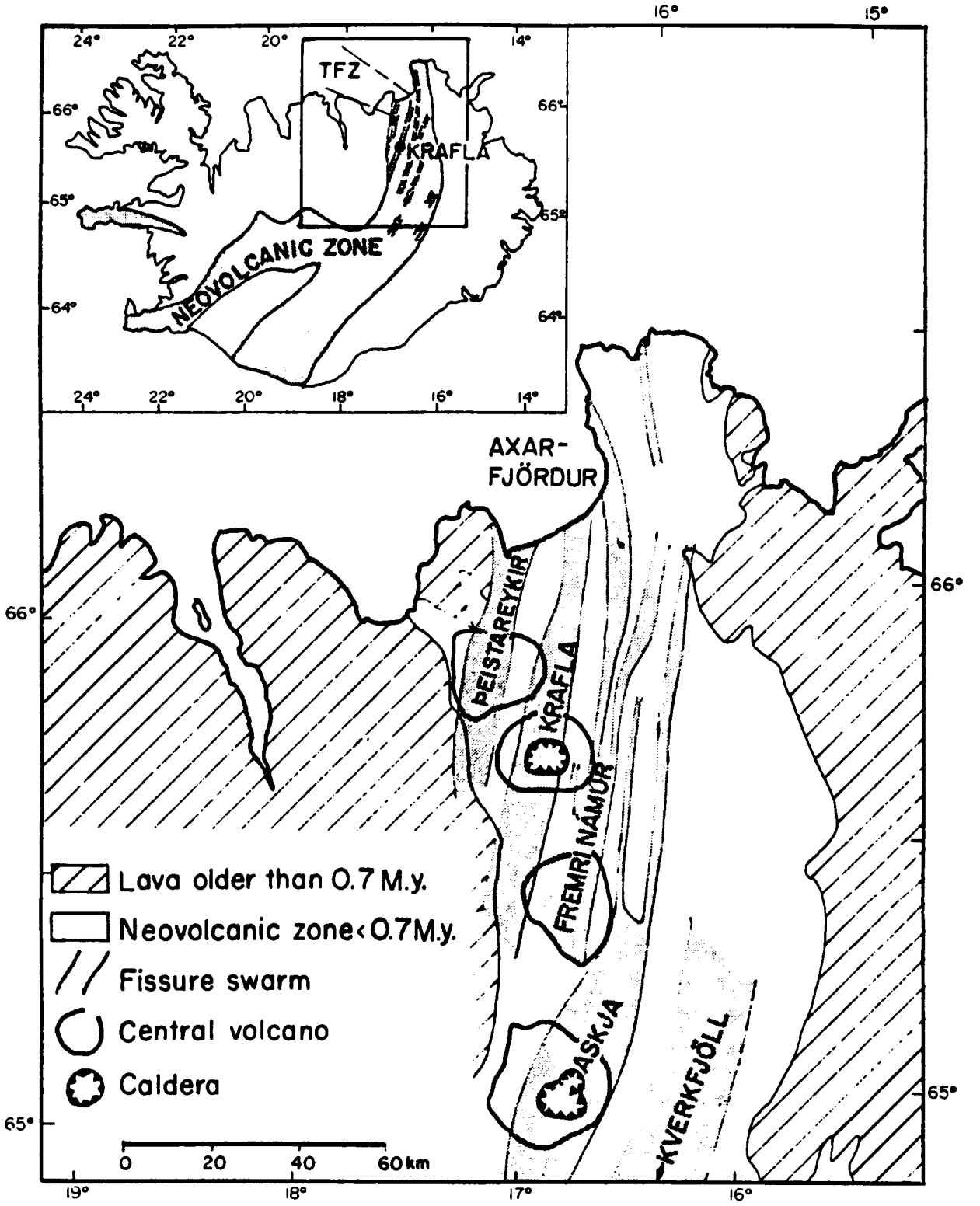

Figure 97. The spreading zone in North Iceland. Mapped by Kristjan Saemundsson (after Bjornsson et al., 1979). [XBL 793-8932]

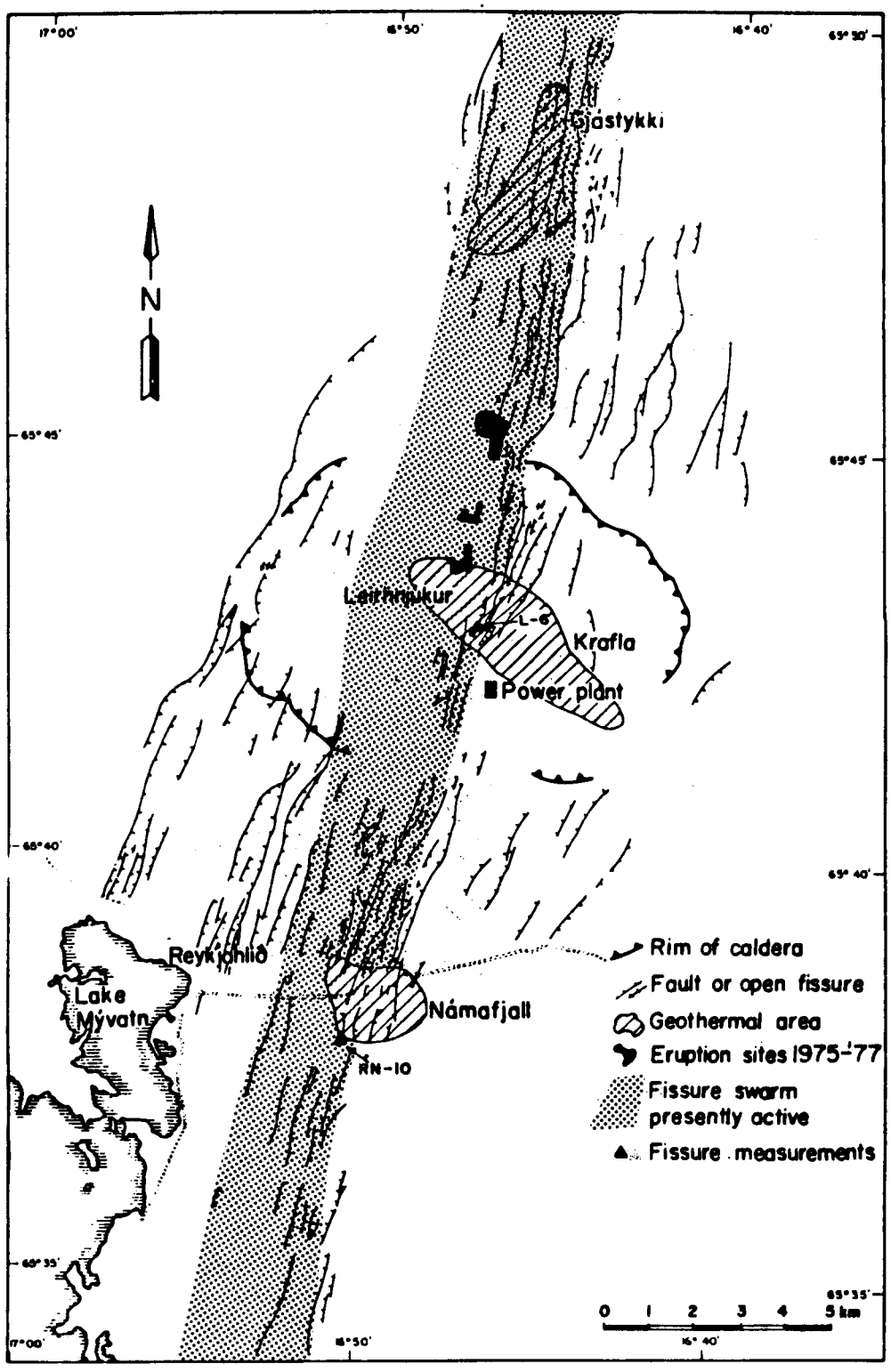

Figure 98. Outline geological map of the Krafla Caldera and associated fissure swarm. Mapped by Kristjan Saemundsson (after Bjornsson et al., 1979). [XBL 793-8931]

indicated the presence of a high-temperature (>300°C) geothermal field. Presently, 18 wells have been drilled at Krafla and data from these wells provide the basis for the reservoir model to be described in the next section. The locations of the wells are shown in Figure 99.

Reservoir Model

The subsurface geology of the wells inferred from cuttings have been described by Kristmannsdottir et al. (1975-1977) and Gudmundsson and Steingrimsson (1981). Basically, the subsurface rocks can be subdivided into three formations: the hyaloclastite formation, the lava formation, and the intrusive formation (Figure 100). The hyaloclastite formation is predominant in the top 800 m but it is subdivided by a lava layer at depths of 200-400 m. At depths of 800-1100 m, a thick layer of the lava formation prevails. A multiple sill is located at depths of 1100-1300 m, and below that the intrusive formation dominates. In the new well field south of the Krafla volcano, the uppermost hyaloclastite and lava sequences are not present but the intrusive formation dominates from ground surface down [Gudmundsson and Steingrimsson, 1981].

In 1977, a model of the Krafla field was presented [Stefansson et al., 1977]. This model was later slightly modified to yield the presently accepted model of the field [Steingrimsson and Stefansson, 1977]. Stefansson (1981) presented a detailed description of the model which is summarized in the following discussion.

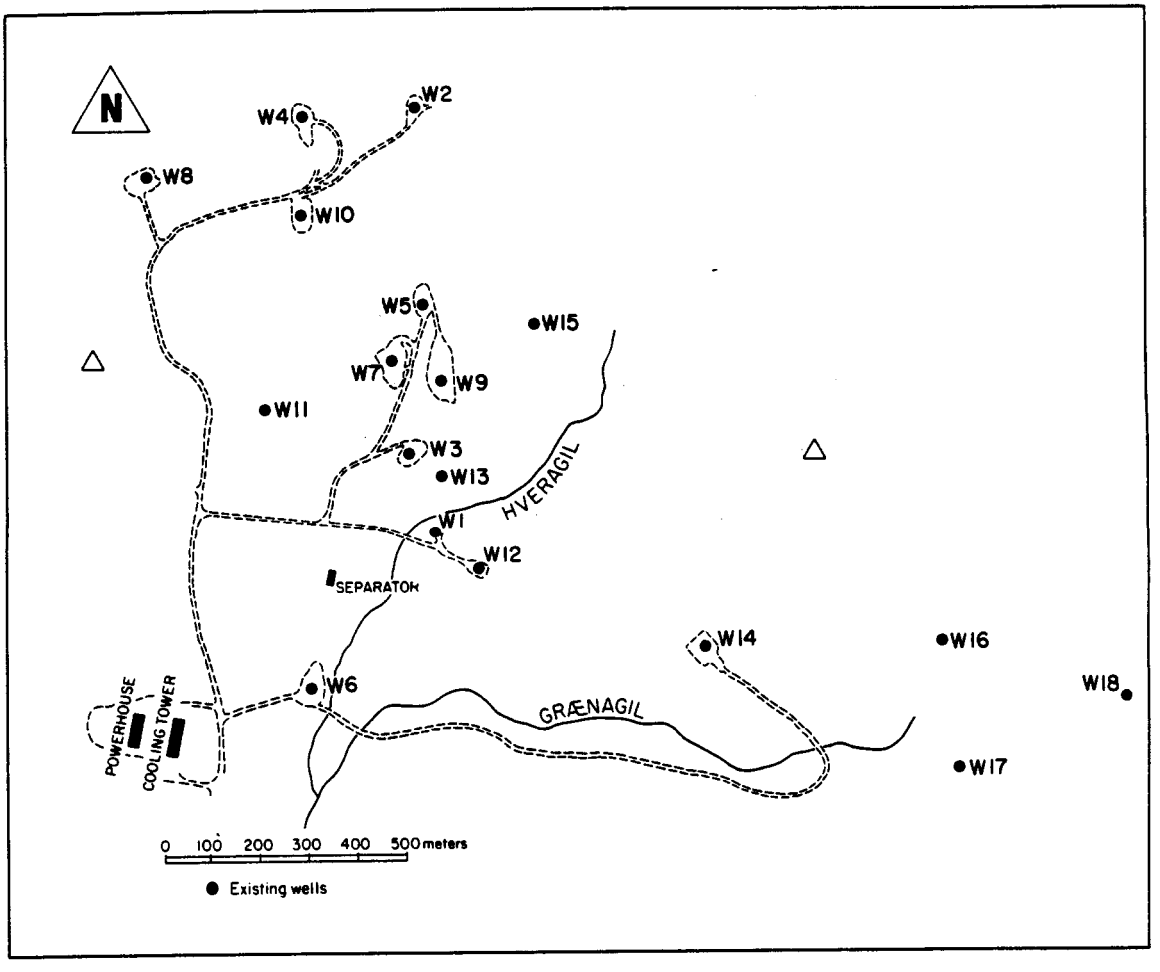

Figure 99. Wells drilled to date at Krafla geothermal field (after Stefansson, 1981). [XBL 812-2598]

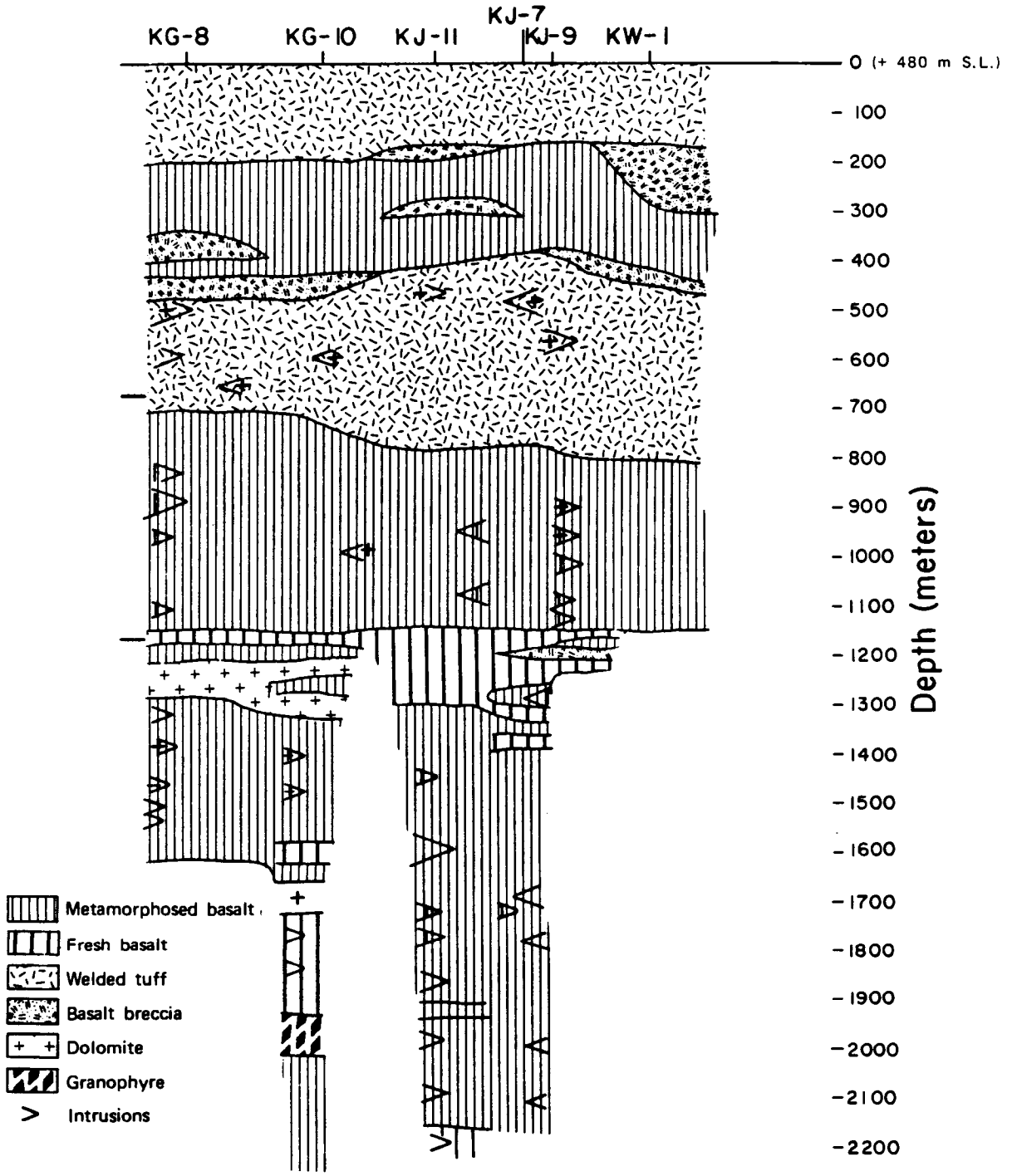

Figure 100. Sectional geological drawing of the Krafla geothermal field (after Stefansson, 1981). [XBL 788-1474]

In the old well field (wells 1-12, 15), the pressure and temperature data from the wells have indicated the presence of two reservoirs. The upper reservoir contains single-phase liquid water at a mean temperature of 205°C. This reservoir extends from a depth of 200 m to a depth of about 1100 m. The deeper reservoir is two-phase, with temperatures and pressures following the saturation curve with depth. This reservoir directly underlies a thin confining layer (the multiple sills) at a depth of 1100-1300 m to greater than 2200 m (the depth of the deepest well). The two reservoirs seem to be connected near the gully, Hveragil. In the new well field (south of the Krafla volcano), the upper reservoir has not been identified and only a single two-phase liquid-dominated reservoir seems to be present.

Well testing at Krafla

A common procedure at Krafla is to perform an injection test in a new well soon after drilling is completed. This procedure has been applied to the last 12 wells drilled at Krafla (wells 7 to 18). The purpose of the injection test is twofold:

(1) to attempt to stimulate the well, i.e., increase the injectivity;

(2) to obtain data that can be analyzed to yield the transmissivity of the well.

The experience obtained from injection testing of wells in Krafla as well as in several other geothermal fields (e.g., Wairakei, New Zealand; Namafjall, Iceland; Tongonan, the Phillippines), has shown that in many

cases apparently dry wells (small water losses) have been sufficiently stimulated to become reasonably good producers [Stefansson, personal communication, 1980]. The reasons for this are not presently known, but several possible explanations have been proposed:

(1) cleaning of fractures

(2) opening up of fractures due to increases in pore fluid pressure

(3) thermal cracking close to the well due to the temperature difference between the injected water and the hot reservoir water.

Conventional analysis of the well test data has been reported by Sigurdsson and Stefansson (1977) and Sigurdsson (1978). In this present study the use of numerical simulators for well test analysis is illustrated. Also, a clear illustration of permeability increases occurring during an injection test is given.

Analysis of injection test data

Well KJ-13 at Krafla was drilled in June-July 1980 (Figure 99). A simplified casing diagram for the well is shown in Figure 101. The figure shows that the well is cased down to a depth of 1021 m, with 9 5/8 in. casing; below that a 7 5/8 in. slotted liner extends down to the bottom of the well (at 2050 m). The figure also shows the location of a major fracture feeding the well at a depth of 1600-1700 m.

A few days after drilling, two injection tests were performed on July 10 and 11, 1980, respectively. During the tests a pressure transducer was located at a depth of approximately 200 m below ground surface

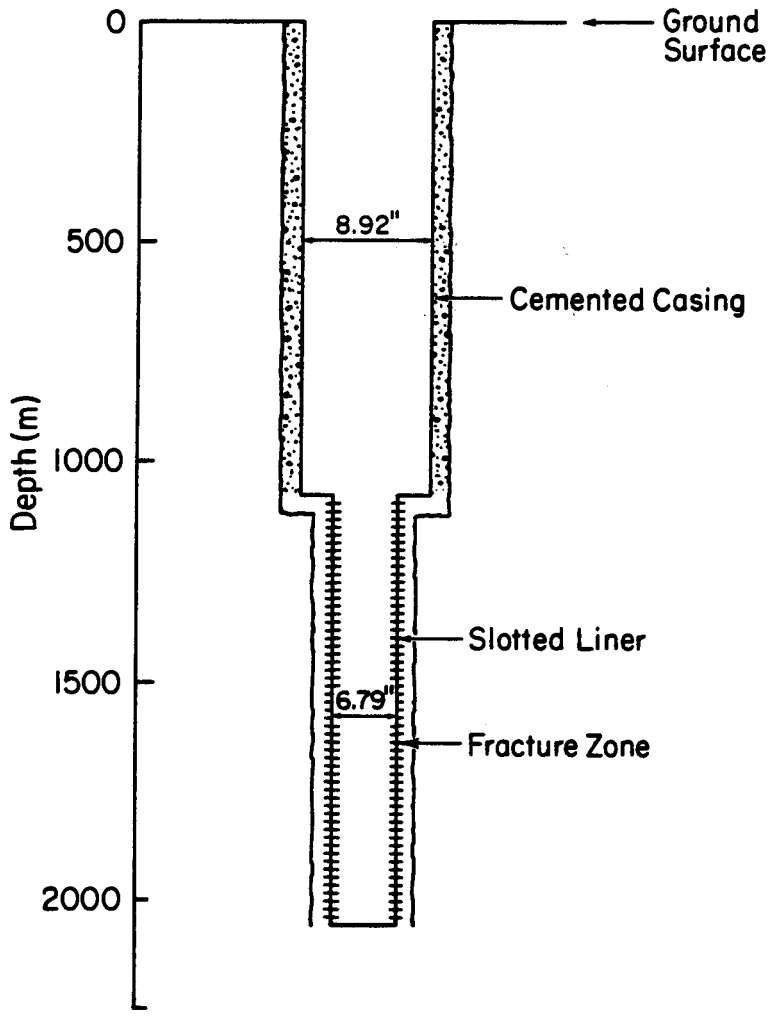

Figure 101. Simplified casing diagram for Krafla well K3-13.
[XBL 812-2600]

and continuous readings were obtained at the surface. The approximate temperature of the injected water was 20°C.

The injection rates at the surface are shown in Figure 102 along with the water-level data for the second test. After the first injection test was completed (July 10), continuous injection was made during the night, with a stable injection rate of approximately 29 kg/s for the last few hours before the second test started (at time t = 0 as shown in Figure 102). The second injection test consisted of an initial falloff, three injection segments with increasing flow rates, and finally a second falloff. During the test, a free surface water table is present in the well and consequently wellbore storage effects are present. Furthermore, the analysis of the injection test seemed to be complicated by thermal effects as 20°C temperature water is injected into a two-phase reservoir of much higher temperature. In the present analysis it is assumed that the fracture zone at 1600-1700 m depth is the primary aquifer; thermodynamic conditions at this depth correspond to a temperature of approximately 320°C.

The first step in the analysis of this well test was to correct for the wellbore storage effects. This can be easily accounted for by using variable flow rate analysis rather than the constant step-rate surface flow rates shown in Figure 102. As the wellhead flow rate and the water level in the well are known, the sandface flow rate can be calculated on the basis of simple mass balance as follows:

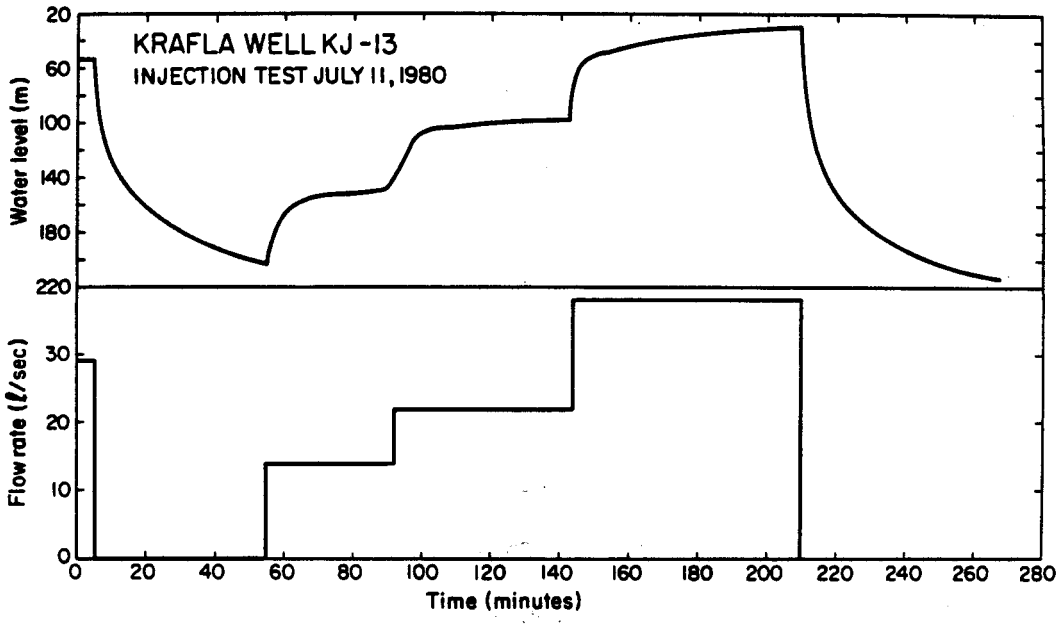

Figure 102. Injection-test data for well KJ-13. [XBL 812-2597]

$$q_s = q_w - \Delta s \pi r_w^2 \rho_w \tag{123}$$

where Δs denotes the change in the water level. Equation (123) simply states that the water entering the well (q_w) must leave the well (q_s) or be contained in the well, causing a change in the water level (Δs). Certainly, after some time a steady-state condition will be reached where the flow rates at the wellhead and at the sandface are identical and consequently the water level is stable ($\Delta s = 0$). However, for the Krafla wells (casing diameter 9 5/8 in.) the wellbore storage effects will last for approximately 1 1/2 hours, and therefore the variable-flow rate approach must be employed in the test analysis.

In attempting to match the water-level data shown in Figure 102, the two-phase simulator SHAFT79 [Pruess and Schroeder, 1979] and later the single-phase nonisothermal simulator PT were used. However, these attempts were unsuccessful as a reasonable match with the water-level data for the entire test (the initial falloff, the three injection steps, and the second falloff), could not be obtained. Further attempts were made using the simulator PT in its isothermal mode and the variable-flow rate Theis-type simulator ANALYZE [McEdwards and Benson, 1981]. A reasonable match with the field data for the entire test was obtained (Figure 103). The match is very good at all times, except for the third injection step where the calculated water-level values are slightly less than the observed values. Figure 103 also shows the sandface flow rates used in the simulation as well as the wellhead flow rates.

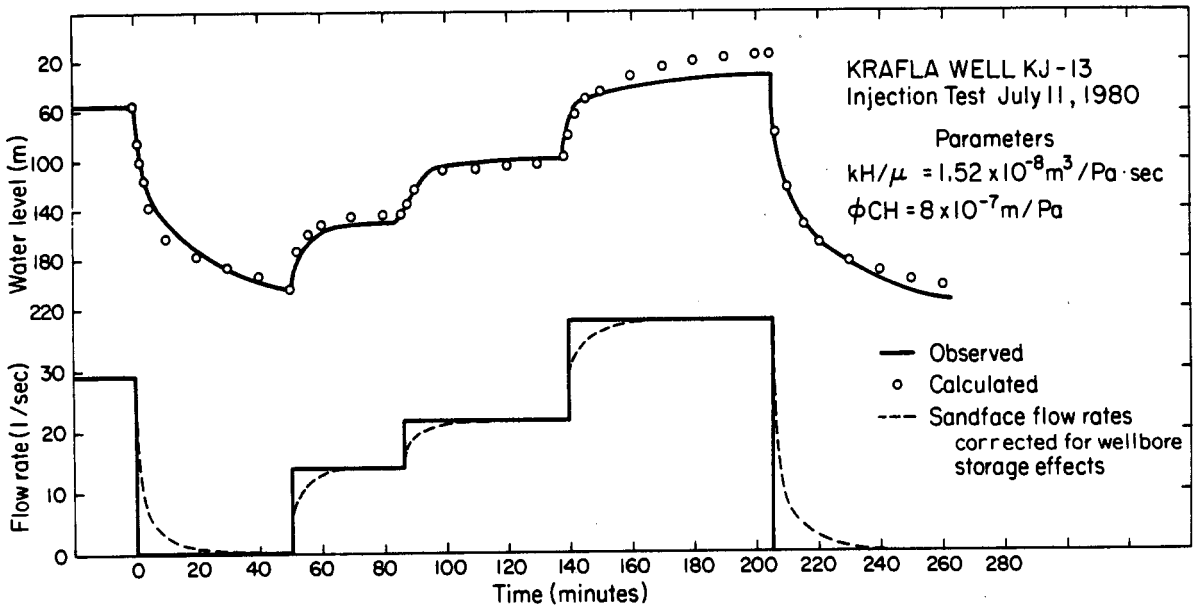

Figure 103. Comparison between observed and calculated water-level data for well KJ-13. [XBL 817-3298]

The parameters obtained from the match were:

$$\frac{kH}{\mu} = 1.52 \times 10^{-8} m^3/pa \cdot sec \tag{124}$$

$$\phi\beta_t H = 8 \times 10^{-7} \ m/pa \tag{125}$$

The transmissivity (kH) of the reservoir cannot be determined, as it is not obvious if the viscosity of the cold injection water or the hot reservoir water should be used in the analysis. Furthermore, the total compressibility (β_t) cannot be explicitly calculated, as the porosity (ϕ) and the effective reservoir thickness (H) are not known. Further discussion of the reservoir parameters determined from the injection test is given later in this section.

Now let us examine the apparent isothermal behavior observed in the injection-test data. Since the fluid viscosity changes by more than an order of magnitude over the temperature range 20 to 320°C, one would not expect isothermal pressure behavior in the data, especially when the data are taken during both injection and falloff periods. This is because, for a constant thickness, infinite, horizontal reservoir, the pressure changes during injection will correspond to the cold-water fluid properties whereas during the falloff period, the pressure changes will correspond to the fluid properties of the hot reservoir. This has been illustrated in an earlier section where nonisothermal effects in well tests of hot-water reservoirs were studied.

In an attempt to explain the isothermal behavior of the data from the injection test, two possibilities must be explored:

(1) the undisturbed reservoir conditions (e.g., T = 320°C) control the pressure response at the well, and

(2) the temperature of the injected water is the controlling factor.

As cold water has been injected into the well at all times during drilling (approximately 45 days) and also during the few days after drilling but prior to the second injection test (the test being considered), there must be a cold-water zone around the well. Consequently, the first possibility seems unlikely. If the cold water zone around the well is the controlling factor, this zone must extend further from the well than the pressure disturbance during each injection step. As the reservoir is fracture-dominated, the theory developed earlier (injection into fractured geothermal reservoirs) can be used to estimate the size of the cold-water zone around the well. Using typical values for the rock properties and an injection rate of 20 kg/s (the average injection rate prior to test), the curve in Figure 104 was calculated. If only the injection period from the end of drilling to the start of the test is considered (i.e., neglecting cooling effects due to injection during drilling), the figure shows that the cold-water front will have advanced approximately 50 m from the well (time period of 2-3 days). This estimate is independent of the size of the fracture zone, since θ is very small (see equation (56) for definition of θ).

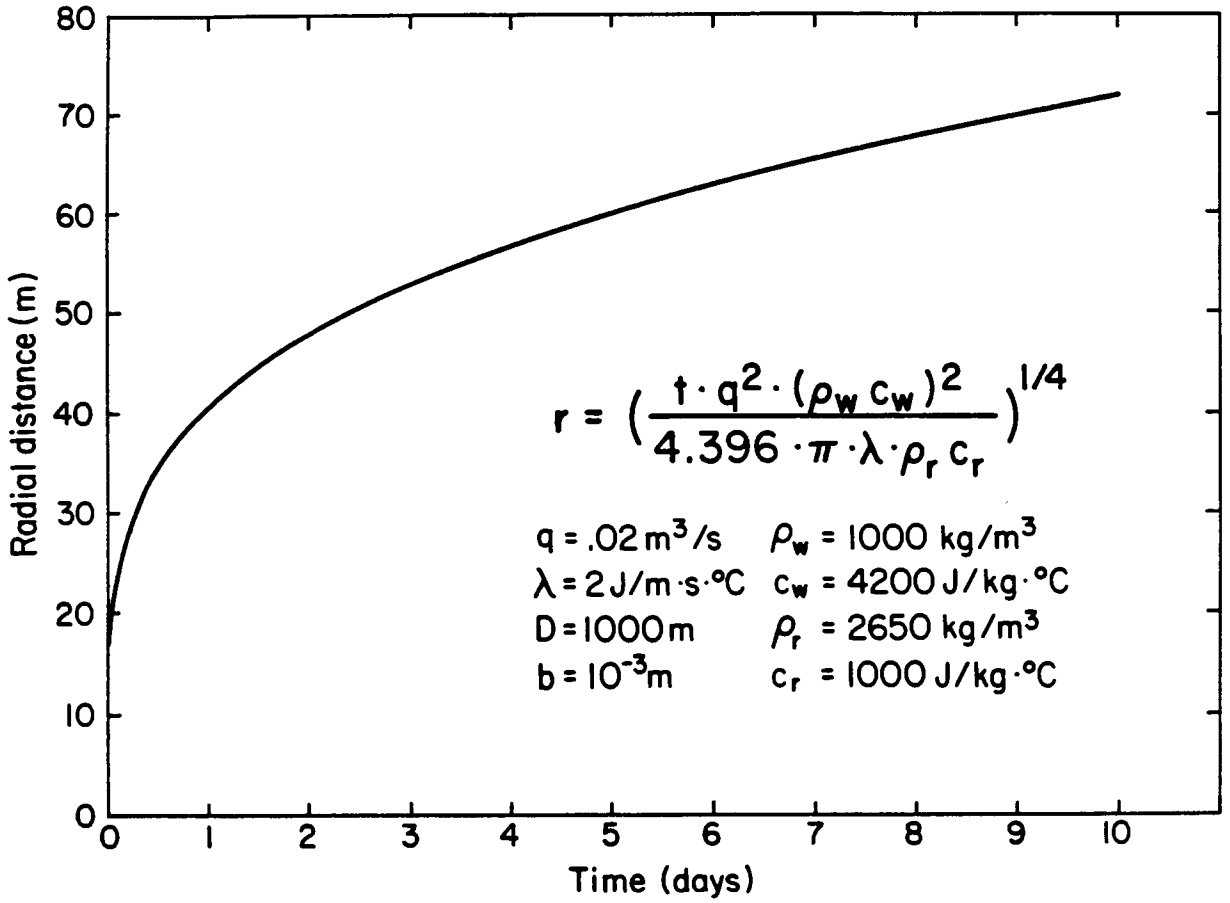

Figure 104. Advancement of the cold water front along the fracture.
[XBL8111-4841]

The radius of influence for the pressure disturbance due to a typical injection step can be calculated directly from the reservoir diffusivity as follows:

$$r = \sqrt{\frac{4kt}{\phi\mu\beta_t}} \tag{126}$$

Multiplying the numerator and the denominator by the effective thickness of the fracture zone H, the parameter groups determined from the well test (see equations (124) and (125)) can be used to determine the radius of influence (r). For an injection step lasting 1 hour, a radius of influence of 16.5 m can be calculated. As this value is less than the calculated radial extent of the cold-water zone (~50 m), isothermal pressure behavior can be expected. If this analysis is correct, the fluid parameters corresponding to the cold injection water should be used, and consequently this implies a transmissivity of $kH = 1.5 \times 10^{-11}\ m^3$ (15 Darcy-m).

The fracture zone (aquifer) feeding Krafla well KG-13 is believed to be very thin, on the order of 1 m (Stefansson, personal communication, 1981). If one assumes a reasonable value for the porosity (ϕ) for this zone, say $\phi = .10$, a very high total compressibility, $\beta_t = 8 \times 10^{-6}\ pa^{-1}$ can be calculated using equation (125). This high total compressibility can be explained by the two-phase conditions in the reservoir or by high fracture compressibility. The compressibility of two-phase fluids is two to four orders of magnitude larger than those of single-phase liquid or steam water [Grant and Sorey, 1979]. The two-phase compressibility

depends on many parameters such as temperature, saturation, porosity, and the relative permeability curves [Bodvarsson and Pruess, 1981]. Figure 105 shows the relationship between fluid compressibility and vapor saturation for various values of porosity. In calculating the curves shown in Figure 105, a reservoir temperature of 300°C and the Corey relative permeability curves were used. Comparison of the total compressibility β_t (previously determined to be $\beta_t = 8 \times 10^{-6}$ pa^{-1}) the curves shown in Figure 105 yields a porosity value of $\phi \simeq .05$ and vapor saturation of $S_v < .20$. These values agree very well with values of porosity and vapor saturation inferred from other field data [Stefansson, 1981]. However, it is doubtful that the high compressibility determined from the injection tests is due to the presence of two-phase fluids, because of the cold water zone surrounding the well. It is therefore more likely that the high compressibility is due to deformable fractures. In that case, the increase in well losses during injection tests may be due to opening up of fractures caused by increased pore pressures.

The second injection test that was analyzed was performed on KG-12. This well is cased with 9 5/8 in. casing down to a depth of 952 m, and below that to the bottom of the well (2222 m), a 7 in. slotted liner is in place. The major fracture zone is located at a depth of 1600 m, but some contribution to the production from the well may come from fractures located at a depth of 1000 m (Stefansson, private communication, 1981).

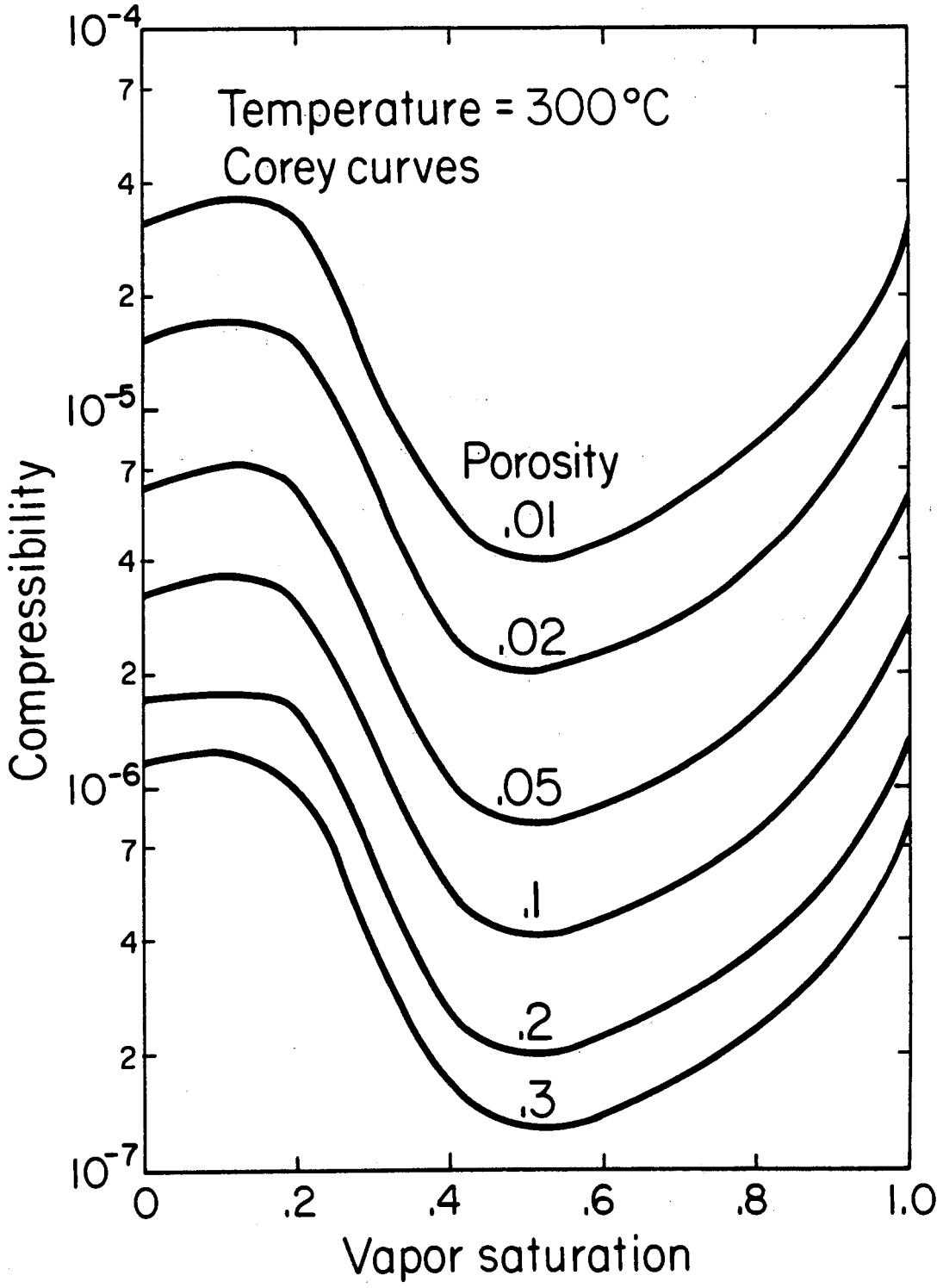

Figure 105. Fluid compressibility versus vapor saturation for a temperature of 300°C and the Corey relative permeability curves. [XBL 817-3293]

The injection-test data, consisting of water-level data and wellhead flow rates are given in Figure 106. As the figure shows, at some time prior to the test, cold water at a rate of 30 l/s was injected into the well. After an initial falloff lasting for approximately 1 1/2 hours, four injection-falloff segments with increasing injection rates were used. On the average, each of the injection steps only lasted 40 minutes, so that wellbore storage effects are quite important.

Analysis of the injection test of well KG-12 was carried out using the simulator PT in its isothermal mode. Figure 107 shows the best match obtained between the observed and the calculated water-level values. It also shows the variable flow rate used in the simulation (broken line) to account for the wellbore storage effects. As the figure shows, the calculated values compare very well with the observed data. However, the entire test could not be simulated using a constant value for kH/μ. For the initial falloff and the first injection-falloff cycle, the data were matched reasonably well using $kH/\mu = 1.2 \times 10^{-8}$; however, approximately 200 minutes after the injection test began, a certain decrease in the water level is observed although the injection rate is kept constant (Figure 107). This implies an instantaneous change in the transmissivity of the reservoir at this time. This was verified by the numerical simulation since, if the kH/μ factor was kept constant at $kH/\mu = 1.2 \times 10^{-8}$ over the entire simulation, the calculated pressure changes would greatly exceed the observed ones. Therefore, in the simulation the kH/μ factor had to be increased to account for the apparent stimulation effects due

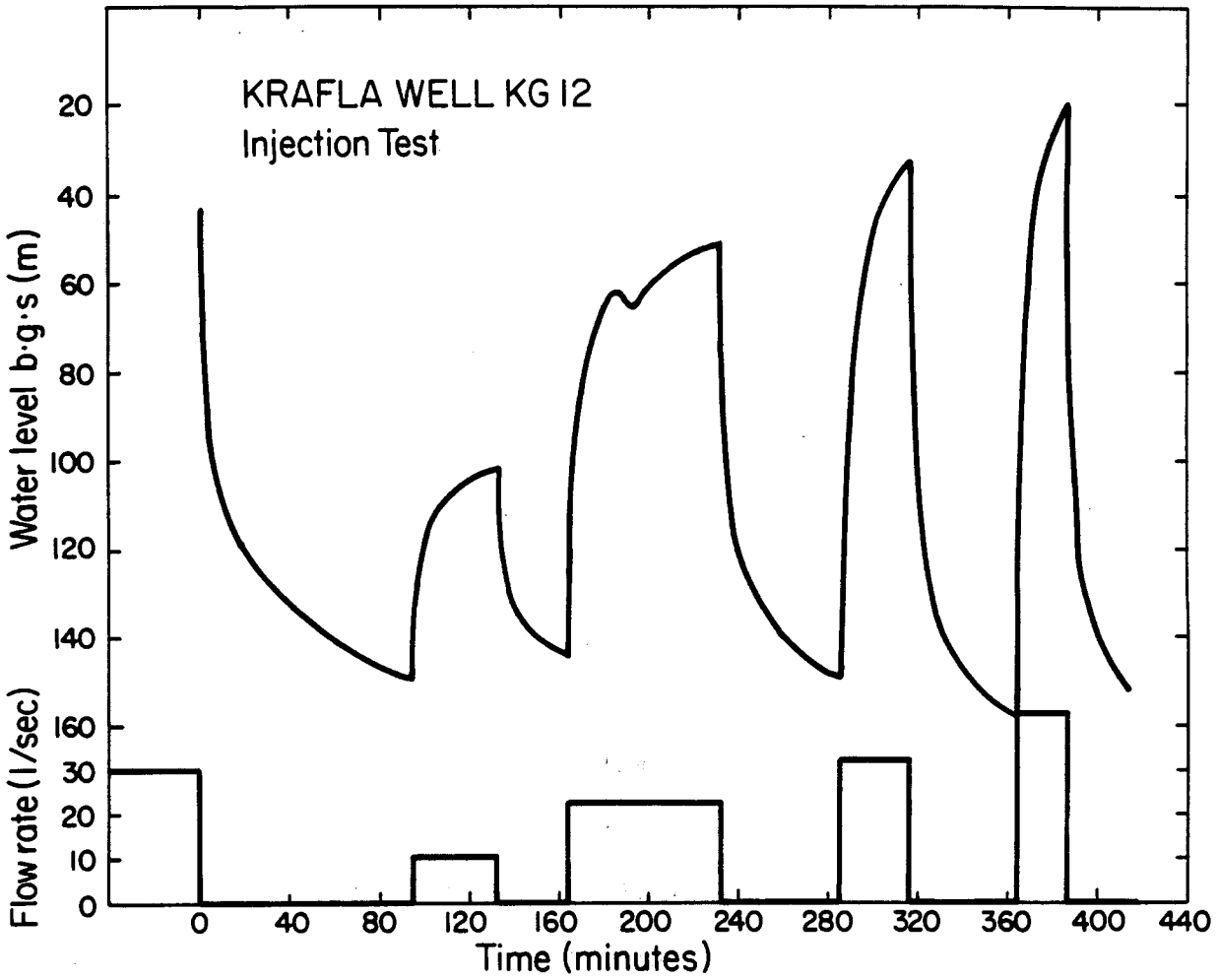

Figure 106. Injection-test data for well KG-12. [XBL 817-3300A]

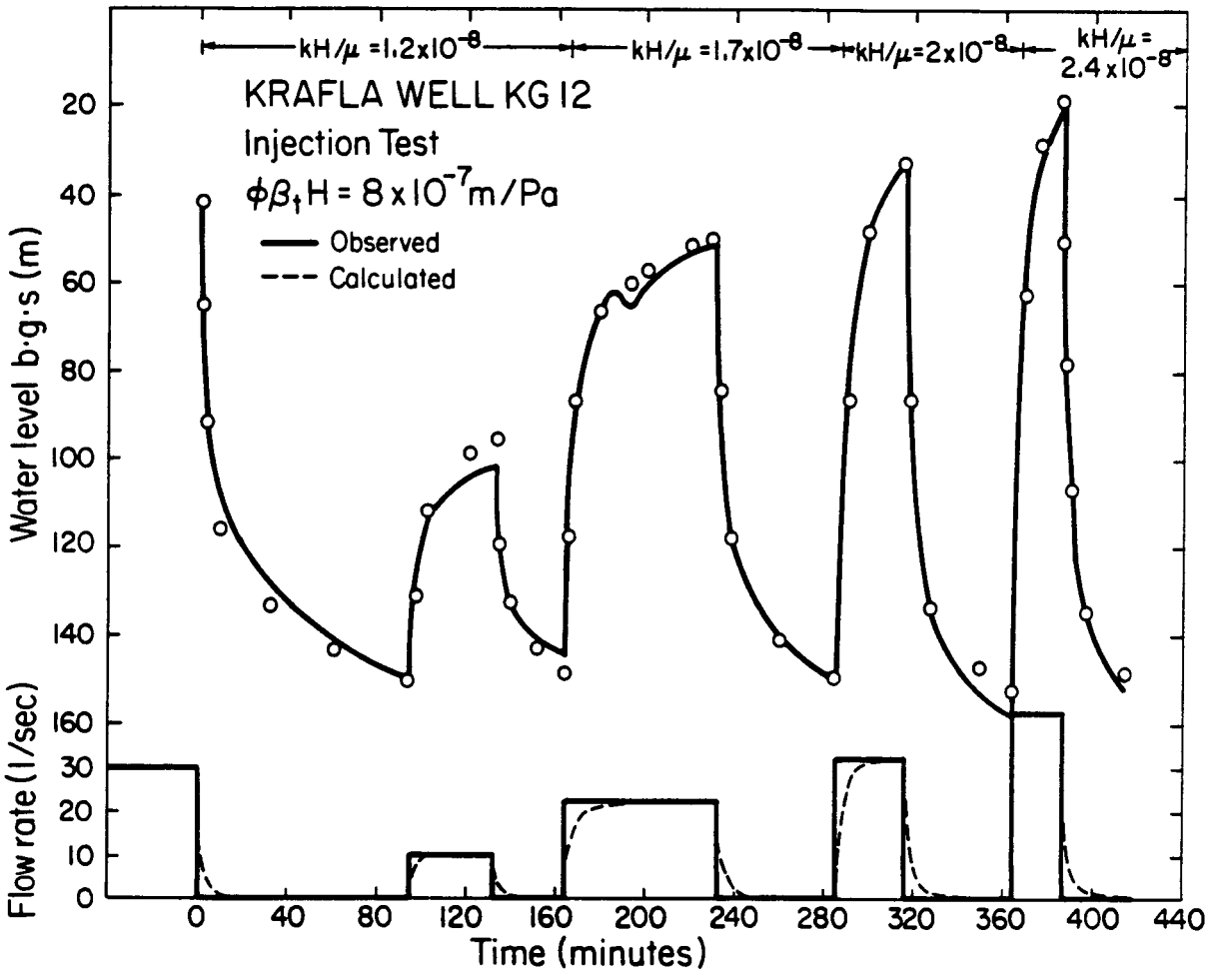

Figure 107. Comparison between calculated and observed water-level data for well KG-12. [XBL 817-3300B]

to the cold-water injection. In the simulation shown in Figure 107, the kH/μ factor was increased by a factor of two, from an initial value of 1.2×10^{-8} to a final value of 2.4×10^{-8}. This clearly illustrates that injection tests can greatly stimulate geothermal wells and probably increase the future productivity of the wells.

In the simulation shown in Figure 107, a constant storativity value was used, $\phi\beta_t H = 8 \times 10^{-7}$. This value is identical to the value obtained from the analysis of well KG-13. This indicates either a rather constant vertical distribution of the fluid reserves (ϕ and S_v rather uniform), or more likely, a fairly uniform fracture compressibility.

Conclusions

Injection tests from two wells at the Krafla field have been successfully analyzed using the numerical code PT in its isothermal mode. The tests were complicated by wellbore storage effects and possible non-isothermal effects. The analysis of the tests showed that nonisothermal effects are not present in the data; the probable explanation being that a cold-water zone is present around the wells during the tests. The results of the simulations provided an estimate of the transmissivity and the storativity of the formation around the wells. High values of the total compressibility is attributed to a high fracture compressibility. It was also shown in the analysis of one of the tests (KG-12), that permeability increases occur during the test. This indicates that injection tests may stimulate geothermal wells to become better producers.

FIELD-WIDE MODELING OF THE BACA GEOTHERMAL FIELD, NEW MEXICO

The Baca geothermal field is located in the Valles Caldera, New Mexico, about 55 miles north of Albuquerque. The field is being developed by the Union Oil Company of California and the Public Service Company of New Mexico. To date, over 20 geothermal wells have been drilled in the Valles Caldera, varying in depth from 2000 to over 9000 ft [Union, 1978]. Six of the wells have been drilled in the Sulfur Creek area, the remainder along Redondo Creek (Figure 108).

The wells in the Sulfur Creek area have penetrated a high-temperature but low-productivity formation. In the Redondo Creek area, the wells have encountered a high-temperature ($\geq$550°F) liquid-dominated reservoir. Interpretation of the well data by Union Oil (1978) indicates the presence of a liquid-dominated reservoir and a separate steam reservoir, which are not in hydraulic communication. However, a recent study by Grant (1979a) suggests that there is actually only one liquid-dominated reservoir, with an overlying two-phase zone.

It is extremely important to make reliable estimates of the mass of hot water in place (reservoir capacity) and the length of time the reservoir can supply steam for a 50 MW_e power plant (reservoir longevity). The reservoir longevity depends both on the reservoir capacity and on the overall development plan for the field (flow rates, injection, etc.). In this first study the reservoir capacity is estimated by volumetric calculations, using existing geological, well, and geophysical data.

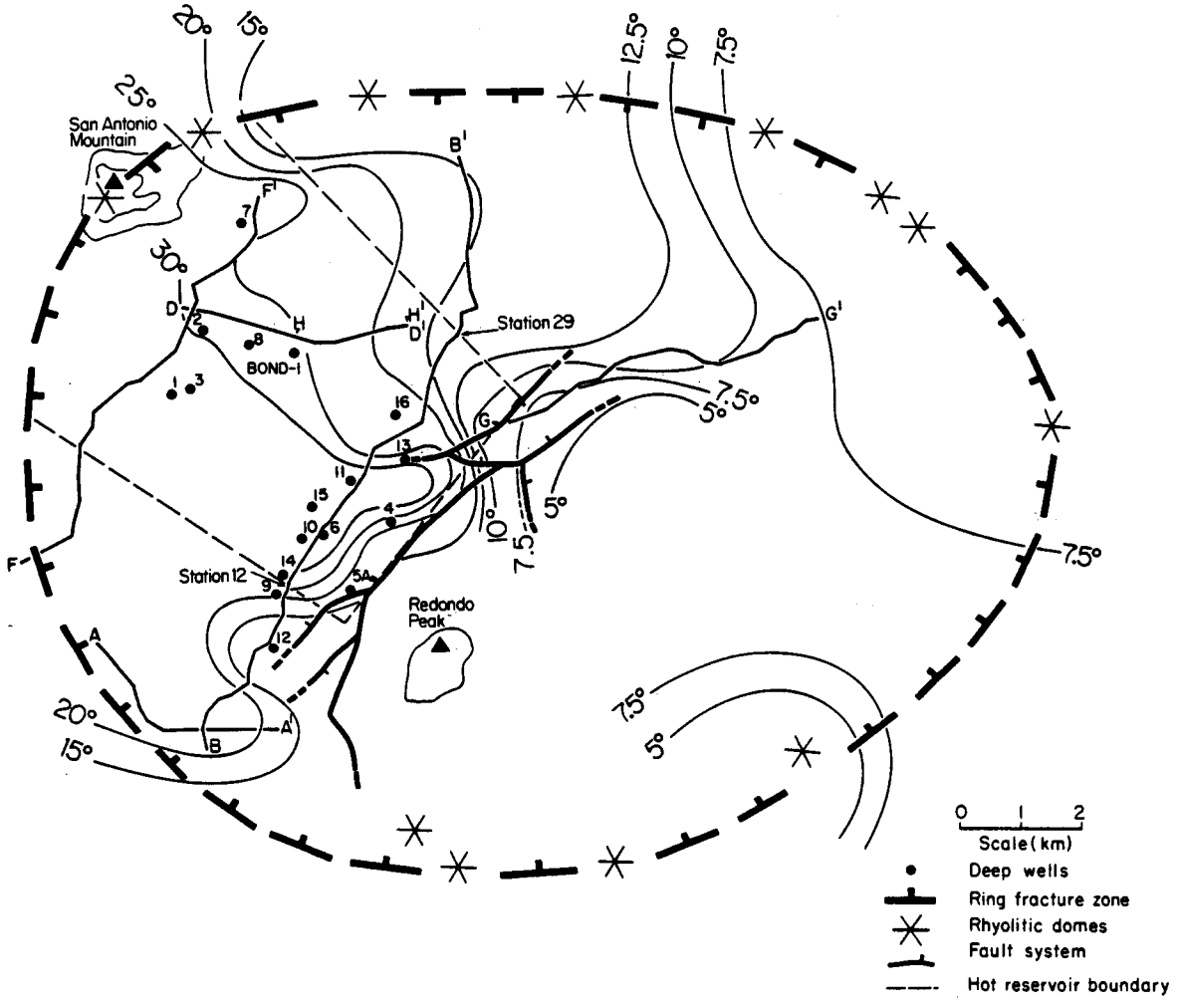

Figure 108. Base map of the Valles Caldera showing shallow temperature gradients (°F/100 ft), geophysical survey lines (e.g., A-A'), specific faults, and the estimated hot water reservoir boundary. [XBL 7912-13349]

An initial study of the reservoir longevity is also made using the two-phase numerical simulator SHAFT79 [Pruess and Schroeder, 1979]. Because of the lack of available data, a number of assumptions were made during the course of the study. Therefore, the results presented here should only be considered as estimates.

Geology

The topographically high Valles Caldera is a subcircular volcanic depression, 20 to 25 km in diameter, formed 1.1 million years ago. This resurgent caldera is characterized by a ring fracture zone where a number of rhyolitic volcanic domes are found [Union, 1978]. A broad structural dome, with a summit at Redondo Peak, is located near the center of the caldera and is bisected by a large northeast trending central graben (Redondo Creek). A detailed geological description of the Valles Caldera region can be found in Bailey and Smith (1978), Dondanville (1971), Slodowski (1977), and Sterbentz (1981). Geologic cross sections of the Valles Caldera region are shown in Figure 109.

The Bandelier Tuff is composed of several members of closely welded to nonwelded rhyolitic tuff and tuff breccia [Bailey and Smith, 1978]. Up to 1900 m (6300 ft) of the tuff have been penetrated by the wells in Redondo Creek. The matrix permeability of the tuff is generally low, but open fractures provide permeable channels in its deeper layers. The bulk of the produced water in the existing commercial wells comes from the Bandelier Tuff [Union, 1978].

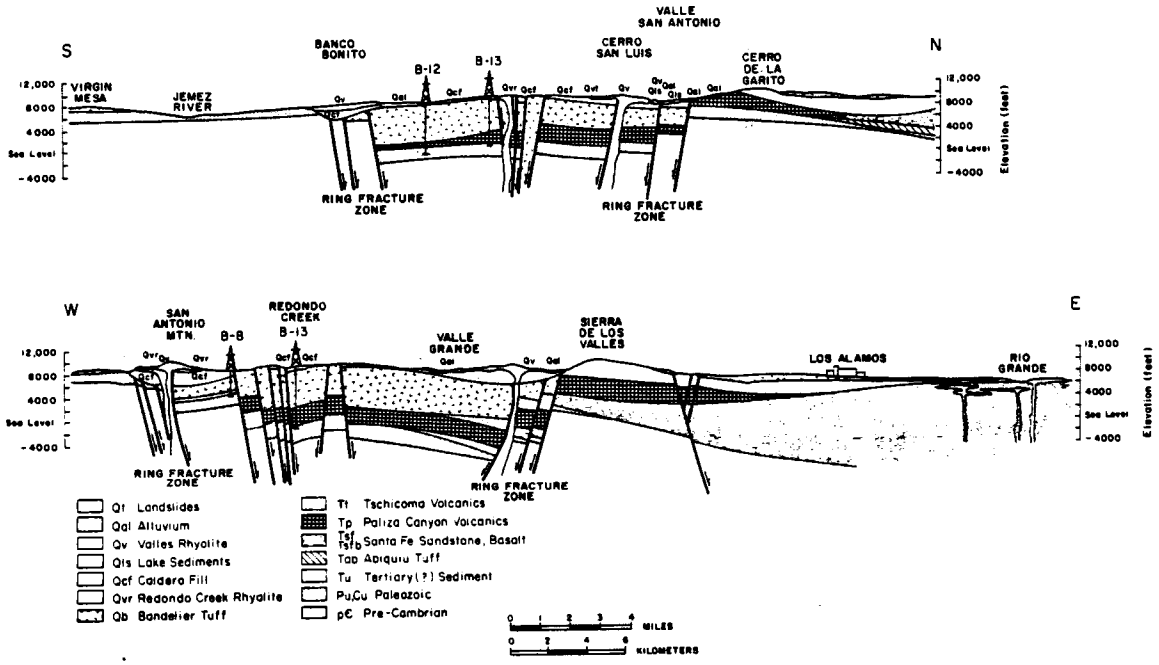

Figure 109. Geologic cross sections of the Valles Caldera region (after Bailey and Smith, 1978). [XBL 799-11548A]

The Paliza Canyon Andesite underlies the Bandelier Tuff and varies in thickness from 0 to over 600 m (2000 ft). It is believed to have low permeability due to its low matrix permeability and lack of open fractures [Union, 1978].

Some of the wells in Valles Caldera have penetrated a thin layer of poorly consolidated Tertiary sands and deeper layers of sedimentary rocks (Abo Formation). These overlie the basement rock in the Valles Caldera region, a Precambrian granite.

Reservoir Capacity

Volumetric Estimation

As a first step, we have made a volumetric estimation of the hot water contained in the reservoir (reservoir capacity). The parameters needed to calculate the reservoir capacity are the areal extent of the hot water zone and the average thickness and porosity of the reservoir. Geological information, well data, and shallow thermal-gradient contours were used to estimate the areal extent of the hot water zone. These data are supported by geophysical data from telluric and magnetotelluric (MT) surveys performed by Geonomics (1976), and a controlled-source electromagnetic (EM) survey performed by Group 7 (1972). Telluric data can give information regarding lateral variations in resistivity while magnetotelluric and electromagnetic soundings are mainly sensitive to resistivity variations with depth. The telluric and magnetotelluric lines are shown in Figure 108; the electromagnetic sounding points are not shown but they

form a discrete series of measurements through Redondo and Jaramillo creeks.

The reservoir temperature contours are coarse and not very reliable due to the limited amount of available data. The contours indicate, however, a sharp temperature gradient southeast of the main temperature anomaly (Figure 110). The shallow temperature gradient contour map (Figure 108) shows a similar sharp decrease in temperature to the east.

These gradients probably result from either the presence of a permeability barrier between Redondo Creek and Redondo Peak or an inflow of colder water from the southeast into the hotter reservoir. The mapped fault between Redondo Creek and Redondo Peak [Bailey and Smith, 1978] detected by telluric profile G-G' (Figure 108) tends to support the former explanation. We therefore assume that the hot reservoir boundary to the east lies between Redondo Creek and Redondo Peak.

The shallow temperature gradients and geophysical data were used to estimate the hot reservoir boundaries in the north-south direction. The deep reservoir contour map is too localized to give this information. Figure 111 shows the shallow temperature gradients and the telluric profiles along line B-B'. The telluric data indicate a resistivity low extending from station 12 to station 28 or 29, which corresponds well to the area of high thermal gradients. The higher frequency plots do not show this anomaly, suggesting that the conductor lies deep (the lower frequency signal penetrates deeper). Magnetotelluric data also show a

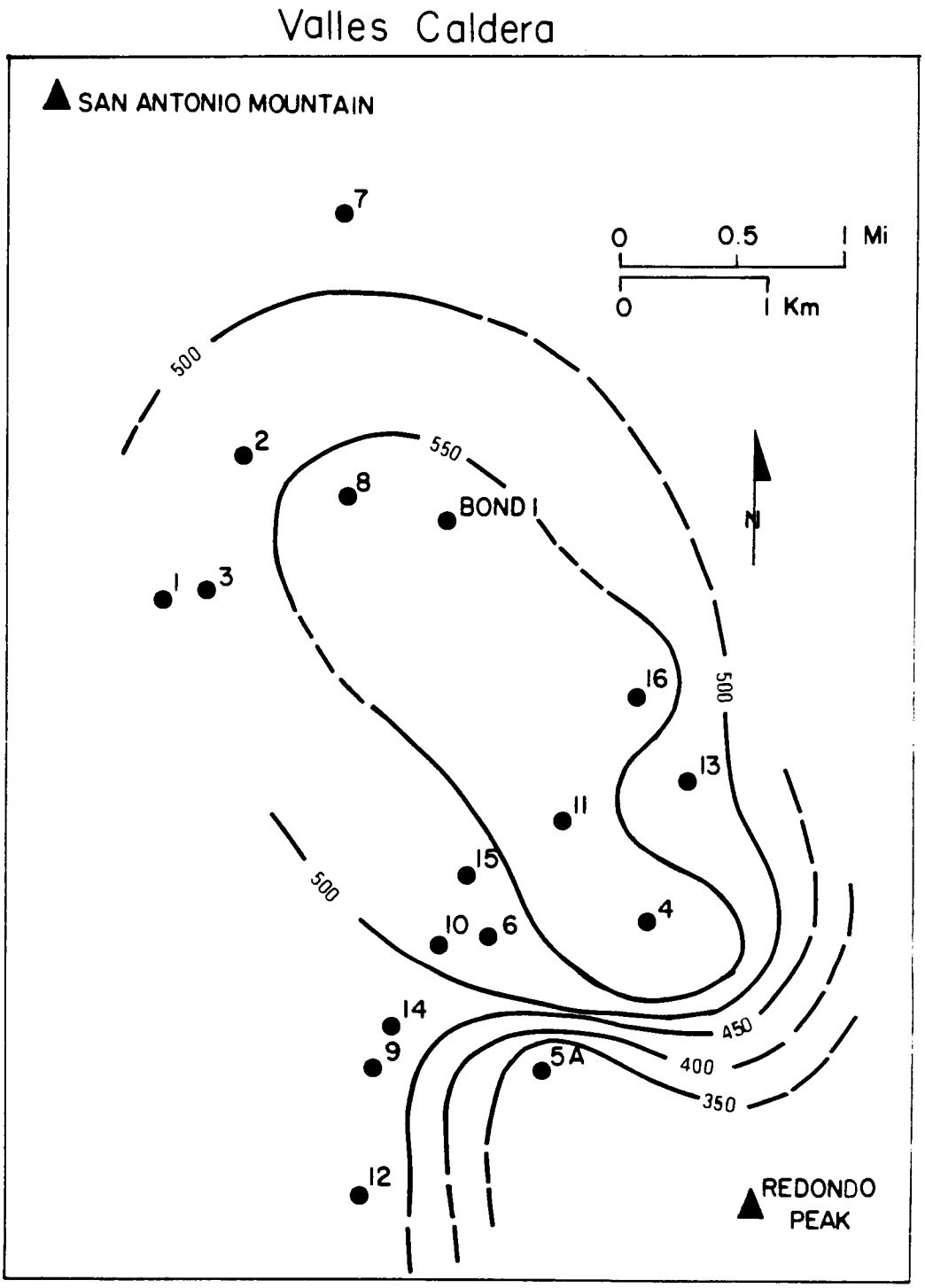

Figure 110. Deep reservoir temperature contour (3000 ft ASL) in °F (after Union, 1978). [XBL 794-7414B]

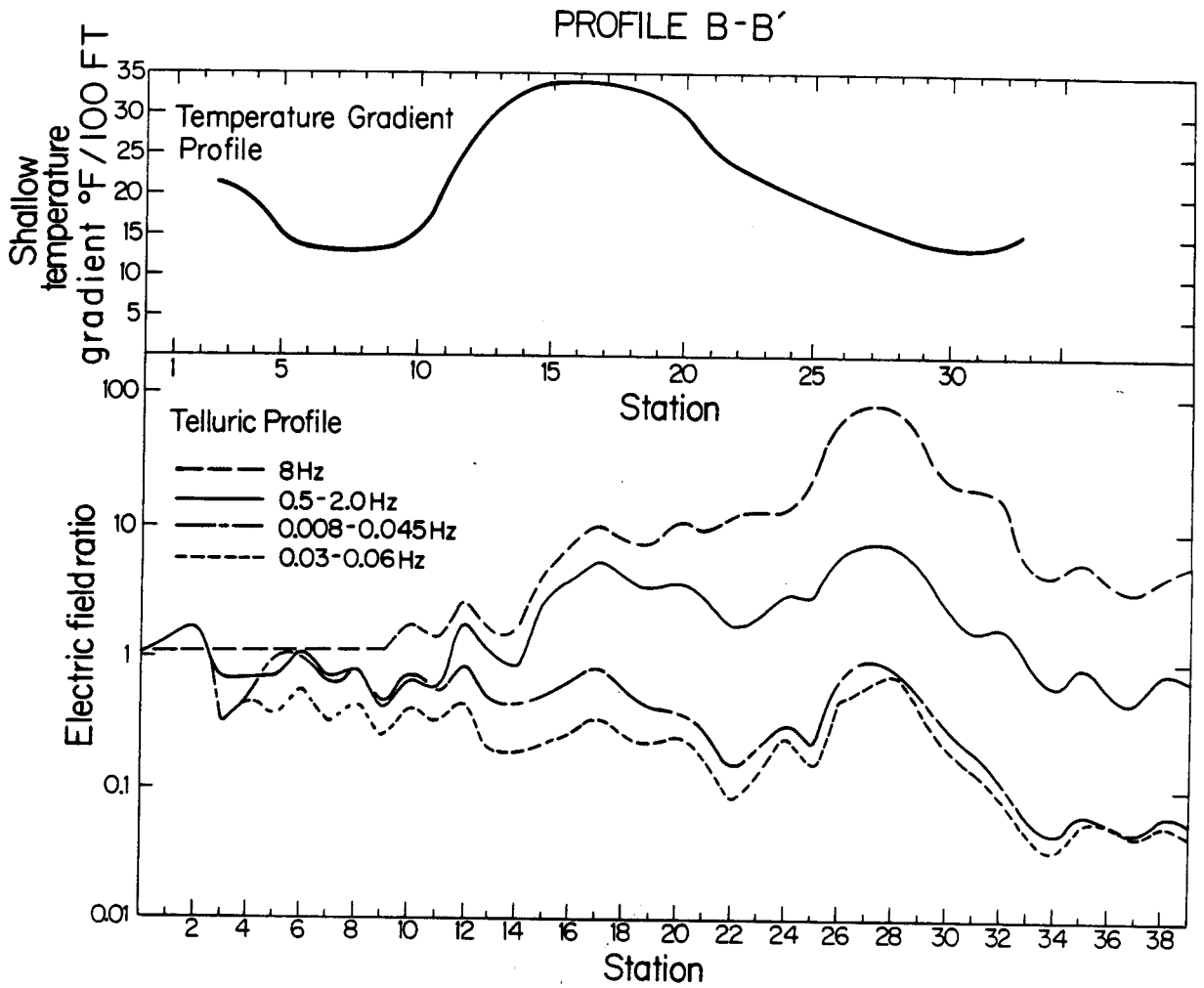

Figure 111. Shallow temperature gradients and telluric profiles along survey line B-B'. [XBL 7912-13350]

resistivity low over the same area and a layered resistivity model fit to the data indicates a conductor (5-20 ohm-m) at an approximate depth of 1 km [Group 7, 1972]. We will assume that the resistivity anomaly is due to the presence of the hot reservoir and that the boundaries of the hot reservoir correspond to stations 12 and 29 in the south and the north, respectively.

To the west, the temperature data are too limited to help establish the hot water reservoir boundary. The telluric profiles along lines D-D' and H-H' together with magnetotelluric data do, however, show a distinct resistivity contrast near the Bond-1 well; the low resistivity anomaly extends to the east. As the Sulfur Creek wells are hot but not productive, the resistivity anomaly seems to reflect formation porosity variations. Due to the lack of additional data to support this possibility we will assume that the reservoir extends as far west as the primary reservoir formation, the Bandelier Tuff. This assumption places the western limit of the reservoir at the ring fracture zone. From the above criteria, the estimated areal extent of the hot reservoir is approximately 40 km^2 (Figure 108).

The average thickness of the reservoir was estimated using the well temperature logs and geological data. The base of the caprock was estimated from the temperature logs as the depth at which convection starts to control the heat transfer (i.e., the depth where the temperature gradient becomes small). The bottom of the reservoir was assumed to

correspond to the bottom of the Bandelier Tuff (Figure 109), yielding an average reservoir thickness of 600 m (2000 ft).

Few data are available regarding the matrix porosity of the Bandelier Tuff. After studying well resistivity logs and core data [Core Laboratories, Inc., 1975], an average porosity of 5% was assumed. The product of the porosity and the thickness (ϕH) is then 30 m (100 ft), corresponding very closely to the value of 27 m (90 ft) obtained from the interference test in the Redondo Creek area [Union, 1978].

The estimated reservoir capacity can be calculated as a product of the areal extent of the hot reservoir and its average porosity-thickness product. Using a density of 825 kg/m^3 (for a temperature of 230°C) the reservoir capacity is 1.0×10^{12} kg (2.2×10^{12} lbs) of hot fluid.

Sensitivity of Results

In estimating the reservoir capacity, a number of assumptions were employed. Some of the more important ones are listed below.

1. The reservoir contains liquid water only.
2. The hot fluid reservoir extends to the northwest as far as the ring fracture zone.
3. The subsurface resistivity low is due to the presence of the hot-water reservoir.
4. The reservoir resides in the lower part of the Bandelier Tuff and does not extend into deeper formations.

If a two-phase zone overlies the main liquid water reservoir, the first assumption could lead to overestimation of the reservoir capacity. Similarly, if the reservoir does not extend all the way to the ring fracture zone as the dry wells in Sulphur Creek might indicate, the reservoir capacity might again be overestimated. If, on the other hand, the production reservoir is fed by a deeper source of hot water, the estimated value of the reservoir capacity may be too conservative.

Reservoir Longevity

Numerical Approach

The longevity of the Baca field was studied using the two-phase distributed-parameter model SHAFT79. The reservoir was simulated using one basic rectangular mesh, with overall dimensions corresponding to those estimated in the previous section (Figure 112). Due to symmetry, only half of the system was modeled. Rather than simulating individual wells, the fluid was produced uniformly over one node representing half of the well field (assumed to be 1 km^2).

The parameters used in the simulation are given in Table 10. Most of these parameter values were taken directly from open-file Union reports. For the permeability-thickness product (kH), the value 1.8×10^{-12} m^3 (or 6000 md•ft) obtained from the interference test performed by Union Oil (October 1975 to April 1976) was used. This value compares favorably with well test data from individual wells. The porosity-thickness product used was the value estimated in the previous section (30 m).

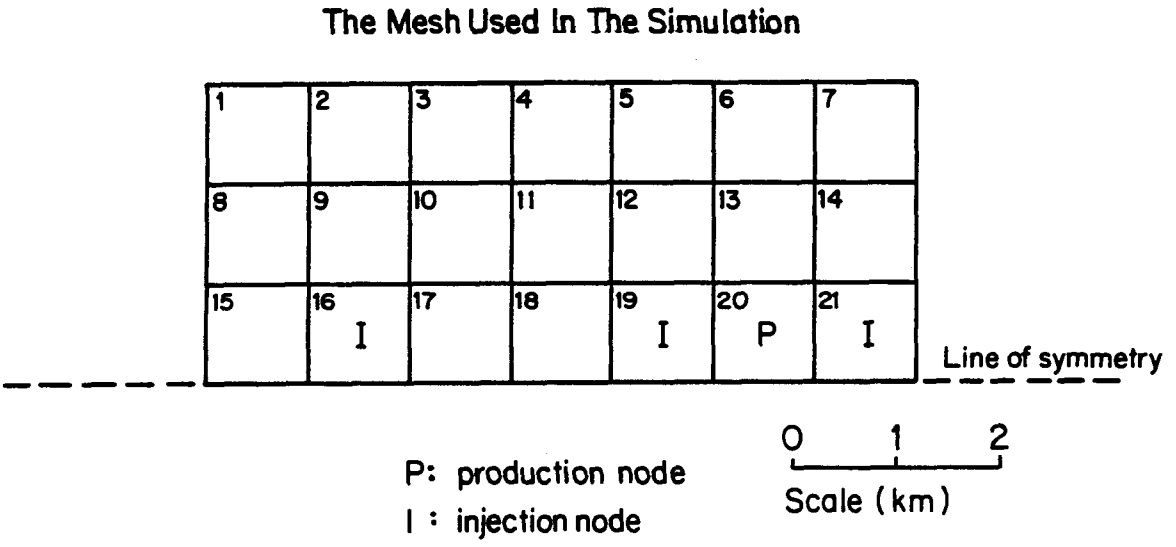

Figure 112. The mesh used in the longevity study for "closed reservoir" cases. [XBL 7912-13354]

Table 10. Parameters used in simulation of Baca Field.

Constant flow rate	q_t = 330 kg/s
Rock heat capacity	c_v = 950 J/kg·°C
Perm. thickness	kH = 1.8 x 10^{-12} m^3 (6,000 md·ft)
Thermal conduct.	λ = 2.0 J/s·m°C
Porosity thickness	ϕH = 30 m (100 ft)
Initial pressure	P_i = 110 bars
Initial temperature	T_i = 300°C

In the simulations a version of Corey's relative permeability equations was used [Faust and Mercer, 1979]. Mathematical expressions for Corey's 4th order equations are given in Table 5. The residual liquid and steam saturations were fixed at 0.30 and 0.05, respectively. In order to study the effects of the relative permeability curves on the results, various other curves were used. The findings of this study are discussed below.

Simulations Using a Constant Mass Flowrate

We studied five cases using a constant mass flow rate. The withdrawal rate was based on the amount of steam theoretically required for a 50 MW_e power plant and a constant value for the mass fraction of steam in the separators [Union, 1978]. The five cases studied were a bounded reservoir, an infinite reservoir, and three injection cases. Each case was run until the pressure in the production node dropped below the designed wellhead pressure of 10 bars [Union, 1978]. The longevity of the field in each case was defined as the time it took to reach this point.

The pressure, temperature, and vapor saturation at the production node are plotted versus time for three of these cases in Figure 113.

The simulation of the closed reservoir was terminated after 7.4 years due to the low pressure in the production node. As Figure 113 shows, the pressure falls very rapidly until the production node goes two-phase. Under two-phase conditions, the pressure is not related to the density but to the temperature. The pressure first stabilizes after the node becomes two-phase because of the the large heat capacity of the node and the low initial boiling rates. Later the pressure gradually declines along with the temperature. When the vapor saturation reaches 1.0, the pressure again becomes dependent on density, and the low inflow of fluid from adjacent nodes (due to the low absolute permeability and the effect of the relative permeability curves) causes the pressure to drop very rapidly.

Figure 114 shows the variation with time of the boiling rate at the production node, the vapor saturation of the produced fluids, and the vapor saturation in the adjacent nodes for the bounded reservoir case. The boiling rate increases rapidly soon after the production node becomes two-phase and reaches a maximum when only steam is produced. At that time the boiling rate corresponds to the production rate. Later, the boiling rate decreases again due to the decreasing mass of fluid entering the production region. The increasing vapor saturation in the nodes adjacent to the production node causes a reduction in the mobility of the

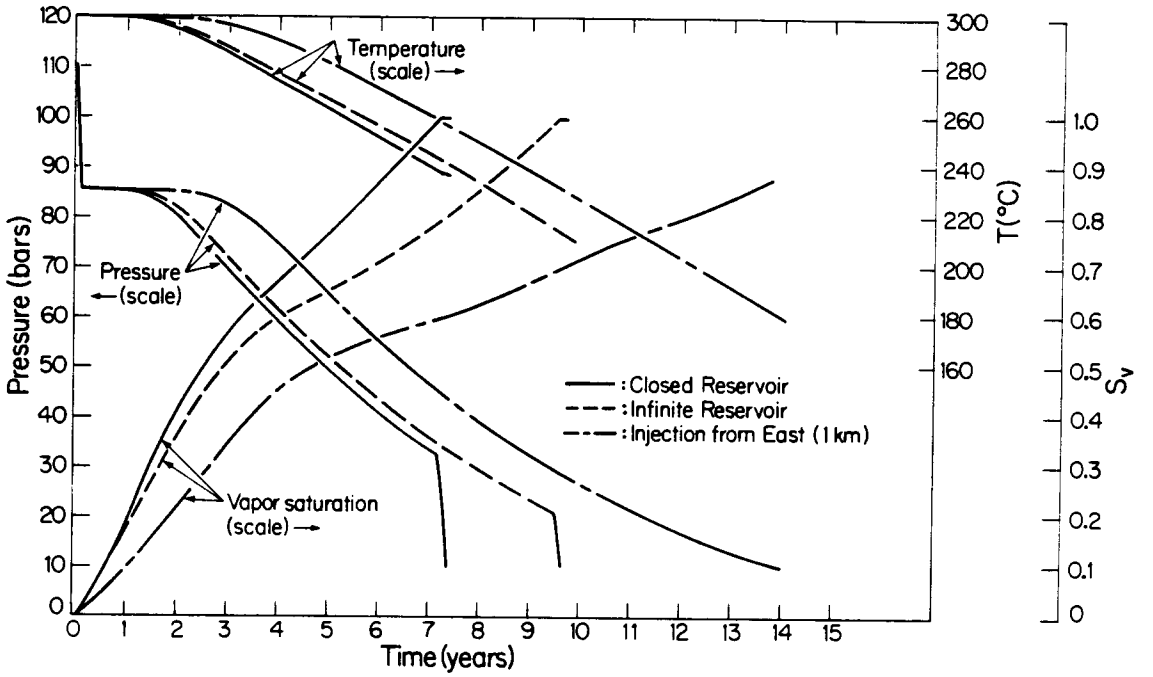

Figure 113. The temperature, pressure, and saturation behavior in the production node for three of the constant flow rate cases. [XBL 7912-13352]

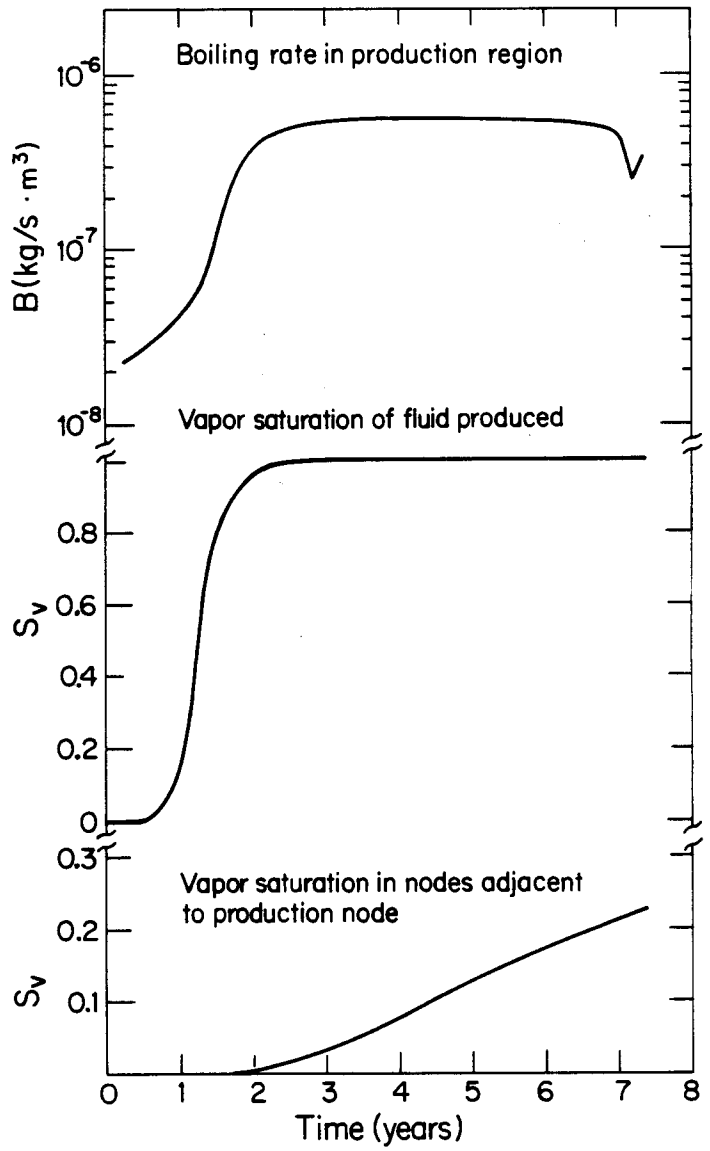

Figure 114. Variation with time of boiling rates and vapor saturation for the constant production, closed-boundary case.
[XBL 7912-13351]

liquid phase and consequently decreases the mass of fluid entering the production node.

For the infinite reservoir case a larger mesh (20 x 21 km^2) was used. The results indicate that the pressure in the production region will drop below 10 bars after about 10 years, again due to the limited flow of fluids into the production node (low permeability effects). The general behavior of the temperature, pressure, and vapor saturation is the same as for the bounded reservoir case (Figure 113). This shows that the factor controlling the longevity appears to be the low permeability-thickness product rather than the amount of hot water in place.

Three injection cases were simulated using an injection flow rate equal to half the production mass flow rate. The reservoir boundaries were closed. The water was injected 1 km to the southeast (node 21), 1 km to the northwest (node 19), and 4 km to the northwest (node 16) of the production region for the three cases. In each case the pressure in the production node dropped below 10 bars after 13 to 14 years.

Figure 113 also includes a plot of the temperature, pressure, and vapor saturation versus time in the production node when water is injected through node 21. The curves are similar to those for the no-injection case, except that the pressure falls below 10 bars before the production node reaches superheated steam conditions. This behavior is due to increased boiling in the production node since more water is coming in. The boiling causes the temperature, and consequently the

pressure, to drop steadily. The other two injection cases show similar behavior. Table 11 summarizes the results for the five cases.

Table 11. Summary of cases and primary results.

				Conditions at the end of the run			
Case	Flow rate	Boundary conditions	Injection	Time (yrs)	Pressure (bars)	Temp °C	Vapor saturation
1	Constant	Closed	None	7.4	10	237	1.0
2	Constant	"Infinite"	None	9.6	10	214	1.0
3	Constant	Closed	4 km to NW	12.9	10	180	0.99
4	Constant	Closed	1 km to NW	13.7	10	180	0.91
5	Constant	Closed	1 km to NE	14.0	10	180	0.87
6	Variable	Closed	None	25	10	214	1.0
7	Variable	"Semi-infinite"	None	26	10	213	1.0
8	Variable	"Infinite"	None	35	10	185	1.0
9	Variable	Bounded with a fault	None	50	10	180	0.48

Simulations Using a Variable Flow Rate

Generally during a simulation, the vapor saturation in the production node constantly changes, and consequently the steam quality in the separators changes. For a given power production a certain mass of steam is needed, and the amount of fluid mixture from the reservoir should be adjusted to meet that requirement. The assumption of a constant mass flow rate, which was used in the simulation described above, is therefore

inaccurate and leads to lower estimates of reservoir longevity. The variable flow rates are calculated using the same approach as is used in the section on exploitation strategies (see equations (45 and 46)).

Four cases were simulated using a variable flow rate; a closed reservoir, a semi-closed reservoir, an infinite reservoir, and a closed reservoir with recharge from deeper layers. In the semi-closed case, the northeast and the southwest boundaries were expanded from 3 to 10 km, leaving the other two boundaries unchanged. No injection runs were made, because very little separated water was obtained after about three years of simulation, and injecting such a small amount of water would not alter the results significantly. Figure 115 shows the calculated flow rate as a function of time for the bounded reservoir case.

The closed reservoir case and the semi-closed reservoir case gave very similar results; the pressure in the production node dropped below 10 bars after 25 and 26 years, respectively. In the "infinite reservoir" case the same large mesh was used (20 x 21 km^2), and the required amount of steam was supplied for 35 years before the pressure fell below 10 bars.

Finally, a run was made assuming that the reservoir was recharged from deeper layers through a 20 m-wide fault zone extending along Redondo Creek (recharging nodes 6, 13, and 20). The fault zone was modeled as a constant-pressure boundary 600 m below the assumed reservoir, having a permeability-thickness product of 1.8×10^{-12} m^3 (60,000 md·ft). The results obtained indicate a reservoir longevity of 49 years under these

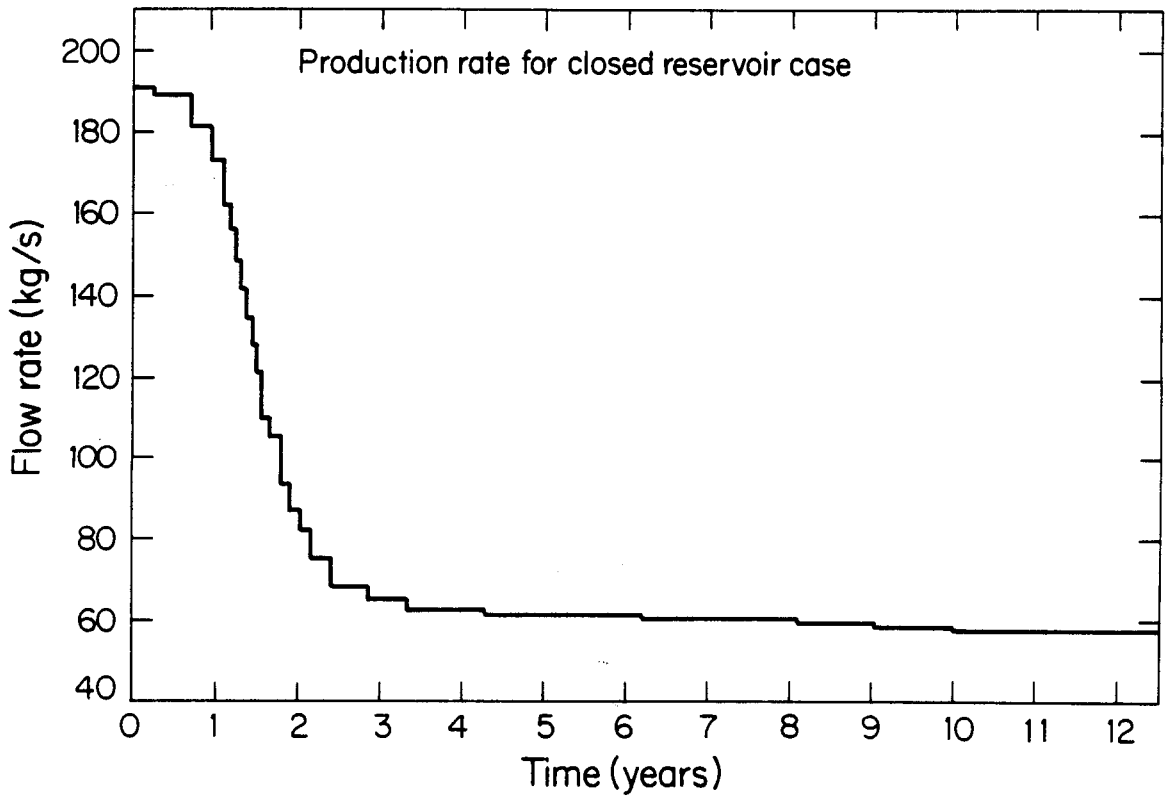

Figure 115. Production rate versus time for the closed-boundary case.
[XBL 7912-13353]

conditions. A summary of the results from these variable flow rate cases is included in Table 11.

Sensitivity of Results

In modeling two-phase flow in geothermal reservoirs, one must consider two important factors: the mesh dependence of the results, and how dependent the results are upon the particular relative permeability curves used. We conducted a brief study to determine the sensitivity of our results to these factors.

In order to determine the sensitivity of the results to the mesh used in the simulations, a new, finer mesh was constructed. The fine mesh consists of 81 elements, each element having a volume four times smaller than the corresponding element used in the earlier simulations (Figure 112). The production element, however, remained the same size. Using the fine mesh we studied the case of a constant mass flow rate with closed reservoir boundaries (case #1). Figure 116 shows a comparison between the fine and the coarse mesh results for the pressure behavior in the production node. Although the two curves are quite similar at early times, the curve corresponding to the fine mesh is shifted about 2 bars above the curve corresponding to the coarse mesh.

This behavior can be explained if one considers that in the case of the fine mesh, the nodes adjacent to the production node undergo phase transition (to a two-phase condition) at an earlier time than the larger nodes in the coarse mesh, and consequently steam flows into the production

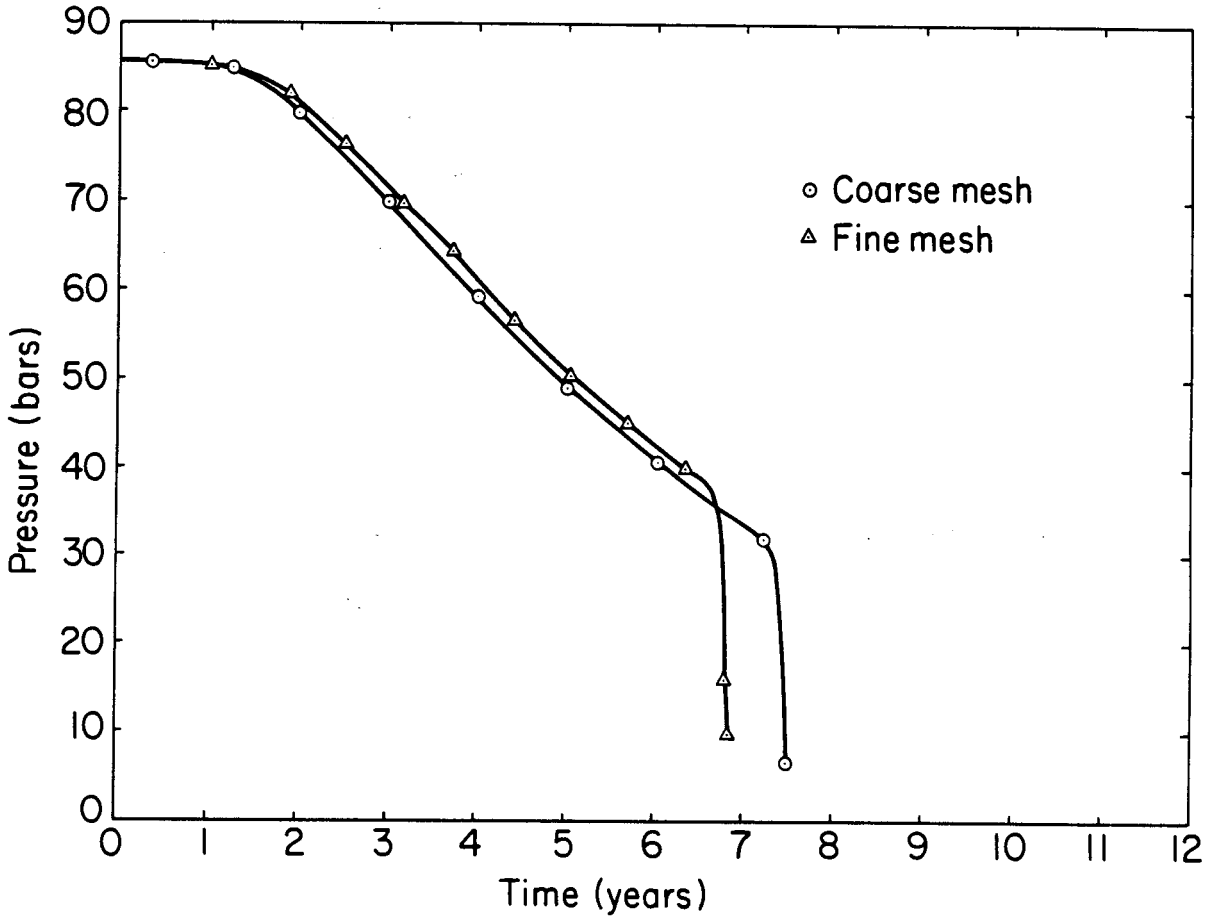

Figure 116. Mesh-dependence: pressure behavior in the production node.
[XBL 807-7248]

node at an earlier time. This in turn implies that less boiling will be required in the production node in the case of the fine mesh at any given time, resulting in a smaller pressure drop. However, the higher steam flow into the production node in the case of the finer mesh causes a higher vapor saturation at any given time in the node, so that superheated conditions are reached earlier. It is therefore apparent that in terms of longevity, the coarser mesh gives results that are slightly more optimistic (increased longevity) than what might be expected.

In our study of the effects of the relative permeability curves on our results, we used curves suggested by Counsil and Ramey (1979) and Grant (1977) in addition to the Corey curves. The curves by Counsil and Ramey are based upon experimental results over a small range of vapor saturation ($.20 < S < .30$), and for our simulation studies the data was linearly extrapolated to cover the full range of saturation. The curves developed by Grant are based upon data from the Wairakei geothermal field. The relative permeability of the liquid is the same as given by the 4th order Corey equations, but the steam phase is considerably more mobile. Mathematical expressions for the curves used in this study are given in Table 12, and the curves are illustrated in Figure 117.

Figure 118 shows pressure behavior at the production node for case #1 and different relative permeability curves. The figure shows that the longevity (the time when the pressure falls below 10 bars) is basically unaffected by the particular relative permeability curve chosen. The pressure plots based on the Counsil and Ramey curves lie at all times

Table 12. Relative permeability equations (plots are shown in Figure 117).

1. Corey's Curves:

$$k_{rw} = \begin{cases} [S^*]^4 & S < S_{rw} \\ 0 & S \geq S_{rw} \end{cases}$$

$$k_{rv} = \begin{cases} 1 - S^*]^2[1 - (S^*)^2] & S > S_{rv} \\ 0 & S \leq S_{rv} \end{cases}$$

where $S^* = \dfrac{1 - S_{rw} - S}{1 - S_{rw} - S_{rv}}$

2. Grant's Curves:

$$k_{rw} = \begin{cases} [S^*]^4 & S < S_{rw} \\ 0 & S \geq S_{rw} \end{cases}$$

$$k_{rv} = 1 - k_{rw}$$

3. Counsil and Ramey's Curves:

$$k_{rw} = \begin{cases} 1 - \dfrac{S}{.30} & S < .30 \\ 0 & S \geq .30 \end{cases}$$

$$k_{rv} = \begin{cases} \dfrac{S - .20}{80} & S > .20 \\ 0 & S \leq .20 \end{cases}$$

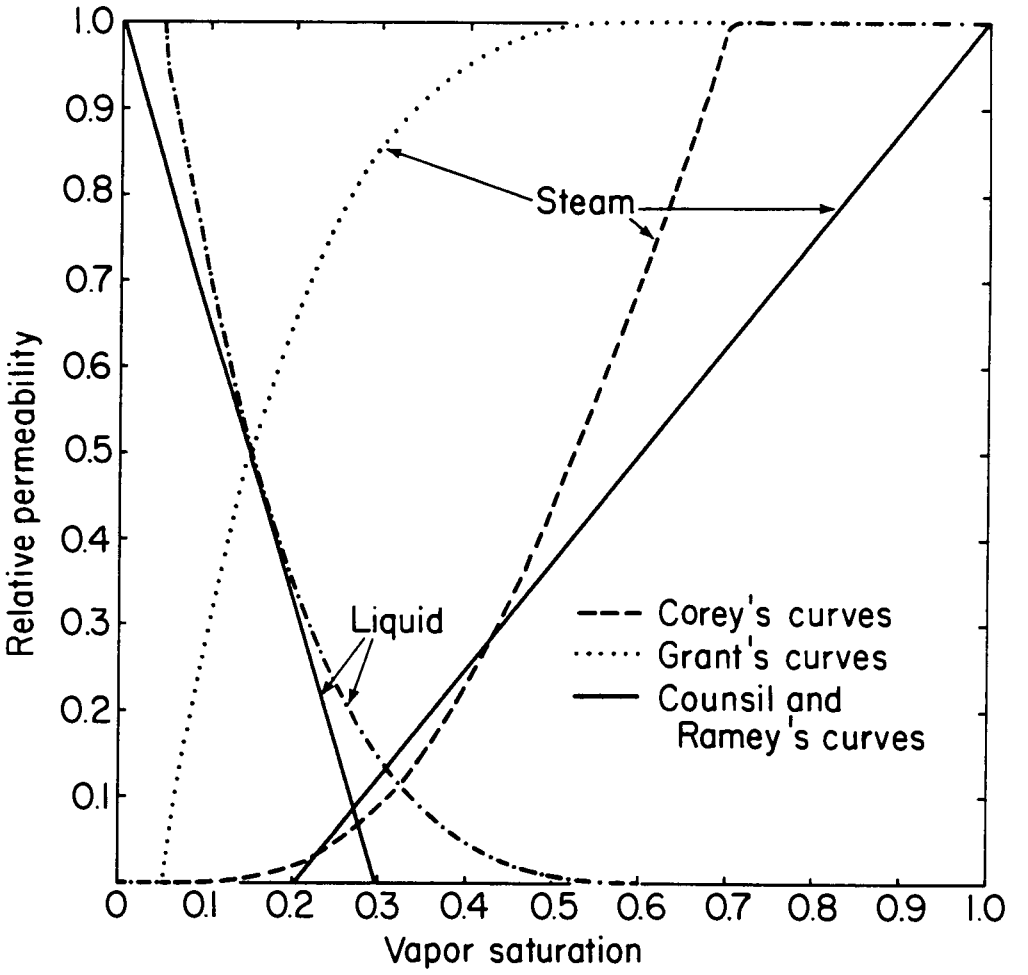

Figure 117. Relative permeability curves used in the study.
[XBL 807-7250]

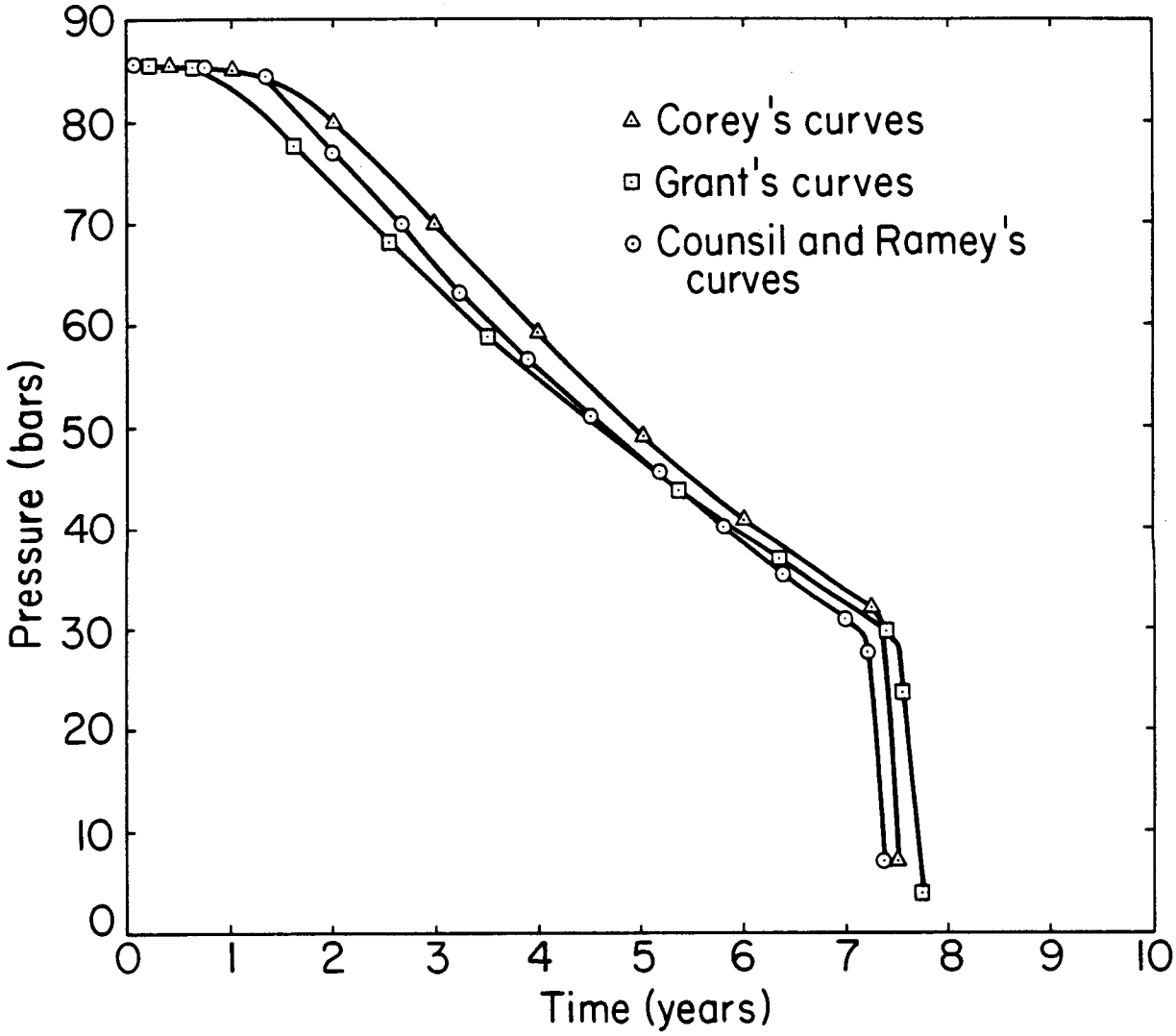

Figure 118. Effects of relative permeability curves. [XBL 807-7249]

below the results based upon Coreys equations. This is to be expected since the mobilities of the steam and the liquid are generally less in the case of the Counsil and Ramey curves. The pressure behavior based on Grant's curves is less at early times than in the case of Corey's curves, because more of the steam is being produced and consequently, more boiling occurs in the production node. One must keep in mind that the mass ratio of steam and liquid produced depends on the relative permeability curves used. However, in the case using Grant's curves, the longevity is slightly higher, because of the much more mobile steam phase.

In addition to the runs shown in Figure 118, a couple of runs were made using modifications of the curves by Counsil and Ramey. In the first run the steam was made immobile at a vapor saturation of 0.60, but the relative permeability of the steam increased linearly, becoming fully mobile at a vapor saturation of 1.0. The results obtained agreed very closely with the former run using Counsil and Ramey's curves, indicating that the steam relative permeability curve may not be very important for this problem.

In the second case studied, the residual water saturations were fixed at 0.60, and the curves were again linearly extrapolated so that the liquid phase becomes fully mobile at a vapor saturation of 0.0. In this case the longevity increased to almost 9 years. The increased mobility of the water phase causes considerably more liquid to enter the production node and consequently the longevity increases.

A brief study was made of the effects of the relative permeability curves on the longevity when a variable mass flow rate is used. In the study the curves of Counsil and Ramey were used and the results compared to those obtained when the Corey curves were used. The results compared quite well and a longevity of 23 years was obtained for the former case, compared to 25 years for the latter (case #6).

Comparison between lumped- and distributed parameter models with application to Baca.

It is of interest to compare the lumped-parameter approach to the distributed-parameter approach for the Baca field. As lumped-parameter models are widely used for predicting the response of geothermal reservoirs to exploitation, some discussion of the basic approach is in order. In the lumped-parameter method the reservoir is characterized by one, two, or three homogeneous blocks, and therefore spatial variations in thermodynamic variables (T,P,S), fluid and rock properties are more or less neglected. Application of mass and energy balances to these blocks results in a set of linear ordinary differential equations. The equations are generally readily solvable analytically, although in some cases numerical integration is necessary.

The first lumped-parameter model developed for a geothermal field is that of Whiting and Ramey (1969) for the Wairakei geothermal field in New Zealand. They obtained excellent fit with average field pressure for the time period 1956-1965, and predicted the field behavior from 1966-2000.

More recent data from Wairakei have not corresponded well to the predicted pressure behavior by the lumped-parameter model [Witherspoon et al., 1975]. Other lumped-parameter models have been developed and applied to the Wairakei geothermal field [McNabb, 1975; Grant, 1977a; Robinson, 1977]; these are summarized by Fradkin et al. (1981). Other developers of lumped-parameter models are Castanier et al. (1980), who applied their model to the East Mesa geothermal field in the Imperial Valley, and Brigham and Morrow (1974) who developed a lumped-parameter model (the so-called P/Z model) for vapor-dominated fields.

Distributed-parameter models, as discussed in an earlier section, are those which consider spatial variations in the dependent variables in addition to the variations with time [Brigham and Morrow, 1974]. In addition, the physical properties of the fluid and/or the rocks are allowed to vary spatially. Therefore, numerical models are in general much more flexible than analytical models. Numerical methods involve dividing the area of interest (the geothermal reservoir) into elements (blocks), and applying mass and energy balance principles to each element. For each element two equations are present, and simultaneous solution of all of the equations for all of the nodes will enable determination of the unknowns (e.g., pressure and temperature). The numerical model requires a prior knowledge of the initial conditions, but the boundary conditions are in the geometric design of the problem. Advancement in time is acquired by solving the equations at each time step, and then reassigning the primary variables their new value, before attempting the next time step.

In recent years there has been considerable discussion regarding the distributed-parameter models, and their application to geothermal reservoir engineering. These models have frequently been compared to lumped-parameter models [Fradkin et al., 1981; Castanier et al., 1980; Castanier and Sanyal, 1980; Donaldson and Sorey, 1979], and evidence was advanced that the lumped-parameter models have been more accurate in predicting the field behavior of the Wairakei geothermal field than distributed-parameter models [Fradkin et al., 1981; Donaldson and Sorey, 1979]. However, it appears that some important considerations have been overlooked or simply neglected in this comparison. It is also generally stated that distributed-parameter models are far too complicated and expensive for modeling of geothermal fields for which data are limited. However, one must realize that lumped-parameter models are the complete equivalent of distributed-parameter models with coarse space discretization and constant fluid and rock parameters. Instead of developing a lumped-parameter model, one therefore need only employ a distributed-parameter model, with only a few nodes representing the geothermal system. In this way the same accuracy (or inaccuracy) will be obtained at a very low cost, as the cost of running distributed models with few elements is negligible.

Another point that is generally overlooked is that lumped-parameter models are only applicable when spatial variations in rock properties and the distribution of the fluid reserves can be neglected. The most important parameter in determining the applicability of lumped-parameter

models to a geothermal field may be the rock (fracture) permeability. In cases of low-permeability reservoirs, production will generate large spatial variations in pressures, and the fluid transport in the reservoir becomes a critical issue. As lumped-parameter models are equivalent to distributed-parameter models, with a severely limited transport function, the potential generating capacity of the geothermal reservoir will be grossly over-estimated if the lumped-parameter approach is employed.

In the case of the Wairakei geothermal field, the lateral permeability is very high [Fradkin et al., 1981], and therefore lumped-parameter models may adequately predict the reservoir's response to exploitation. However, in cases where the permeability is low (e.g. East Mesa, California; Baca, New Mexico; Olkaria, Kenya; Krafla, Iceland), the use of lumped-parameter models will lead to gross over-estimation of the generating capacity of the reservoir.

Fiqure 119 shows how the lumped-parameter models can overestimate the recovery of energy from low-permeability geothermal fields. A simple radial geometry of a geothermal reservoir is considered, with a well field of radius r_w, and a reservoir radius of r. Figure 119 was developed by assuming various values for r^2/Hr_w and running models for a range of values for q/kH. Results from a distributed-parameter model are compared to those from a lumped-parameter model. For a high value of permeability (or low extraction rate q), the lumped-parameter model correctly predicts the recovery ratio, as uniform depletion will occur in the reservoir. However, at low values of permeability (or equivalently high

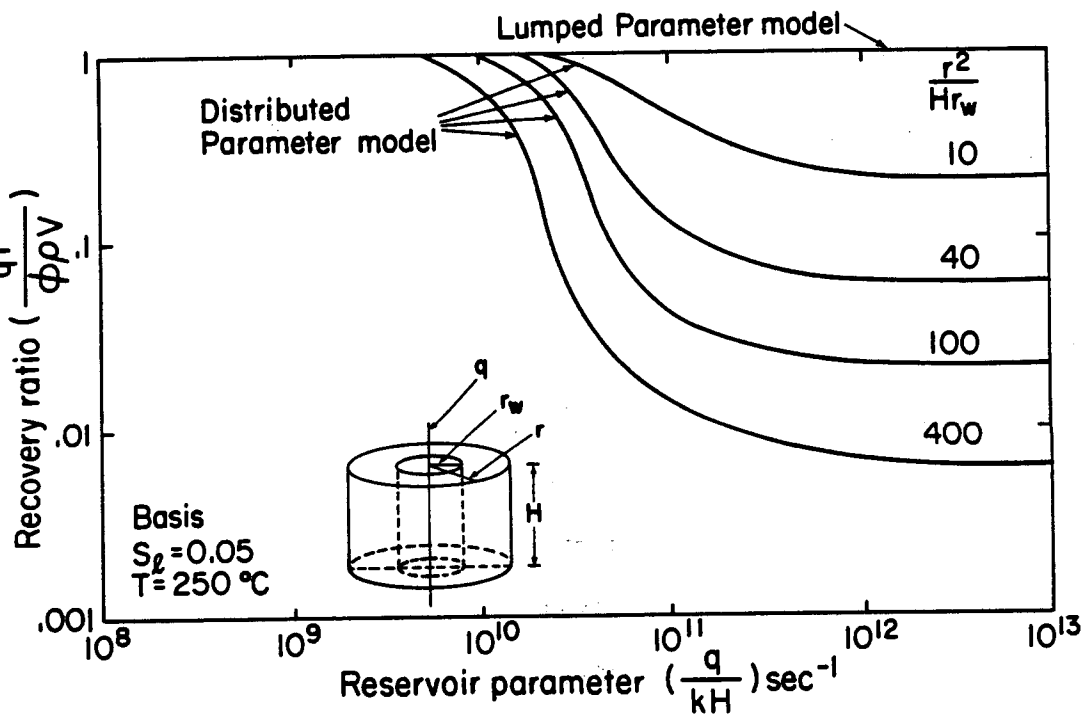

Figure 119. Comparison between lumped- and distributed-parameter models. [XBL 8111-4840]

extraction rates), the predicted recovery ratio by the lumped-parameter model is much too high. Consequently, if the developer of the field utilizes results given by the lumped-parameter model he will grossly overestimate the generating potential of the field, and an incorrect development plan will result.

For direct comparison with the distributed-parameter results some calculations for the Baca reservoir were carried out using the lumped-parameter method. In the lumped-parameter approach a single element representing the entire reservoir was used. The steam required for a 50 MW_e power plant was produced from this element in an identical manner as previously explained in the simulations using the distributed-parameter model. The reservoir volume, previously estimated, was used as the volume of the reservoir element. The reservoir boundaries were assumed closed to mass and heat flow. The results obtained indicated that the Baca reservoir was capable of providing steam for a 50 MW_e power plant for 400 years. At the end of the simulation, the reservoir had become saturated with superheated steam; thus, the bulk of the mass initially contained in the reservoir had been depleted.

Comparison of the results of the lumped-parameter model to those of the distributed-parameter model (Table 11) clearly illustrate why lumped-parameter models are not applicable to low-permeability geothermal reservoirs such as the Baca reservoir. The lumped-parameter approach assumes an infinite fluid transport potential of the reservoir. In cases of low-permeability reservoirs such as the Baca reservoir, this leads to a gross

overestimate of the potential power-generating capacity of the reservoir. The results from the simulation studies using the distributed-parameter model clearly illustrates that the longevity of the Baca reservoir is limited by the restricted flow from the reservoir into the production region. The limited transport functions inherent in the lumped-parameter approach, therefore, make lumped-parameter models inapplicable to the Baca reservoir. This can be illustrated using Figure 119. For a 50 MW_e power plant, $q/kH = 2 \times 10^{11}$ for Baca, and using the estimated areal and vertical dimensions of the reservoir, $r^2/Hr_w \simeq 40$. Comparison of these numbers with the data in Figure 119 yields a recovery ratio of only .03. This value is consistent with the results obtained using the distributed-parameter model.

Conclusions

We have estimated the reservoir capacity of the Baca field using the volumetric approach, and the longevity using a volumetric approach and the numerical simulator SHAFT79. The areal extent of the hot reservoir was estimated to be 40 km^2 and the porosity-thickness product to be 30 m. These values correspond to a reservoir capacity of 1.0×10^{12} kg of hot fluid in place.

We also studied the longevity of the Baca field, using either constant or time-dependent production rates. Five cases were studied using the constant rate: one closed reservoir, one infinite reservoir, and three injection cases. All of these cases showed that the flow rate could be maintained no longer than 15 years due to the resulting low

pressure in the production region. In a low-permeability reservoir which the Baca reservoir appears to be, the boiling is very localized, causing a rapid drop in the temperature and, subsequently, in the pressure in the production region. The constant flow rate cases represent an overly pessimistic situation, because the steam quality of the produced fluids increases with time, and consequently a smaller total amount of fluid is actually needed for a 50 MW_e power plant.

For the cases of variable production the flow rates are calculated based on the steam required for a 50 MW_e power plant and the steam fraction in the separators. These runs indicate a reservoir life of 25 to 49 years, depending upon the assumed reservoir boundary conditions.

In studying the sensitivity of our longevity estimates, we have found that the results are mesh-dependent to some degree and that the longevity values obtained by using the coarse mesh may be slightly optimistic. A brief study using relative permeability curves suggested by Counsil and Ramey and by Grant seems to indicate that the results on longevity are not very sensitive to the particular relative permeability curves chosen. The key factor is the mobility of the liquid phase. If relative permeability curves are employed where the liquid phase is more mobile than in the curves we have used, the longevity may increase considerably.

In general, the studies of the longevity of the Baca field seem to indicate the following:

1. The controlling factor in determining the longevity of the Baca reservoir is the kH product of the system. The low kH product (6000 md·ft) obtained from well tests at Baca drastically limits the longevity of the field (see Table 11). This indicates the urgent need to determine the kH product more accurately, perhaps using an injection test rather than drawdown tests.

2. Placing the production wells over as large an area as possible will help to obtain the required steam supply, without reducing the pressure below a critical value.

3. Injecting the waste water should increase the lifetime of the field considerably, but the available waste water may become very limited shortly after power production starts.

4. The use of lumped-parameter models to estimate the generating potential of a low-permeability reservoir such as the Baca reservoir will lead to very optimistic results. This is obvious, when one compares the distributed-parameter model results to those obtained by the lumped-parameter method.

Since a number of assumptions were necessary in carrying out this analysis, it should be realized that the results should only be considered as rough estimates.

SUMMARY OF FIELD APPLICATIONS

In this chapter, the use of numerical simulators for the analysis of geothermal reservoir data has been illustrated. Numerical analysis of two injection tests of wells at the Krafla geothermal field in Iceland yielded values for important reservoir parameters, kH/μ and $\phi\beta_t H$. The simulation results indicated that the isothermal nature of the injection test data is due to the cold water zone around the wells, from cold water injection during drilling as well as directly prior to the injection tests. The high compressibility values obtained from the tests could be due to the presence of two-phase fluids as well as to fracture deformability. The analysis indicates that the latter explanation is more likely.

Field-wide simulation studies are carried out for the Baca geothermal field in New Mexico. Existing geological, geophysical, and well data are used to estimate the reservoir capacity of the field. Numerical simulation studies are carried out to examine the longevity of the field when fluids equivalent to 50 MW_e are produced. These studies indicate that, due to the low transmissivity of the Baca reservoir, it is questionable whether the reservoir will be able to deliver steam for a 50 MW_e power plant for the designed lifetime of 30 years. It is emphasized that the size of the production area is of great importance, and in the case of Baca the production area should be kept as large as possible. It is furthermore illustrated that the low transmissivity will cause a rapid

increase in the steam quality at the separators with time and consequently waste water available for reinjection purposes will be severely limited soon after production starts.

In summary, the examples illustrated above show that numerical simulators can be of great use to the developers of geothermal fields. In the case of well-test analysis the simulator can account for wellbore storage effects, nonlinear thermal effects, and nonsymmetrical heterogeneous fractured or porous media formations. This will greatly increase the confidence of the field developer in the results, and he will be able to use them in his future decision making.

The results from the Baca simulations show how numerical simulators can help in determining the power potential of a geothermal field. This may be one of the most important applications of numerical simulators, as it is of great economic importance that the potential capability of a geothermal resource is not over- or underestimated. On the other hand, results obtained using the lumped-parameter approach may considerably overestimate the generating potential of a field. The economic feasibility of geothermal projects should therefore be determined based on numerical simulation results.

CONCLUSIONS

The primary objective of the work presented in this dissertation is to apply mathematical modeling techniques to geothermal systems in order to obtain a better understanding of their behavior under exploitation. The presently available mathematical techniques for simulations of geothermal systems can be classified into three groups, empirical, analytical, and numerical methods. Of these, the numerical methods are undoubtedly the most general, as numerical simulators have been developed to solve highly nonlinear problems such as heat and mass transfer in geothermal reservoirs. However, analytical methods are quite useful in solving simplified linear problems, as basic parameter groups of particular importance in the problem can be identified. Having identified these parameter groups by the analytic methods, a more complete solution of the real nonlinear problem can be obtained using numerical simulators. Empirical methods can sometimes be used in predicting the flow rate decline of individual wells, and also for predicting future pressure decline of a geothermal field. However, this method is not applicable in general and will therefore not be discussed further.

The approach taken in the present work is to apply analytical and numerical methods to geothermal systems. As a first step, a new three-dimensional numerical simulator capable of solving mass and heat transfer problems involving the flow of single-phase liquid water in heterogeneous porous or fractured medium is developed. The simulator named PT (Pressure and Temperature) uses the integrated finite difference method (IFDM)

for discretizing the flow regime and for the numerical formulation of the basic mass and energy transport equation. It is quite general, as it allows for temperature-dependent rock properties, and temperature- and pressure-dependent fluid properties. The simulator employs an efficient sparse matrix solver for the linear equations developed in each time step.

Along with analytical techniques, the simulator PT as well as the two-phase simulator SHAFT79 have been employed in solving some theoretical problems of current interest to the geothermal community. These include well-test analysis of single- and two-phase reservoirs, production strategies from two-phase geothermal reservoirs, injection of cold water into fractured geothermal reservoirs, and recharge into fault-charged geothermal reservoirs. Some of the primary conclusions obtained from these studies are summarized below.

The pressure response during cold-water injection into hot water reservoirs shows two distinct straight lines in a pressure versus logarithm of time plot. The first straight line corresponds to the Theis solution using the fluid properties of the undisturbed reservoir; the second straight line corresponds to the Theis solution using the fluid properties of the injected cold water. In the case of falloff after injection, two linear segments can also be observed, but in the reverse order compared with the injection behavior. When a production test is conducted right after injection, three linear segments in a plot of pressure versus logarithm of time can be observed. The first straight line has a slope corresponding to twice the cold water Theis solution; the

second has a slope of twice the hot-water Theis solution, and finally the last linear segment corresponds to the hot-water Theis solution. The reason for the double slopes is the combined effects of the initial pressure gradient (due to injection) and the fluid production.

In studying the effects of the relative permeability parameters on well tests in two-phase reservoirs, it is found that these parameters are introduced into the equations through the total kinematic mobility and the flowing enthalpy. The relative permeability parameters can be determined from production tests, if transient pressure and enthalpy data are obtained and the transmissivity is known, as for example from an injection test. The in-place saturation can not be obtained and consequently the conventional relative permeability curves cannot be determined from production tests. However, the relative permeability parameters can be expressed in terms of flowing enthalpy, and this can yield the general shape of the relative permeability curves.

The most important characteristic of the relative permeability curves is the immobile liquid cutoff because the total kinematic viscosity and the flowing enthalpy are most sensitive to this factor. The other cutoffs as well as the general shape of the relative permeability curves are less important. The relative permeability curves greatly affect the rise in the flowing enthalpy during a production test. However, the rise in flowing enthalpy is also dependent on the porosity, flow rate, and the initial thermodynamic conditions of the reservoir. If these other

factors are known, the rise in the flowing enthalpy will yield important information regarding the functional forms of the relative permeability curves.

Reservoir exploitation strategies are studied using reservoir parameters corresponding to the Olkaria geothermal field in Kenya. The Olkaria reservoir consists of a vapor-dominated zone overlying a two-phase liquid zone. It is found that production from deeper formations will greatly enhance the energy recovery from the field. Production from depth will cause upflow of steam that condenses in the shallow vapor zone causing an increase in the temperatures and pressures. Therefore, uniform boiling conditions over the entire reservoir will evolve and optimum energy extraction will result. On the other hand, when only steam is produced from the shallow steam zone, high-enthalpy fluids will be produced at early times but the reservoir life will be limited. Thus, this study contradicts the common belief that the production of higher-enthalpy fluids is beneficial.

The problem of cold-water injection into fractured geothermal reservoirs is studied using the integrated approach of both analytical and numerical techniques. Analytical methods are used to study the effects of thermal conduction on the advancement of the thermal front away from the injection well. It is found that contrary to common belief, the cold water will not short-circuit through the fractures into the production region, if the production region is a reasonable distance from the

injection wells. Instead, the cold water in the fractures will be heated rapidly by the conducting rock medium and a short distance away from the injection well the thermal fronts in the fracture and the rock matrix will coincide. This will result in an optimal, uniform energy sweep of the reservoir system.

The numerical simulator PT is used to study the importance of the assumptions employed in the analytical approach and extend the work to cases where the rock matrix is permeable. A combined use of the results from analytical and numerical work will enable realistic estimates of the rate of advancement of the thermal front away from the injection well to be made.

Analytical methods are used to study fault-charged geothermal reservoirs. In this work, temperature variations within the aquifer are neglected but the transient heat losses to the caprock and bedrock are rigorously modeled. A natural geothermal gradient is included in the solution. The model developed can be used for theoretical studies of the development of fault-charged geothermal reservoirs or for practical applications such as estimating the recharge rate into such systems. Theoretical studies of of the development of the thermal field, heat losses from the aquifer, and heat losses at the surface are carried out. It is found that the heat losses through the caprock to the ground surface are of primary importance. Soon after a linear temperature profile in the caprock is established, the thermal field in the aquifer becomes steady.

This model was applied to the Susanville hydrothermal system in California, and the recharge rate into the system approximated. It was found that the recharge from an inferred fault may increase the power potential of the Susanville anomaly for space heating purposes threefold.

Finally, the applicability of numerical simulators to the analysis of well-test data and for predicting the longevity of a geothermal field is illustrated. Analysis of injection tests from the Krafla geothermal field using the simulator PT is described. This analysis enabled determination of the transmissivity and the storativity of the formation around the wells. It was found that the injection-test data implies high total compressibility for the Krafla reservoir that is due either to fracture compressibility or two-phase conditions near the wells. Furthermore, the transmissivity of the wells could be determined. In the case of one of the well tests analyzed, it was found that the water-level changes during the injection test cannot be matched using the numerical simulator unless the permeability of the reservoir is increased during the simulation. This provides additional support to the theory that cold-water injection tests can stimulate the rock formation around the well.

Field-wide simulation studies of the Baca geothermal field in New Mexico were carried out using the two-phase simulator SHAFT79. The reservoir capacity of the field was estimated by volumetric means using the existing geological, geophysical, and well data. Then numerical simulation studies were carried out using the determined reservoir dimensions

in an attempt to estimate the longevity of the field when fluids equivalent to 50 MW_e are extracted from the field. The simulation studies were carried out using various reservoir boundary conditions and constant and variable rates. It was found that the low transmissivity of the reservoir severely limits fluid flow from the reservoir into the production region. The longevity results therefore indicate that it is questionable if 50 MW_e can be produced from the reservoir for thirty years. It was also found that the Baca wells will produce superheated steam soon after exploitation begins. Therefore, the available waste water for injection purposes may become limited.

Comparison of results from lumped- and distributed-parameter models for the Baca reservoir clearly illustrates that lumped-parameter models can lead to a serious overestimation of the generating capacity for a low-permeability reservoir such as the Baca reservoir. The use of lumped-parameter models for such reservoirs may mislead the field developers to the extent that an incorrect development plan will result.

REFERENCES

Allis, R. G., Changes in heat flow associated with exploitation of the Wairakei geothermal field, Proceedings New Zealand Geothermal Workshop, University of Auckland, New Zealand, 1, 11-13, 1979.

Assens, G. E., Derivation, by averaging, of the equations of heat, mass, and momentum transfer in a geothermal reservoir, Summaries 2nd Workshop Geothermal Reservoir Engineering, Stanford University, Stanford, California, 5-7, (December) 1976.

Arps, J. J., Analysis of decline curves, Transactions, AIME, 228, 1945.

Arps, J. J., Estimation of primary oil reserves, Transactions, AIME, 207, 1956.

Bailey, R. A., and R. L. Smith, Volcanic geology of the Jemez Mountains, New Mexico, Circular 163, New Mexico Min. Mines, 184-196, 1978.

Benson, S. M., and M. O'Brien, Reservoir evaluation of Klamath Falls, Oregon, Annual Report of the Earth Sciences Division of Lawrence Berkeley Laboratory, Berkeley, California, LBL-12100, 1980.

Benson, S. M., Goranson, C. B., McEdwards, D., and R. C. Schroeder, Well tests, Geothermal Resource and Reservoir Investigation of U. S. Bureau of Reclamation Leaseholds at East Mesa, Imperial Valley, California, LBL-7094, (October) 1978.

Benson, S. M., Goranson, C. B., Noble, J., Schroeder, R., Corrigan, D., and H. Wollenberg, Evaluation of the Susanville, California geothermal resource, Lawrence Berkeley Laboratory, Berkeley, California, LBL-11187, 1981.

Bjornsson, S., Estimations of the reservoir potential of the Olkaria geothermal field, Kenya, paper presented at the Nordic Symposium on Geothermal Energy, (May 29-31) 1978.

Bjornsson, A., Johnsen, G. V., Sigurdsson, S., Thorbergsson, G., and E. Tryggvason, Rifting of the plate boundary in North Iceland 1975-1979, Journal of Geophysical Research, 1979.

Bjornsson, A., Saemundsson, K., Einarsson, P., Tryggvason, E., and K. Gronvold, Current rifting episode in North Iceland, Nature, London, 266, 318-323, 1977.

Bodvarsson, G., On the temperature of water flowing through fractures, Journal of Geophysical Research, 74, 8, (April) 1969.

Bodvarsson, G., Thermal problems in the siting of reinjection wells, Geothermics, 1, 2, 1972.

Bodvarsson, G., Unconfined aquifer flow with a linearized free surface condition, Jokull, 27, 1977.

Bodvarsson, G. S., and K. Pruess 1981, Two-phase compressibility revisited, paper to be submitted to Water Resources Research, 1982.

Bodvarsson, G. S., and C. F. Tsang, Injection into fractured geothermal reservoirs, Annual Report of the Earth Science Division of Lawrence Berkeley Laboratory, Berkeley, California, LBL-12100, 1980a.

Bodvarsson, G. S., and C. F. Tsang, Injection into a fractured geothermal reservoir, Transactions, Geothermal Resources Council, 4, (September) 1980b.

Bodvarsson, G. S., Vonder Haar, S., Wilt, M., and C. F. Tsang, Preliminary estimation of the reservoir capacity and the longevity of the Baca geothermal field, New Mexico, paper presented at the SPE 55th Annual Fall Technical Conference and Exhibition, Dallas, Texas, SPE-9273, (September 21-24) 1980.

Brigham, W., and W. Morrow, P/Z behavior for geothermal steam reservoirs, Society of Petroleum Engineers, SPE-4899, 1974.

Brixley, P. F., and M. A. Grant, Reinjection testing at Broadlands, Proceedings 4th Workshop on Geothermal Reservoir Engineering, Stanford University, Stanford, California, 1979.

Brownell, Jr., D. H., Garg, S. K., and J. W. Pritchett, Computer simulation of geothermal reservoirs, Society of Petroleum Engineers, SPE-5381, 1975.

Buscheck, T. A., Equation of state for liquid water, LBL-Internal Memo, Lawrence Berkeley Laboratory, Berkeley, California, 1980.

Carslaw, H. S., and J. C. Jaeger, Conduction of heat in solids, Oxford, London, 510, 1959.

Castanier, L. M., and S. K. Sanyal, Geothermal Reservoir modeling - a review of approaches, Transactions, Geothermal Resources Council, 4, 313-314, (September) 1980.

Castanier, L. M., Sanyal, S. K., and W. E. Brigham, A practical analytical model for geothermal reservoir simulation, paper presented at SPE 50th Annual California Regional Meeting, Los Angeles, California, SPE-8887, (April 9-11) 1980.

Chasteen, A. J., Geothermal steam condensate reinjection, Proceedings 2nd U.N. Symposium on The Development and Use of Geothermal Resources, San Francisco, California, 2, (May) 1975.

Chen, H. K., Counsil, J. R., and H. J. Ramey, Experimental steam-water relative permeability curves, Transactions, Geothermal Resources Council, 2, 102-104, 1978.

Cheng, P., Heat-transfer in geothermal systems, Advances in Heat-Transfer, 14, 1978.

Cinco-Ley, H., Samaniego, V. F. and A. N. Dominguez, Transient pressure behavior for a well with a finite-conductivity vertical fracture, Journal of the Society of Petroleum Engineers, 253-264, (August) 1978.

Coats, K. H. Geothermal reservoir modeling, paper presented at the SPE 52nd Annual Fall Technical Conference and Exhibition, Denver, Colorado, SPE-6892, (October) 1977.

Core Laboratories, Inc., Special core analysis study of Baca No. 13 Well, private study performed for Union Oil Company, 1975.

Corey, A. T., The interrelation between gas and oil relative permeabilities, Producers Monthly, 19, 38-41, 1954.

Cortez A., C., Reinjection tests without treatment at Cerro Prieto, Abstracts Third Symposium on the Cerro Prieto Geothermal Field, Baja California, Mexico, San Francisco, California, LBL-11967, (March 24-26) 1981.

Counsil, J. R., and H. J. Ramey, Drainage relative permeabilities obtained from steam-water boiling flow and external gas drive experiments, Transactions, Geothermal Resources Council, 3, 141-143, 1979.

Cuellar, G., Behavior of silica in geothermal waste waters, Proceedings 2nd U.N. Symposium on The Development and Use of Geothermal Resources, San Francisco, California, 2, (May) 1975.

Donaldson, I. G., Temperature gradients in the upper layers of the earth's crust due to convective water flows, Journal of Geophysical Research, 67, 3449, 1962.

Donaldson, I. G., The simulation of geothermal systems with a simple convective model, Geothermics, Special Issue 2, U. N. Symposium on the Development and Utilization of Geothermal Resources, Pisa, Italy, 2, 1, 1970.

Donaldson, I. G., and M. L. Sorey, The best uses of numerical simulators, Proceedings 5th Workshop on Geothermal Reservoir Engineering, Stanford University, Stanford, California, SGP-TR-40, (December) 1979.

Dondanville, R. F., Hydrological geology of the Valles Caldera, New Mexico, Union Baca Project Report, 1971.

Duff, I. S., MA28--A set of Fortran subroutines for sparse unsymmetric linear equations, Report AERE - R 8730, Harwell/Oxfordshire, Great Britain, 1977.

Dykstra, H., Reservoir assessment of The Geysers field - Reservoir Engineering, unpublished report to the California Division of Oil and Gas, Sacramento, California, (April) 1981.

Earlougher, Jr., R. C. Advances in well test analysis, Society of Petroleum Engineers, Monograph 5, 1977.

Edwards, A. L., TRUMP: A computer program for transient and steady state temperature distribution in multidimensional systems, Lawrence Livermore Laboratory, Livermore, California, UCRL-14754, Rev. 3, 1972.

Einarsson, P., S-wave shadows in the Krafla caldera in NE-Iceland, evidence for a magma chamber in the crust, Science Institute, Reykjavik, Iceland, RH-78-9, 1978.

Einarsson, S. S., Vides, A. R., and G. Cuellar, Disposal of geothermal waste water by reinjection, Proceedings 2nd U.N. Symposium on The Development and Use of Geothermal Resources, San Francisco, California, 2, (May) 1975.

Faust, C. R., and J. W. Mercer, Mathematical modeling and geothermal systems, Proceedngs 2nd U. N. Symposium on the Development and Use of Geothermal Resources, San Francisco, California, 3, 1635-1641, (May) 1975.

Faust, C. R., and J. W. Mercer, An analysis of finite-difference and finite-element techniques for geothermal reservoir simulation, paper presented at the SPE 4th Symposium on the Numerical Simulation of Reservoir Performance, Los Angeles, California, 337-354, (February) 1976.

Faust, C. R., and J. W. Mercer, Geothermal reservoir simulation - numerical solution techniques for liquid and vapor-dominated hydrothermal systems, Water Resources Research, 15, 1, 1979.

Fetkovich, M., Decline curve analysis using type curves, Society of Petroleum Engineers, SPE-4629, 1973.

Fradkin, L. J., Sorey, M., and A. McNabb, On identification and validation of some geothermal models, Water Resources Research, 17, 4, 929-936, (August) 1981.

Fridleifsson, I. B., Lithology and structure of geothermal reservoir rocks in Iceland, Proceedings 2nd U.N. Symposium on The Development and Use of Geothermal Resources, San Francisco, California, (May) 1975.

Garg, S. K., Pritchett, J. W., and D. H. Brownell, Transport of mass and energy in porous media, Proceedings 2nd U. N. Symposium on The Development and Use of Geothermal Resources, San Francisco, California, 3, 1651, 1975.

Garg, S. K. Pressure transient analysis for two-phase (liquid water/steam) geothermal reservoirs, paper presented at the SPE 53rd Annual Meeting, Houston, Texas, (October 1-3) 1978.

Gentry, R., Decline-curve analysis, Journal of Petroleum Technology, (January) 1972.

Gentry, R., and A. McCray, The effect of reservoir and fluid properties on production decline curves, Journal of Petroleum Technology, (September) 1978.

Geonomics, Inc., Magnetotelluric-telluric profile survey of the Valles Caldera prospect, private geophysical study performed for Union Oil Company, 1976.

Goyal, K. P., and D. R. Kassoy, A plausible two-dimensional vertical model of the East Mesa geothermal field, California, U.S.A., paper to appear in Journal of Geophysical Research, 1981.

Grant, M. A., Approximate calculations based on a simple one phase model of a geothermal field, New Zealand Journal of Science, 20, 19-25, 1977a.

Grant, M. A., Permeability reduction factors at Wairakei, paper presented at the AICHE-ASME Heat Transer Conference, American Institute of Chemical Engineers, Salt Lake City, Utah, (August 15-27) 1977b.

Grant, M. A., Two-phase linear geothermal pressure transient: a comparison with a single-phase transient, New Zealand Journal of Science, 21, 355-364, 1978.

Grant, M. A., Interpretation of downhole measurements at Baca, Proceedings 4th Workshop on Geothermal Reservoir Engineering, Stanford University, Stanford, California, 1979.

Grant, M. A., Quasi-analytic solutions for two-phase flow near a discharging well, Applied Mathematics Division, D.S.I.R., Report No. 86, Wellington, New Zealand, 1979.

Grant, M. A. and M. L. Sorey, The compressibility and hydraulic diffusivity of water-steam flow, Water Resources Research, 15, 3, 684-686, 1979.

Grant, M. A., Truesdell, A. H., Manan, A., Janik, C. J., Fausts, J., Jimenez, M. E., and R. J. Sanchez, Production induced boiling and cold water entry in the Cerro Prieto geothermal reservoir indicated by chemical and physical measurements, Abstracts Third Symposium on the Cerro Prieto Geothermal Field, San Francisco, California, LBL-11967, 23, (March 24-26) 1981.

Gringarten, A. C., Unsteady-state pressure distributions created by a well with a single horizontal fracture, partial penetration, or restricted entry (Ph.D. dissertation), Department of Petroleum Engineering, Stanford University, Stanford, California, 1971.

Gringarten, A. C., and J. P. Sauty, A theoretical study of heat extraction from aquifers with uniform regional flow, Journal of Geophysical Research, 80, 5, 4956, 1975.

Gringarten, A. C., Witherspoon, P. A., and Y. Onishi, Theory of heat extraction from fractured hot dry rock, Journal Geophysics Research, 80, 8, (March) 1975.

Group 7, Additional electrical geophysical surveys of the Valles Caldera area, private geophysical study performed for Union Oil Company, 1972.

Gudmundsson, A., and B. Steingrimsson, Krafla, Well KJ-16, report in Icelandic, National Energy Authority of Iceland, 1981.

Hayashi, M., Mimura, T., and T. Yamasaki, T., Geological setting of reinjection wells in the Otake and the Hatchobaru geothermal field, Japan, Transactions, Geothermal Resources Council, 2, 263-266, (July) 1978.

Henley, R. W., Evolution of the Tanhara geothermal system, Proceedings New Zealand Geothermal Workshop, University of Auckland, New Zealand, 1, 7-9, 1979.

Horne, R. N. and M. J. O'Sullivan, Oscillatory convection in a porous medium heated from below, Journal of Fluid Mechanics, 66, 2, 339-352, 1974.

Horne, N. R., and H. J. Ramey, Steam/water relative permeabilities from production data, Transactions, Geothermal Resources Council, 2, 291-293, 1978.

Horne, R., Geothermal reinjection experience in Japan, paper presented at the California Regional SPE meeting, Bakersfield, California, SPE-9925, (March 25-26) 1981.

Huyakorn, P. S., and G. F. Pinder, A pressure-enthalpy finite element model for simulating hydrothermal reservoirs, Advances in Computer Methods for Partial Differential Equations II, R. Vichnevetsky (ed.), IMACS, 284, 1977.

Jacob, C. E., and S. W. Lohman, Nonsteady flow to a well of constant drawdown in an extensive aquifer, Transactions, American Geophysical Union, 33, 559-569, 1952.

Jakobsson, S. P., Jonsson, J., and F. Shido, Petrology of the Western Reykjanes Peninsula, Journal of Petrology, 1978

James, R., Wairakei and Lardarello geothermal power systems compared, New Zealand Journal of Science and Technology, II, 706-719, 1968.

Jonsson, V., Simulation of the Krafla geothermal field, Lawrence Berkeley Laboratory, Berkeley, California, LBL-7076, 1978.

Kasameyer, P., and R. Schroeder, Thermal depletion of liquid-dominated geothermal reservoirs with fracture and pore permeability, UCRL-77323 preprint, (December) 1975.

Kilty, K., Chapman, D. S., and C. Mase, Aspects of forced convective heat transfer in geothermal systems, Topical Report 78-1701.a.6.4.1, University of Utah, Salt Lake City, Utah, 61, 1978.

Kristmannsdottir, H., Fridleifsson, G. O., Gunnlaugsson, E., Gudmundsson, A., and M. Kjartansdottir, Lithology of the Krafla wells, reports in Icelandic, published by the National Energy Authority, 1975-1977.

Kruger, P., and C. Otte, Geothermal energy, Stanford University Press, Stanford, California, 1973.

Kubota, K., and K. Aosaki, Reinjection of geothermal hot water at the Otake geothermal field, Proceedings 2nd U. N. Symposium on The Development and Use of Geothermal Resources, San Francisco, California, 2, (May) 1975.

Lasseter, T. J., Witherspoon, P. A., and M. J. Lippmann, Multiphase multidimensional simulation of geothermal reservoirs, Proceedings 2nd U. N. Symposium on the Development and Use of Geothermal Resources, San Francisco, California, 3, 1715-1723, (May 20-29) 1975.

Lauwerier, H. A., The transport of heat in an oil layer caused by the injection of hot fluid, Applied Scientific Research, Section A., 5, 145, 1955.

Lippmann, M. J., Bodvarsson, G. S., Witherspoon, P. A., and J. Rivera R., Preliminary simulation studies related to the Cerro Prieto field, Geothermics, 9, 197-207, 1980.

Maini, T., In situ hydraulic parameters in jointed rock - their measurement and interpretation (Ph.D thesis), Imperial College of Science and Technology, London, 1971.

Mangold, D. C., Tsang, C. F., Lippmann, M. J., and P. A. Witherspoon, A study of thermal effects in well test analysis, Journal of Petroleum Technology, (June) 1981.

Mathias, K. E., The East Mesa geothermal field--a preliminary evaluation of five geothermal wells, Proceedings 2nd U. N. Symposium on The Development and Use of Geothermal Resources, San Francisco, California, 2, (May) 1975.

McEdwards, D. G., Multiwell variable rate well test analysis (Ph.D. dissertation), Lawrence Berkeley Laboratory, Berkeley, California, LBL-9459, 1981.

McEdwards, D. G., and S. M. Benson, User's Manual for ANALYZE, variable-rate, multiple-well, least-squares matching routine for well-test analysis, Lawrence Berkeley Laboratory, Berkeley, California, LBL-10907, 1981.

McNabb, A., A model of the Wairakei geothermal field report, Department of Science and Industrial Research, Wellington, New Zealand, 1975.

McNitt, J. R., Origin of steam in geothermal reservoirs, paper presented at SPE 52nd Annual Fall Technical Conference and Exhibition, Denver, Colorado, SPE-6764, (October 9-12) 1977.

Mercer, Jr., J. W., and C. R. Faust, Geothermal reservoir simulation, 3, Application of liquid- and vapor-dominated hydrothermal modeling techniques to Wairakei, New Zealand, Water Resources Research, 15, 3, 653-671, 1979.

Mercer, Jr., J. W., Faust, C. R., and G. F. Pinder, Geothermal reservoir simulation, Proceedings NSF/RANN Conference on Research for the Development of Geothermal Resources, Jet Propulsion Laboratory/ California Institute of Technology, Pasadena, California, 256, 1974.

Mercer, Jr., J. W., Pinder, G. F., and I. G. Donaldson, A Galerkin finite-element analysis of the hydrothermal system at Wairakei, New Zealand, Journal of Geophysical Research, 80, 17, 2608-2621, 1975.

Moench, A. F., Steam transport in porous media, Proceedings 2nd Workshop on Geothermal Reservoir Engineering, Stanford University, Stanford, California, 1976.

Moench, A. F., The effect of thermal conduction upon pressure drawdown and buildup in fissured, vapor-dominated geothermal reservoirs, Proceedings 4th Workshop Geothermal Reservoir Engineering, Stanford University, Stanford, California, SGP-TR-30, 112-117, (December 13-15) 1978.

Moench, A. F., and P. G. Atkinson, Transient-pressure analysis in geothermal steam reservoirs with an immobile vaporizing liquid phase, Geothermics, 7, 1978.

Morris, C. W., and D. A. Campbell, Geothermal reservoir energy recovery: A three-dimensional simulation study of the East Mesa field, paper presented at the SPE 54th Annual Fall Technical Conference and Exhibition, Las Vegas, Nevada, SPE-8229, (September 23-26) 1979.

Narasimhan, T. N., A unified numerical model for saturated-unsaturated groundwater flow (Ph.D. thesis), University of California, Berkeley, 244, 1975.

Narasimhan, T. N., and P. A. Witherspoon, An integrated finite-difference method for analyzing fluid flow in porous media, Water Resources Research, 12, 1, 57-64, 1976.

Neuzil, C. E., and J. V. Tracy, Flow through fractures, Water Resources Research, 17, 1, 191-199, 1981.

Newcomb, R. C., Strand, J. R., and F. J. Frank, Geology and groundwater characteristics of the Hanford Reservation of the U. S. Atomic Energy Commission, Washington, Geological Survey professional paper 717, 1972.

Noble, J. W., and S. B. Ojiambo, Geothermal explanation in Kenya, Proceedings 2nd U. N. Symposium on the Development and Use of Geothermal Resources, San Francisco, California, 1, 189-204, 1975.

O'Brien, M., Benson, S. M., and C. B. Goranson, Subsurface geology of three geothermal wells, Klamath Falls, Oregon, Lawrence Berkeley Laboratory, Berkeley, California, LBL-11240, 1981.

O'Neill, K., The transient three-dimensional transort of liquid and heat in fractured porous media (Ph.D. thesis), Department of Civil Engineering, Princeton University, Princeton, New Jersey, (January), 1978.

O'Neill, K., Pinder, G. F., and W. G. Gray, Simulation of heat transport in fractured, single-phase geothermal reservoirs, Preprint, (October) 1976.

O'Sullivan, M. J., A similarity method for geothermal well test analysis, to be published, 1980.

O'Sullivan, M. J., and K. Pruess, Analysis of injection testing of geothermal reservoirs, Geothermal Resources Council, 4, (September) 1980.

Palen, W. A., The roles of pore pressure and fluid flow in the hydraulic fracturing process (Ph.D. dissertation), University of California, Berkeley, California, (June) 1980.

Pinder, G. F., State-of-the-art review of geothermal reservoir modeling, Report for Golder Associates, (March) 1979.

Pritchett, J. W., Garg, S. K., and D. H. Brownell, Numerical simulation by production and subsidence at Wairakei, New Zealand, Proceedings 2nd Workshop on Geothermal Reservoir Engineering, Stanford University, Stanford, California, SGP-TR-20, 310-323, (December 1-3) 1976.

Pritchett, J. W., Garg, S. K., and T. D. Riney, Numerical simulations of the effects of reinjection on performance of a geopressured geothermal reservoir, Transactions, Geothermal Resource Council, 1, 1977.

Pruess, K., private communication, 1981.

Pruess, K., and T. N. Narasimhan, On fluid reserves and the production of superheated steam from fractured, vapor-dominated geothermal reservoirs, submitted to Economic Geology, 1981.

Pruess, K., Bodvarsson, G. S., Schroeder, R. C., Witherspoon, P. A., Marconcini, R., Neri, G, and C. Ruffilli, Simulations of the depletion of two-phase geothermal reservoirs, paper presented at the SPE 54th Annual Fall Technical Conference, Las Vegas, Nevada, SPE-8266, (September 23-26) 1979a.

Pruess, K., and R. C. Schroeder, SHAFT79 user's manual, Lawrence Berkeley Laboratory, Berkeley, California, LBL-10861, (March) 1980.

Pruess, K. Zerzan, J. M. Schroeder, R. C., and P. A. Witherspoon, Description of the three-dimensional two-phase simulator SHAFT78 for use in geothermal reservoir studies, paper presented at the SPE 5th Symposium on Reservoir Simulation, Denver Colorado, SPE-7699, (February 1-2) 1979.

Pruess, K., Weres, O., Schroeder, R., Marconcini, R., and G. Neri, History math simulation of Serrazzano geothermal reservoir, paper presented at the SPE Annual Meeting, Dallas, Texas, SPE-9276, 1980.

Raghavan, R., Pressure behavior of wells intercepting fractures, Proceedings Invitational Well Testing Symposium, Lawrence Berkeley Laboratory, Berkeley, California, LBL-7027, 1977.

Riney, T. D., Pritchett, J. W., Rice, L. F., and S. K. Garg, A preliminary model of the East Mesa hydrothermal systems, Proceedings 5th Workshop in Geothermal Reservoir Engineering, Stanford University, Stanford, California, SGP-TR-40, 211-214, 1979.

Rivera R., J., Decline curve analysis - a useful reservoir engineering tool for predicting the performance of geothermal wells, Transactions, Geothermal Resources Council, 1, 1977.

Rivera R., J., Application of type curve procedures for the analysis of production data from geothermal wells, Transactions, Geothermal Resources Council, 2, 1978.

Robinson, J. L., An estimate of the lifetime of the Wairakei geothermal field, New Zealand Journal of Science, 20, 27-29, 1977.

Romm, E. S., On one case of heat transfer in fractured rock, All-Union Institute for Scientific Research and Geological Exploration for Petroleum, U.S.S.R., preprint 1966.

Saemundsson, K., Evolution of the axial rifting zone in Northern Iceland and the Tjornes fracture zone, Geologic Society of America Bulletin, 85, 495-504, 1974.

Saemundsson, K., Fissure swarms and central volcanoes of the neovolcanic zones of Iceland, Geological Journal Special Issue, 10, 415-432, 1978.

Schroeder, R. C., O'Sullivan, M. J., and K. Pruess, Reinjection studies of vapor-dominated systems, paper presented at the Italian-American Workshop, Berkeley, California, (October) 1980.

Sigurdsson, O., and V. Stefansson, Lekt i borholum i Kroflu, report in Icelandic, National Energy Authority of Iceland, 1977.

Sigurdsson, O., Rennsliseiginleikar efra jardhitakerfisins i Kroflu, report in Icelandic, National Energy Authority of Iceland, 1978.

Slider, H. C., A simplified method of hypertolic decline curve analysis, Journal of Petroleum Technology, (January) 1968.

Slodowski, T. R., Geological resume of the Valles Caldera, Union Baca Project Report, 1977.

Sorey, M. L., Numerical modeling of liquid geothermal systems (Ph.D. thesis), University of California, Berkeley, 1975.

Sorey, M. L., Grant, M. A., and E. Bradford, Nonlinear effects in two-phase flow to wells in geothermal reservoirs, Water Resources Research, 16, 4, 767-777, 1980.

Stanford Geothermal Program, Proceedings Special Panel on Geothermal Model Intercomparison Study, 6th Workshop on Geothermal Reservoir Engineering, Stanford University, Stanford, California, (December 17) 1980.

Stefansson, V., Kristmannsdottir, H., and G. Gislason, Krafla model, Holubref No. 7, National Energy Authority of Iceland, 1977.

Stefansson, V., The Krafla geothermal field, Northeast Iceland, Geothermal Systems, L. Ryback and L. J. P. Muffler (editors), 1981.

Stehfest, H., Numerical inversion of Laplace transforms, Communications of ACM, 13, 44-49, 1979.

Steingrimsson, B. and V. Stefansson, Modified Krafla model, Holubref No. 9, National Energy Authority of Iceland, 1977.

Sterbentz, B., Geology and fault interpretations of Valles Caldera, New Mexico (M.S. thesis), Lawrence Berkeley Laboratory, Berkeley, California, LBL-13079, 1981.

Studt, F. E., Geothermal fluid injection-experience in New Zealand and the Philippines, paper presented at the NATO CCMS Geothermal Conference, Paris, France, (July 15) 1980.

Sun, H., and I. Ershaghi, The influence of steam-water relative permeability curves on the numerical results of liquid dominated geothermal reservoirs, Transactions, Geothermal Resources Council, 3, 697-700, 1979.

Terzaghi, K., Settlement and consolidation of clay, Engineering News Record, 26, 1925.

Thomas, L. K., and R. Pierson, Three-dimensional geothermal reservoir simulation, paper presented at SPE 51st Annual Fall Technical Conference and Exhibition, New Orleans, Louisiana, SPE-6104, 1976.

Toronyi, R. M., and S. M. Forouq Ali, Two-phase, two-dimensinoal simulation of a geothermal reservoir and the wellbore system, paper presented at the SPE 50th Annual Fall Meeting, Dallas, Texas, SPE-5521, (September) 1975.

Theis, C. V., The relationship between the lowering of piezometric surface and the rate and duration of discharge using groundwater storage, Transactions, American Geophysical Union, 2, 519-524, 1935.

Truesdell, A. H., and D. E. White, Production of superheated steam from vapor-dominated geothermal reservoirs, Geothermics, 2, 154-173, 1973.

Tsang, C. F., Bodvarsson, G. S., Lippmann, M. J., and J. Rivera R, A study of alternate reinjection schemes for the Cerro Prieto geothermal field, Baja California, Mexico, Transactions, Geothermal Resources Council, 1978.

Tsang, C. F., Buscheck, T., and C. Doughty, Aquifer thermal energy storage - a numerical simulation of Auburn University field experiments, Water Resources Research, 17, 3, 647-658, (June) 1981.

Tsang, C. F., Mangold, D. C., and M. J. Lippmann, Simulation of reinjection at Cerro Prieto using an idealized two-reservoir model, Proceedings 2nd Symposium on the Cerro Prieto geothermal field, Baja California, Mexico, (October 17-19) 1979.

Tsang, Y. W., and C. F. Tsang, An analytic study of geothermal reservoir pressure response to cold water reinjection, Proceedings 4th Workshop on Geothermal Reservoir Engineering, Stanford University, Stanford, California, SGP-TR-30, 322-331, (December 13-15) 1978.

Union Oil Company of California and Public Service Company of New Mexico, Geothermal demonstration plant technical and management proposal to DOE, 1978.

UN/Kenya Government, Feasibility report for the Olkaria geothermal project, SWECO, and VIRKIR, 1 and 2, 1976.

U. S. Department of Energy, Geothermal direct heat applications, program summary, Report of the Semi-annual Review Meeting, Las Vegas, Nevada, U. S. Department of Energy, Geothermal Energy Division, 87, 1980.

van Everdingen, A. F., and W. Hurst, The application of Laplace transformation to flow problems in reservoirs, Transactions, AIME, 186, 305, 1949.

Voss, C. I., Finite element simulation of multiphase geothermal reservoirs (Ph.D. thesis), Department of Civil Engineering, Princeton University, Princeton, New Jersey, 1978.

Wang, J. S. Y., Sterbentz, R. A., and C. F. Tsang, The state-of-the-art of numerical modeling of thermohydrologic flow in fractured rock masses, Lawrence Berkeley Laboratory, Berkeley, California, LBL-10524, (February) 1980

Weres, O., Tsao, K., and B. Wood, Resource, technology, and environment at The Geysers, Lawrence Berkeley Laboratory, Berkeley, California, LBL-5231, (July) 1977.

White, D. E., Characteristics of geothermal resources, in Geothermal Energy, P. Kruger and C. Otte (eds.), Stanford University Press, Stanford, California, 1972.

White, D. E. Muffler, L. J. P., and A. H. Truesdell, Vapor-dominated hydrothermal systems compared with hot-water systems, Economic Geology, 66, 75-97, 1971.

Whiting, R. L., and H. J. Ramey, Jr., Application of material and energy balances to geothermal steam production, Journal of Petroleum Technology, 893-900, (July) 1969.

Witherspoon, P. A., private communication, 1981.

Witherspoon, P. A., Javandel, I., Neuman, S. P., and R. A. Freeze, Interpretation of aquifer gas storage conditions from water pumping tests, monograph published by the American Gas Association, 1967.

Witherspoon, P. A., Wang, J. S. Y., Iwai, K., and Gale, J. R., Validity of cubic law for fluid flow in a deformable rock fracture, Water Resources Research, 16, 6, 1016-1024, 1980.

Witherspoon, P. A., Newman, S. P., Sorey, M. L., and M. J. Lippmann, Modeling geothermal systems, paper presented at Accademia Nazionale dei Lincei, Rome, Italy, 68, LBL-3263, (March 3-5) 1975.

Zais, E. J., and G. Bodvarsson, Analysis of production decline in geothermal reservoirs, Lawrence Berkeley Laboratory, Berkeley, California, LBL-11215 (GREMP-10), (September) 1980.

Zyvolski, G. A., and M. J. O'Sullivan, Simulation of the Broadlands geothermal field, New Zealand, Proceedings 4th Workshop on Geothermal Reservoir Engineering, Stanford University, Stanford, California, SGP-TR-30, 332-342, (December 13-15) 1978.

APPENDIX A: INPUT GUIDE FOR PROGRAM PT

The input guide to the numerical code PT is conveniently organized into input blocks as shown in Table 13. Each input block must start with a card with its name in the first five (5) columns, except for input block A (the problem identification card(s)). Input blocks A to F and input block K (the end card) must be specified. Other input blocks are optional and required only for specific problems. The input guide is given below:

Table 13. Input Blocks for Program PT.

Block	Name	Description
A	PROBLEM IDENTIFICATION CARD(S)	
B	SPECS	Problem controls, limits, and constants
C	ROCKS	Material properties of the rocks Mode 1: No compaction calculations Mode 2: Compaction calculations
D	FLUID	Properties of the fluid
E	NODES	Node description
F	CONNE	Connections between nodes
G	INCON	Initial conditions
H	GENER	Generation rates of production or injection
I	FLOWS	Constant mass flow rates between nodes
J	DIMEN	Dimensionless parameters
K	ENDED	Cards that end data deck

A. PROBLEM IDENTIFICATION CARD, Format (A1, 14A5)

Any number of problem identification cards using columns 2 through 70. The last identification card should have the symbol "*" in the first column.

B. SPECS: Problems Controls, Limits, and Constants

Card 1b. Format (4I5, 6E10.4). Output and time step controls.

Columns	Variables	Description
0-5	KDATA	Controls option on output data, normal amount (0), minimum (-1), or maximum (1) number of parameters printed.
6-10	IPRINT	Number of time steps between data output, in addition to output on first and last time steps, and output controled by TIMEP. IPRINT is not used if negative, zero, or unspecified.
11-15	MCYC	Maximum allowed number of cycles. MCYC will not be used if zero or unspecified.
16-20	MSEC	Maximum allowed machine time in seconds. MSEC will not be used if zero or unspecified. If negative, problem will end after the first cycle.
21-30	TAU	Initial problem time. Will be set to zero if unspecified.
31-40	TIMEP	Problem time interval between data output, in addition to output on first and last cycles, and output controlled by IPRINT. TIMEP is ignored if negative, zero, or unspecified. Output will be written at exact multiples of TIMEP, if possible, by adjusting the time steps in the range from SMALL to DELTO. The adjustment is also limited to a range from 2/3 to 3/2 of the same step that would otherwise be used.
41-50	TIMAX	Maximum allowable problem simulation time. TIMAX will not be used if zero or unspecified. If it is negative, problem will end after the first cycle.

Columns	Variables	Description
51-60	FIRST	Initial time step. FIRST is set to 10^{-12} if less than 10^{-12} or unspecified.
61-70	SMALL	Minimum allowed time step. May be used with DELTMX to limit range of time step. Not usually needed. SMALL is set to 10^{-12} if less then 10^{-12} or unspecified.
71-80	DELTMX	Maximum allowed time step. May be used with SMALL to limit range of time step. DELTMX is set to 10^{12} if unspecified or not in the range from 10^{-10} to 10^{12}.

Card 2b. Format (2I5, 7E10.4). Constraints and Limits

Columns	Variables	Description
0-5	KT	Number of large, constant temperature/pressure boundary nodes. These nodes should be listed last in input block "NODES".
6-10	NUM	Identification number of a node for which temperature, rate of temperature change, pressure, rate of pressure change, time, and dimensionless parameters will be written out after each cycle. NUM will not be used if zero or unspecified.
11-20	PINI	Initial pressure of node NUM. PINI is used to calculate the total change in pressure of node NUM.
21-30	GF	Acceleration due to gravity. GF is set equal to 9.80665 cm/sec^{-2} if unspecified.
31-40	SCALE	Scale factor. Set to 1.0 if negative, zero, or unspecified. Will be applied to all geometric input data in input blocks "NODES" and "CONNE".
41-50	TMAX	Maximum allowable problem temperature. Will be set to 400 if unspecified.
51-60	TMIN	Minimum allowable problem temperature.

Columns	Variables	Description
61-70	RMAX	Maximum allowable problem pressure. Will be set to 10^8 if unspecified.
71-80	RMIN	Minimum allowable problem pressure.

Card 3b. Format (4I5,6E10.4). Numerical controls

Columns	Variables	Description
0-5	NOPT	Parameter that specifies if both mass and energy equations are to be solved: 0 or blank: both mass and energy equations 1: only mass equation 2: only energy equation (fluid density has to be constant)
6-10	NPUNCH	If greater than zero, causes decks of punched cards in the format of input blocks "INCON" and "FLOWS" to be produced when the problem ends normally. If less than zero, only a deck in the format of input block "INCON" is produced. These decks may be inserted in the input deck, which may then be resubmitted to continue the problem.
11-15	NEWTON	Parameter specifying if Newton Raphson iteration is to be used: 0 or blank: Newton Raphson 1: No Newton Raphson
16-20	NUTS	Maximum number of iterations to be used in the Newton Raphson iteration procedure. If convergence is not achieved, the time step will be cut in half. Default is five iterations if NOPT is equal to 2.
21-30	ERRM	Maximum allowable residual for mass equation for any node. Default is 10^{-4}. Used as a convergence criteria in Newton Raphson iteration procedure.
31-40	ERRE	Maximum allowable residual for energy equation for any node. Default (if blank or not specified) is 1.0. Used as a convergence criteria in Newton Raphson iteration procedure.

Columns	Variables	Description
41-50	RVARY	Desired maximum pressure change during a time step. RVARY is set to 1000.0 if unspecified or zero. Controls size of the time step between limits of SMALL and DELTMX.
51-60	TVARY	Desired maximum temperature change during a time step. TVARY is set to 5.0 if unspecified or zero. Controls size of the time step between limits of SMALL and DELTMX.
61-70	QSTEADY	Steady flow for all connections not specified in input block "FLOWS". If identical for all connections, the input block "FLOWS" is not needed. QSTEADY is only used if NOPT is equal to 2.
71-80	WUP	Upstream weighting parameter. WUP is set equal to 0.7 if unspecified, less than 0.5, or greater than 1.0.

Card 4b. Format (6E10.3). General initial conditions

Columns	Variables	Description
1-10	TONE	Initial temperature for all nodes for which no TI is specified in input block "INCON".
11-20	DONE	Initial fluid density for all nodes.
21-30	PONE	Initial pressure for all nodes for which no PI is specified in input block "INCON".
31-40	PCONE	Initial preconsolidation pressure for all nodes for which no PCI is specified in input block "INCON".
41-50	GMONE	Mass injection rate for all nodes for which no GI is specified in input block "GENER".
51-60	HCONE	Heat content of injected fluid for all nodes for which no HCL is specified in input block "GENER". (Units: energy/unit mass)

C. ROCKS. Material Properties for the Solids

MODE I: If no compaction calculations are required

Card 1c. Format (A5, 4I5, 5X, 5E10.4). Material Description.

Columns	Variables	Description
1-5	AMAT	Material name. Do not use "SYSTM" as a material name.
6-10	MAT	Material identification number. Must not be zero or left blank.
11-15	LTABC	Number of points listed on Specific Heat Table card or cards (following Card 2), positive if vs temperature, zero if specific heat is constant (equal to CAPT).
16-20	LTABK	Number of points listed on thermal-conductivity table card or cards (following Card 2 and any specific heat table cards), positive if vs temperature, zero if conductivity is constant (equal to CONDUC(X)).
21-25	LTABP	Number of points listed on intrinsic permeability table card or cards (following Card 2 and any specific heat and/or thermal conductivity table cards), positive if vs temperature, zero if permeability is constant.
31-40	DENS	Density of the solid. Set to 10^{-12} if less than 10^{-12} or not specified.
41-50	CAPT	Specific heat of the solid, if constant. Initial value, if variable, set to 10^{-36} if less than 10^{-36} or not specified.
51-60	CONDUC(X)	Thermal conductivity of the solid-liquid mixture along the X-axis of anisotropy, if constant. Initial value, if variable, set to 10^{-24} or not specified.
61-70	PERMEAB(X)	Intrinsic permeability of the porous media along the X-axis of anisotropy, if constant. Initial value, if variable, set to 10^{-24} if less than 10^{-24} or not specified.
71-80	COMPR	Matrix compressibility.

Card 2c. Format (8E10.3). Material Description

Columns	Variables	Description
1-10	ANISCON	Anistropy for thermal conductivity. It is the ratio between the conductivities along the Y and X axes (i.e., CONDUC(Y)/CONDUC(X)). Axes X and Y are arbitrarily fixed in space and are parallel to the principal axes of material anisotropy. Set to 1.0 if zero or not specified.
11-20	ANISPER	Anisotropy for intrinsic permeability. It is the ratio between PERMEAB(Y) and PERMEAB(X). Set to 1.0 if zero or not specified.
21-30	POR	Porosity. Set to 10^{-12} if less than 10^{-12} or not specified. Set to .9999 if specified equal to 1.0.
31-40	EXPR	Coefficient of thermal expansion for rock matrix.

Card 3c, etc. Format (8E10.3). Specific Heat Table
(omit if specific heat is constant)

Columns	Variables	Description
1-10	CAPT(1)	Specific heat.
11-20	TVARC(1)	Temperature or time corresponding to CAPT(1).
21-30	CAPT(2)	Specific heat.
	(etc.)	

Card 4c, etc. Format (8E10.3). Thermal Conductivity Table
(omit if thermal conductivity is constant)

Columns	Variables	Description
1-10	CONT(1)	Thermal conductivity.
11-20	TVARK(1)	Temperature corresponding to CONT(1).
21-30	CAPT(2)	Thermal conductivity.
	(etc.)	

Card 5c, etc. Format (8E10.3). Intrinsic Permeability Table
(omit if intrinsic permeability is constant)

Columns	Variables	Description
1-10	PERT(1)	Intrinsic permeability
11-20	TVARP(1)	Temperature corresponding to PERT(1).
21-30	PERT(2)	Intrinsic permeability.
	(etc.)	

Card 6c

Repeat card sequence from 1c to 5c for each different material. Following the cards corresponding to the last material, place a blank card.

MODE II: If compaction calculations are required

Card 1cc. Format (A5, 25X, 2E10.4). Average properties of overburden and flow region

Columns	Variables	Description
1-5		Punch the word "SYSTM"
31-40	THICK	Thickness of total system (overburden plus flow region)
41-51	DENSBUR	Average density of total system.

Card 2cc. Format (A5, 415, 5X, 5E10.4). Material description

Same as Card 1 in MODE 1. Set COMPR equal to zero, or leave columns 71-80 blank.

Card 3cc. Format (5E10.3). Material description

Columns	Variables	Description
1-10	ANISCON	Same as in MODE I
11-20	ANISPER	Same as in MODE I
21-30	AV	Coefficient of compressibility (a_v)
31-40	EZ	Reference void ratio (e_o)
41-50	PZ	Reference effective stress (σ_o') at which $e = e_o$

Card 4cc. Format (5E10.3). Material description

Columns	Variables	Description
1-10	CS	Swelling index (c_s)
11-20	CC	Compression index (c_c)
21-30	CK	Slope of straight line on the e versus log k plot; (c_k)
31-40	EK	Reference void ratio (e_k)
41-50	CONZ	Reference intrinsic permeability

Cards 5cc, 6cc,7cc, and 8cc are the same as Cards 3c, 4c, 5c, and 6c of MODE I.

Note: If some materials are deforming according to Terzaghi's one-dimensional theory (i.e., COMPR = 0, AV = 0, CC, CS $\neq$ 0) and others are not, use MODE II, reserving MODE I only for those materials with nonzero rock matrix impermeability (COMPR).

D. FLUID: Material Properties for the Fluid

Card 1d. Format (8E10.4). Fluid Properties description

Columns	Variables	Description
0-10	DENSF	Fluid density if constant. If blank or zero, the fluid density will be calculated as a function of pressure and temperature.
11-20	VISCF	Dynamic viscosity of fluid if constant. If blank or zero the fluid viscosity will be calculated as a function of temperature.
21-30	COMPRF	Compressibility of fluid if constant. If blank or zero, the compressibility will be calculated as a function of pressure and temperature.
31-40	SHEATF	Specific heat of fluid. Set to 10^{-36} if zero or unspecified.
41-50	EXPF	Thermal expansion of fluid if constant. If zero or unspecified, EXPF will be calculated as a function of pressure and temperature.

E. NODES: Node Descriptions

Card 1e. Format (4I5, 3E10.3)

Columns	Variables	Description
1-5	NODE	Node identification number.
6-10	NSEQ	Number of additional nodes of same volume.
11-15	NADD	Increment between successive values of NODE in the sequence of NSEQ + 1 nodes generated when NSEQ is used.
16-20	NODMAT	Identification number of the material of which the node is a part.
21-30	VOLUME	Volume of node. Multiplied by $(SCALE)^3$ to obtain volume to be used in the simulation.

Columns	Variables	Description
31-40	DELZ	Increment in elevation, when multiplied by SCALE, between successive nodes when NSEQ is used.
41-50	Z	Elevation of nodal point with respect to datum level, when multiplied by SCALE.

Card 2e.

Following the card describing the last node, place a blank card.

Note: Place the boundary nodes at the end of the sequence. There should be KT of these nodes as specified in input block "SPECS".

F. CONNE: Connections Between Nodes

Card 1f. Format (6I5, 4E10.3)

Columns	Variables	Description
1-5	NOD1	Identification numbers of the connected nodes.
6-10	NOD2	
11-15	NSEQ	Number of additional identical connections.
16-20	NAD1	Increments between successive values of NOD1 and NOD2, respectively, in the sequence of NSEQ+1 connections generated when NSEQ is used.
21-35	NAD2	
26-30	NSOTRPY	Anisotropy parameter. If nonzero, it is set equal to 1, indicating that this connection is parallel to the Y-axis of anisotropy (see input block "ROCKS").
31-40	DEL1	Distance, when multiplied by SCALE, from the nodal points in NOD1 and NOD2 to the connected interface
41-50	DEL2	
51-60	AREA	Interface area between nodes NOD1 and NOD2. Multiplied by $(SCALE)^2$ to obtain interface area to be used in simulation.

Columns	Variables	Description
61-70	HINT	Heat-transfer coefficient for conduction and convection across the space between the connected surfaces. If HINT is not specified or set = 0, it will be set to 10^{50}.

Card 2.

Following the card describing the last connection between nodes, place a blank card.

G. INCON: Initial Conditions

Card 1g. Format (3I5, 5X, E10.4, E20.9, 2E10.3)

Columns	Variables	Description
1-5	NOTE	Node identification number.
6-10	NSEQ	Number of additional nodes with identical initial conditions.
11-15	NADD	Increment between successive node numbers in sequence of NSEQ+1 nodes generated when NSEQ is used.
21-30	TI	Initial temperature. If not specified, TI is set to TONE (input block "SPECS").
31-50	PI	Initial pressure. If not specified, PI is set to PONE (input block "SPECS").
51-60	POR	Initial porosity.
61-70	PCI	Initial preconsolidation stress. PCI is set to PCONE (input block "SPECS") if not specified.

Card 2.

Following the card specifying the initial condition of the last node, place a blank card.

Note: The order on which the nodes are described in this block may differ from the order followed in input block "NODES".

H. GENER: Generation Rate

Card 1h. Format (4I5, 5, 2E10.4)

Columns	Variables	Description
1-5	NODG	Identification number of generation node.
6-10	NSEQ	Number of additional nodes with identical generation rates.
11-15	NADD	Increment between successive node numbers in sequence of NSEQ+1 nodes generated when NSEQ is used.
16-20	LTABG	Number of points listed on generation rate table. Zero or one if generation rate is constant with time.
21-30	G	Generation rate if constant for node NODG.
31-40	HCI	Specific enthalpy of injected water (temperature times specific heat). HCI is set to HCONE (input block "SPECS") if not specified.

Card 2h. Format (8E10.3). Generating rate table (omit if generation rate is constant)

Columns	Variables	Description
1-10	G(1)	Generation rate.
11-20	TIMX(1)	Time corresponding to generation rate.

Columns	Variables	Description
21-30	G(2)	Generation rate.
31-40	TIMX(2)	Time corresponding to generation rate.
	(etc.)	

Card 3h.

Following last card in table, place a blank card.

I. FLOWS: Constant Flow Rates Between Connections

Note: This input block is required only if NOPT = 2 (input block "SPECS")

Card 1i. Format (4(I5, E15.6))

Columns	Variables	Description
1-5	CONNEC(1)	Connection number (index number assigned in BLOCK 5)
6-20	FLOW(1)	Mass flow rate for CONNEC(1)
21-25	CONNEC(2)	Connection number
	⋮	
66-80	FLOW(4)	Mass flow rate for CONNEC(4).

Note: Specify only connections which have nonzero flow rates. In each card, give data for four connections, last card may specify less than four connections. FLOW is positive when it is from NOD2 towards NOD1 (see input block "CONNE").

Card 2.

Following the last card, specifying mass flow rates, place a blank card.

J. DIMEN: Dimensionless Parameters.

Card 1j. Format (I5, 5X, 2E10.4)

Columns	Variables	Description
1-5	NDIM	Parameter that specifies if dimensionless pressure or flowrate is to be calculated. 0 or blank: dimensionless pressure 1: dimensionless flowrate
11-20	DIMTIM	Constant that gives dimensionless time when multiplied with total time.
21-30	DMPAR	Constant that gives dimensionless pressure/flowrate when multiplied with total pressure change for node NUM (dimensionless pressure) or flow through connection 1 (dimensionless flow rate).

Card 2j.

To end input block "DIMEN", place a blank card.

K. ENDED: Cards that end data deck

Card 1k.

The last card of the deck must be a Final Card with the word "*SPLIT" in colums 1 through 6. This card stops the program.

APPENDIX B: EQUATION OF STATE FOR LIQUID WATER

The viscosity of liquid water is calculated based on the following expression:

$$\mu = d_1 10^{\left[\frac{d_2}{T+d_3}\right]} \tag{B1}$$

where $d_1 = 2.414 \times 10^{-5}$, $d_2 = 247.8$, and $d_3 = 133.15$. The fluid density is calculated as a function of pressure and temperature as follows (Buscheck, 1980):

$$\rho(P,T) = A(T) + C(T) \cdot B(P) \tag{B2}$$

where

$$A(T) = a_1 + a_2(T - T_{ref}) + a_3(T - T_{ref})^2 + a_4(T - T_{ref})^3 + a_5(T - T_{ref})^4 \tag{B3}$$

$$B(P) = b_1 + b_2(P - P_{ref}) + b_3(P - P_{ref})^2 + b_4(P - P_{ref})^3 \tag{B4}$$

$$C(T) = c_1 + c_2(T - T_{ref}) + c_3(T - T_{ref})^2 + c_4(T - T_{ref})^3 + c_5(T - T_{ref})^4 + c_6(T - T_{ref})^5 + c_7(T - T_{ref})^6 \tag{B5}$$

The coefficients are:

$0 < T < 199°C, \quad T_{ref} = 100°C$

$a_1 = .96628$

$a_2 = -.70650 \times 10^{-3}$

$a_3 = -.28521 \times 10^{-5}$

$a_4 = .59365 \times 10^{-8}$

$a_5 = .32285 \times 10^{-10}$

$199 < T < 350°C, \quad T_{ref} = 260°C$

$a_1 = .79829$

$a_2 = -.14906 \times 10^{-2}$

$a_3 = -.57448 \times 10^{-5}$

$a_4 = .40265 \times 10^{-7}$

$a_5 = .17661 \times 10^{-9}$

$0 < P < 4 \times 10^{7}$ pa

$b_1 = -.12953 \times 10^{-2}$

$b_2 = .51594 \times 10^{-4}$

$b_3 = -.99714 \times 10^{-8}$

$b_4 = .10275 \times 10^{-9}$

$0 < T < 149°C, \; C(T) = 1.0$

$140 < T < 220°C, \quad T_{ref} = 180°C$

$c_1 = 1.2092$

$c_2 = .70811 \times 10^{-2}$

$c_3 = .71415 \times 10^{-4}$

$c_4 = -.79423 \times 10^{-6}$

$c_5 = -.53925 \times 10^{-8}$

$c_6 = .5148 \times 10^{-9}$

$c_7 = -.54612 \times 10^{-11}$

$220 < T < 350°C, \quad T_{ref} = 260°C$

$c_1 = .2.2437$

$c_2 = .23865 \times 10^{-1}$

$c_3 = .215671 \times 10^{-4}$

$c_4 = .81759 \times 10^{-7}$

$c_5 = .54541 \times 10^{-8}$

$c_6 = .36389 \times 10^{-8}$

$c_7 = .48355 \times 10^{-11}$

This density function is accurate to within 1% for $0 < T < 300°C$, and 5% for $300 < T < 350°C$. The fluid compressibility and thermal expansivity are calculated from the density function on the basis of their definitions:

$$\beta_w = \left[\frac{1}{\rho}\frac{d\rho}{dP}\right]_T \tag{B6}$$

$$\alpha_w = \left[\frac{1}{\rho}\frac{d\rho}{dT}\right]_P \tag{B7}$$

APPENDIX C

SIMULTANEOUS SOLUTION OF THERMAL EQUATIONS FOR FRACTURE AND ROCK

In dimensionless form, the equation governing the temperature in the fracture and the rock are:

Fracture:

$$(2 + \theta) \frac{\partial T_{D_f}}{\partial \xi} + \theta \frac{\partial T_{D_f}}{\partial \tau} - 2 \left. \frac{\partial T_{D_r}}{\partial \eta} \right|_{\eta=0} = 0. \tag{C1}$$

Rock:

$$\frac{\partial^2 T_{D_r}}{\partial \eta^2} = \frac{\partial T_{D_r}}{\partial \tau} . \tag{C2}$$

The initial and boundary conditions are:

$$T_{D_f}(\xi,0) = T_{D_r}(\xi,\eta,0) = 0, \tag{C3}$$

$$T_{D_f}(0,\tau) = \begin{cases} 0 & \tau < 0 \\ 1 & \tau \geqslant 0 \end{cases} , \tag{C4}$$

$$T_{D_f}(\xi,t) = T_{D_r}(\xi,0,\tau), \tag{C5}$$

$$\left. \frac{\partial T_{D_r}}{\partial \eta} \right|_{\eta=1} = 0. \tag{C6}$$

After applying Laplace transformation with respect to τ, equations (C1) and (C2) become:

$$(2 + \theta) \frac{\partial u}{\partial \xi} + \theta p u - 2 \left. \frac{\partial v}{\partial \eta} \right|_{\eta=0} = 0, \tag{C7}$$

$$\frac{\partial^2 v}{\partial \eta^2} - p v = 0, \tag{C8}$$

where u and v are the temperatures of the fracture and the rock matrix in

the Laplace space, respectively. In the Laplace domain, the boundary conditions (equations (C4)-(C7)) become:

$$u(0) = 1/p, \tag{C9}$$

$$u(\xi) = v(\xi,0), \tag{C10}$$

$$\left.\frac{\partial v}{\partial \eta}\right|_{\eta=1} = 0. \tag{C11}$$

The solution to equation (C9) is:

$$v = A \cosh \sqrt{p}\,\eta + B \sinh \sqrt{p}\,\eta, \tag{C12}$$

where A and B are constants. Applying boundary conditions given by equations (C10) and (C11), A and B can be determined:

$$B = -A \tanh \sqrt{p}\,, \tag{C13}$$

$$A = u\,. \tag{C14}$$

Substituting equations (C13) and (C14) into (C12) yields:

$$v = u(\cosh \sqrt{p}\,\eta - \sinh \sqrt{p}\,\eta \tanh \sqrt{p}). \tag{C15}$$

Solving the equation for the temperature in the fracture (equation (C8)):

$$\left.\frac{\partial v}{\partial \eta}\right|_{\eta=0} = -\,u\sqrt{p}\tanh\sqrt{p}\,. \tag{C16}$$

Substitution of equation (C16) into equation (C8) yields:

$$(2+\theta)\frac{du}{d\xi} + \theta p u + 2u\sqrt{p}\tanh\sqrt{p} = 0 \tag{C17}$$

rewriting (C17):

$$\frac{du}{d\xi} + \frac{(\theta p + \sqrt{p}\tanh\sqrt{p})\xi}{(2+\theta)} = 0. \tag{C18}$$

The solution of equation (C17) is:

$$u = C \exp - \frac{(\theta p + 2\sqrt{p}\tanh\sqrt{p})\xi}{(2+\theta)}\,. \tag{C19}$$

Applying boundary conditions given by equation (C9) enables determination

of the constant C as C = 1/p and equation (C19) becomes:

$$u = \frac{1}{p} \exp\left[- \frac{(\theta p + 2\sqrt{p} \tanh \sqrt{p})\xi}{(2 + \theta)}\right] \tag{C20}$$

Finally, having obtained a solution for the fracture temperature in the Laplace domain (u) one can write the complete solution for the rock temperature in the Laplace domain (v):

$$v = \frac{1}{p} \exp\left[- \frac{(\theta p + 2\sqrt{p} \tanh \sqrt{p})\xi}{(2 + \theta)}\right] (\cosh \sqrt{p}\, \eta - \sinh \sqrt{p}\, \eta \tanh \sqrt{p}). \tag{C21}$$

Assymtotic Solutions

At early times ($p \to \infty$) the temperature in the fracture in the Laplace domain is given by:

$$u = \frac{1}{p} \exp - \left[\frac{\theta\xi}{2 + \theta} p\right]. \tag{C22}$$

The temperature in the rock matrix in the Laplace domain at early times is zero as $\sinh x \to \cosh x$ and $\tanh x \to 1$ when $x \to \infty$. Equation (C22) can easily be inverted to yield:

$$T_{D_f} = U\left[\tau - \frac{\theta}{(2 + \theta)} \xi\right] \tag{C23}$$

where U denotes the unit function. At late times ($p \to 0$), the equation for the temperature in the fracture in the Laplace domain (equation (C20)) reduces to:

$$u = \frac{1}{p} \exp - [\xi p] \tag{C24}$$

Inversion of equation (C24) from the Laplace domain to real space yields:

$$T_{D_f} = U(\tau - \xi). \tag{C25}$$

Similar development for equation (C21) yields identical results for the temperature in the rock matrix as $\sinh x \to 0$ and $\cosh x \to 1$ when $x \to 0$.

APPENDIX D

SOLUTION OF EQUATIONS FOR FAULT-CHARGED RESERVOIR

In dimensionless form the equations governing the temperature in the aquifer, caprock and bedrock are:

$$\eta = 0: \quad \left.\frac{\partial T_{D_1}}{\partial \eta}\right|_{\eta=0} - \kappa \left.\frac{\partial T_{D_2}}{\partial \eta}\right|_{\eta=0} - \frac{\partial T_{D_a}}{\partial \xi_1} - \theta_1 \frac{\partial T_{D_a}}{\partial \tau_1} = 0, \tag{D1}$$

$$\eta > 0: \quad \frac{\partial^2 T_{D_1}}{\partial \eta^2} = \frac{\partial T_{D_1}}{\partial \tau_1} \tag{D2}$$

$$\eta < 0: \quad \frac{\partial^2 T_{D_1}}{\partial \eta^2} = \frac{\gamma}{\kappa} \frac{\partial T_{D_2}}{\partial \tau_1} \tag{D3}$$

The initial conditions are:

$$T_{D_a}(\xi_1,0) = T_{D_1}(\xi_1,\eta,0) = T_{D_2}(\xi_1,\eta,0) = -T_g(\eta - 1) \tag{D4}$$

The boundary conditions are:

$$T_{D_a}(0,\tau_1) = \begin{cases} 0 & \tau < 0 \\ 1 & \tau > 0 \end{cases} \tag{D5}$$

$$T_{D_a}(\xi_1,\tau_1) = T_{D_1}(\xi_1,0,\tau_1) = T_{D_2}(\xi_1,0,\tau_1) \tag{D6}$$

$$T_{D_1}(\xi_1,1,\tau_1) = 0. \tag{D7}$$

$$T_{D_2}(\xi_1, -\sigma,\tau_1) = T_g(\sigma + 1) \tag{D8}$$

After applying Laplace transformation with respect to τ_1, equations (D1)-(D3) become:

$$\eta = 0: \quad \left.\frac{\partial v_1}{\partial \eta}\right|_{\eta=0} - \kappa \left.\frac{\partial v_2}{\partial \eta}\right|_{\eta=0} - \frac{\partial u_a}{\partial \xi_1} - \theta_1 p u_a + \theta_1 T_g = 0 \tag{D9}$$

$$\eta > 0: \quad \frac{\partial^2 v_1}{\partial \eta^2} - p v_1 - T_g(\eta - 1) = 0 \tag{D10}$$

$$\eta < 0: \quad \frac{\partial^2 v_2}{\partial \eta^2} - q v_2 - T_g(\eta - 1) = 0 \tag{D11}$$

where q is defined as $q = (\gamma/\kappa)p$. The boundary conditions become:

$$u_a(0) = \frac{1}{p} \tag{D12}$$

$$u_a(\xi_1) = v_1(\xi_1, 0) = v_2(\xi_1, 0) \tag{D13}$$

$$v_1(\xi_1, 1) = 0 \tag{D14}$$

$$v_2(\xi_1, -\sigma) = \frac{T_g}{p}(\sigma + 1) \tag{D15}$$

Equations (D10) and (D11) are nonhomogeneous second-order ordinary differential equations. The general form of the equations for a dependent variable y is:

$$\frac{\partial^2 y}{\partial \eta^2} - p y = T_g(\eta - 1) \tag{D16}$$

To solve equation (D16) one must obtain a solution to the homogeneous equation (y_c) and a particular solution to the nonhomogeneous equation (y_p). The complete solution is then:

$$y = y_c + y_p \tag{D17}$$

The solution to the homogeneous equation is simply:

$$Y_c = A \cosh \sqrt{p}\,\eta + B \sinh \sqrt{p}\,\eta \tag{D18}$$

where A and B are constants. Now we guess a solution to the nonhomogeneous equation as:

$$y_p = C\eta + D \tag{D19}$$

where C and D are constants. Substituting equation (D19) into equation (D16) and equating the coefficients yields:

$$C = -\frac{T_g}{p} \tag{D20}$$

$$D = \frac{T_g}{p} \tag{D21}$$

The complete solution to equation (D16) can now be written as:

$$y = A \cosh \sqrt{p}\,\eta + B \sinh \sqrt{p}\,\eta - \frac{T_g}{p}(\eta - 1) \tag{D22}$$

After obtaining a solution for equation (D16), the solutions for equations (D10) and (D11) are:

$$\eta > 0: \quad v_1 = a_1 \cosh \sqrt{p}\,\eta + b_1 \sinh \sqrt{p}\,\eta - \frac{T_g}{p}(\eta - 1) \tag{D23}$$

$$\eta < 0: \quad v_2 = a_2 \cosh \sqrt{p}\,\eta + b_2 \sinh \sqrt{p}\,\eta - \frac{T_g}{p}(\eta - 1) \tag{D24}$$

where a_1, a_2, b_1, b_2 are constants. Applying boundary condition given by equation (D13) yields:

$$a_1 = a_2 = u_a - \frac{T_g}{p} \tag{D25}$$

Similarily, the boundary conditions given by equations (D14) and (D15)

can be used to determine b_1 and b_2:

$$b_1 = -\frac{\left[u_a - \frac{T_g}{p}\right]}{\tanh\sqrt{p}} \tag{D26}$$

$$b_2 = \frac{\left[u_a - \frac{T_g}{p}\right]}{\tanh\sqrt{q}\,\sigma} \tag{D27}$$

Substituting equations (D25)-(D27) into equations (D23) and (D24) yields:

$$\eta > 0: \qquad v_1 = \left[u_a - \frac{T_g}{p}\right]\cosh\sqrt{p}\,\eta - \frac{\sinh\sqrt{p}\,\eta}{\tanh\sqrt{p}} - \frac{T_g}{p}(\eta - 1) \tag{D28}$$

$$\eta < 0: \qquad v_2 = \left[u_a - \frac{T_g}{p}\right]\cosh\sqrt{q}\,\eta + \frac{\sinh\sqrt{q}\,\eta}{\tanh\sqrt{q}} - \frac{T_g}{p}(\eta - 1) \tag{D29}$$

Since the equations for the temperature in the caprock and bedrock have been solved in the Laplace domain, one can proceed to solve equation (D9):

$$\left.\frac{\partial v_1}{\partial \eta}\right|_{\eta=0} = -\frac{\sqrt{p}\left[u_a - \frac{T_g}{p}\right]}{\tanh\sqrt{p}} - \frac{T_g}{p} \tag{D30}$$

$$\left.\frac{\partial v_2}{\partial \eta}\right|_{\eta=0} = -\frac{\sqrt{q}\left[u_a - \frac{T_g}{p}\right]}{\tanh\sqrt{q}\,\sigma} - \frac{T_g}{p} \tag{D31}$$

Substitution of equations (D30) and (D31) into equation (D9) yields:

$$\frac{\sqrt{p}\left[u_a - \frac{T_g}{p}\right]}{\tanh\sqrt{p}} - \kappa\frac{\sqrt{q}\left[u_a - \frac{T_g}{p}\right]}{\tanh\sqrt{q}\,\sigma} - \frac{\partial u_a}{\partial \xi_1} - \theta_1 p u_a + \theta_1 T_g = 0 \tag{D32}$$

Rearrangement of equation (D32) yields:

$$\frac{\partial u_a}{\partial \xi_1} + \left[\theta_1 p + \frac{\sqrt{p}}{\tanh \sqrt{p}} + \kappa \frac{\sqrt{q}}{\tanh \sqrt{q}\,\sigma}\right] u_a$$

$$- \frac{T_g}{p}\left[\theta_1 p + \frac{\sqrt{p}}{\tanh \sqrt{p}} + \frac{\kappa\sqrt{q}}{\tanh \sqrt{q}\,\sigma}\right] = 0 \qquad \text{(D33)}$$

Now let us define $\bar{u}$ as:

$$\bar{u} = u_a - \frac{T_g}{p} \qquad \text{(D34)}$$

Substitution of equation (D34) into equation (D33) yields:

$$\frac{\partial \bar{u}}{\partial \xi_1} + \left[\theta_1 p + \frac{\sqrt{p}}{\tanh \sqrt{p}} + \frac{\kappa\sqrt{q}}{\tanh \sqrt{q}\,\sigma}\right] \bar{u} = 0 \qquad \text{(D35)}$$

The solution of equation (D35) is:

$$\bar{u} = C_1 \exp - \left[\theta_1 p + \frac{\sqrt{p}}{\tanh \sqrt{p}} + \frac{\kappa\sqrt{q}}{\tanh \sqrt{q}\,\sigma}\right] \xi_1 \qquad \text{(D36)}$$

where C_1 is a constant. Applying equation (D34) in terms of u_a yields:

$$u_a = C_1 \exp - \left[\theta_1 p + \frac{\sqrt{p}}{\tanh \sqrt{p}} + \frac{\kappa\sqrt{q}}{\tanh \sqrt{q}\,\sigma}\right] \xi_1 + \frac{T_g}{p} \qquad \text{(D37)}$$

The constant C_1 can now be determined using the boundary condition given by equation (D12):

$$C_1 = \frac{1}{p}\,[1 - T_g] \qquad \text{(D38)}$$

Substitution of equation (D38) into equation (D37) yields:

$$u_a = \frac{1}{p}\,[1 - T_g] \exp - \left[\theta_1 p + \frac{\sqrt{p}}{\tanh \sqrt{p}} + \frac{\kappa\sqrt{q}}{\tanh \sqrt{q}\,\sigma}\right] \xi_1 + \frac{T_g}{p} \qquad \text{(D39)}$$

Equation (D39) represents the temperature in the aquifer in the Laplace domain.

Asymptotic Solutions

At early times, the solution for the temperature in the Laplace domain is:

$$\eta = 0: \qquad u_a = \frac{T_g}{p} \tag{D40}$$

$$\eta > 0: \qquad v_1 = -\frac{T_g}{p}[\eta - 1] \tag{D41}$$

$$\eta < 0: \qquad v_2 = -\frac{T_g}{p}[\eta - 1] \tag{D42}$$

Equations (D40)-(D42) can easily be inverted from the Laplace domain to real space to yield:

$$\eta = 0: \qquad T_{D_a} = T_g \tag{D43}$$

$$\eta > 0: \qquad T_{D_1} = -T_g[\eta - 1] \tag{D44}$$

$$\eta < 0: \qquad T_{D_2} = -T_g[\eta - 1] \tag{D45}$$

Equations (D43)-(D45) represent the initial conditions specified in the problem. However, at a slightly later time, the temperature in the aquifer in the Laplace domain is:

$$u_a = \frac{1}{p}[1 - T_g] \exp - [\theta_1 p \xi_1] + \frac{T_g}{p} \tag{D46}$$

Equation (D46) can be inverted to real space to yield:

$$T_{D_a} = [1 - T_g]\, U_1[\tau_1 - \theta_1 \xi_1] + T_g \tag{D47}$$

At late times as $p \to 0$, $\tanh \sqrt{p} \to \sqrt{p}$ and the equations for the temperature in the Laplace domain simplify to:

$$\eta = 0: \qquad u_a = \frac{1}{p}\,[1 - T_g]\,\exp - \left[1 + \frac{\kappa}{\sigma}\right]\xi_1 + \frac{T_g}{p} \tag{D48}$$

$$\eta > 0: \qquad v_1 = \frac{1}{p}\,[1 - T_g][1 - \eta]\,\exp - \left[1 + \frac{\kappa}{\sigma}\right]\xi_1 - \frac{T_g}{p}\,(\eta - 1) \tag{D49}$$

$$\eta < 0: \qquad v_2 = \frac{1}{p}\,[1 - T_g]\,\left[1 + \frac{\eta}{\sigma}\right]\exp - \left[1 + \frac{\kappa}{\sigma}\right]\xi_1 - \frac{T_g}{p}\,(\eta - 1) \tag{D50}$$

Equations (D48)-(D50) can be inverted to real space to yield:

$$\eta = 0: \qquad T_{D_a} = [1 - T_g]\,\exp - \left[1 + \frac{\kappa}{\sigma}\right]\xi_1 + T_g \tag{D51}$$

$$\eta > 0: \qquad T_{D_1} = [1 - T_g][1 - \eta]\,\exp - \left[1 + \frac{\kappa}{\sigma}\right]\xi_1 - T_g(\eta - 1) \tag{D52}$$

$$\eta < 0: \qquad T_{D_2} = [1 - T_g]\,\left[1 + \frac{\eta}{\sigma}\right]\exp - \left[1 + \frac{\kappa}{\sigma}\right]\xi_1 - T_g(\eta - 1) \tag{D53}$$

Equations (D51)-(D53) give the steady state temperature distribution in the aquifer caprock and bedrock.

The steady state total heat losses from the aquifer can be calculated using the Fourier law of heat conduction. In dimensionless form the equation for the dimensionless total heat losses from the aquifer is:

$$Q_{D_t} = \left.\frac{\partial T_{D_1}}{\partial \eta}\right|_{\eta=0} + \left.\frac{\partial T_{D_2}}{\partial \eta}\right|_{\eta=0} \tag{D54}$$

Equations (D52) and (D53) can easily be differentiated with respect to η and evaluated at $\eta = 0$. Equation (D54) thus becomes:

$$Q_{D_t} = -[1 - T_g]\,\left[1 + \frac{1}{\sigma}\right]\exp - \left[1 + \frac{\kappa}{\sigma}\right]\xi_1 \tag{D55}$$